Imperial College London
Department of Mechanical Engineering

Influence of Inlet Distortion on Fan Aerodynamic Performance

Wenqiang Zhang

July 2019

Supervised by Prof. Mehdi Vahdati

Submitted in part fulfilment of the requirements for the degree of
Doctor of Philosophy in Mechanical Engineering of Imperial College London
and the Diploma of Imperial College London

Declaration of Originality

I herewith certify that all materials in this thesis which are not my own work has been properly acknowledged. No part of the work presented here has been submitted to any other University or Institution for any other qualification.

In this thesis, I has used parts of the contents from the papers published in the following conferences and journals:

Global Power and Propulsion Society 2017, ASME Turbo Expo 2018, ASME Turbo Expo 2019, 13th European Conference on Turbomachinery and Journal of Turbomachinery.

The copyright items from these conference and journals declare that the author retains the rights to continue using the contents.

— Wenqiang Zhang
July 2019

Copyright Declaration

The copyright of this thesis rests with the author. Unless otherwise indicated, its contents are licensed under a Creative Commons Attribution-Non Commercial 4.0 International Licence (CC BY-NC). Under this licence, you may copy and redistribute the material in any medium or format. You may also create and distribute modified versions of the work. This is on the condition that: you credit the author and do not use it, or any derivative works, for a commercial purpose. When reusing or sharing this work, ensure you make the licence terms clear to others by naming the licence and linking to the licence text. Where a work has been adapted, you should indicate that the work has been changed and describe those changes. Please seek permission from the copyright holder for uses of this work that are not included in this licence or permitted under UK Copyright Law.

Abstract

Inlet distortion can lead to loss in efficiency and stability margin of the fan which in return jeopardises flight safety. These aspects driven by inlet distortion are becoming increasingly challenging for the designers of next-generation turbofan engines. With the increase of computational capability and improvements in numerical models, computational fluid dynamics (CFD) is becoming increasingly powerful and favoured by scientific researchers and industrial engineers. Time-accurate, high-fidelity CFD simulations of the compressor behaviour at extreme operational conditions (such as during stall with inlet distortion) has become possible. In the present thesis, CFD is used to determine the effects of inlet distortion on fan aerodynamic stability and stall hysteresis. NASA stage 67 is used for this study. At the very beginning an appropriate numerical strategy was developed and validated with extensive experimental data. A good match was obtained for both the flow field variables at the peak efficiency point and the stall boundary.

In this research, two types of inlet distortion were examined. One is the consistent distortion which mimics the setup in experiments with slow throttling; another type is the abrupt distortion (due to sudden maneuver) whose effect is poorly understood. It will be shown that abrupt distortion can result in larger stall margin loss than consistent distortion. Therefore, experimental tests based on consistent distortion tend to be more optimistic in stall margin prediction. Thereafter the stall and recovery process of a transonic fan with both types of inlet distortions were performed. The results showed that the stall process with inlet distortion can be very different from that in uniform inflow. However, distortion has minor effect on the recovery point (corrected mass flow) of the fan and the clean flow region plays the most important role in the recovery process. In the presence of abrupt distortion, it was found that the stall margin of a fan can be influenced by the length of exit duct. This phenomenon was explained using the wave propagation theory. A shorter exit duct reduces the time lag of expansion pressure wave reflected from the nozzle, which upon arriving at fan trailing edge can prevent the fan from stalling. A critical length ratio was proposed which provides useful guidelines on test rig and engine design.

A preliminary study of the behaviour of the BLI fan with serpentine intake (S intake) at near stall condition and its stall process was performed. It was found that the distortion pattern upstream of the fan is complex and can be divided into different zones radially. The stall behaviour of the fan is similar to that with a circumferential distortion, but more complex because of the coupling with the swirl distortion near the casing. Although the present work is restricted to NASA stage 67, some of the conclusions gained are general and expected to be valid for modern fan and compressor designs.

Finally, during this research it has become apparent that there is a significant lack of open published measured data for fans and compressors operating under inlet distortions, which is mainly due to the difficulties and costs involved in setting up such experimental campaigns. The

above indicates that validated CFD codes are going to play an even more important role in development of distortion tolerant fans. The objective of this work is to show the suitability of CFD for the modelling of fan aerodynamic performance and stability with inlet distortion, which can provide an economical alternative strategy to subscale rig tests.

Acknowledgement

First and foremost, I would like to express my deepest appreciation to my supervisor, Professor Mehdi Vahdati, who provides me the precious chance to study in Imperial College London. In the past four years, he has given me so many invaluable instructions. He even corrected my paper and thesis word by word. He offers me a successful starting point for future research. I benefit so much from his meticulous character.

I would like to thank my second supervisor, Dr. Sina Stapelfeldt who spends lots of time reviewing my paper and provides me many useful instructions. Her encouragements actuate me to be more energetic in the pursuing of higher research achievements.

I must say that I am so luck to work with and study from Dr. Fanzhou Zhao, who behaves like my second supervisor as well. He granted me so much fruitful help in both research and daily life. I want to thank Mr. Yaozhi Lu (but will soon be Dr. Lu) for his useful tips which makes my life in London much better. Dr. Prathiban Sureshkumar helps me a lot with my English writing and documents proof read.

Next, I would like to acknowledge a number of people that provides me help and instructions. Professor Nick Cumpsty for the useful guidance on my research and intuitive instructions for job application. Dr. Mashy Green for the supervision of the GPU computing programme. Mr. Peter Higgs, Mr. Suriyanarayanan Venkatesh, Mr Kai Ye from Imperial College London and Dr. Feng Wang from Oxford University are appreciated.

Here I need to mention that my roommates, Dr. Yuqi Hu and Miss Cen Chen. Thank you for providing me a warm family which makes my life colorful.

Great thanks are given to China Scholarship Council (CSC) which supports my PhD study. The awards from ASME IGTI Turbo Expo and Great Britain-China Educational Trust (GBCET) are also acknowledged.

Finally, I would like to thank my parents which always support and encourage me. No matter how far I travel, you are always my warmest harbour.

Contents

1 Introduction **1**

1.1 Background . . . 1
1.2 Motivation . . . 2
1.3 Research Objectives . . . 3
1.4 Dissertation Overview . . . 3
1.5 Publication List . . . 4

2 Literature Review **6**

2.1 Classification of Inlet Distortion . . . 6
2.1.1 Total Pressure Distortion . . . 6
2.1.2 Total Temperature Distortion . . . 7
2.1.3 Swirl Distortion . . . 8
2.1.4 Rotating Inlet Distortion and Abrupt Inlet Distortion . . . 8
2.2 Compressor-distortion Interactions . . . 9
2.2.1 Effects of Inlet Distortion on Compressor Stall Margin . . . 10
2.2.2 Efficiency Loss Due to Inlet Distortion . . . 11
2.2.3 Distortion Transfer through the Compressor . . . 12
2.2.4 Interactions between Different Distortions . . . 13
2.2.5 Operational Condition of the Blade with Inlet Distortion . . . 13
2.2.6 Interaction between the Compressor and Its Upstream and Downstream Components . . . 17
2.3 Compressor Stall with Inlet Distortion . . . 19
2.3.1 Rotating Stall and Stall Inception Process . . . 19
2.3.2 Effects of Inlet Distortion on the Stall Inception Process . . . 21
2.3.3 Recovery from Stall . . . 23
2.4 Methods for Inlet Distortion Attenuation and Control . . . 24
2.5 Method to Study the Effects of Inlet Distortion . . . 25
2.5.1 Experimental Methods . . . 25
2.5.2 Analytical Models and Numerical Methods . . . 26
2.6 Boundary Layer Ingesting Propulsion . . . 31
2.7 Chapter Summary . . . 34

3 Methodology and Case Validation **35**

3.1 Challenges for CFD with Inlet Distortion . . . 35

3.2 Numerical Methodology . . . 36
3.2.1 CFD Solver . . . 36
3.2.2 Test Case . . . 37
3.2.3 Computational Domain and Boundary Conditions . . . 38
3.2.4 Steady Computations and Mesh Independence Validation . . . 39
3.3 Validation of the Unsteady Case with Inlet Distortion . . . 46
3.4 Influence of the Temporal Resolution . . . 53
3.5 Validation of Stall Boundary Prediction . . . 58
3.6 Chapter Summery . . . 63

4 Effect of Abrupt Inlet Distortion on Fan Stability 65
4.1 Introduction . . . 65
4.2 Influence of the Inlet Distortion on Rotor Performance at NS Condition . . . 67
4.3 Behaviour of the Tip Leakage Flow with Inlet Distortion . . . 70
4.4 Stall Process with Abrupt Inlet Distortion . . . 74
4.5 The Effect of the Abrupt Inlet Distortion Strength . . . 77
4.6 Influence of the Rotational Speed on Compressor Stall Margin . . . 81
4.7 Chapter Summery . . . 85

5 Stall and Recovery Process with Inlet Distortion 86
5.1 Introduction . . . 86
5.2 Case Setup . . . 86
5.3 Overview of the Entire Process . . . 87
5.4 Comparisons of the Stall Process . . . 88
5.5 Comparisons of the Recovery Process . . . 94
5.6 Comparisons of the Stall Hysteresis between Two Types of Inlet Distortion . . . 96
5.7 Chapter Summery . . . 97

6 Influence of the Exit Duct on Fan Stall Margin 99
6.1 Introduction . . . 99
6.2 Influence of the Length of the Exit Duct on Fan Stall Margin with Inlet Distortion 99
6.3 Wave Propagation within the Exit Duct . . . 105
6.3.1 Computational Model for Isolated Exit Duct . . . 105
6.3.2 Propagation of Distortion-induced Waves . . . 107
6.3.3 Reflection by the Sonic Front in Choked Nozzle . . . 112
6.3.4 Reflection due to Geometry Change . . . 113
6.3.5 Compression System Geometry and Aerodynamic Stability . . . 116
6.3.6 Influence of the Exit Duct Length on Stall Margin with Clean Inflow . . . 118
6.4 Chapter Summery . . . 120

7 Performance of the Boundary Layer Ingesting Fan 122
7.1 Computational Domain with S Intake . . . 122
7.2 Analysis of the Distortion Pattern . . . 125

7.3 Coupling between the S Intake and the Fan 128
7.4 Stall Process of the BLI Fan 133
7.5 Chapter Summary 137

8 Conclusions and future work **139**
8.1 Conclusions 139
8.2 Recommendations for Future work 141

9 Appendix I **144**

Bibliography **147**

List of Tables

3.1 Mesh quality of three different grids 40
3.2 Mesh quality of different components 40
3.3 The strength of the inlet distortion for different rotational speeds 62

4.1 Loss in stall margin and total pressure for different rotational speeds 84

6.1 Setups for two different exit duct cases 106

7.1 Total pressure ratio and isentropic efficiency of the cases with straight intake and S intake 129

List of Figures

2.1 Effect of varying circumferential angle of distortion on compressor [Reid, 1969] . 7
2.2 Flow pattern at fan-face with cross wind: (a) streamlines around the intake (b) total pressure contours [Lee et al., 2019] 8
2.3 Flow coefficients at stall versus distortion rotation rate for compressors with (a) spike and modal wave (b) perturbation [Longley et al., 1996] 9
2.4 A typical steady state performance map of a compressor 10
2.5 Compressor response to inlet total temperature distortion [Longley and Greitzer, 1992] 11
2.6 Local operating points around the annulus of NASA stage 35 subjected to a total pressure distortion [Gong, 1999] 14
2.7 (a) Streamtrace rakes at rotor LE and TE [Fidalgo, 2013] (b) Matching of inlet and exit sectors by using time-averaged particle paths [Fidalgo et al., 2012] . . . 15
2.8 Operating conditions for the orbits and the overall compressor [Fidalgo et al., 2012] 15
2.9 Main drivers of orbit shape [Fidalgo, 2013] 16
2.10 Response time of the rotor to inlet distortion: (a) Distance a particle of fluid must travel to the throat of the blade passage to reach the start of the major diffusion process (b) Blade time constant comparison to a distorted inflow determines the magnitude of the blade response [Cousins, 1997] 17
2.11 Angle-of-attack distortion with and without fan coupling [Motycka, 1985] 18
2.12 Effect of downstream components on static pressure distortion at compressor exit-experimental results [Greitzer et al., 1978] 18
2.13 Effects of downstream components on compressor performance with inlet distortion [Greitzer et al., 1978] 19
2.14 Typical fixed-speed performance characteristic for an axial flow compressor [Day, 2016] 20
2.15 Criteria of spike stall: (a) Spillage of tip-leakage flow at the leading edge (b) Tip-clearance backflow at the trailing edge [Tan et al., 2010] 21
2.16 Measured inlet axial velocity profile in front of the fan at the design operating point [Perovic et al., 2015] 23
2.17 Schematic of radial and forward swept rotors and rotor blisk photos [Wadia et al., 2004] 24
2.18 Tests with inlet distortion: (a) a typical total pressure distortion screen [Lieser et al., 2010] (b) burner installed in inlet plenum [Mehalic, 1988] 26
2.19 Swirl distortion generators: (a) Stream vane [Guimares et al., 2017] (b) A versatile swirl generator [Sheoran and Bouldin, 2008] 26

2.20 Illustration of parallel compressor theory [Cousins and Davis, 2011] 28
2.21 Aircraft propulsion system design for boundary layer ingesting: (a) Blended wing body (BWB) [Liebeck, 2004] (b) Distributed propulsion system [Wick et al., 2015] (c) NASA's STARC-ABL concept [Jansen et al., 2016] and the (d) D8 double-bubble [Uranga et al., 2014] 32
2.22 Distortion pattern generated by the S intake: (a) Total pressure [Arend et al., 2017] and (b) Swirl distribution [Giuliani and Chen, 2016] at the exit of the serpentine duct 33
2.23 Preliminary fan stage map showing the approximate achievement in stability margin [Cousins et al., 2017] 34

3.1 Schematic of the W8 single-stage axial compressor test facility [VanZante et al., 2009] 38
3.2 (a) Flow path schematic for NASA 67 fan stage (b) Isometric view of the computational domain of NASA rotor 67 with inlet distortion 38
3.3 Characteristic of the rotor 67 with different grids 40
3.4 Rotor 67 characteristics in clean flow 41
3.5 Circumferentially averaged, radial distributions downstream of the rotor for peak efficiency (PE) and near stall (NS), 100% speed 42
3.6 CFD and LDV results of blade-to-blade flow at 30% span from hub, PE, 100% speed 43
3.7 CFD and LDV results of blade-to-blade flow at 70% span from hub, PE, 100% speed 43
3.8 CFD and LDV results of blade-to-blade flow at 90% span from hub, PE, 100% speed 44
3.9 CFD and LDV results of blade-to-blade flow at 30% span from hub, NS, 100% speed 44
3.10 CFD and LDV results of blade-to-blade flow at 70% span from hub, NS, 100%speed 45
3.11 CFD and LDV results of blade-to-blade flow at 90% span from hub, NS, 100% speed 45
3.12 Stage 67 performance map in clean flow 46
3.13 Time-averaged absolute circumferential total pressure at middle span upstream of the rotor at station 1, CFD (solid curve) and Experimental data (circle) 47
3.14 Time-averaged circumferential results at mid-span downstream of the rotor (station 2), CFD (solid curve) and Experimental data (circle) 47
3.15 Amplitude of the harmonics of the total pressure at mid-span upstream of the rotor, PE 48
3.16 Amplitude of the harmonics of the total pressure at mid-span downstream of the rotor, PE 48
3.17 Time-averaged radial profile of the total pressure upstream of the rotor at circumferential angle =322.5° and =175.5°, CFD (solid curve) and Experimental data (circle) 49
3.18 Time-averaged absolute circumferential swirl angle at mid-span at rotor upstream, CFD (solid curve) and Experimental data (circle) 50
3.19 Time-averaged circumferential measurement results downstream of the rotor at mid-span, CFD (solid curve) and Experimental data (circle) 51

3.20 Time-averaged radial profile of total pressure downstream of the rotor at circumferential angle =283°, CFD (solid curve) and Experimental data (circle) 51
3.21 Time-averaged radial profile of total pressure downstream of the rotor at circumferential angle =73°, CFD (solid curve) and Experimental data (circle) 52
3.22 Time-averaged circumferential measurement results downstream of the stator at mid-span, CFD (solid curve) and Experimental data (circle) 52
3.23 Amplitude of the circumferential wave numbers of the total pressure at the mid-span downstream of the rotor, PE and NS, 2,200 time steps/rev 53
3.24 Stall margin loss with inlet distortion running with different time steps/rev . . . 54
3.25 Mass flow history at the rotor outlet with different time step size 55
3.26 Axial velocity of the rotor outlet, (a) 3,300 and (b) 550 time steps/rev 55
3.27 Circumferential contour of the axial velocity at 98% rotor span, 550 (left) and 3,300 time steps/rev (right) 56
3.28 Spectrum of the casing static pressure signal for (a) 550 time steps/rev and (b) 3,300steps/rev (c) experimental data [Perovic et al., 2015] 58
3.29 NASA stage 35 actuation and instrumentation schematic with inlet distortion . . 59
3.30 Computational domain of stage 35 60
3.31 Compressor map of (a) NASA stage 35 and (b) rotor alone 61
3.32 Compressor map with DC120 distortion 63

4.1 Initial clean and final operational points for NS and RS at 90% corrected speed . 66
4.2 Physical mass flow history at the rotor exit for NS and RS 66
4.3 Instantaneous contours at the stator inlet for (a) NS and (b) RS at the 6^{th} revolution 67
4.4 Absolute swirl angle and incidence at the rotor inlet, middle span, NS 68
4.5 Circumferential contour of the axial velocity for NS, 98% rotor span 68
4.6 Orbit map of the PE and the NS, 22 sectors 69
4.7 The vortex in front of the rotor for NS 71
4.8 Tip leakage flow of the initial clean flow solution for NS 72
4.9 Tip leakage flow for NS at different circumferential positions 74
4.10 The circumferential contour of the axial velocity at 98% span of the rotor for NS (left) and RS (right) at different time (legend is the same with Figure 4.5) 76
4.11 The effects of the strength of the inlet distortion on the stall margin loss 77
4.12 The performance of the rotor with 2% inlet distortion 78
4.13 Total pressure at the rotor outlet for (a) Case I and the (b) Case II 79
4.14 (a) Circumferential-averaged radial total pressure (b) Total temperature profile of Case I and Case II 79
4.15 Contour of the axial velocity at rotor middle span (a) The thick boundary layer in Case I (b) Vortex shedding in Case II 81
4.16 Stall lines of the single rotor with inlet distortion at different rotational speeds . 82
4.17 Time-averaged incident angle at 98% span of the rotor at the NS condition . . . 83
4.18 Radial distribution of total pressure at rotor exit for the PE condition at different rotational speeds 84

4.19 Stall margin loss of stage 67 with inlet distortion at different rotational speeds . 85

5.1 Mass flow history of the stall and recovery process for Case 1 and Case 2 87
5.2 Computed hysteresis curves in (a) Case 1 and (b) Case 2 88
5.3 Axial velocity contours of stator inlet at different time during stall process, Case 1 89
5.4 Axial velocity at 98% rotor span (stationary frame) during stall process of Case 2 89
5.5 Time traces of axial velocity of 6 upstream probes, (a) Case 1 and (b) Case 2 . . 91
5.6 (a) Stall cell size defied with the volume enveloped by the iso-surface of zero axial velocity (b) Reference volume marked with black box 91
5.7 Mass flow and static pressure oscillations during stall process in (a) Case 1 and (b) Case 2 92
5.8 Influence of the inlet distortion on stall cell pattern 94
5.9 Time traces of axial velocity from 6 upstream probes during recovery process, Case 1 94
5.10 Time traces of axial velocity from 6 upstream probes during recovery process, Case 2 95
5.11 Axial velocity of stator inlet at different instants of time 95
5.12 Axial velocity contours at 98% rotor span during recovery process: (a) Case 1 and (b) Case 2 96
5.13 Computed hysteresis for the cases with abrupt distortion and consistent distortion 97

6.1 Typical compressor test rig 99
6.2 Computational domain of NASA Stage 67 with (a) long and (b) short exit duct . 100
6.3 Compressor map for 90% corrected speed 100
6.4 Axial velocity contour at fan exit for the case with (a) short exit duct and (b) long exit duct 101
6.5 Analysis approach in the exit duct (contour is only for illustration) 101
6.6 Circumferential modal contents of static pressure perturbations at *t=2 rev* 102
6.7 Time history of static pressure axial profile at middle span in the short and long exit duct 103
6.8 Time history of the mass flow at the stator exit 104
6.9 Stall margin loss for different exit duct length 104
6.10 3-D and meridian view of the computational domain 106
6.11 (a) Meridian view of the exit duct and nozzle; (b) Clean flow Mach number contour on the periodic boundary (Case 1) 107
6.12 Time history of Riemann invariants at station A 108
6.13 Standard shock tube model 109
6.14 Half shock tube model 109
6.15 Time history of static pressure, density and axial velocity perturbations at station A 111
6.16 Wave transmission and reflection at the sonic front 112
6.17 Time history of Riemann variables at station B 112
6.18 Time history of static pressure, density and axial velocity perturbations at station B 113
6.19 Meridian view of the exit duct and nozzle 113

6.20 Time history of Riemann variables at station E (solid curves) and station F (dashed curves) . . . 114
6.21 Time history of static pressure, density and axial velocity perturbations at station E . . . 115
6.22 Meridian view of the slowly varying exit duct . . . 115
6.23 Time history of Riemann variables at station G (solid curves) and station H (dashed curves) . . . 116
6.24 Schematic illustration of the simple model . . . 117
6.25 Time history of the mass flow at the stator exit . . . 119
6.26 Time history of static pressure axial profile at middle span in the short (left) and long (right) exit duct . . . 120

7.1 Computational domain of the NASA stage 67 with S intake . . . 122
7.2 Main geometry parameters of the S duct (normalized by the rotor diameter D) . . . 123
7.3 Comparisons of the nose geometry: (a) original and (b) shorted . . . 123
7.4 (a) Contour of the total pressure (b) Radial distribution of the total pressure at the inlet surface of the S intake . . . 124
7.5 Compressor map of NASA stage 67 with straight intake and S intake . . . 125
7.6 Flow pattern at NS condition at the exit of the S intake: (a) total pressure contour, (b) swirl angle, (c) radial angle (d) vortex pattern upstream of the rotor . . . 127
7.7 Circumferential Total pressure profile at different radial positions (NS - solid line and PE - dashed line), rotor inlet (circumferential coordinate is marked in 7.6b) . . . 128
7.8 Circumferential swirl angle profiles at different radial positions at NS condition, rotor inlet . . . 128
7.9 Circumferential averaged radial profile of the rotor total pressure ratio . . . 130
7.10 Comparisons of the axial velocity of on the stator with (a) straight intake and (b) S intake . . . 131
7.11 Radial profile of the inflow circumferential angle at stator inlet . . . 131
7.12 Total pressure contour at the rotor inlet of (a) PE and (b) NS . . . 132
7.13 Meridian contour of the axial velocity in the S intake with stall cell at lower annulus:(a) and (b), stall cell at upper annulus: (c) and (d) . . . 133
7.14 Axial velocity contour at 98% span . . . 133
7.15 Orbits of the BLI fan at NS condition . . . 134
7.16 Physical mass flow at the rotor inlet . . . 135
7.17 Contour of the axial velocity at 98% span of the rotor . . . 136
7.18 History of the axial velocity of 6 numerical probes . . . 137

8.1 Computational domain of a low-speed fan stage . . . 142

9.1 Radial profiles downstream of the stator, 100% rotational speed, corrected mass flow=21.0 kg/s . . . 144
9.2 Radial profile downstream of the stator, 100% rotational speed, corrected mass flow=19.6 kg/s . . . 145

9.3 Bleeding slot in front of the rotor 145
9.4 Radial profiles downstream of the stator, 70% rotational speed (corrected mass flow=14.46 kg/s) 146

Nomenclature

Acronyms

Symbol	Description
BLI	Boundary Layer Ingesting
BPR	Bypass Ratio
DC	Distortion Coefficient
DFT	Discrete Fourier Transform
EXP	Experimental Data
FPR	Fan Pressure Ratio
HP	High Pressure
IGV	Inlet Guide Vane
LDV	Laser Doppler Velocimetry
LE	Leading Edge
LES	Large Eddy Simulation
LP	Low Pressure
NS	Near Stall
PE	Peak Efficiency
PR	Pressure Ratio
$RANS$	Reynolds-Averaged Navier-Stokes
RS	Rotating Stall
SFC	Specific Fuel Consumption
SM	Stall Margin
TE	Trailing Edge
TVD	Total Variation Diminishing

$URANS$	Unsteady Reynolds-Averaged Navier-Stokes
$VIGV$	Variable Inlet Guide Vane

Greek Symbols

Symbol	**Description**
α	Swirl Angle
δw	Riemann Invariant
γ	Heat Capacity Ratio
ω	Frequency
ρ	Density
θ	Angle

Roman Symbols

Symbol	**Description**
$\dot{m}$	Mass Flow Rate
B	Half Chord Length
c	Sound Speed
D	Diameter
f	Frequency
L	Axial Length
Ma	Mach Number
N	Rotational Speed
n, i	Integer Counter
P	Total Pressure
p	Static Pressure
R	Gas Constant
T	Total Temperature
t	Time
U, V	Velocity

W	Weight Flow
x	Axial Coordinate

Subscripts

Symbol	**Description**
bp	Blade Passing
$corr$	Corrected
$crit$	Critical
d	Distorted Value
g	Gas
o	Standard Sea Level Pressure/temperature
ref	Reference Value
rev	Revolution
s	Near Stall Value
t	Stagnation Value
t	Total Pressure/temperature

1 Introduction

1.1 Background

Inlet distortion refers to the non-uniform inflow in front of the aero engine. The performance of the fans and compressors can be detrimentally affected by inlet distortion in terms of efficiency and stability. Nevertheless inlet distortion can hardly be avoided in the engine operation.

In the last few decades, the environmental effects of flight have been a big concern. The noise and air pollution generated by the aircraft engines place a threat on the environment and this has become a driving force for the research and development of the new generation of engines. The trends of the engine design have concentrated on cutting down specific fuel and noise reduction lead to larger bypass ratio and lower fan pressure ratio [Suder et al., 2013]. To increase the fan diameter without incurring the penalty of weight and drag, reduced axial length intakes are adopted [Hughes, 2011]. The capability of the short inlet duct to attenuate the inlet distortion via internal flow diffusion is decreased and this makes the occurrence of inlet distortion more severe.

Another example involved with distortion problem is BLI propulsion [Kawai et al., 2006]. By utilizing fluid from the fuselage boundary layer as part of the entire propulsive stream, BLI can enable potential fuel consumptions savings and effectively attenuating the noise generated by the engines. One of the main challenges with BLI is the fact that the compression system of the engines is forced to operate with significant levels of total pressure and swirl distortions due to the ingestion of the boundary layer as well as secondary flow within the S intake. Therefore, the engine must be robust against distortion. The configurations of the distortion pattern studied before [Soeder and Bobula, 1982, Rabe et al., 1995, Soeder et al., 1985] are usually simple while the real distortion can be very complex ahead of a BLI fan. How such distortion affects the operation and safety of the fan needs to be figured out in order to facilitate the design of the engine.

As can be seen from the above challenges in the development of new aero-engines, the understanding of inlet distortion is still not enough and further investigations are needed. Considering that full scale tests with the engine are expensive, subscale models are typically adopted. Such kind of tests fail to reproduce the flow field in a real engine as the Reynolds numbers are very different although the Mach number are the same which will result in large areas of laminar flow. Moreover, experimental tests are very costly and distortion can cause damage to the engine. In contrast, CFD simulations provide an economical and faster way. With the development of computational capability and the advance of the numerical algorithms, CFD is becoming more and more prevalent in the field of turbomachinery. High-fidelity simulation can display more details of the flow field inside the compressor and shed lights on the mechanisms of distortion

interaction.

1.2 Motivation

To the author's best knowledge, CFD studies with inlet distortion are generally performed at the design operational condition [Fidalgo et al., 2012, Yao et al., 2007, Yao et al., 2010a, Hah et al., 1996]. The high-fidelity simulation of the stall process with inlet distortion is still challenging and hence appropriate strategy is needed. Due to the lack of experimental data, especially the compressors stall boundary with inlet distortion, the simulations are usually performed without validation which calls their credibility into question. The reliability of the code and simulation strategies used need to be verified before conducting further computations.

In the compressor tests with inlet distortion, a distortion screen is imposed in front of the compressor to generate a total pressure loss of a fixed pattern. By gradually throttling the compressor, the stall/surge boundary can be obtained by inspecting the mass flow and pressure ratio of the compressor. The distortion exists during the whole process and the strength of the distortion is stable. Most of the inlet distortions tested are consistent distortion. Such kind of tests have revealed a lot of useful knowledge about the steady or quasi-steady performance of the compressor with inlet distortion. However, such a method cannot be used to estimate the potential influence of abrupt inlet distortion, in which the transient response of the compressor is of concern. Abrupt distortion denotes the distortion which occurs unexpectedly in front of the fan before which the inflow is uniform. Such kinds of distortion can be generated by cross wind or the ingestion of the vortex which are quite common during the flight. With abrupt distortion, the inflow condition undergoes a sudden corruption which can severely disturb the condition of the compressor instantaneously. It will be shown that such kind of distortion can be more harmful. However, such kind of inlet distortion is less studied. The potential influence of this abrupt inlet distortion on the compressor thus needs to be explored.

Rotating stall and surge represent the aerodynamic instability of the flow through a compressor. In this research, the instability phenomenon concerned is rotating stall caused by the interaction between the inlet distortion and the blade row. Surge is a system instability due to the interaction between the compressor and the attached volumes in a given compression system [Barrera-Medrano et al., 2017]. The research on compressor rotating stall mainly focus on the pre-stall behaviour of the compressor and the stall control methodologies. The recovery process from the rotating stall, however, receives less attention. This may be due to the safety considerations in experiments and the limitations of the CFD capability. However, the ability of the compressor to recover from rotating stall is very important to evaluate its robustness and operational range. Moreover, the potential influence of inlet distortion on the compressor recovery process is unknown. It is considered that the distortion might aggravate the difficulty for the compressor to remove the stall cell and postpone the recovery. Consequently computations need to be conducted to figure out the potential effects of the distortion on the stall hysteresis loop. Preliminary studies have already revealed the response of a BLI fan to the distortion at [Gunn and Hall, 2014, Giuliani, 2016, Giuliani and Chen, 2016, Arend et al., 2017]. However, the near

stall behaviour and the stall process of the BLI fan are seldomly reported. Besides, in some computations, truncated computational domain (without using an S intake) with a fixed inlet boundary condition is adopted to mimic the flow pattern at the exit of the S intake [Gunn and Hall, 2014]. Such kind of setup fails to include the interactions between the S intake and the fan especially in the stall process.

1.3 Research Objectives

This research mainly concentrates on the understanding of the basic flow mechanism with inlet distortion in a transonic fan. Specifically, the goal of this research can be presented as:

"How inlet distortion affects the stall behaviour of the compressor and its underlying mechanisms."

The above question can be broken down into three different objectives, which basically determine the structure of this thesis:

1. Establish a suitable computational strategy to accurately reproduce the performance of the fan with inlet distortion; compare CFD against available experimental data.

2. Determine how inlet distortion affects the operational condition of the fan especially at the near stall point, identify the stall and recovery process of the fan with abrupt inlet distortion; investigate the performance of a BLI fan with an S intake.

3. Conduct a parametric study to explore how different parameters influence the stall margin of a fan with inlet distortion and the underlying mechanism.

1.4 Dissertation Overview

Chapter 2 presented a literature review of the inlet distortions relevant to axial fan and compressors. The classification of the inlet distortion and how the inlet distortion affects the compressor were summarised in detail. The focus was the effects of the inlet distortion on the compressor stability margin. The methodologies for distortion control were also listed. In the last section of this chapter, the history of the development of the BLI propulsion was briefly introduced.

In chapter 3, NASA stage 67 was adopted to validate the simulation strategy with DC120 distortion and good match was obtained between the experimental data and CFD. The effects of inlet distortion on the compressor at peak efficiency point and near stall point were presented. The sensitivity of the predicted stall margin to temporal and spatial resolution was discussed. Thereafter NASA stage 35 was computed to validate the stall margin prediction capability of the simulation strategy. An approach was proposed to estimate how distortion strength changes with the compressor rotational speed. The simulation results successfully captured the distorted stall margin at different rotational speed, which confirms the suitability of the numerical strategy.

Chapter 4 studied the stall process with abrupt inlet distortion. It was shown that such kind of inlet distortion is more harmful to the fan than consistent distortion. The working condition of the blade around the annulus at near stall point was demonstrated with orbit method. The fluctuation of the tip leakage flow was also illustrated to show how the blade loading changes when it went through the clean flow sector and distorted sector. The flow in the tip region was

inspected to show the route that compressor fell into rotating stall. Thereafter the influence of the strength of the inlet distortion as well as the compressor rotational speed was simulated to study the effects on the fan stall margin.

In Chapter 5, it was found that the axial length of the exit duct downstream of the fan plays an important role in the compressor stability. The short exit duct can facilitate the reflected waves from the nozzle to reduce the loading of the compressor before it falls into stall, and thus this is beneficial to the compressor. Quasi-one-dimensional simulations of a straight duct with a nozzle showed that an abrupt inlet distortion can generate different waves propagating downstream. How the nozzle reflects these waves and the influence of the reflected waves on the flow field were studied. An analytical "half shock wave tube" model was built to predict the behaviour of the distortion-generated waves. Two critical ratios about the axial length of the compression system was proposed based on stability considerations.

In Chapter 6 the stall and recovery process with and without inlet distortion were performed and compared. The downstream nozzle was gradually closed to push the fan into stall and opened to unstall the compressor. The difference in the stall inception was compared between two cases. The in-stall behaviour of the fan (stall cell size and the rotational speed of the stall cell) was investigated. By examining the mass flow difference between the stall point and the recovery point, how the inlet distortion influences the hysteresis loop was demonstrated and explained.

A preliminary study of the BLI fan at different operational conditions and its stall process was shown in Chapter 7. The pattern of the typical distortion upstream of the fan was decomposed and analysed, which shed light on its effects on the fan performance. It was also shown that the conclusions obtained with DC120 distortion are general and can be applicable for complex distortion patterns.

The last chapter lists all the conclusions reached in this research. The future work will be carried out with a modern low-speed fan. The response of a low-speed fan to the inlet distortion will be investigated and potential control strategy will be tested.

1.5 Publication List

In this section, the publications in journals and conferences during the PhD course are listed below. The synopses of these papers are briefly introduced.

Wenqiang Zhang, Mehdi Vahdati. Influence of the inlet distortion on fan stall margin at different rotational speed. GPPS conference paper, 2017-0207

Wenqiang Zhang was the lead author of this conference paper, Prof. Mehdi Vahdati acts as the supervisory role. This paper forms part of Chapter 3 and Chapter 4 in the thesis. In this paper, the validation of the methodology used for the simulations with inlet distortion was presented. A parametric study regarding the influence of temporal resolution and rotational speed of the compressor on stall margin was investigated and discussed.

Wenqiang Zhang, Mehdi Vahdati. A Parametric Study of the Effects of Inlet Distortion on Fan Aerodynamic Stability. Journal of Turbomachinery 141.1 (2019): 011011.

Wenqiang Zhang performed all the simulations in this paper with the supervision of Prof. Mehdi Vahdati. This paper forms part of the Chapter 4 in the thesis. The performance of the compressor with inlet distortion at near stall condition was demonstrated in this paper. It was also the first publication that shows the length of the exit duct affects the stall margin of the compressor under distorted inflow condition.

Wenqiang Zhang, Mehdi Vahdati, Sina Stapelfeldt. Stall and Recovery Process of a Transonic Fan in Presence of Inlet Distortion. Proceedings of 13th European Conference on Turbomachinery Fluid dynamics and thermodynamics, ETC2019-371

This conference paper was authored by Wenqiang Zhang and it was instructed by Prof. Mehdi Vahdati and Dr. Sina Stapelfeldt. In this paper, the stall and recovery process of a transonic compressor with and without inlet distortion was carried out to explore how inlet distortion changes the stall hysteresis of the compressor. Chaper 5 in the thesis was based on this paper.

Wenqiang Zhang, Mehdi Vahdati, Fanzhou Zhao. Impact of exit duct dynamic response on compressor stability. GT2019-90864, ASME Turbo Expo, Phoenix, 2019

Wenqiang Zhang finished this conference paper under the supervision of Prof. Mehdi Vahdati. Dr. Fanzhou Zhao provided important suggestions and corrected this paper. In this paper. the underlying mechanism of how the length of the exit duct influence the stall margin of the compressor was demonstrated in detail, which forms Chapter 6 in the thesis.

2 Literature Review

In this chapter, the published literature relevant to inlet distortion are reviewed. In the first section the classification of inlet distortion and their main features are briefly introduced. The influence of inlet distortion on the performance and stability of a compressor is discussed in the second section. The third section presents some basic knowledge about compressor stall and how inlet distortion influences the stall process. The experimental and numerical study on the recovery process of the compressor from stall is mentioned as well. Afterwards, the experimental, analytical and numerical methodologies used to investigate inlet distortion are listed and presented. The methods for inlet distortion control are also summarized concisely. In the last part of this chapter, the concept and development progress of BLI propulsion are reviewed.

2.1 Classification of Inlet Distortion

Although the configurations of distortions are complex in the operation of a compressor, they can be roughly classified according to their effect, pattern, motion state or duration time. Regarding their effects on the flow field, distortions are categorized into total pressure distortion, total temperature distortion and swirl distortion; in terms of pattern, distortions are usually classified into circumferential distortion and radial distortion; when motion state is considered, distortions can be divided into two types: stationary distortion and rotating distortion. Depending on the duration time of distortions, they can be sorted into consistent distortion or abrupt distortion. It is noted that the real distortion in front of a compressor or within a compressor can be very complex. For example, it can be a combination of different types of distortions, which can be highly non-linear and coupled; the pattern might not be purely circumferential or radial. Typically a distortion is usually named depending on its dominant component.

Considering the fact that most of the research focus on circumferential, stationary, total pressure distortion, total temperature distortion and swirl distortion, distortions will be introduced based on their effects, i.e. which parameter of the flow field is influenced. Particularly, in this section the total pressure distortion refers to the inlet flow with lower total pressure than the clean inflow; total temperature distortion means the total temperature is higher in the distorted region.

2.1.1 Total Pressure Distortion

Total pressure distortion is frequently encountered ahead of the aircraft engine during the flight. It can be caused by intake flow separation, boundary layer ingestion, grounded vortex ingestion and cross wind. Total pressure distortion can reduce the stable operating range of the compressor

and jeopardize the safety of the engine. Efficiency of the engine is also reduced due to flow loss caused by off-design inflow conditions. The mechanism of the stall margin and efficiency reduction will be discussed in section 2.2. A lot of experiments have been carried out to investigate the influence of total pressure distortion on aero-engines [Biesiadny et al., 1986]. Experimental studies provide precious empirical knowledge of how total pressure distortion influence the compressor efficiency and stall margin. A good summary of the discoveries from these studies can be found in [Reid, 1969] and [Longley and Greitzer, 1992]. The main conclusions in [Reid, 1969] are briefly introduced as following:

1. Both circumferential distortion and radial distortion are tested and circumferential distortion is more harmful to compressor stall margin than radial distortion.

2. For circumferential distortion, the delivery pressure at stall can be improved if it is divided into several parts of equal area while the total angular area is fixed.

Another observation indicates that there exists a circumferential angle extent for the circumferential distortion above which the exit static pressure at stall does not change (see Figure 2.1). This angle (referred to as critical angle) is around 60 degrees for many compressors. Critical angle is not fixed for all compressors. It was also mentioned by Reid [Reid, 1969] that the critical angle is substantially larger for new designed engines when they possess better tolerance to distortion.

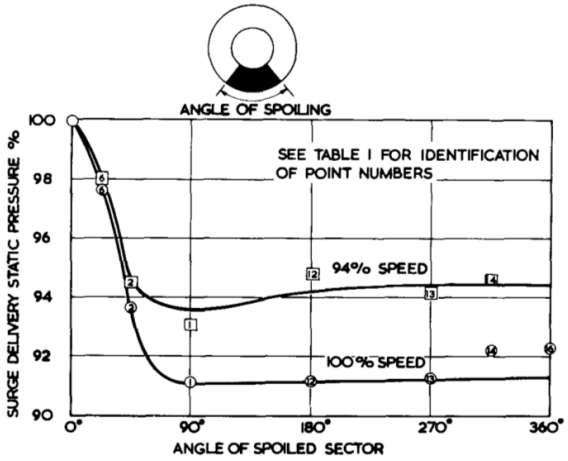


Figure 2.1: Effect of varying circumferential angle of distortion on compressor [Reid, 1969]

To evaluate the strength and size of total pressure distortion, the inlet distortion descriptor was developed. Detailed introduction is referred to [SAE Standard, 2013].

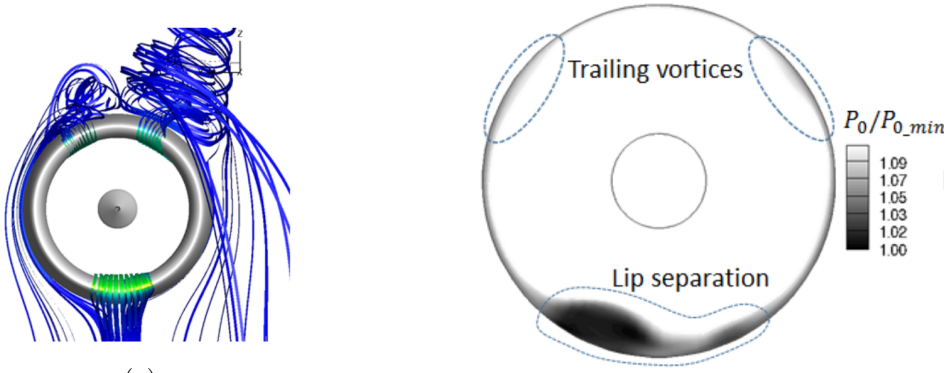
2.1.2 Total Temperature Distortion

Total temperature distortions are generally caused by thrust reverser exhaust ingestion, weapon hot gas ingestion, vertical take-off and landing, steam ingestion from catapult launch systems on an aircraft carrier and mid-air refuelling. The overall effect of total temperature distortion on the compressor, namely a reduction in stall margin and efficiency, is basically the same with total pressure distortion. The compressor usually possesses the ability to attenuate the total pressure distortion but amplifies the temperature distortion [Reid, 1969, Yao et al., 2007, Yao et al., 2010a].

Total temperature distortion from upstream components will propagate and influence the stability of the downstream components such as the combustion chamber.

2.1.3 Swirl Distortion

Swirl distortions are generated ahead of the compressor due to tortuous inlet systems, cross wind or ingestion of the ground vortex. Inside the compressor, upstream flow field redistribution and secondary flow can also give rise to swirl distortion. Swirl distortions are further divided into four main categories: bulk swirl, tightly-wound vortices, paired swirl and cross-flow swirl [SAE Standard, 2017]. Real swirl patterns can be quite complex and they are often accompanied by total pressure distortion and flow separation. For example, it was observed that for sufficiently high amplitudes of crosswind, the flow near intake lip separates and two contra-rotating trailing vortices are generated (Figure 2.2) [Lee et al., 2019].



(a) (b)

Figure 2.2: Flow pattern at fan-face with cross wind: (a) streamlines around the intake (b) total pressure contours [Lee et al., 2019]

2.1.4 Rotating Inlet Distortion and Abrupt Inlet Distortion

Rotating distortion refers to the distortion which moves around the annulus. For example, a stalled upstream blade row will impose a rotating distortion on the downstream blade rows. The influence of such distortion on the compressor is determined by its rotational direction and speed. Experimental study [Longley et al., 1996] found that co-rotating distortion (distortion that has the same direction as the rotor) will cause larger stall margin degradation than the counter-rotating distortion (distortion with opposite rotational direction as the rotor). How stalling mass flow rate changes with the rotational speed of the distortion was found to be compressor specific and varies with the type of stall inception disturbances. With co-rotating distortion, the compressors which stall via modal wave type inception exhibit one resonant peak (Figure 2.3a), while the compressors stall via spike type inception exhibit two resonant peaks (Figure 2.3b). For a compressor with modal wave stall type, significant stall margin loss will occur when the distortion speed is close to the propagation speed of modal wave or stall cell. For a compressor with spike type stall route, peak stall margin degradation occurs when the rotational speed of inlet distortion corresponds close to the spike propagation speed. The distortion seems to promote

the development of the flow disturbance. Similar conclusions can be found in [Nie et al., 2006] and [Salunkhe and Pradeep, 2010].

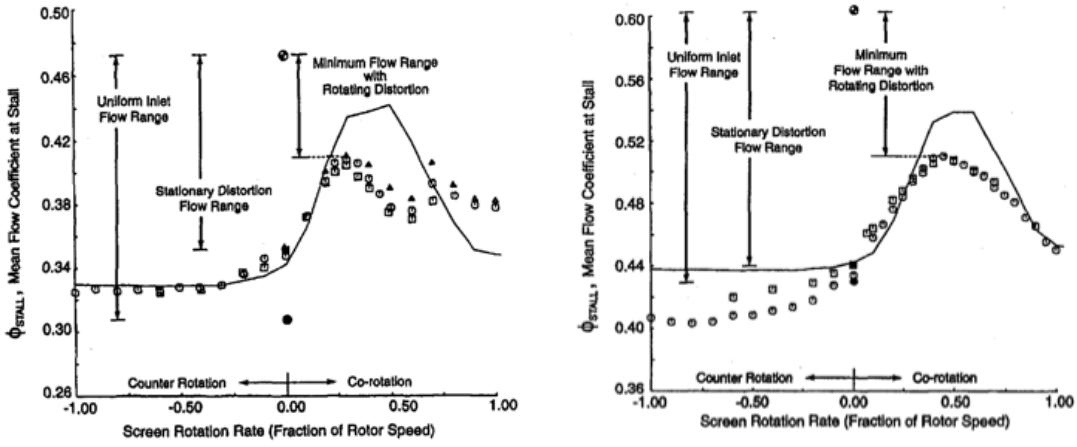


Figure 2.3: Flow coefficients at stall versus distortion rotation rate for compressors with (a) spike and modal wave (b) perturbation [Longley et al., 1996]

Some inlet distortions, like the distortion due to the ingestion of the boundary layer in a BLI engine, are consistent during the whole flight. On the other hand, some distortions such as the swirl distortion caused by the cross wind, occur instantaneously but may last only a short time. Such kind of the distortion is classified as abrupt distortion. Leinhos et al. [Leinhos et al., 2000] investigated the influence of transient distortion on compressor stall margin as well as the stall inception process. The transient distortion is a combination of fixed total pressure distortion and a slowly changing swirl distortion. The total pressure distortion is generated by a wire gauze and the swirl distortion is generated by a delta-wing whose angle of attack can be slowly increased from 0 to 20 degree. Datum test was carried out with consistent distortion pattern, which is a combination of same total pressure distortion and swirl distortion with the delta-wing fixed at an angle of attack of 20 degree. The stalling mass flow was compared between these two setups. It was found that such transient distortion does not change the stall boundary when compared with the consistent distortion. One possible reason is the relative slow moving speed of the delta-wing compared with the compressor shaft speed. No experimental tests were found regarding fast changing distortion (abrupt distortion). Gong [Gong, 1999] simulated the compressor response to an abrupt total pressure distortion and found that the compressor can establish an equilibrium state almost instantaneously when it operates away from stall.

2.2 Compressor-distortion Interactions

In this section, interactions between the compressor and inlet distortion are reviewed. On one hand, the inlet distortion cripples the performance of the compressor; on the other hand, the amplitude and the distribution of inlet distortion will be changed when it passes through the compressor. Besides, one type of distortion can give rise to other types of distortion, which makes

the distortion configuration more complicated. In the last part of this section, compressor's response to inlet distortions are discussed when it is coupled with upstream or downstream components.

2.2.1 Effects of Inlet Distortion on Compressor Stall Margin

The most destructive effect of inlet distortion on the compressor is the corrected flow reduction and stall margin loss. A reduction in corrected mass flow results in a drop of thrust. The stall margin is the operating range between the nominal operation line and the stall line which is demarcated as the stability boundary [Tan et al., 2010]. This effect can be best described by a performance map of a compressor (see Figure 2.4). A typical compressor map covers the full operating range of the machine from low to high rotational speed. Corrected mass flow is the mass-flow rate through the compressor corrected for inlet total temperature and total pressure. The pressure ratio is defined as the ratio of the exit total pressure to the inlet total pressure. Two routinely used methods to measure the loss of stall margin are the loss of pressure rise at constant speed or loss of pressure rise at constant corrected mass flow.

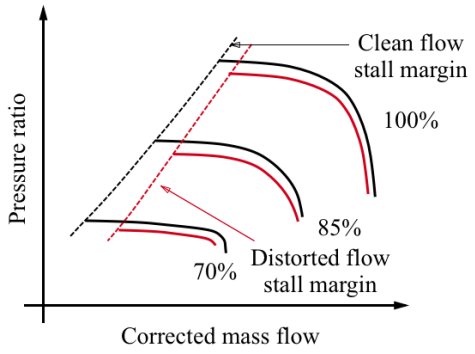


Figure 2.4: A typical steady state performance map of a compressor

Different types of inlet distortions reduce the stall margin through different mechanisms. The axial velocity in the distorted region is less than the clean flow region, which increases the incidence of the rotor and hence flow separation is prone to occur. In addition, the compressor sector in the distorted flow works with higher pressure ratio if the exit pressure is uniform. Consequently, the operating point of distorted compressor sector approaches to the stall line.

As total temperature determines the corrected rotational speed of the compressor at a fixed shaft speed (see equation 2.1), total temperature distortion will cause the compressor sector to work on a different characteristic line. The blade passages in the hot stream parts and hence with lower correct speed are closer to the stall line, as shown in Figure 2.5. The stable flow range suffers a decrease due to the change of the corrected mass flow (see equation 2.2).

$$N_{corr} = N \cdot \sqrt{T_o/T_t} \tag{2.1}$$

$$\dot{m}_{corr} = \dot{m} \cdot \frac{\sqrt{T_t/T_o}}{P_t/P_o} \tag{2.2}$$

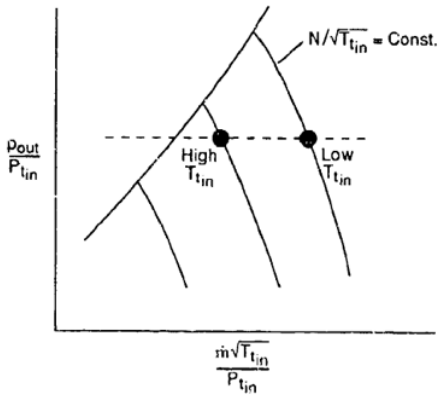


Figure 2.5: Compressor response to inlet total temperature distortion [Longley and Greitzer, 1992]

Similar to total temperature distortion, swirl distortion can push the compressor working condition to higher or lower corrected rotational speed depending on its direction relative to the rotor [Sheoran et al., 2010]. The incidence in the distorted region is larger, which causes blade separation and ensue rotating stall [Sghaier et al., 2013].

2.2.2 Efficiency Loss Due to Inlet Distortion

The off-design flow field in the compressor due to inlet distortion suffers from blade separation, corner separation and secondary flows which lead to efficiency deficit. Research is mainly conducted to figure out the underlying mechanism of distortion-induced flow loss and its distribution in the compressor.

Experimental and numerical studies [Hah et al., 1996] of a transonic compressor rotor with inlet distortion indicate that the flow loss is localised and varies spanwise at different rotational speed. At low rotational speed, the blade section efficiency is increased at above 70% span compared with uniform inflow condition. The possible reason is the low momentum flow near the blade surface is energised by the shedding vortex resulting from the interaction between the inlet distortion and the blade boundary layer. However, at high rotational speed, the blade section efficiency above 60% span was decreased while the efficiency near the hub was still increased. It was observed that the circumferential distortion causes large oscillation of the shock wave in the outer part of the blade. This oscillating shock wave interacts with the blade boundary layer and generates larger loss.

Gunn et al. [Gunn et al., 2013] studied how the flow loss is distributed in a fan stage with total pressure distortion experimentally. By comparing measured flow field of the design operating points with and without distortion, it was found the asymmetry inflow in front of rotor generates swirl distortion and thus change the circumferential and radial distribution of the rotor incidence. The non-uniform diffusion through the rotor passages and flow separation generate flow loss in the rotor. The largest flow loss in the rotor occurs in the sector where the rotor just leaves the distorted region. In this sector, substantial flow separation is caused by the increased tip loading because of the high incidence. For transonic fans, additional flow loss comes from the interaction

between shock and boundary layer. The efficiency of the downstream stator is influenced by the swirl distortion at the rotor exit. Deviated circumferential and radial angle distributions downstream of the rotor lead to corner separations in the stator row [Gunn and Hall, 2014].

2.2.3 Distortion Transfer through the Compressor

It has been noticed that the amplitude and the spatial phase of inlet distortions will change when the distortions go through the compressor stages [Gunn and Hall, 2014, Reid, 1969]. Different types of distortions exhibit different characters, which will be discussed in this section.

The amplitude of total pressure distortion can be attenuated by the compressor when the compressor works away from stall. The compressor works harder in the distorted region and more energy is put into the fluid which decreases the total pressure difference between the clean sector and distorted sector at the compressor exit. It is considered that compressor with steeper characteristics possesses greater distortion attenuation capability [Longley and Greitzer, 1992]. Such kind of compressor is able to create large total pressure increase without substantial reduction in mass flow. Even for one single compressor blade, the capability of distortion attenuation varies with the span. It was observed in [Yao et al., 2010b] that tip section of the blade is more capable to attenuate the distortion because the tip section has steeper characteristics. While the total pressure distortion is usually attenuated, this is not the case for total temperature distortion and swirl distortion. Total temperature distortion and swirl distortion can be created and amplified [Yao et al., 2010b] by the compressor even when the inflow contains no such distortions. This phenomenon will be discussed in next section.

The circumferential phase shift of different distortions comes from the interactions between the distortion and the blade row. The mechanism of the phase shift is complicated and mainly two factors are responsible: the circumferential non-uniform work input into the flow and the transportation effect of the blade. As the work input varies circumferentially due to the asymmetry of the inflow total pressure and rotor incidence, the peak of the total pressure at the rotor exit shifts along the annulus. In addition, the distortion is carried by the rotor when it passes through the passage and is transported to a different circumferential position. This transportation displacement can be calculated with the residence time in the rotor blade and its angular velocity [Mazzawy, 1977].

Similarly, the phase change of total temperature distortion is determined by the work input and the angular movement of the rotor blade. It was found [Yao et al., 2010a] that the phase shift of the total pressure distortion is relative smaller than total temperature distortion when they propagate through the blade rows. The phase change of swirl distortion is more complex and it can be additionally influenced by the flow separation and secondary flow.

Besides the abovementioned factors, the phase change of distortions varies with the working condition of the compressor. It was found that the phase shift and the amplitude of total temperature distortion are larger when the fan approaches stall [Weston et al., 2015]. For complex distortion patterns, it is hard to directly calculate the phase change of the distortion. Peterson [Peterson et al., 2017] employed Fourier analysis to show how different harmonics in the distortion transfer quantitatively. The phase change of different distortion might be interrelated. For

example, a 90-degree phase shift was found between the inlet total pressure distortion and the generated temperature distortion in two different fans, yet whether this conclusion is general or case specific still needs more investigations [Yao et al., 2010a]. Based on this finding, it was further considered that by studying the relations of the phase and amplitude between total pressure distortion and other distortions, the performance of the compressor can be predicted [Weston et al., 2015]. However, currently no such methods are found in published literature. Accurate prediction of the circumferential phase change for different types of distortion is also important for the consideration of compressor stability. For example, it was observed that stall margin loss of the compressor will be larger when total pressure distortion and total temperature distortion overlap in the flow field [Davis, 1991]. Therefore, it must be avoided to have the peak of different kinds of distortion to appear in the same circumferential position when distortions propagate through the blade rows.

2.2.4 Interactions between Different Distortions

While the features (amplitude and circumferential phase) of one type of inlet distortion can be changed through its interaction with the compressor, the behaviour of different types of inlet distortions are coupled as well. In brief, one type of inlet distortion can generate, amplify or reduce another type of inlet distortion by altering the work input of the compressor into the flow. For instance, circumferential total pressure distortion in front of the rotor can change the work input around the annulus and thus the flow at different circumferential position will have different enthalpy increment, which leads to a non-uniform temperature distribution around the annulus and hence a total temperature distortion. In this process, the flow turning determined by the blade loading no more maintains circumferential uniform and a swirl distortion comes into being.

Similarly, the total temperature distortion changes the corrected rotational speed of the compressor and thus alter the blade loading, which contributes to the generation of total pressure distortion and swirl distortion [Yao et al., 2010a]. The swirl distortion generates other types of distortion by varying the rotor incidence and hence the loading of the blade [Pazur and Fottner, 1990]. However, under some specific conditions, one type of inlet distortion might reduce or cancel another type of inlet distortion. Experiments on a three-stage fan showed that the swirl distortion counter to the rotation of the fan can reduce the amplitude of the total pressure distortion transmitted to the core compressor [Flitcroft et al., 1987].

2.2.5 Operational Condition of the Blade with Inlet Distortion

According to the classical parallel compressor theory [Stenning, 1980], the compressor blade around the annulus has only two working conditions: one with clean inflow and another with distorted inflow while both charge into the same exit plenum; both working conditions fall on the same compressor characteristic of clean inflow. As found in [Mazzawy, 1977], the upstream flow redistribution in front of the compressor can change the performance of the blade, which makes it no longer fits the clean flow characteristic; in addition, some blades can work beyond the stability margin when they rotate through the distorted segment [Plourde et al., 1968]. The

underlying mechanisms of these two observations about the operational condition of the blade will be discussed.

Gong [Gong, 1999] investigated the performance of a transonic compressor with circumferential total pressure distortion. It was found that the local operating points of the compressor sectors at different circumferential positions are quite scattered on the compressor map (Figure 2.6) and they even disperse over different speedlines. The mass flow fluctuation of the compressor sectors around the annulus is larger than the clean mass flow range (from choked to stall) of the same shaft speed. This means that significant fluctuations occur in the operational condition of the blade when it rotates around the annulus. Deviation also exists between the local performance of a blade and the overall performance of the compressor (black dot in Figure 2.6). Gong considered the significant flow angle variation exists in front of the compressor which is induced by the flow redistribution in the intake.

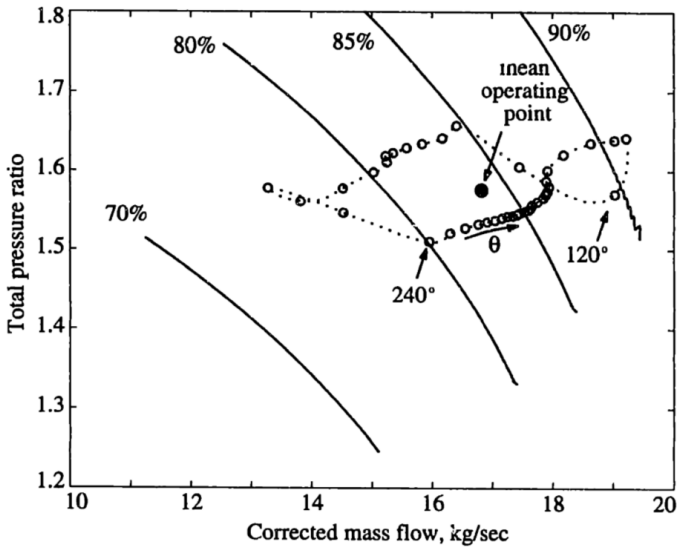
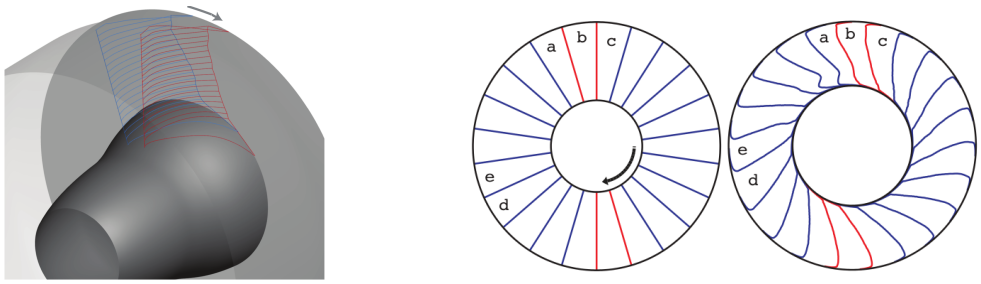


Figure 2.6: Local operating points around the annulus of NASA stage 35 subjected to a total pressure distortion [Gong, 1999]

A more comprehensive and accurate demonstration of the operational condition for the blade with circumferential total pressure distortion is given in [Fidalgo, 2013]. The quasi-steady working condition of the blade sectors at different circumferential positions can be computed with a orbit method when inlet distortion is stationary. In the first step, a time-averaged flow solution of the rotor domain (with 22 blades) in the absolute frame is calculated. During this process the blades are removed and the rotor domain is transformed into a whole annulus duct. Afterwards radial streamtrace rakes are released at rotor leading edge (LE) surface and they end at the rotor trailing edge (TE) surface (Figure 2.7a). Every single streamtrace can be regarded as a time-averaged particle path. These rakes split the inlet surface into 22 sectors with equal area. The shape of the streamtrace rakes change when they arrive at the rotor TE due to circumferential turning and radial migration of the flow. The TE surface is also split into 22 sectors with these streamtrace rakes. In this way, the LE and TE sectors are accurately matched and the entire time-averaged rotor domain is sliced into 22 separate parts (Figure 2.7b). Each part can be regarded as a

time-average blade passage at different circumferential position. In the final step, the working condition (corrected mass flow and total pressure ratio) of these sectors are calculated. They are plotted against clean flow compressor characteristic and connected with a dashed line to form an orbit, as shown in Figure 2.8. Also shown in this figure is the overall compressor working point with inlet distortion. Large deviations of the orbits from the overall compressor performance can be seen in this plot.



(a) (b)

Figure 2.7: (a) Streamtrace rakes at rotor LE and TE [Fidalgo, 2013] (b) Matching of inlet and exit sectors by using time-averaged particle paths [Fidalgo et al., 2012]

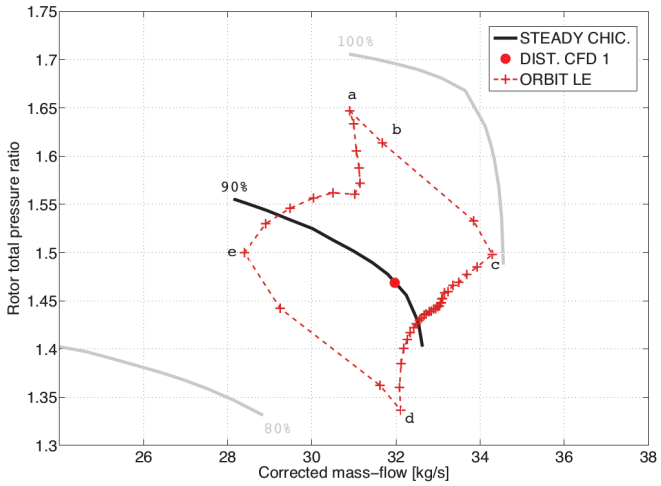


Figure 2.8: Operating conditions for the orbits and the overall compressor [Fidalgo et al., 2012]

The variations in the rotor blade performance around the annulus can be explained with Figure 2.9. As already mentioned, the existence of inlet distortion leads to non-uniform axial velocity distribution and circumferential swirl angle in front of the compressor. On one hand, different inlet axial velocity (mass-flow) will move the local operating condition roughly left and right along the steady characteristic. On the other hand, variations in the inlet swirl angle changes the effective rotational speed of the rotor and thus its operational condition will be pushed to the characteristics of higher or lower corrected speed. The local operational condition of the blade is a combination of both effects when it rotates through the distorted and clean flow sectors alternatively.

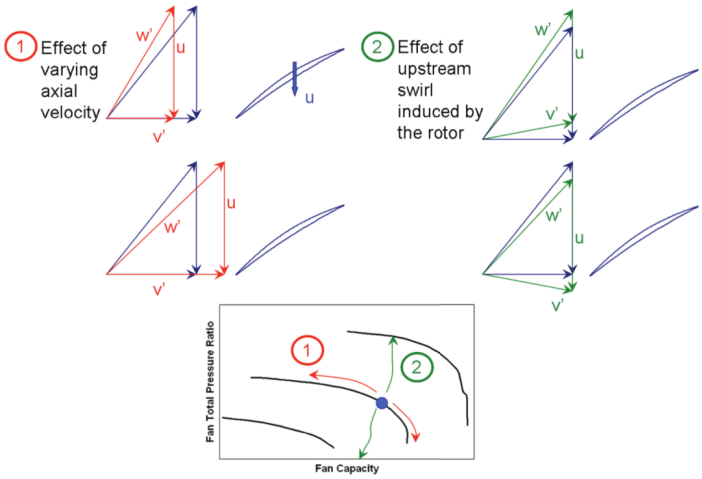


Figure 2.9: Main drivers of orbit shape [Fidalgo, 2013]

The "orbit" basically represents the quasi-steady performance of the blade. To explain why some blades can work beyond the stall line without stalling the whole compressor, the dynamic behaviour of the blade must be taken into consideration. Numerical studies [Giuliani, 2016] show that the blade experiences a three-dimensional dynamic stall [Visbal and Shang, 1989] when it passes through the distorted region. In this region the higher incidence caused by lower axial velocity induces flow separation on the blade surface. Before this separation grows larger and rotate (i.e., it evolves into a stall cell), the incidence angle drops when the blade moves into the clean flow region and the flow reattaches. Therefore, the clean flow region can assist the blade to recover before the local blade separation corrupts into a full-developed rotating stall. Moreover, the blade separation might not even happen if the blade passes through the distorted region very fast. The hysteresis in the response of the blade boundary layer to inlet distortion permits the blade to work in adverse conditions for a short time without flow separation. Cousins [Cousins, 1997] defined a rotor response time for an axial blade as the time for a flow particle to travel from blade LE to the throat of the blade passage (Figure 2.10a). This length is the distance that a fluid particle must travel to start the major diffusion process and change the pressure rise of the blade. The rotor response time determines the sensitivity of the blade to inlet distortion. Figure 2.10b shows that if the rotor response time is longer than the time interval for the blade to traverse through the distorted sector, the blade response will be less and hence the stability is less influenced. Cousins successfully used this rotor response time to explain why radial compressor is less sensitive to inlet distortion than axial compressor.

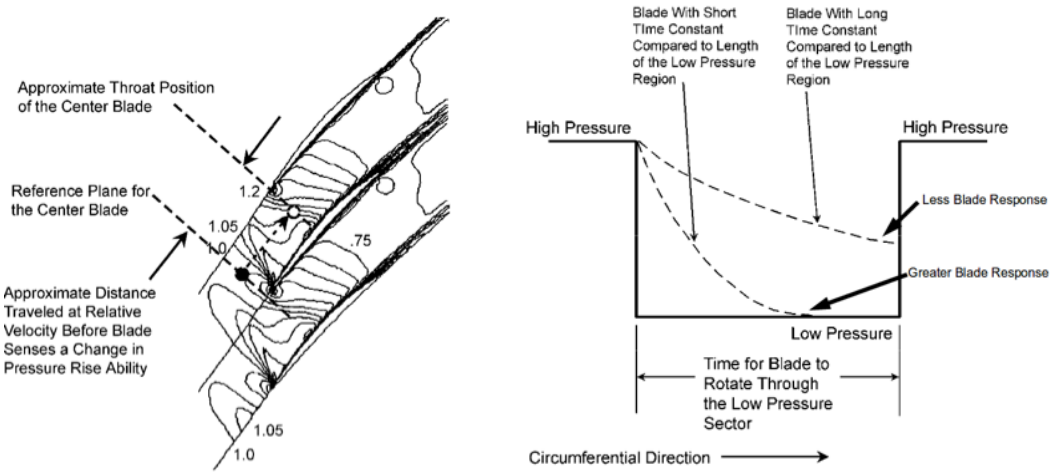


Figure 2.10: Response time of the rotor to inlet distortion: (a) Distance a particle of fluid must travel to the throat of the blade passage to reach the start of the major diffusion process (b) Blade time constant comparison to a distorted inflow determines the magnitude of the blade response [Cousins, 1997]

2.2.6 Interaction between the Compressor and Its Upstream and Downstream Components

The coupling between the compressor and its upstream and downstream components affects the compressor behaviour. For example, the post-stall mode of compression system, surge or stable rotating stall, can be influenced by the size of the plenum downstream of the compressor [Greitzer, 1976]. The coupling can be more complex in distorted flow regarding the performance and stability of the compressor. Relevant research results are summarized in this section.

In civil engines, a typical upstream component of the compressor is a straight intake. As the diameter of the fan becomes larger and shorter intake is preferred in the new designed civil engines [Cumpsty, 2010], the interaction between the intake and the compressor will be more significant. In general, the compressor can promote the flow redistribution between the distorted sector and clean flow sector within the intake. The overall flow non-uniformity can be reduced but this process is usually accompanied with the generation of additional secondary flows. The compressor-modulated flow field within the intake in turn influences the performance of the compressor. Greizter et al. [Greitzer, 1973, Hodder, 1981] found that such coupling behaviour between the intake and the compressor varies with inlet Mach number. Some research focus on how the presence of the aero-engine alters the evolvement of the distortion within the intake [Motycka, 1985, Cao et al., 2017]. The results showed that the presence of the fan (or the engine) can reduce the amount of inlet total pressure distortion at the exit of an intake when compared with the same situation without the fan (or with the fan located sufficiently far downstream). Because of the reduced distortion levels in the intake, the intake can work at and beyond the separation angle-of-attack experienced without engine interaction [Motycka, 1985], as shown in Figure 2.11. Simulations [Cao et al., 2017] showed that the ability of the fan to increase the separation-free operating range in a straight duct is dependent on L/D, where D is the diameter

of the intake and L is the distance of the fan from the intake lip. When L/D is low, the main effect of the compressor on intake is to increase the separation-free operating range while such effects no more exits when L/D is high. The fan always reduces the distortion level regardless the value of L/D. The capability of the fan to reduce the distortion levels increase at higher rotational speed and consequently stall margin of the fan blade is extended [Lee et al., 2019].

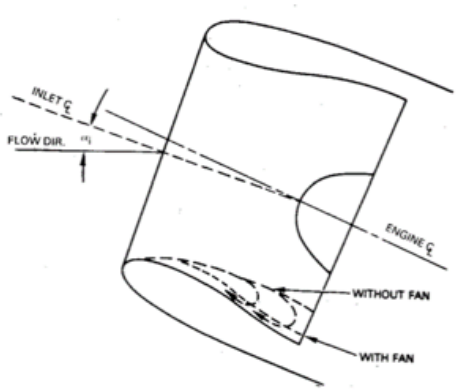


Figure 2.11: Angle-of-attack distortion with and without fan coupling [Motycka, 1985]

Experimental study shows that for clean inflow, the choice of the downstream components has no obvious influence on the compressor stall margin. Greitzer [Greitzer and Griswol, 1976, Greitzer et al., 1978] studied the coupling between different downstream components (straight duct with constant section area, nozzle and diffuser) and the compressor when a circumferential total pressure inlet distortion is imposed. An analytical method based on a nonlinear, multisegment parallel compressor model was used to predict the compressor behaviour. It was found that different downstream components lead to the phase difference in the compressor exit pressure. This phenomenon is demonstrated with experimental data in Figure 2.12, where the total pressure distortion extends from 90 degree to 270 degree circumferentially at the inlet. The static pressure non-uniformity would be zero at the compressor exit for straight ducts, in phase with the inlet distortion pattern with a nozzle and out of phase for a diffuser.

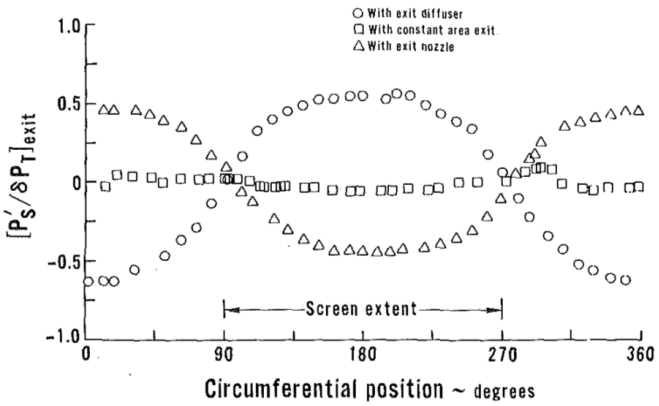


Figure 2.12: Effect of downstream components on static pressure distortion at compressor exit-experimental results [Greitzer et al., 1978]

The stall margin of the compressor is also influenced by different downstream components. As shown in Figure 2.13, the exit nozzle decreases the static pressure non-uniformity compared with a straight duct. Thus the compressor sector with low inlet total pressure will have a lower back pressure which decreases its loading. On the contrary, the existence of a diffuser at the compressor exit will increase the non-uniformity of the exit static pressure. Therefore, the stall margin of the compressor with an exit diffuser is reduced but increased with a nozzle when compared with a straight exit duct. Both findings obtained from the analytical method were validated in experiments.

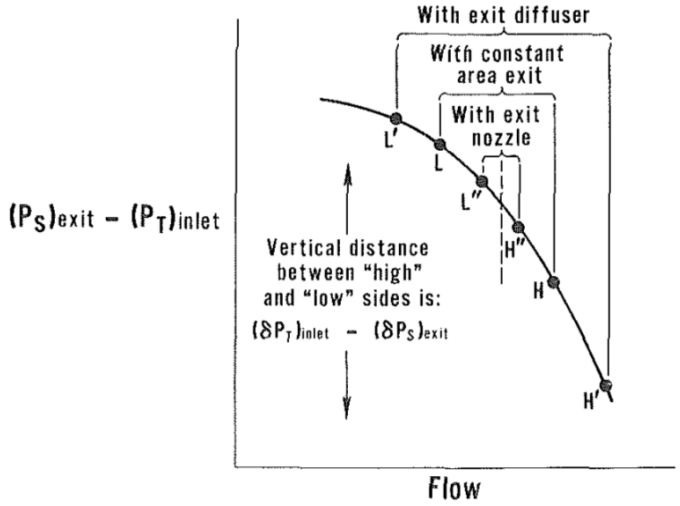


Figure 2.13: Effects of downstream components on compressor performance with inlet distortion [Greitzer et al., 1978]

2.3 Compressor Stall with Inlet Distortion

2.3.1 Rotating Stall and Stall Inception Process

Rotating stall is an aerodynamic instability when uniform flow corrupts in the compressor, accompanied with a very large loss of mass flow and pressure rise [Cumpsty, 1989]. A typical axial compressor characteristic is shown in Figure 2.14. A large full-span stall cell which occupies considerable annulus area is sketched. The stall margin of a compressor denotes the operating range between the design point (B) and the stall point (C). This stall point almost coincides with the peak of the total-to-static pressure rise characteristic. The mass flow and pressure ratio of the compressor drop to D after stall occurs. By opening the discharge throttle downstream of the compressor, the compressor can be unstalled and regain its pressurization capability. However, the discharge throttle needs to be opened further than that at stall point (C) and the compressor recovers at point (H). This compressor behaviour gives rise to a hysteresis loop (C-D-F-H). Compressors with higher design pressure rise and flow rate typically has larger hysteresis loop.

Experimental studies have uncovered some important features of the stall cell [Day and Cumpsty, 1978, Day, 1991, Day, 1991, Day et al., 1999]. Stall cells always rotate in the same direction as the rotor blades but with a slower speed. The number and the size of the stall cells vary with

the blade design: highly loaded, short blades usually generate a single full-span stall cell; blades of high aspect ratio usually give rise to multiple part-span cells near the casing. The absolute rotational speed of the stall cell is related with its size. In general, part-span stall cells have a larger speed than full-span ones and smaller disturbance can rotate faster.

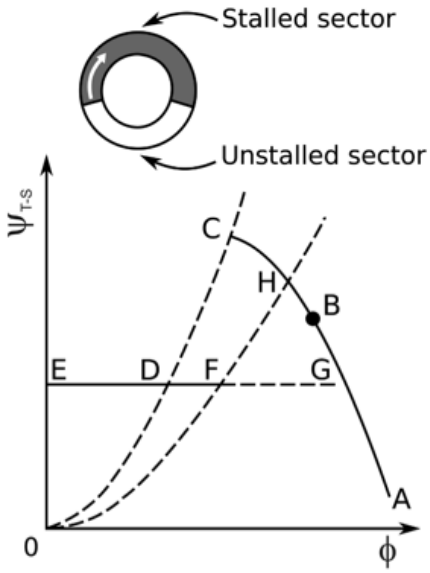


Figure 2.14: Typical fixed-speed performance characteristic for an axial flow compressor [Day, 2016]

Compressor stall can be initiated by two typical routes [Camp and Day, 1998]: long length-scale disturbances (modal wave) or short length-scale disturbances (spike). Some compressors have been found to exhibit both types of unsteady disturbances [Camp and Day, 1998, Day et al., 1999] under different conditions. However, usually only one type is dominant in the stall transient process. More introduction about modal wave and spike can be found in [Greitzer and Moore, 1986, McDougall et al., 1990].

The criteria of the flow feature (spillage of tip-leakage flow at the rotor LE and tip-clearance backflow at the rotor TE) associated with compressors exhibiting spike stall was proposed by [Vo et al., 2008]. Figure 2.15a illustrates the trajectory of the spillage of tip-clearance flow of one blade to the adjacent blade passage ahead of the rotor LE and below the tips radius. And Figure 2.15b demonstrates the second feature, in which fluid originating from the tip-clearance region of one blade passes around its TE and impinges on the pressure surface of the neighbouring blade passage.

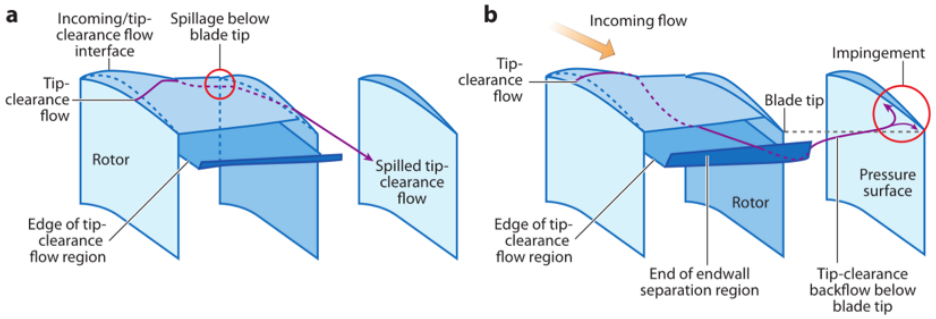


Figure 2.15: Criteria of spike stall: (a) Spillage of tip-leakage flow at the leading edge (b) Tip-clearance backflow at the trailing edge [Tan et al., 2010]

2.3.2 Effects of Inlet Distortion on the Stall Inception Process

Most of the research carried out during the second half of last century concentrate on how inlet distortion influences the compressor stall margin and efficiency. Relatively less studies focus on the stall inception process due to the lack of high response measurement instruments until recently [Jahnen et al., 1999, Jiang et al., 2009, Leinhos et al., 2000, Lin et al., 2005, Perovic et al., 2015]. CFD studies, on the other hand, were initially performed at near design point or near stall point [Mehdi, 2014], but now the high-fidelity simulations are capable to supplement important flow details of compressor stall inception process with inlet distortion [Page et al., 2018, Perovic et al., 2015]. Based on these experimental and CFD studies, the effects of inlet distortion on the compressor stall inception process can be summarized as following:

1. Inlet distortion changes the circumferential or radial position where stall is initialized.
2. Inlet distortion can alter the type of pre-stall disturbance.
3. Stall margin prediction criterion for clean flow is inapplicable in the distorted flow.

As mentioned in section 2.3.1, compressors can exhibit different types of pre-stall disturbance (modal wave or spike) under different circumstances. Experimental tests showed that compressor can stall via different routes when inflow becomes distorted. Jahnen et al. [Jahnen et al., 1999] found that the life span of the flow disturbance was influenced by different types of inlet distortions. For the tests with total pressure distortion, it was observed that the flow disturbance detected in the distorted region can soon develop into rotating stall within one revolution. When the compressor operates with swirl distortion, the life span of flow disturbance is longer before it finally developed into a stall cell. This observation indicates that the stall might be triggered by spike or modal wave depending on the distortion type. It was found that the compressor exhibits different types of pre-stall disturbances (modal wave or spike) at different shaft speeds in clean inflow but stall is always triggered by spike-type disturbances with constant or transient distortions [Leinhos et al., 2000]. Similar observation was presented in [Arshad et al., 2018]. Under the uniform inflow condition as well as with hub distortion, stall inception is caused by the modal type disturbance whereas the stall precursor switched to spike type due to the highly loaded blade tip with tip distortion. The direction of rotating distortion also has influence on the pre-stall disturbance. Experiments carried in a single-stage fan showed short length-scale disturbances causes the stall inception within clean inflow and counter-rotating inlet distortions

while long length-scale disturbances initialize the stall with static and co-rotating inlet distortions [Salunkhe and Pradeep, 2010].

In experimental tests the stall cells developing via short-length scale disturbance always originate at the same circumferential position in the annulus [Day, 1993]. Comparing the tests [McDougall et al., 1990], it was considered that localized irregularities are likely to be dominant in the compressor working with clean inflow. For distorted inflow, the circumferential or radial position for stall inception can be more governed by the configuration of inlet distortion. The tests [Jahnen et al., 1999] of the stall process with inlet distortion in a high speed 5-stage HP compressor shows that the stall cell appears at random circumferential position with clean inflow. However, the position where the stall cell appears with distorted inflow always remain the same. This position is at the exit of the distorted region (i.e., where the rotor just rotates out of the distorted region).

In a compressor with circumferential inlet distortion, the working condition of the blade around the annulus can be quite different with that in clean flow. As a consequence, the criterion (such as rotor tip incidence criterion [Camp and Day, 1998]) which can be used for clean flow stall margin prediction, will be invalid in the compressor operating with inlet distortion. It can be very difficult to find the critical incidence due to the complex working condition of the blade in the distorted region. It is also noted that some stall warning strategies, such as the detection of spike before stall, will also be unreliable. For the compressor running with inlet distortion, spike-type disturbance is detected inside the distorted region. Nevertheless this spike can be damped out in the clean flow region [Jahnen et al., 1999], which explains why the whole compressor can still sustain an overall stability even the pre-stall disturbances are produced. The compressor will fall into rotating stall only when the damping of the disturbances in the clean flow region is insufficient to suppress their growth. This behaviour is quite different with that in a clean flow situation, in which the compressor will soon stall once the spike appears.

More details about the generation and decay of the pre-stall disturbance are shown in recent study of BLI fan [Perovic et al., 2015]. The BLI distortion pattern (Figure 2.16) is produced by a non-uniform porous gauze. It was observed that disturbances resembling local flow separation are initialized in the region of high incidence (distorted flow sector) and decay in the region of low incidence (clean flow sector); rotating stall will happen when high incidence regions are widespread enough to sustain the disturbance to travel around the entire annulus. It was found that rotor incidence is the dominant variable affecting the generation and growth of flow disturbance. In this study the disturbances in the frequency range $0.7f_{bp} \leq f < f_{bp}$ were considered to be key to the stall inception. The fan will stall when such frequencies propagates around the whole annulus.

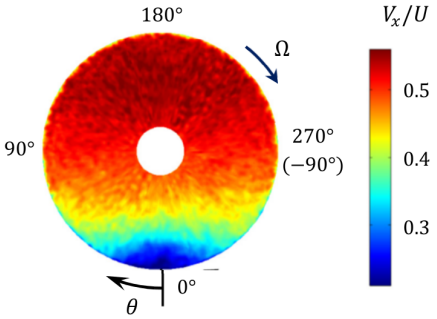


Figure 2.16: Measured inlet axial velocity profile in front of the fan at the design operating point [Perovic et al., 2015]

2.3.3 Recovery from Stall

Rotating stall has received a lot of attention since the early days of the aircraft engine development [Day, 2016]. Most research focused on the stall inception and control while the recovery process has been less studied. However, the ability for the compressor to recover from stall is also an important consideration for evaluation of its performance. The stall hysteresis has a significant influence on the compressor operation as rotating stall can exist at higher mass flow functions than the stall point. The point at which stall cell disappears and the operating point returns to the steady characteristic defines an operating line which ensures recovery from rotating stall. A compressor designed with better recoverability (less hysteresis) will expand the safe operating range and hence makes the engine more suitable for working in complex flight conditions.

Experimental studies on low-speed compressors has provided important fundamental knowledge about the in-stall and recovery performance [Day and Cumpsty, 1978]. Experiments [Small and Lewis, 1985] were also carried out on a three-stage high-speed, highly loaded, compressor to document the performance during stall and recovery process. Levels of blockage in the compressor were measured as the stalled fraction of the annulus, and it was found to vary between 80% and 30% during the recovery process. When the blockage dropped below approximately 30%, the compressor recovered. A parametric study into the influence of shaft speed, discharge throttle setting and variable geometry settings on rotating stall and recovery process of a 10-stage, high-speed compressor test rig was carried out in [Copenhaver and Okiishi, 1993]. The results highlighted the significance of stage matching on stall and recovery.

The stall and recovery process has also been studied in modern wide-chord civil fan blades. Measurements [Anderson and Smith, 2006] showed the existence of two stall cells during the stall process, which disappeared one after another when the throttle was opened. Choi and Vahdati [Choi and Vahdati, 2011] were the first to numerically investigate these processes for a transonic fan. In their study, rotating stall of a wide-chord fan at 70% of the design speed was simulated using a whole-annulus model. The simulation adopted the same approach as the experiments; the fan was stalled by closing the exit nozzle and unstalled by opening the exit nozzle. A good qualitative agreement was obtained between CFD and experimental data, which provides confidence in the reliability of CFD.

2.4 Methods for Inlet Distortion Attenuation and Control

A body of knowledge on inlet distortion were built through large amount of research and this enables the compressor designers to explore possible methods to make the compressor more robust when subjected to distortion; these methods can be classified into two categories: passive control and active control.

Passive control of inlet distortion can be implemented with casing treatment or blade modification. Casing treatment has been proved to effectively extend the stable operating range of the compressor under clean inflow conditions when the blade is tip critical [Prince et al., 1975, Smith and Cumpsty, 1984]. It is also validated in experiments with distorted inflow for both low-speed compressor [Takata and Tsukuda, 1977] and transonic compressor [Bailey and Voit, 1970]. Essential modification of the blade can reduce the sensitivity of the blade to inlet distortion. It was found that the stator chord does not affect the distortion tolerance but increasing the chord length of the stalling rotor enhances the distortion tolerance of the compressor [Plourde et al., 1968]. Moreover, their results also showed that a rotor with longer chord can endure larger incidence before stall. Forward-sweep blades are proved to be more tolerant to inlet distortion [Wadia et al., 2002]. Comparisons between a forward sweep fan and a radial fan (Figure 2.17) has demonstrated improvement in both efficiency and stall margin in clean flow and distorted flow. This improvement is mainly due to the reduction in the tip loading [Wadia, 2011]. Similar conclusion was also reported in [Yang and G., 2012]. They found that the forward-skewed blades can generate more uniform loading distribution along the span than datum design with radial distortion at the tip region. As mentioned in section 2.2.2, inlet distortion can cause flow loss in the stator with corner separation. The non-axisymmetric strategy can be adopted in the stator blade design to tackle the spoiled inflow and thus reduce the flow loss. The tests [Gunn and Hall, 2017] showed that the blade designs with a combination of non-axisymmetric inlet angle, chord and lean are effective in distorted flow and a 10% loss reduction was obtained with the final design compared with the original one.

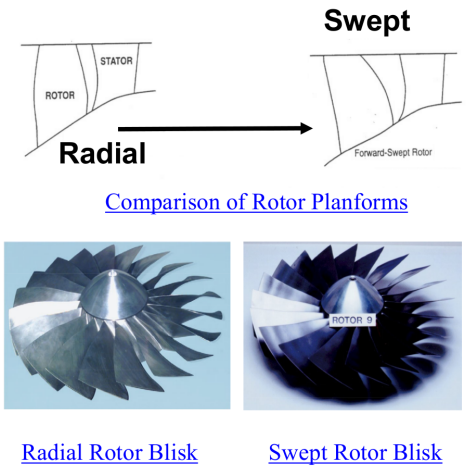


Figure 2.17: Schematic of radial and forward swept rotors and rotor blisk photos [Wadia et al., 2004]

Active control methods for inlet distortion include tip blowing (i.e. tip injection), bleeding and the application of variable inlet guide vane (VIGV). Both tip blowing and bleeding can improve the stall margin with inlet distortion when the rotor stalls at tip, though bleeding is relative less effective compared with blowing [Koch, 1970]. Spakovszky et al. [Spakovszky et al., 1999] used an annular array of 12 jet-injectors located upstream of the rotor tip to extend the compressor stable operating range when radial distortion occurred. Steady state injection results in a range extension of 9.7% in stalling mass flow relative to the case with distortion and no injection. Similar conclusions are also shown in [Salunkhe and Pradeep, 2010]. Numerical study showed that the self-recirculation casing treatment [Hathaway, 2002] (by combining casing bleed and injection) may increase compressor stall range with minimal or no loss in efficiency with inlet distortion. The effects of VIGV for distortion attenuation and stall margin extension have been validated both experimentally [Wadia, 2011] and numerically [Yao et al., 2007]. Its underlying mechanism is the attenuation of the inlet swirl [Shaw et al., 2014]. The non-symmetric arrangement can also be adopted in the VIGV installation. Simulations [Chen et al., 1987] presented that the asymmetric vane stagger scheme can significantly increase the distortion attenuation by adjusting the stagger of inlet guide vane (IGV) in the distorted part of the compressor.

Some other active control strategies were also proposed such as plasma actuator [Jothiprasad et al., 2012,Saddoughi et al., 2015] and synthetic jets used in BLI inlet [Anders et al., 2004,Owens et al., 2008]. Besides, some work has been conducted on the development of the warning and feedback system [Freeman et al., 1997,Sun et al., 2018,Schalkwyk et al., 1997] for active control of rotating stall with inlet distortion.

2.5 Method to Study the Effects of Inlet Distortion

2.5.1 Experimental Methods

Large number of experiments with inlet distortion have been carried out using low-speed compressors, transonic compressors and whole engines since pre-1960s [Biesiadny et al., 1986, Day et al., 1999,Jr and Braithwaite, 1974,Longley, 1990]. In experimental tests, steady measurements can provide accurate information of the stall margin with inlet distortion as well as how distortion evolves when it propagates across the blade row. With the assistance of fast response probes, the study of some transient processes like rotating stall are possible. Extensive knowledges of inlet distortion are obtained in experiments which contribute to the development and validation of the analytical models and simulation algorithms.

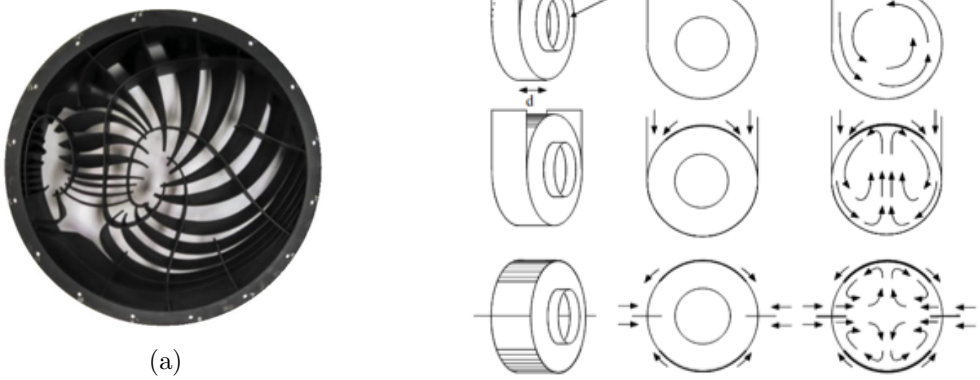
Test rigs normally need to be adapted for the tests with inlet distortion. Different devices have been designed to generate various types and patterns of inlet distortion. Total pressure distortions are usually produced by a fixed or rotating mesh screen in front of the compressor [Burstadt et al., 1971,Lieser et al., 2010]. The circumferential and radial area as well as the mesh density of the screen could be adjusted to mimic the distortion of specific spatial range and strength (Figure 2.18a). Temperature distortion is generated using a gaseous-fuelled burner [Mehalic, 1988], as shown in Figure 2.18b. The air passing through the burner is heated to reach a given temperature rise. The design of swirl distortion generators depends on the pattern of the swirl. A few different

designs can be found in [Genssler et al., 1987, Guimares et al., 2017]. For example, stream vane can be used to produce the swirl distortion pattern for engine ground testing (Figure 2.19a); adopting a delta wing [Pazur and Fottner, 1990] in the inlet duct can impose swirl distortion on the flow field but with neglectable total pressure distortion. Typically, a swirl distortion generator can only produce one specific distortion pattern; a versatile swirl generator for different patterns of swirl distortion was designed by [Sheoran and Bouldin, 2008], which can be used to create a few different swirl patterns by simply changing of the number of the inlets (Figure 2.19b). Besides, different distortion devices can be combined to generate a mixed distortion configuration [Viswanath and Govardhan, 1996].



(a) (b)

Figure 2.18: Tests with inlet distortion: (a) a typical total pressure distortion screen [Lieser et al., 2010] (b) burner installed in inlet plenum [Mehalic, 1988]



(a) (b)

Figure 2.19: Swirl distortion generators: (a) Stream vane [Guimares et al., 2017] (b) A versatile swirl generator [Sheoran and Bouldin, 2008]

2.5.2 Analytical Models and Numerical Methods

Based on the findings from the experiments, a few analytical models are developed to tackle with inlet distortion problems. These models can successfully explain the basic behaviours of the compressor with inlet distortion and are ideal as fast diagnosis tools for compressor performance and

stability prediction. With the rapid growth of the computational capability and developments of advanced numerical algorithms, computational fluid dynamics are becoming increasingly powerful and accurate. Considering that detailed flow field measurements are still hard to obtain especially in the rotating domain, CFD can offer an insight into the flow patterns which are difficult, expensive or even impossible to inspect with traditional test techniques. The preparations of experiments are expensive and time-consuming. CFD proves to be an ideal research strategy in terms of cost and safety. Especially for the experiments with inlet distortion, the test rig may suffer potential damage caused by rotating stall and vibration. Depending on the accuracy and complexity, numerical simulations can be categorized into low-fidelity simulations and high-fidelity simulations. Low-fidelity simulations are usually employed in the design stage of a compressor [Denton, 2017]. Suck kinds of calculations are capable to the obtain the essential geometry or flow parameters with economic costs. High-fidelity simulations provide irreplaceable supplements to experimental measurements especially for the transient phenomena.

In this section, according to the complexity and fidelity, parallel compressor theory, actuator disk model, body force method and Unsteady Reynolds-averaged Navier-Stokes (URANS) method are introduced in brief.

(1) Parallel Compressor Theory

First proposed by Pearson and McKenzie [Pearson and McKenzie, 1959], the parallel compressor theory is the most widely used method to approximate the distorted performance of a compressor. Although this theory involves some oversimplifications, it is useful for the qualitative analysis of the compressor behaviour with inlet distortion. The principle of parallel compressor theory is illustrated as Figure 2.20. In this case the compressor subjected to total pressure distortion can be viewed as two separate sectors in parallel: one sector works within clean inflow and another works within distorted inflow. The overall performance of the compressor is the average of two sectors.

Here three assumptions must be satisfied,

1. the performance (pressure ratio and mass flow) of both sectors fall on the same clean-flow characteristic.

2. the static pressure at the exit of the compressor is uniform since both sectors discharge into a common plenum.

3. There is no circumferential cross flow between two sectors (in the ducts and the blade row gaps).

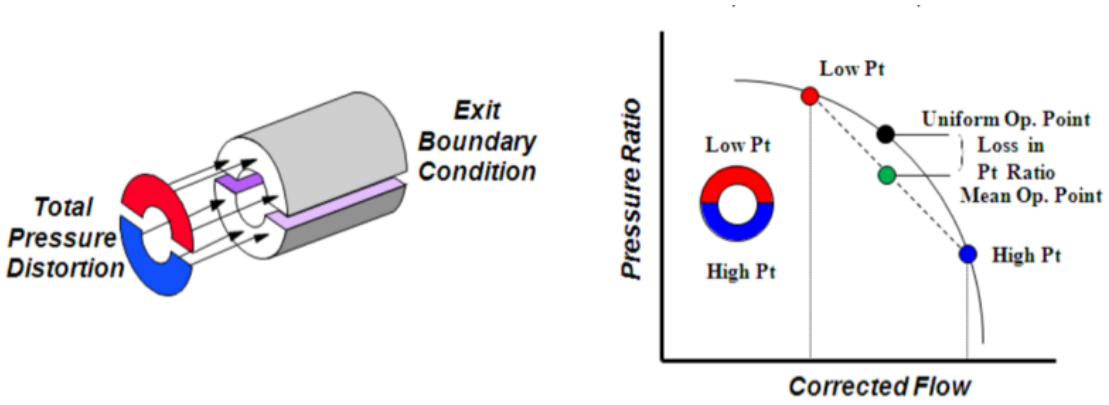


Figure 2.20: Illustration of parallel compressor theory [Cousins and Davis, 2011]

According to the parallel compressor theory, the whole compressor will reach the stability limit when the sector within distorted inflow is pushed across the stall line.

The parallel compressor theory was proved to be a practical tool and yields reasonable estimations for some engine tests [Jr and Braithwaite, 1974, Pazur and Fottner, 1990], although disagreements with experimental data still exist on the attenuation of distortion and the estimation of stall margin loss. These disagreements are mainly due to the above-mentioned assumptions which can be invalid in a true compressor. Therefore, the application scope of the parallel compressor theory must be carefully determined and essential improvements of the theory must be made.

Regarding the applicability domain of the parallel compressor theory, a criterion based on the reduced frequency is proposed in [Plourde et al., 1968]. The reduced frequency is a measure of the chord length of the blade relative to the wave length of the unsteady disturbance. The reduced frequency is defined as:

$$B \times \omega / V \tag{2.3}$$

Where B is one half of the chord length, V is the average velocity of the air relative to the rotor, ω is the frequency of the disturbance in the rotating reference. When the reduced frequency is near to zero, the loss in peak pressure due to inlet distortion predicted by the parallel compressor theory agrees well with experimental data. The parallel compressor theory will underestimate the peak pressure rise at stall with the increase of the reduced frequency.

To avoid the deficiencies, further corrections of the parallel compressor theory are needed. A multiple segment parallel compressor method was proposed by Mazzawy [Mazzawy, 1977]. This revised method can be applicable for total pressure distortion and/or temperature distortion of large-amplitude. In this method, the whole compressor is split into multiple parallel segments. For the prediction of stall margin, it is assumed that the whole compressor will be unstable when a compressor segment with a circumferential angle of 20-60 degree reaches the peak of its characteristic. This multiple segment parallel compressor model provides a good estimation of the compressor performance and stall boundary when compared with experimental data. Nevertheless the demand of empirical parameters in this model may impede the application of such method especially for new-designed engine.

Some essential enhancements of the original parallel compressor theory were discussed in [Cousins and Davis, 2011]. It was also suggested the dynamic response of the blade to inlet distortion must be taken into consideration to improve the prediction capability of the parallel compressor model. Moreover, circumferential and radial mass flow redistribution as well as the swirl in the flow must be resolved with proper methods. With all these modifications, the revised model can be extended into the prediction of more complex distortion patterns. The validation and applicability of this extend parallel compressor model is demonstrated in [Davis and Cousins, 2011].

(2) Actuator Disk Model

Actuator disk model [Horlock, 1958, Hawthorne and Horlock, 1962] takes each blade row as a discontinuity within the flow field while the mass flux and the streamlines are continuous. The blade row is reduced to a disk of zero thickness and thus all the loading along the blade chord is concentrated in the plane discontinuity. Coupled with inlet and exit boundary conditions, the equations (potential flow equation, Euler equations or Navier-Stokes equations) used to describe the flow across the disk can be solved. Due to the neglection of blade chord, the accurate position of this disk, the position of the shock wave in the passage for transonic blades and some other details such as choking related with the geometry of the blade cannot be modelled. Semi-actuator disk model [Marble, 1948, Micklow and Jeffers, 1981], on the other hand, models the rotor passage as a one-dimensional channel of finite axial length and it is able to calculate the flow field inside the passage. Some improvements of the actuator disk model can be found in [Joo and Hynes, 1997]. Different kinds of actuator disk models have been tried for inlet distortion studies [Hawthorne et al., 1978, Yeh, 1959, Perkins, 1979]. Such methods are mainly applicable to the asymmetric flow in which the spoiled flow area has a circumferential length larger than one blade pitch. In this section, two analytical actuator disk model [Hynes and Greitzer, 1987, Longley, 1990] developed for inlet distortion problems are discussed. The key concern in these models is how to model the unsteady pressure rise across the blade row.

(3) Body Force Method

In this section, two different body force methods are introduced: the bulk body force method and the viscous body force method. The bulk body force method models the compressor through flow with a simplified duct and neglects the geometry of the blade. The inviscid blade force and the viscous effects are modelled together as body force terms in Euler equations. The blade force is derived from steady compressor characteristics. The second method uses real blade geometry and solves the Euler equations while modelling viscous effects. In this method, a coarse mesh and large time step size can be applied which will reduce the computational cost compared with URANS.

The bulk body force method [Gong, 1999] takes advantage of two simplifications: the number of blades is infinite, and a local pressure rise characteristic in every small portion of a blade passage can be defined. The flow in the ducts and gaps is depicted by the unsteady, three-dimensional, incompressible inviscid Euler equations. Based on infinite blades assumption, the flow at each circumferential position can be regarded as axisymmetric flow in a coordinate frame fixed to the blade row. A body force field is introduced to simulate the pressure rise and flow turning due to

blades. This body force field is a three-dimensional function of local flow properties.

This method was tested to reproduce the response of a multistage, low-speed compressor to a square-wave circumferential total pressure inlet distortion. Good match between the experimental measurements and computed results was obtained. With essential extension, this method can also be applied to high-speed compressors. The flow field computation of NASA stage 35 with circumferential inlet distortion was computed and compared with experimental data. It was shown that the pressure and velocity distribution at the inlet and the exit of the compressor matched the measurements well.

In general, the body force representing the role of a blade row can be expressed as a sum of two parts, an inviscid body force and a viscous one. In the body force method proposed by [Xu, 2002], the inviscid blade force is calculated properly for each blade passage by solving Euler equations while only the viscous part of the force is modelled.

(4) URANS

The flow field in the compressor is inherently unsteady and three-dimensional. Due to the limitations caused by essential simplifications, analytical models and body force methods can reproduce the overall performance of the compressor with inlet distortion but lack the capability to represent the detailed internal flow field with fairly accuracy. In addition, the body force for low mass flow conditions in the distorted region might be impossible to obtain from clean flow solutions and hence the body force simulations with inlet distortion are confined to the working conditions away from stall. With the soar of the computational capability, high-fidelity simulations like URANS and large eddy simulation (LES) are developed and applied. URANS simulations have already demonstrated its ascendancy in the modelling of complex unsteady phenomena like rotating stall and surge of multi-stage compressors [Dodds and Vahdati, 2015, Zhao et al., 2018]. There has been extensive amount of research using URANS for the investigation of inlet distortion. Some studies focus on the study of the flow field in the compressor with inlet distortion, such as the evolvement of the inlet distortion through the blade rows [Yao et al., 2007], the circumferential variance of the blade performance due to inlet distortion [Fidalgo et al., 2012], the interaction between the distortion and shock wave in the blade passage [Hah et al., 1996] and the flow loss generated by inlet distortion [Gunn and Hall, 2014]; other research take advantage of URANS for the distortion-resist blade design [Cousins et al., 2017, Gunn and Hall, 2017, Wadia et al., 2002]. As can be seen, most URANS simulations for inlet distortion studies are conducted away from stall boundary [Gunn and Hall, 2014, Hah et al., 1996, Yao et al., 2010a]. The stall margin prediction is also tried in [Mehdi, 2014] without the modelling of stall process. Until recently the stall boundary prediction with inlet distortion as well as the distorted stall inception process is tried with different types of inlet distortions [Page et al., 2018]. Large eddy simulation, though of high potential in its accuracy and reliability, still cannot be routinely used due to its prohibitive computational cost. Consequently, URANS is still the most convenient and dominant tool to perform the whole compressor simulations.

The simulations with inlet distortion usually employ whole annulus mesh due to the long-length scale of the inlet distortion. Fourier transformation method [He, 1990] with phase-shifted periodic boundary condition can be used to simulate the distorted case with reduced mesh size [Cornelius

et al., 2014, Sharma et al., 2013]. This method was based on [He, 2010] and found to be effective especially for the simulations with the disturbances of large scale compared with blade passage pitch. Good agreements with whole annulus simulations were obtained and the computational cost can be significantly reduced. However, this method is not capable to accurately capture stall process in which high frequency disturbances and non-rotating flow separations must be accurately resolved. Therefore, it can be used as a fast tool for compressor performance prediction when the operational condition is away from stall line.

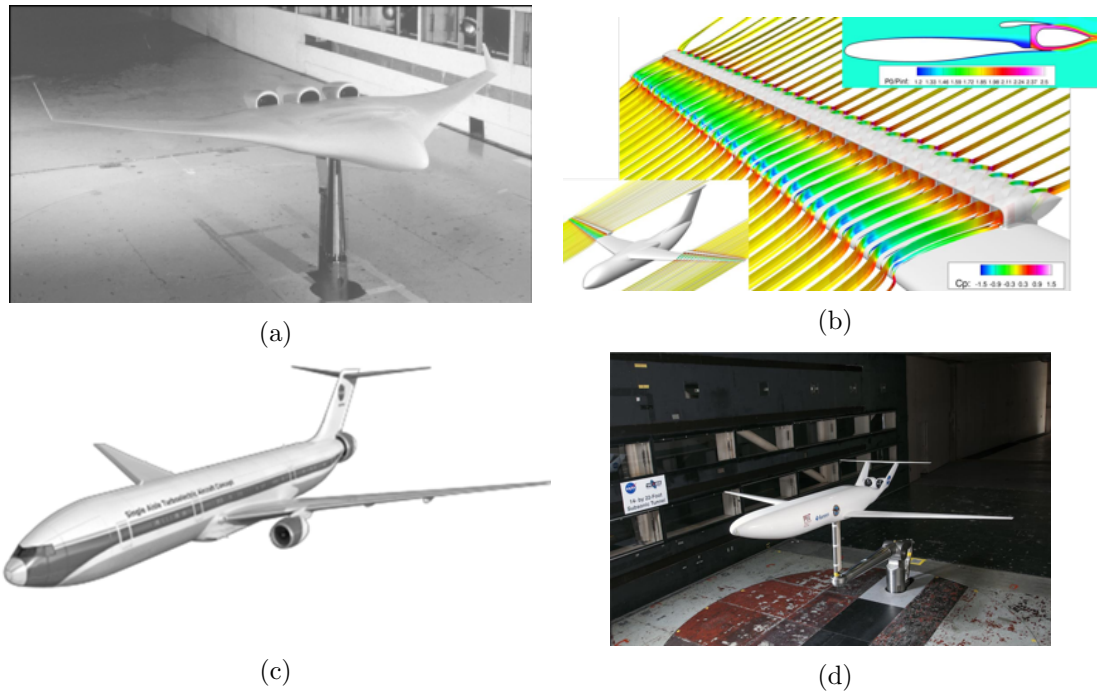
2.6 Boundary Layer Ingesting Propulsion

The engines on current jet aircrafts typically locate away from the aircrafts body to avoid ingesting the boundary layer on the airframe surfaces. A few different designs in service are shown in Figure 2.21. In these designs, the boundary layer can be avoided, diverted or removed. Typical installation of a commercial engine is pylon-mounted and hence keeps a distance from the wing and the airframe; or it is installed on struts extending into the free stream. For military engines, they are integrated into the body with a circular serpentine intake (abbreviated as S intake) to reduce the radar signature. To provide uniform inflow to the engine, various approaches like boundary layer diverter, slots and aerodynamic bump are employed.

In the new propulsion design with boundary layer ingesting, the engine is embedded in the aircraft body as well. Different from the military aircrafts, the BLI engines are aimed to ingest the low-momentum boundary layer flow. Two reasons account for the benefits of such design. Firstly, because the ingested boundary layer has lower velocity, the kinetic energy of engine jet decreases and the jet mixing loss is reduced; Secondly, the drag on the airframe is decreased due to the removal of boundary layer. It was also proposed that embedded boundary layer ingestion propulsion systems can enable nacelles with reduced surface area and associated weight, which further decreases the aircraft propulsive power requirement [Gunn and Hall, 2017]. As a consequence, the overall aircraft efficiency is increased and fuel consumption is reduced. Considerable performance superiority of the BLI propulsion over the conventional baseline airplane has been demonstrated with analytical calculations [Uranga et al., 2018], numerical simulations [Hardin et al., 2012, Kawai et al., 2006, Ochs et al., 2016] and experimental tests [Sabo and Drela, 2015, Uranga et al., 2017].

The concept of BLI propulsion was first proposed by Smith [Smith, 1947] in 1947. In this paper, it was proposed that the boundary layer on the aircrafts body surface could be collected with slots and fed into the turbojet engines through internal ducting. The engines are submerged in the wing and fuselage. However, there were no mature enough theories or any experimental tests to support the potential of such design at that time. No further research on BLI was found in public literature on aircraft until the end of 20th century, although similar designs based on BLI have already been adopted in nautical science [Brandau, 1968, Evanbar and Thurston, 1966, Wislicenus, 1960]. In the past two decades, different concepts and designs of BLI (Figure 2.21) have been proposed such as blended wing body (BWB) [Liebeck et al., 1998, Liebeck, 2004], distributed propulsion system [Felder et al., 2011, Wick et al., 2015], NASA's STARC-ABL concept [Jansen et al., 2016, Welstead and Felder, 2016] and the D8 double-bubble [Greitzer et al., 2010, Hall

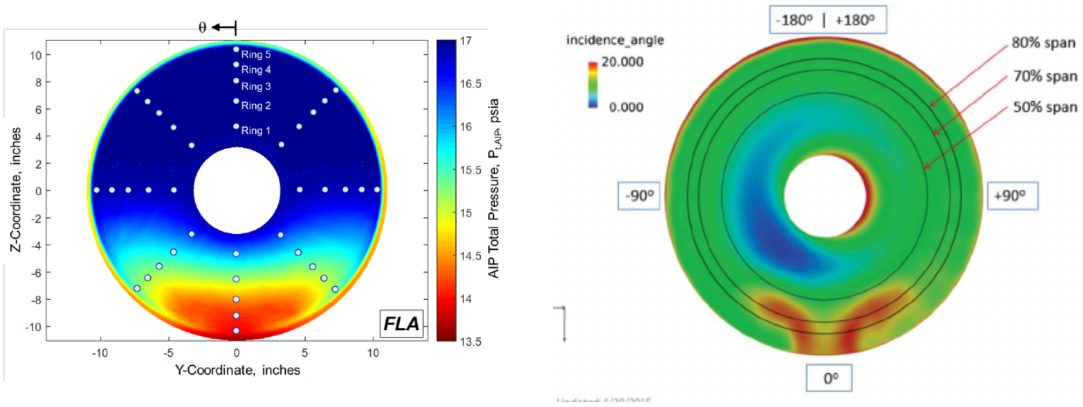
et al., 2017, Uranga et al., 2014].



(a) (b) (c) (d)

Figure 2.21: Aircraft propulsion system design for boundary layer ingesting: (a) Blended wing body (BWB) [Liebeck, 2004] (b) Distributed propulsion system [Wick et al., 2015] (c) NASA's STARC-ABL concept [Jansen et al., 2016] and the (d) D8 double-bubble [Uranga et al., 2014]

The design of aircraft with BLI propulsion system is actually quite challenging. Some preliminary work has been carried out on the design of S intake [Allan et al., 2006, Berrier and Allan, 2004, Florea et al., 2015], nacelles [Campbell et al., 2005, Carter et al., 2006], and engines [Cousins et al., 2017]. Among these different components, the design of a durable engine is the key concern. The difficulties to build a robust engine mainly comes from the constant complex distortion generated in the S intake. Figure 2.22 shows the typical total pressure distribution and swirl pattern at the exit of a typical S intake. This inflow condition will lead to both aerodynamic and mechanical problems: (1) efficiency and stall margin reduction of the fan; (2) distortion-induced fan force response dynamic stress and flutter [Bakhle et al., 2018a]. Therefore, a thorough understanding of the interactions between the fan and inlet distortion is essential; accurate predictions for the aerodynamic and mechanical stability margin of the fan must be achieved at the design stage.



(a) (b)

Figure 2.22: Distortion pattern generated by the S intake: (a) Total pressure [Arend et al., 2017] and (b) Swirl distribution [Giuliani and Chen, 2016] at the exit of the serpentine duct

Different BLI fan test rigs have been built to facilitate the study of distorted fan behaviour and the prototypical fan design. Two representative test rigs are the BLI test rig in Cambridge Whittle lab and Wind tunnel integrated BLI propulsor in NASA Glenn Research Centre. Investigations mainly focus on the BLI fan performance and stall process in whittle lab, which further extend the knowledge on compressor behaviour with inlet distortion. In their research [Gunn et al., 2013, Gunn and Hall, 2014] a distortion screen is used to mimic the inlet distortion pattern at the exit of the S intake in a real BLI. Such a substitution neglects some essential distortion components like swirl distortion. Moreover, the interactions between the fan and the distortion generated by the S intake cannot be well reproduced. In NASA Glenn Centre, a successful fan design was demonstrated through an integrated inlet/fan URANS CFD [Cousins et al., 2017], which proves the necessity and economy of such kind of simulations. However, it can be seen that the tested stall margin of the BLI fan is not well captured by their CFD simulations (Figure 2.23). Consequently more efforts are needed to develop numerical strategies for better prediction of the distorted stall limits.

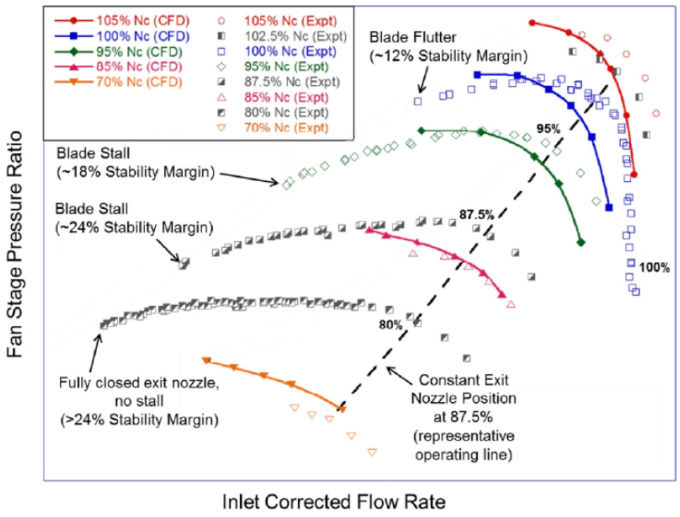


Figure 2.23: Preliminary fan stage map showing the approximate achievement in stability margin [Cousins et al., 2017]

2.7 Chapter Summary

In this chapter, the previous research with inlet distortion and rotating stall have been briefly reviewed. While efforts are increasingly devoted into the research of inlet distortion in compressors, a number of challenges and unknowns still exist in this area. These can be outlined as:

1. The predictions of the stall boundary for compressors in the published literature are not satisfactory and thus a validated CFD methodology needs to be developed.

2. The detailed process of stall inception with inlet distortion remains unclear. Such absence limits the design and application of possible stall control strategies.

3. The influence of abrupt inlet distortion on compressors has been less studied. Such kind of inlet distortion can be quite common in real situation but it is difficult to be tested in the experiments.

4. There has been no research regarding how inlet distortion influences the recovery process from rotating stall, which is important for the performance assessment of a compressor.

Based on the above facts, the current research aims to address these issues, which will be shown in the following chapters.

3 Methodology and Case Validation

3.1 Challenges for CFD with Inlet Distortion

To capture the effects of inlet distortion on compressor performance and stall margin accurately, suitable simulation strategies must be adopted. As the inlet distortion and rotating stall are of the nature of low engine orders, full-annulus computational domain must be used. However, the temporal resolution of the simulations must be fine to resolve the detailed flow structure (such as blade separation and tip leakage flow) and the high harmonics in the distortion. As a result, large mesh size and longer computational time are required to perform such kind of simulations. Therefore, some simple principles are needed on how to seek a balance between the fidelity and the cost. Therefore, the simulated results will be affected by the spatial and temporal resolution needs to be figured out. In addition, instead of modelling the true geometry of the inflow volume and exit plenum in the test rigs, truncated simulation domains are typically used. The selection of appropriate boundary conditions is important to reproduce the flow field with the truncated domain accurately. These two problems are general and are irrelevant to any CFD solver used for such simulations. Detailed discussion is as following:

(1) Spatial resolution (mesh quality)

It is widely known that the spatial resolution has important influence on the accuracy of the simulations. For the stall simulations, high resolution grids must be guaranteed especially in the hub and tip region where rotating stall is initialised. Therefore, a mesh independence study needs to be carried out before proceeding to further computations.

(2) Temporal resolution in the time-accurate simulation

The determination of the temporal resolution usually adopts the role of thumb-choose a time step which is assumed to be fine enough to capture the complex high-frequency phenomenon of interest in the flow field. This is usually because a temporal convergence study incurs much more computational cost on a full-annulus mesh. There are no principles on calculating an '*accurate*' time step size and estimating the possible outcome if inappropriate time step is used. In this section, the frequency range to guarantee accurate modelling both at design condition and stall inception is analysed. The result obtained here indicate that the time step size depends on the flow field. Smaller time steps are required for accurate modelling of the flow near stall boundary. The effects of temporal resolution on the predicted stall margin is also explored.

(3) Inlet and exit boundary condition

At the compressor inlet, the distortion pattern (total pressure, total temperature and flow angle) is usually fixed to mimic the experimental conditions. Such setup is reasonable when the distortion is far upstream of the compressor and no large changes occur in the operational condition of the compressor. Experiments have shown that the averaged inlet flow parameters

are still unchanged when rotating stall occurs in a fan test rig [Anderson and Smith, 2006].

It is difficult to determine a suitable exit boundary condition. Different types of exit boundary conditions can be found in published literature [Yao et al., 2010a,Chima, 2006,Haug and Niehuis, 2018,Bakhle et al., 2018b,Herrick, 2011,Vahdati et al., 2005]. The most ideal boundary condition is an exit pressure distribution measured in the experiments [Yao et al., 2010a]. However, such kind of boundary condition is not usually available and large amount of data need to be collected if the operational condition and rotational speed of the compressor change. Other types of boundary conditions such as non-reflective boundary with static pressure [Yao et al., 2010a], static pressure with radial equilibrium [Chima, 2006,Haug and Niehuis, 2018], mass flow boundary condition [Bakhle et al., 2018b], or a throttle model [Chima, 2006] were also tried. A comparison conducted in [Herrick, 2011] with different boundary conditions shows the obvious differences in the predicted stall margin for these exit boundary conditions. This is because the fan or even a multi-stage compressor is generally not capable of removing all the distortion at the exit. The exit flow pattern can be very complex and this calls a circumferential uniform exit pressure into question. The distortion can also change the blade loading along the span and thus an exit pressure profile with radial equilibrium is also difficult to apply due to the unknown profile beforehand. In addition, the mass flow boundary condition can be used to detect the stability margin when the solver fails to obtain a converged solution, but it fails in a transient process when the amplitude of the oscillation in mass flow is large (e.g. rotating stall). It will be shown in this chapter that a choked nozzle [Vahdati et al., 2005] is an appropriate choice for the non-asymmetric flow and the mass flow oscillation.

It is noted that the stall margin prediction also depends on the turbulence model and numerical scheme used. While these considerations are quite important, they are more solver-specific and will not be discussed here. Based on above analysis, the aim of this chapter is to:

1. Choose a suitable approach for the simulations with inlet distortion using a parametric study.
2. Validate the reliability of the numerical strategy by comparing against experimental data.
3. Study the effects of inlet distortion on fan performance at the PE and NS conditions.

3.2 Numerical Methodology

3.2.1 CFD Solver

The CFD solver used in this study is AU3D which has been developed at Imperial College VUTC over the past 25 years with support from Rolls-Royce. It is an implicit, time-accurate 3D compressible Reynolds-averaged Navier-Stokes (RANS) solver. This flow solver is based on a cell-vertex finite volume methodology and mixed-element unstructured grids. The mesh is characterized by using an edge-based data structure and the grid is presented to the solver as a set of node pairs connected by edges. The central differencing scheme is applied with a mixture of second and fourth-order matrix artificial dissipation for stabilization. In addition, a pressure switch, which guarantees that the scheme is total variation diminishing (TVD) and reverts to a first-order Roe scheme in the vicinity of discontinuities, is used for numerical robustness. The

resulting semi-discrete system of equations is advanced in time using a point-implicit scheme with Jacobi iteration and dual time stepping. Solution acceleration techniques, such as residual smoothing and local time stepping, are employed for steady-state flow calculations. For unsteady computations, an outer Newton iteration procedure is used where the time steps are dictated by the physical restraints and remain fixed through the solution domain. Within a Newton iteration, the solution is advanced to convergence using previously mentioned acceleration techniques. Further details can be found in Sayma et al [Sayma et al., 2000].

The current computations use the one-equation Spalart-Allmaras turbulence model. The parameters in Spalart-Allmaras have been adjusted on previous fans to get good agreement near the stability limit; the parameters are held constant in all the present work. The resulting CFD Code has demonstrated its performance for the flows at off-design conditions with a good degree of success [Choi and Vahdati, 2011, Dodds and Vahdati, 2015, Zhao et al., 2018].

3.2.2 Test Case

NASA rotor 67 [Strazisar et al., 1989] is chosen as the test case in this research, for which a significant amount of measured steady and unsteady data is available. It is an undampered low-aspect-ratio design rotor. Its design pressure ratio is 1.63 at a corrected mass flow of 33.25 kg/sec. The design rotational speed is 16043 rpm, which yields a tip speed of 429 m/sec and inlet tip relative Mach number of 1.38. The mean hub/tip ratio of this blade is 0.43. The rotor row has 22 blades. The stator row S67A used in the distortion experiment has 34 blades. All the experiments were carried out at the W8 Single stage Compressor Test facility at NASA Glenn Research Centre (Figure 3.1). Different rotational speeds were tested with the clean flow. Radial distributions of the total pressure, total temperature and flow angle in the fan stage were measured with probes at fixed circumferential and axial position, shown as Figure 3.2. In the tests with inlet distortion, a mesh screen was installed in front of the rotor. The measured data is available at the near peak efficiency (PE) point at 90% rotational speed.

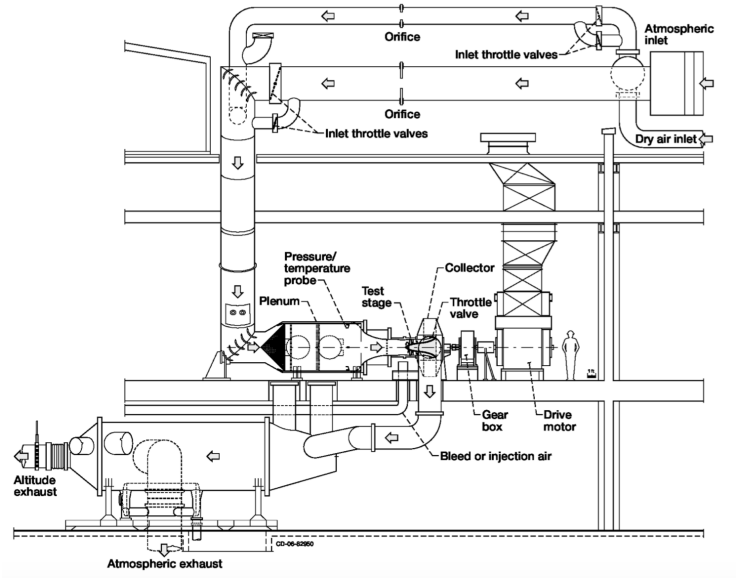


Figure 3.1: Schematic of the W8 single-stage axial compressor test facility [VanZante et al., 2009]

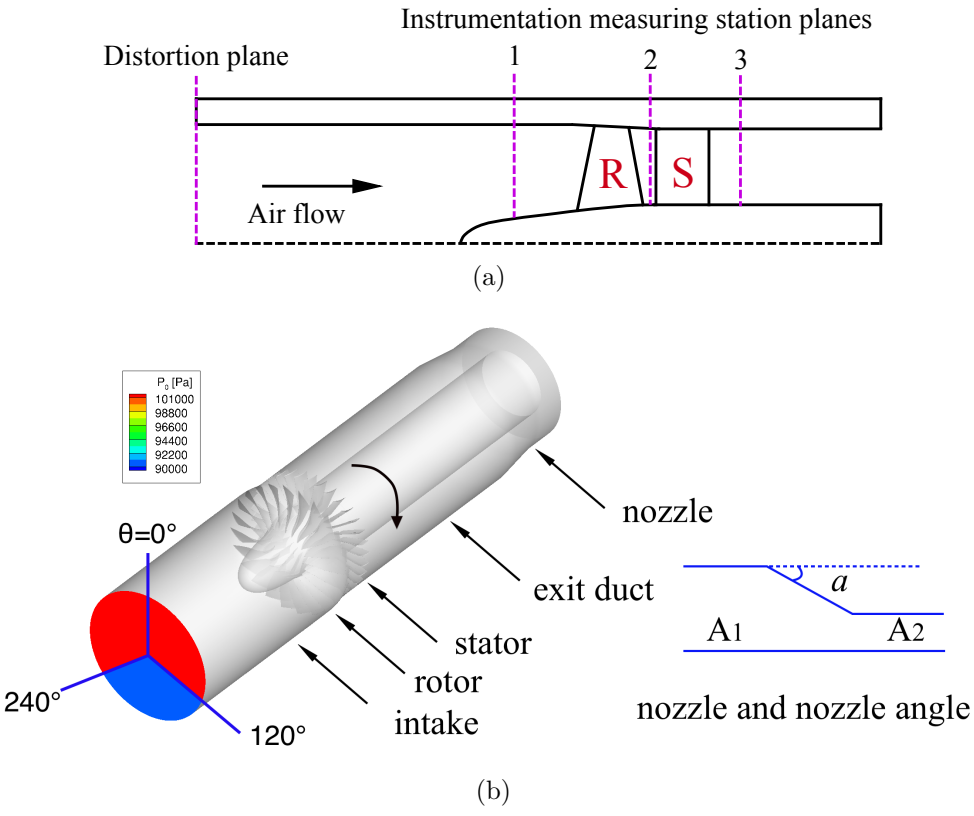


Figure 3.2: (a) Flow path schematic for NASA 67 fan stage (b) Isometric view of the computational domain of NASA rotor 67 with inlet distortion

3.2.3 Computational Domain and Boundary Conditions

The computational domain was constructed by using the actual values of intake length and axial gap (between the rotor and stator) from the test rig. The full annulus simulation domain for

the whole stage includes an intake, a rotor row, a stator row, an exit duct and a nozzle. The boundaries between blade rows is modelled as sliding plane [Barakos et al., 2001]. The plenum is not included as its volume is unknown. The length of the exit duct is 1.5 times that of the rotor diameter (D). The rotor is modelled with a tip clearance of 0.5% span. A shrouded stator mesh is used. The nozzle downstream of the fan is choked, which impedes the disturbance from the exit propagating upstream, i.e. the flow becomes independent of exit pressure. The operating point of the fan is only determined by the nozzle angle; by closing or opening the nozzle, the corrected mass flow of the fan is reduced or increased [Vahdati et al., 2005]. It is found that this form of imposing outlet conditions is ideal for computations with inlet distortion as it would allow radial and circumferential variations of exit flow quantities.

At the inlet, total pressure, total temperature and flow angles are specified. Total temperature is uniform and the circumferential and the radial flow angles are zero. For the steady computations, a single-passage model is used to reduce the computational cost. The boundaries between stationary and rotating blades are treated as mixing planes [Denton, 1990]. The stall boundary is defined as the point on the constant speed characteristic at which the slope becomes positive. Considerable loss occur in the pressure ratio and mass flow when the compressor falls into rotating stall. It needs to be mentioned that the aerodynamic instability of the compressor concerned is rotating stall in this research. Surge is a system instability caused by the interaction between the compressor and the attached volumes [Barrera-Medrano et al., 2017], which is not studied here due to the unknown of the size of the downstream volume in the experiments. It was shown in [Lee et al., 2019] that for a low speed fan, accurate modelling of the stall boundary requires a whole assembly time accurate computation, but for this test case whole assembly time accurate computations did not change the stall boundary of the blade significantly. The steady, single-passage solutions are used as initial solutions for the unsteady computations to improve the convergence. Starting from the steady solution with the fixed nozzle throat area, a distortion plane with a low total pressure sector of 120 circumferential degree is placed at the inlet (blue region in Figure 3.2b), which mimics a very sudden maneuver of the aircraft or an abrupt unstable airflow (abrupt distortion). Convergence of unsteady computations is monitored by tracking the lift coefficient of the rotor blade, and the simulation is deemed as converged when the rotor lift becomes periodic. The tolerance of the periodicity is within 1%.

3.2.4 Steady Computations and Mesh Independence Validation

In this section, the steady CFD results (for a clean inflow) are compared against measured data. Before proceeding with detailed comparisons, a grid size study was performed to obtain an optimum mesh (in terms of computational cost and accuracy) for the rotor blade. Three grids with different densities were used to simulate the flow at 100% rotational speed. The main parameters of the grids are listed in Table 3.1.

Figure 3.3 shows the comparisons of the CFD results against the experimental data (EXP); although the agreement between the CFD and the experimental data for the grid with 1.5 million points is better, the grid with 1.1 million points was chosen to seek a balance between the simulation performance and the computational cost while the predicted stall boundary for both

Table 3.1: Mesh quality of three different grids

	Mesh 1	Mesh 2	Mesh 3
Mesh points (million)	0.64	1.1	1.5
First y^+ value	20	20	10
Radial layers/tip layers	60/10	80/10	90/14

Table 3.2: Mesh quality of different components

Domain	Mesh points (million)
Intake	2.45
Rotor (per passage)	1.1
Stator (per passage)	0.34
Nozzle	1.4

grids are almost the same. The mesh independence study is only carried out with rotor grid. The stator mesh is relatively coarse because it plays a less important role in the distortion transfer. The mesh quality of the different components in the final computational domain are listed in Table 3.2.

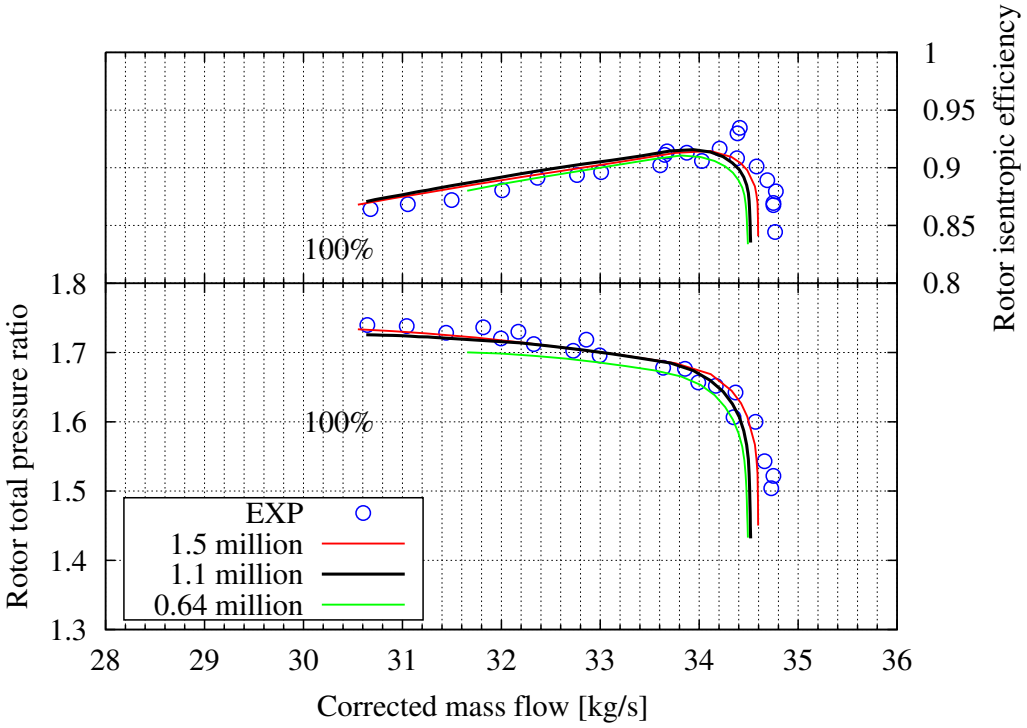


Figure 3.3: Characteristic of the rotor 67 with different grids

Figure 3.4 shows the comparison of computed and measured total pressure and isentropic efficiency characteristic maps for rotor alone (stator vanes were dismantled in these tests). There is a very good agreement between CFD and EXP for the steady characteristics. The CFD results of rotor 67 shown in this study are of the highest quality in the published literature. The corrected mass flow and total pressure ratio of the near stall (NS) points are computed accurately. The

choke mass flow in simulations is slightly lower than that in the test data, which is possibly due to the fact that the blade used in the simulation is more closed than the one used in the experiments. Also, the stalled mass flow is lower but the efficiency is higher at part speed in the experimental data than the CFD results, which is in common with other published CFD results for this test case [Fidalgo et al., 2012]. This is mainly due to the deteriorated flow condition due to the mismatch between the blade rows at lower rotational speed.

Figure 3.5 shows the comparison of the CFD and EXP of the radial profiles for the total pressure, total temperature and swirl angle downstream of the rotor at PE point and NS point at 100% speed. The total pressure and total temperature are normalised with inlet values. Generally, the radial profiles measured in experiments are also accurately captured at both operating points. The computed flow angle is around 3 degrees higher than that in EXP, which is in common with other CFD results for this blade [Arnone, 1994, Jennions and Turner, 1993, Arima et al., 1997].

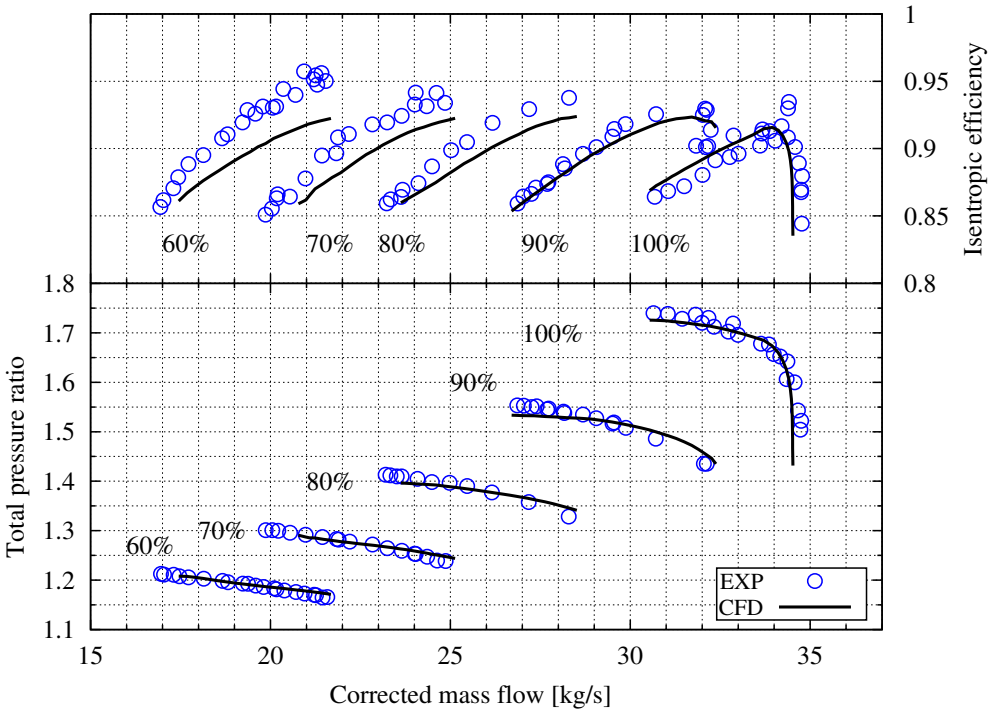


Figure 3.4: Rotor 67 characteristics in clean flow

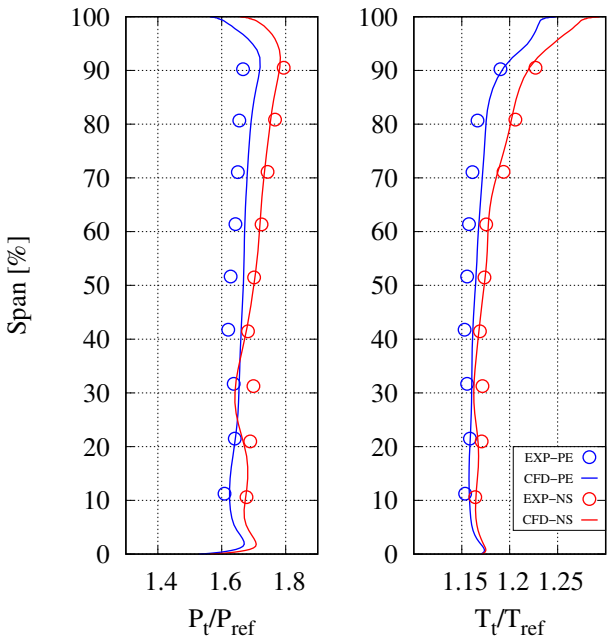


Figure 3.5: Circumferentially averaged, radial distributions downstream of the rotor for peak efficiency (PE) and near stall (NS), 100% speed

Figure 3.6 to Figure 3.11 show the comparisons of the relative Mach number contour obtained from CFD and Laser Doppler Velocimetry (LDV) in [Strazisar et al., 1989]. The plots of the relative Mach number distribution along the laser measurement surfaces at 30%, 70% and 90% span from hub at both PE condition and NS condition match well with the simulation. The position and the strength of the passage shock and bow shock are well reproduced in the simulation. As mentioned in the experimental report [Strazisar et al., 1989], the experimental measurement uncertainty is higher in regions of high-velocity gradients, which occur across the rotor passage shock and across the blade wakes. In these regions, the seeding particles may fail to follow the flow and this will lead to inaccuracy.

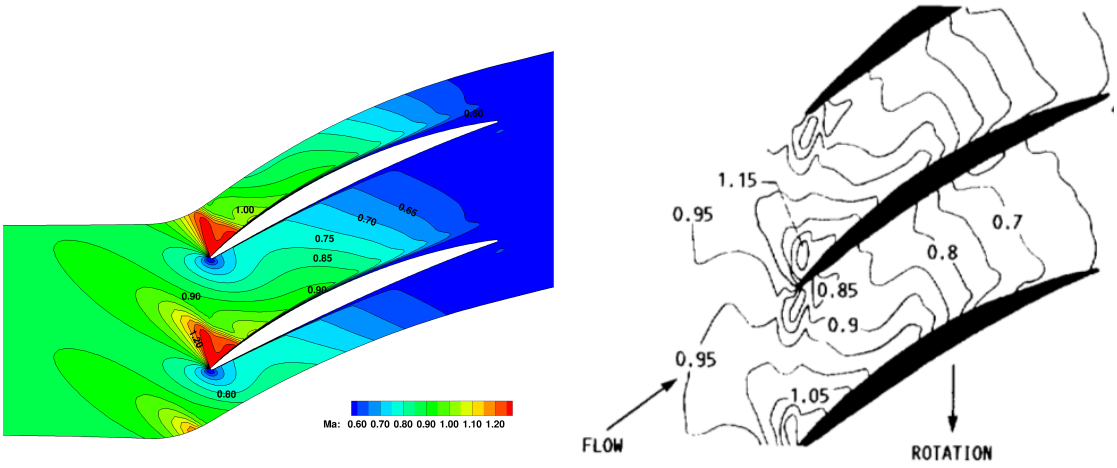


Figure 3.6: CFD and LDV results of blade-to-blade flow at 30% span from hub, PE, 100% speed

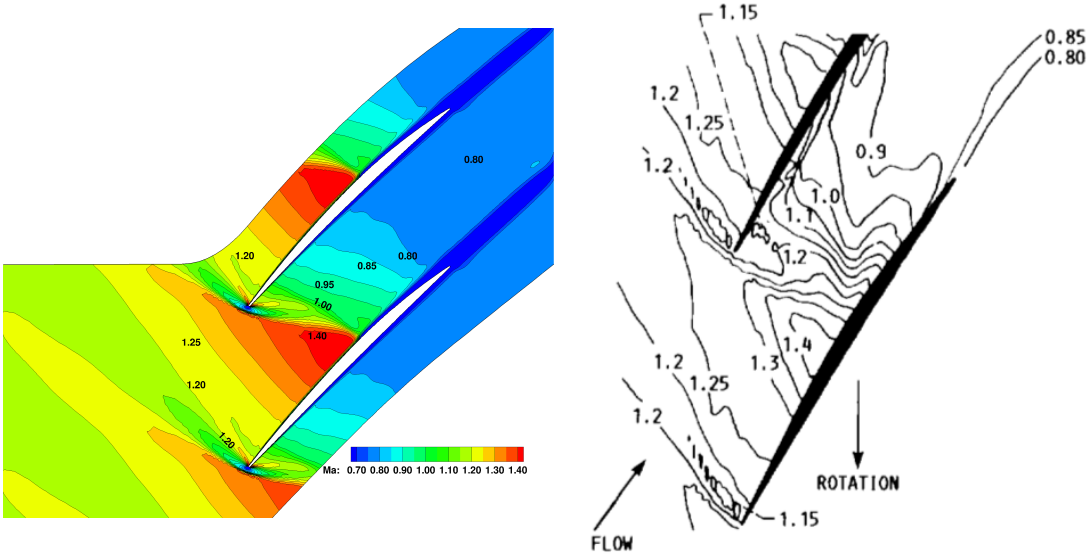


Figure 3.7: CFD and LDV results of blade-to-blade flow at 70% span from hub, PE, 100% speed

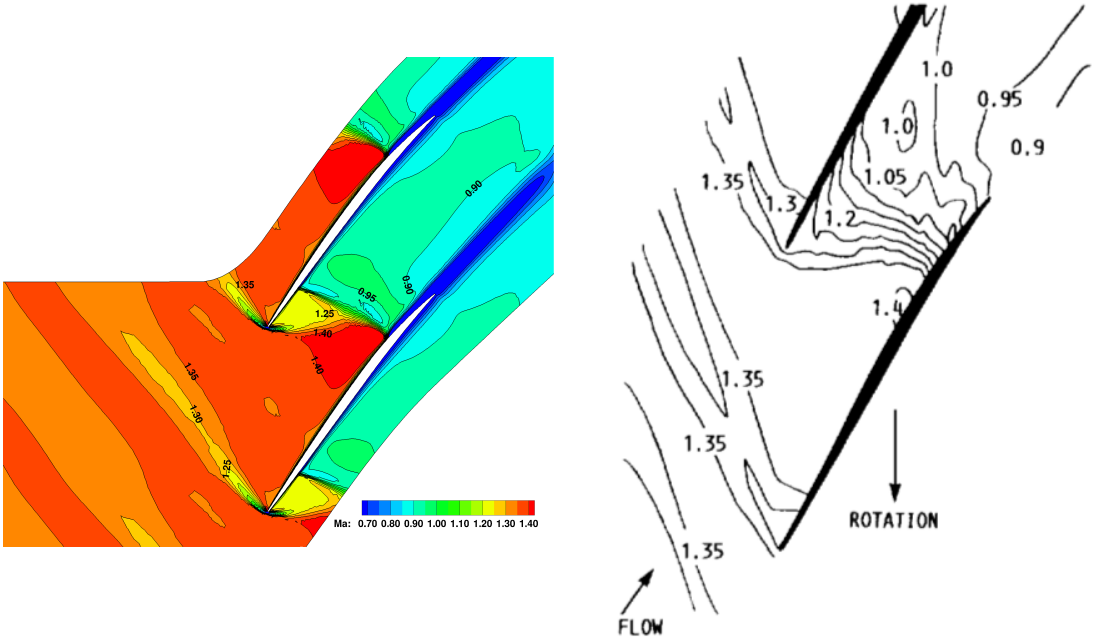


Figure 3.8: CFD and LDV results of blade-to-blade flow at 90% span from hub, PE, 100% speed

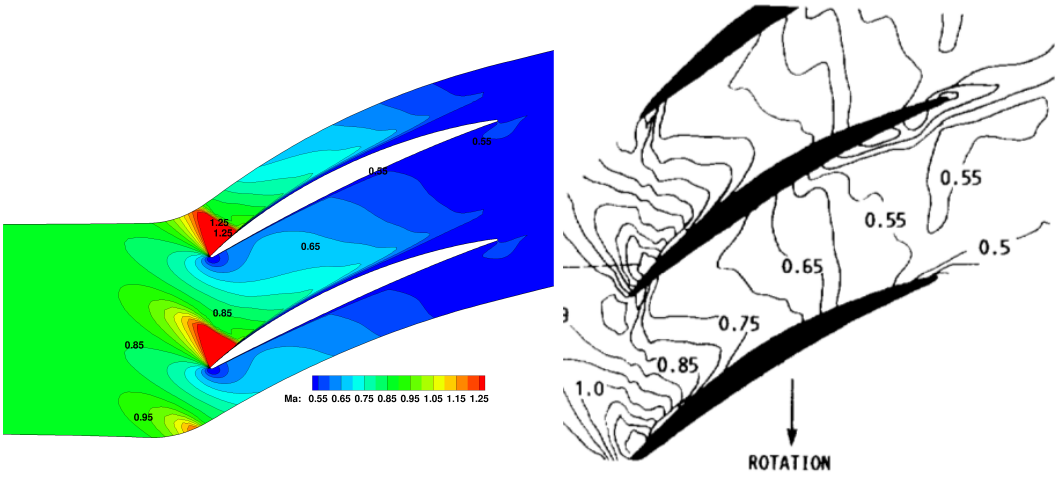


Figure 3.9: CFD and LDV results of blade-to-blade flow at 30% span from hub, NS, 100% speed

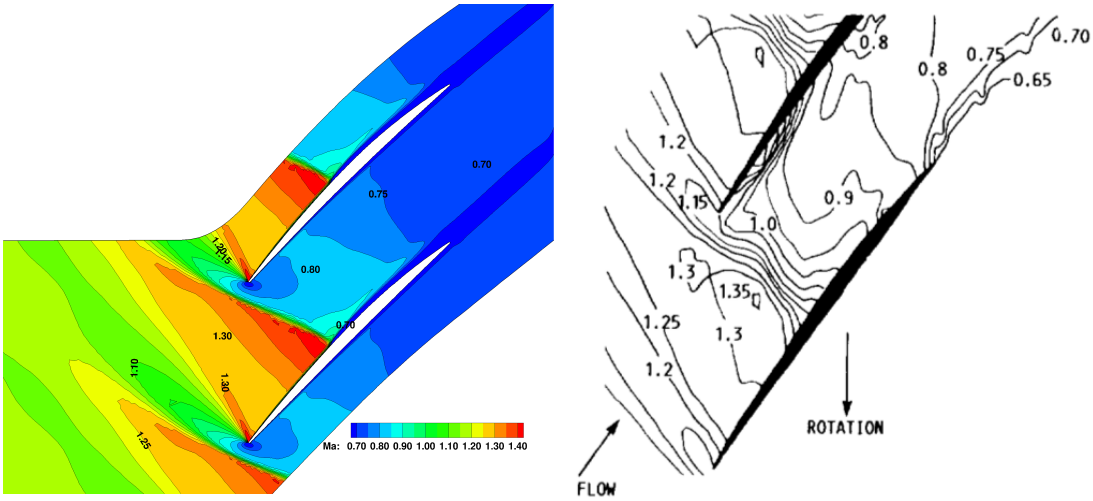


Figure 3.10: CFD and LDV results of blade-to-blade flow at 70% span from hub, NS, 100%speed

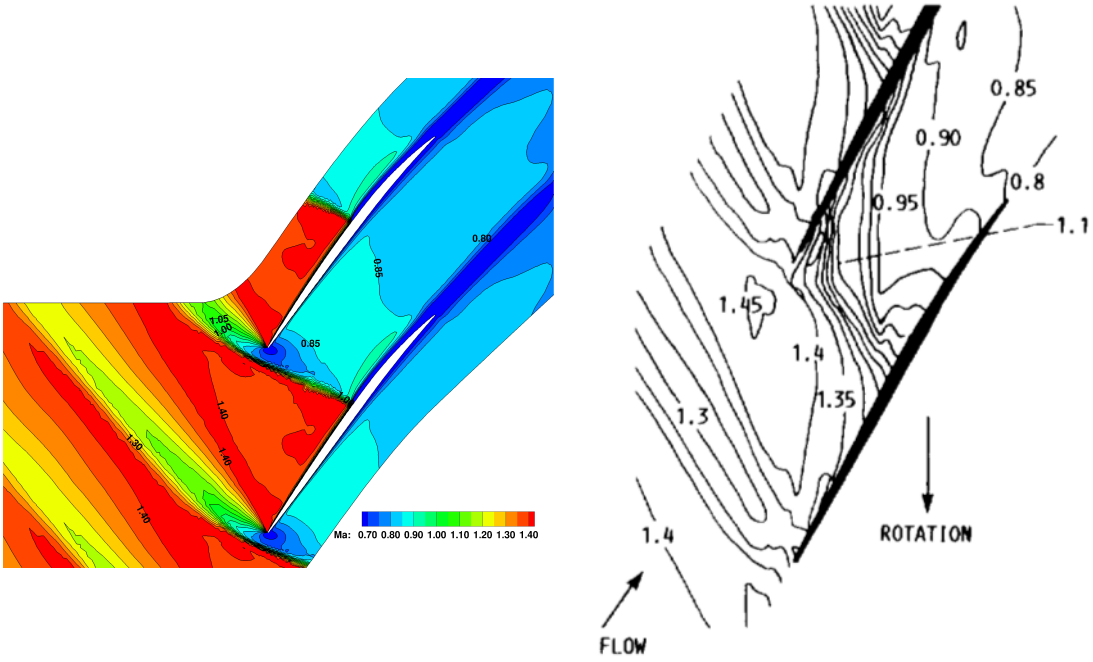


Figure 3.11: CFD and LDV results of blade-to-blade flow at 90% span from hub, NS, 100% speed

Figure 3.12 illustrates the computed and measured total pressure and isentropic efficiency characteristic maps for the whole stage. The overall simulated pressure ratio and efficiency are quite close to the experimental data and the predicted stall boundary at 80% and 90% corrected speed match the measured values. The slight under-prediction of stall boundary at 70% is probably because the same blade geometry is used for all rotational speeds, which would result in a more open blade at 70% speed.

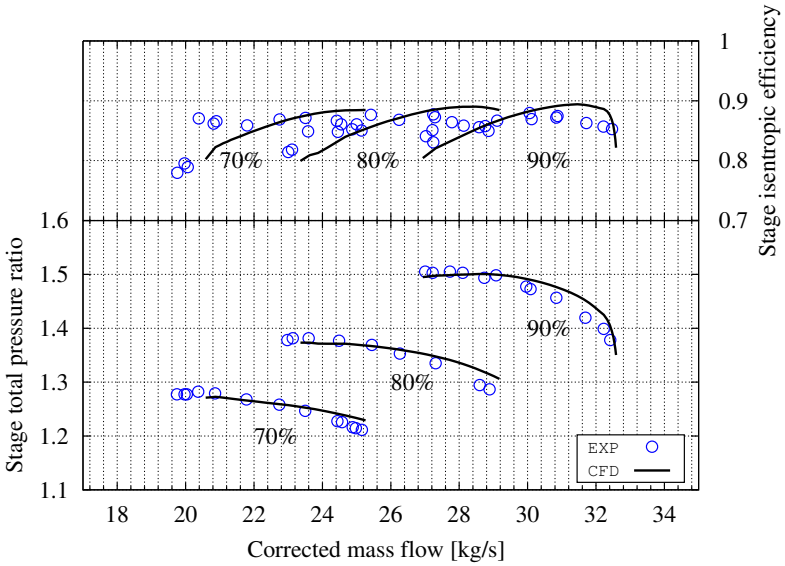


Figure 3.12: Stage 67 performance map in clean flow

3.3 Validation of the Unsteady Case with Inlet Distortion

In the experiment, the total pressure in the distorted sector was 10.5% lower than the total pressure in the clean sector. The experiment was carried out at the corrected mass flow of 32kg/s (near PE) and a pressure ratio of 1.46 at 90% rotational speed. Measurements were performed upstream of the rotor, downstream of the rotor and downstream of the stator (denoted by 1, 2 and 3 in Figure 3.2a). In the simulations the accuracy of the unsteady calculations is dependent on the size of the time step used in the analysis and thus a time step convergence study is required before proceeding with further calculations. The simulated operating condition is the near PE point with a corrected mass flow of 31.81kg/s. Figure 3.13 and Figure 3.14 show the comparison of time-averaged circumferential variations of total pressure upstream and downstream of the rotor for different values of time step against the EXP. The CFD results are presented as solid lines and the experimental data are denoted as circles. There are only minor differences between the computed results of 200, 400 and 2,200 time-steps/cycle and good match with the EXP are obtained for all three simulations. Similar results were obtained for other flow variables and at other stations, and thus it was deemed that 400 time steps/cycle is sufficient for the unsteady analysis at this flow condition. Based on previous experience, it is known that for a given frequency, AU3D requires about 200 time steps per cycle for accurate modelling of that frequency. The above observation (regarding the number of time steps) suggests that, for the near PE operating condition, correct modelling of the first two harmonics of distortion (or Engine Orders) would be sufficient to produce a temporal converged solution.

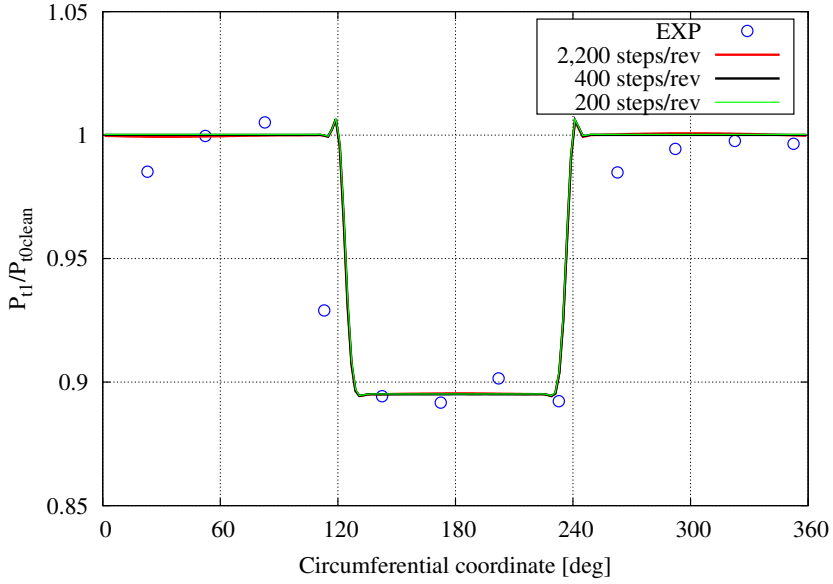


Figure 3.13: Time-averaged absolute circumferential total pressure at middle span upstream of the rotor at station 1, CFD (solid curve) and Experimental data (circle)

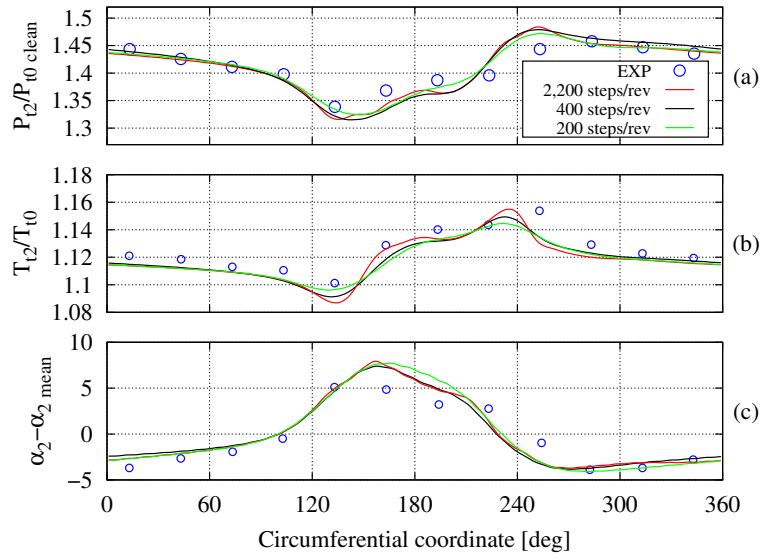


Figure 3.14: Time-averaged circumferential results at mid-span downstream of the rotor (station 2), CFD (solid curve) and Experimental data (circle)

A Discrete Fourier Transform (DFT) of the total pressure at the mid-span of the rotor (station 1 and station 2) is carried out to generate the harmonic spectrum of the flow field with inlet distortion. The circumferential wave number and amplitude of the harmonics are shown in Figure 3.15 and Figure 3.16. The normalized amplitude is calculated as

$$\tilde{P}_{n,i} = P_{n,i}/P_{t,i} \times 100 \tag{3.1}$$

where $P_{t,i}$ is the mass-averaged total pressure at measurement station i (1 or 2) with inlet

distortion, $P_{n,i}$ is the amplitude of the nth harmonic of the distortion. The harmonics with the normalized amplitude less than 0.3 are not presented in the plots. It is seen from Figure 3.15 that the amplitude of the distortion upstream of the fan decreases with increasing circumferential wave number. Moreover, Figure 3.16 shows that, as the distortion propagates through the rotor, there is a significant decrease in the intensity for all the harmonics, and the harmonics higher than 6 are almost eliminated. The loss in amplitude of the distortion when it passes through the fan passage increases as the circumferential wave number increases. Therefore, the amplitudes of the higher harmonics of the distortion are significantly reduced and thus their contributions to the flow field can be ignored.

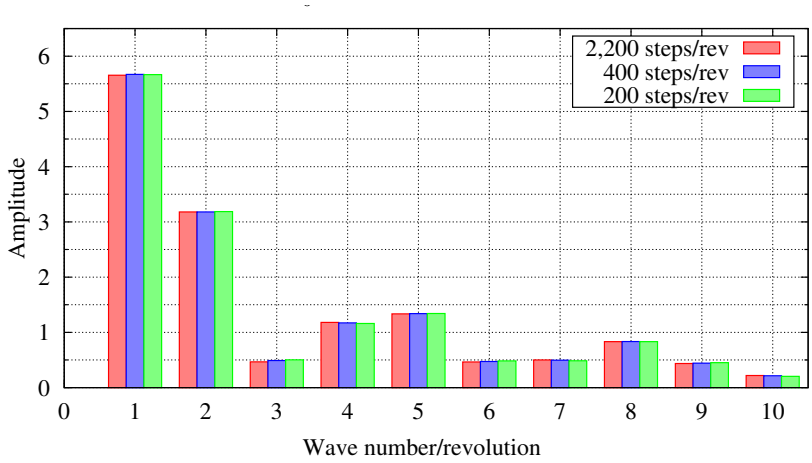


Figure 3.15: Amplitude of the harmonics of the total pressure at mid-span upstream of the rotor, PE

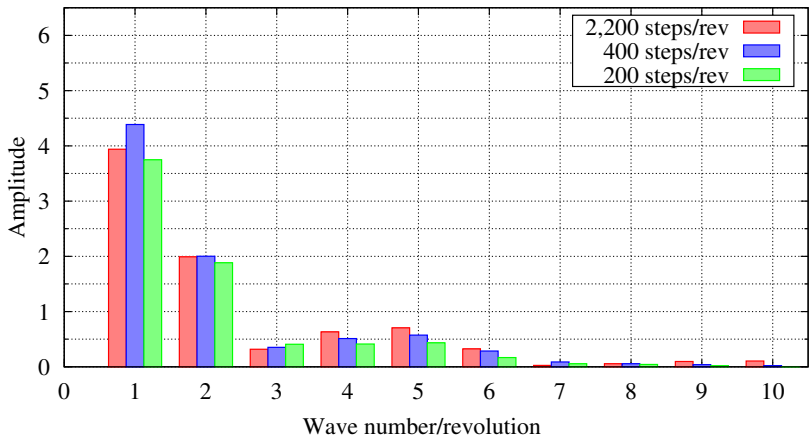


Figure 3.16: Amplitude of the harmonics of the total pressure at mid-span downstream of the rotor, PE

In the following analysis, further validation of the CFD with experimental data (EXP) at PE

condition is presented. As shown in Figure 3.17 to Figure 3.22, the overall performance of the simulation matches well with the test data at PE operating point. The performance of the fan stage in presence of inlet distortion at NS on the same speed line is also computed and compared with PE. The corrected mass flow of NS is 29.3kg/s. Same level of distortion (Figure 2.1) and 2,200 times steps/rev were used at both operating points. There are no measured data at this flow condition.

The two radial profiles in Figure 3.17 correspond to the low-pressure and the high-pressure sector, respectively. The simulation results match well with the experimental data except the hub region in the low-pressure sector. As can be seen there is a bump characterised with higher total pressure near the hub in the experimental data which is over-predicted by the CFD simulations. This bump is formed as a result of the redistribution flow from clean flow sector to distorted flow sector. It is seen from Figure 3.17 that, at the lower flow coefficient (NS), the high-pressure region expands radially, which is due to an increase in the redistribution flow near the hub.

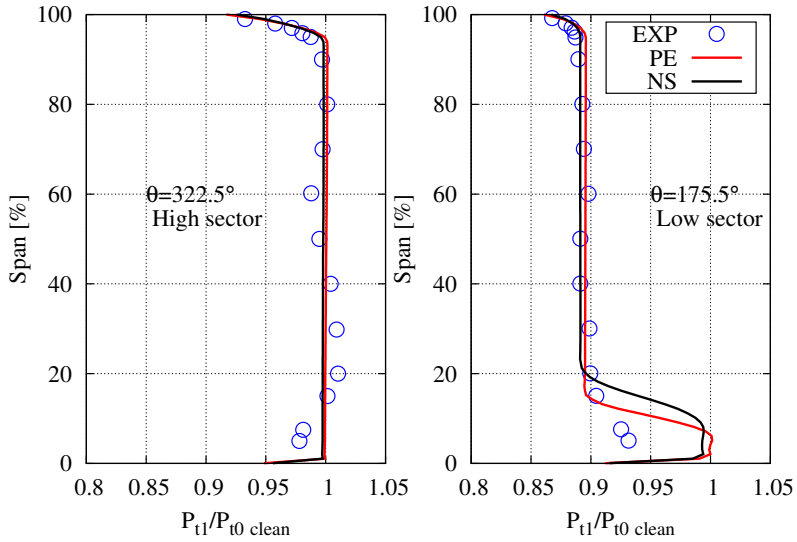


Figure 3.17: Time-averaged radial profile of the total pressure upstream of the rotor at circumferential angle =322.5° and =175.5°, CFD (solid curve) and Experimental data (circle)

Figure 3.18 shows the circumferential profile of the time-averaged swirl angle upstream of the rotor (station 1). Despite the swirl angle being zero at the inlet, a circumferential flow is induced by the static pressure gradient. A positive swirl angle in the plot denotes a reduction in incidence of the rotor. This phenomenon verifies that a swirl distortion can be generated by a total pressure distortion even when there is no vortex in the incoming flow. The amplitude and the phase of the swirl angle are well reproduced with the largest difference being about 1 degree. It is also seen from Figure 3.18 that, the swirl angle at the fan inlet differs between PE and NS point. The main difference is at 240°, which corresponds to the circumferential position where the rotor moves from the distorted sector to the clean sector. The difference in flow angle between these two operating points is due to the fact that at the NS point, the axial flow is reduced but the

amplitude of the circumferential velocity increases (due to an increase in circumferential gradient of static pressure), which means the flow redistribution in front of the rotor is stronger at NS condition.

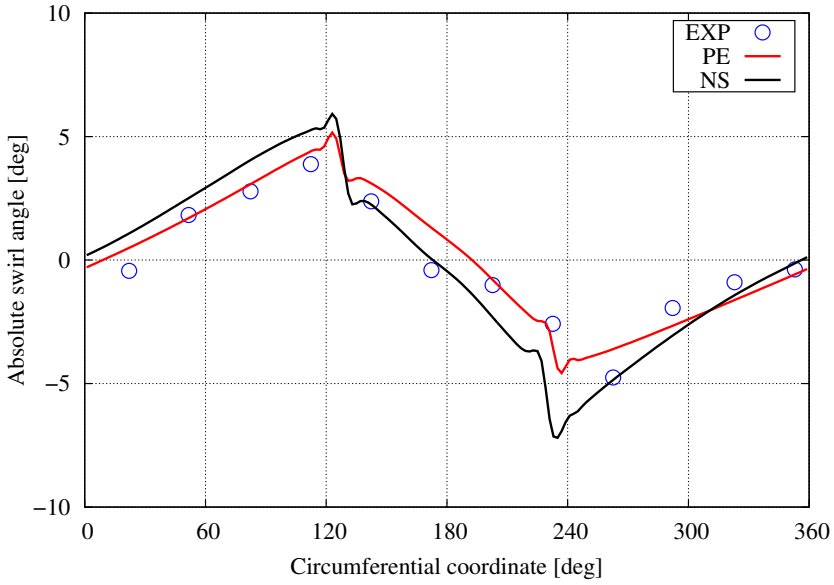


Figure 3.18: Time-averaged absolute circumferential swirl angle at mid-span at rotor upstream, CFD (solid curve) and Experimental data (circle)

Downstream of the rotor (station 2), the time-averaged total pressure, total temperature and the circumferential swirl angle around the annulus are compared with measured data, as shown in Figure 3.19. As can be seen from Figure 3.19, a total temperature distortion has been formed downstream of the rotor. On comparing the PE and NS operating points, it is seen that in the circumferential position between 255°∼275° the pressure rise is lower for the NS operating point than PE point, which indicates the initiation of stall in this region while is held stable by the flow in the neighboring clean flow sector. The above observation can also be seen in the swirl angle plot of Figure 3.19 which shows less turning for the NS point in the region between 255°∼350°.

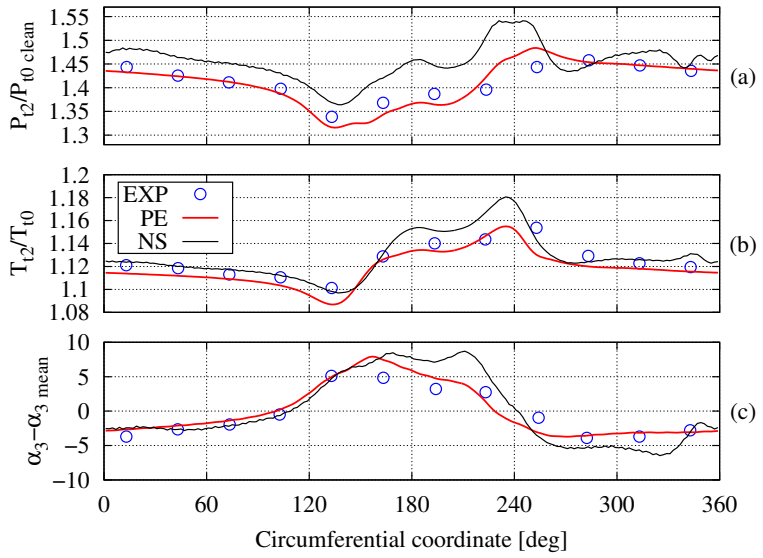


Figure 3.19: Time-averaged circumferential measurement results downstream of the rotor at mid-span, CFD (solid curve) and Experimental data (circle)

Radial profile of total pressure, total temperature and swirl angle are collected at two different circumferential positions (θ=283° and θ=73°, see Figure 3.20 and Figure 3.21). Again, the agreement between CFD and measured data is quite good, showing that most of the main features are captured. Figure 3.20 shows a slight mismatch in total temperature profiles near the blade tip region at θ=283° which is in common with other CFD results for this [Fidalgo et al., 2012]. It is also noticeable from the total temperature plot in Figure 3.20 that the measured data at PE operating point is in a better agreement with CFD results at the NS operating point than the PE operating point.

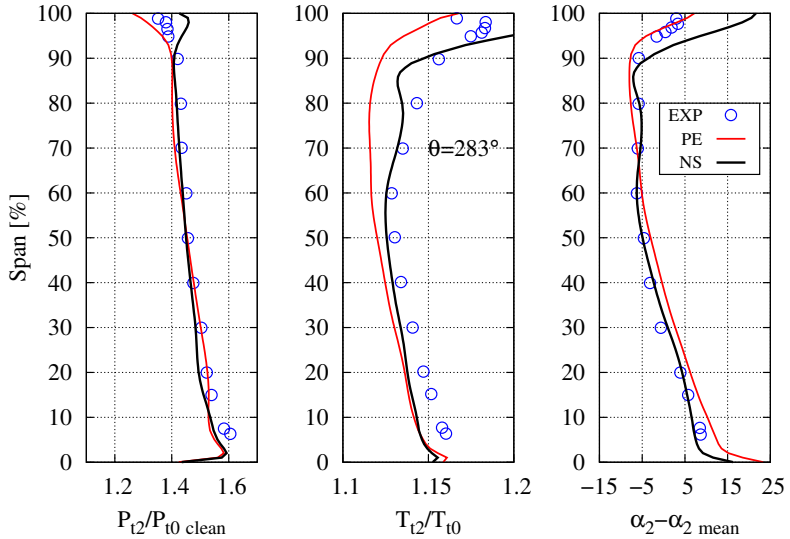


Figure 3.20: Time-averaged radial profile of total pressure downstream of the rotor at circumferential angle =283°, CFD (solid curve) and Experimental data (circle)

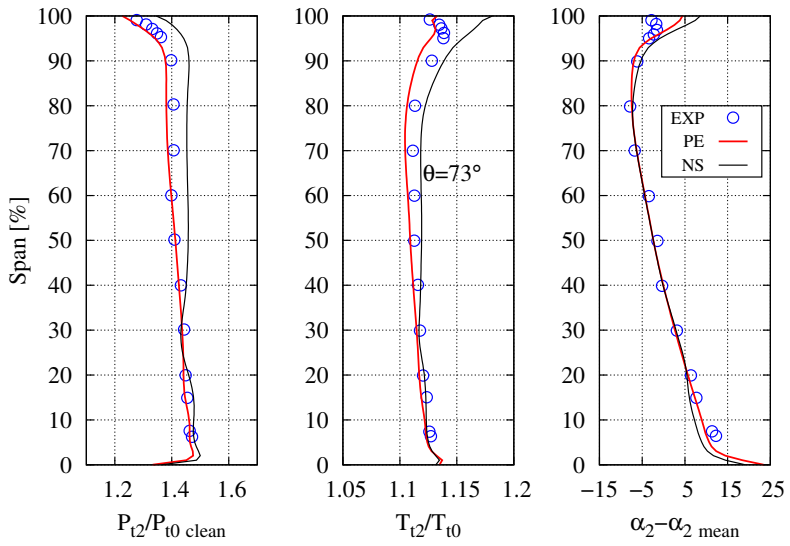


Figure 3.21: Time-averaged radial profile of total pressure downstream of the rotor at circumferential angle =73°, CFD (solid curve) and Experimental data (circle)

Figure 3.22 shows the comparisons of flow variables downstream of the stator vane (station 3). A considerable difference between the NS and PE operating points at this station can be seen from the plot. It is noticeable that the stator vane is unable to remove the swirl from the flow at NS operating conditions.

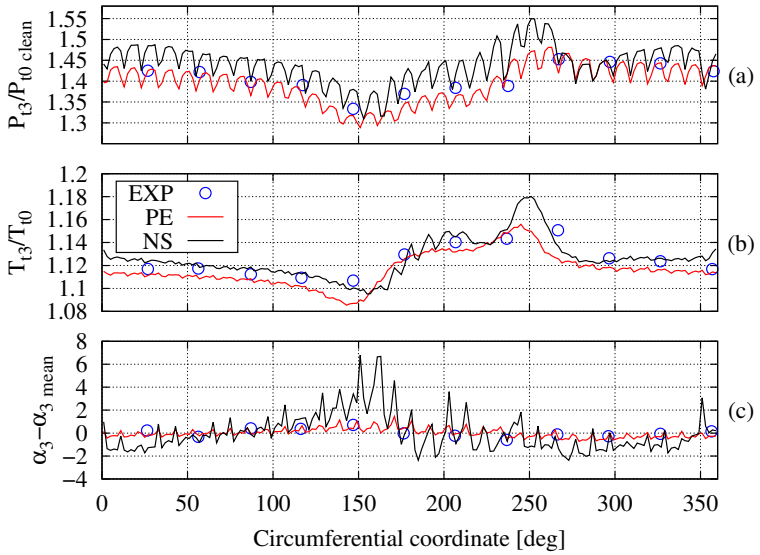


Figure 3.22: Time-averaged circumferential measurement results downstream of the stator at mid-span, CFD (solid curve) and Experimental data (circle)

Figure 3.23 shows the comparison of the harmonics of the distortion for PE and NS operating points downstream of the rotor. It is evident from this plot that, for the NS point the rotor is not capable of attenuating the higher harmonics (not as efficiently as PE operating point) and

therefore for this operating point finer temporal resolution is required for accurate modelling of the flow. The effects of temporal resolution on the computed stall boundary will be discussed in the following section.

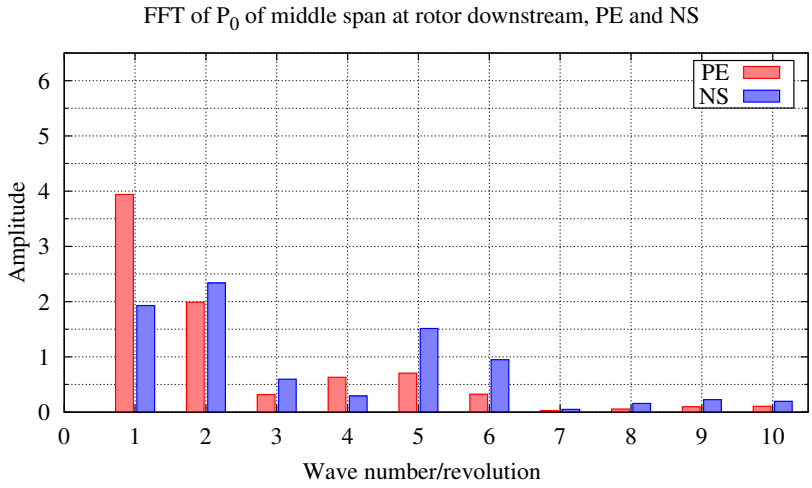


Figure 3.23: Amplitude of the circumferential wave numbers of the total pressure at the mid-span downstream of the rotor, PE and NS, 2,200 time steps/rev

3.4 Influence of the Temporal Resolution

It was shown that for flow conditions away from the stall boundary, 400 time steps/cycle is sufficient to obtain a satisfactory solution compared with experimental data. It will be shown in this section that, the temporal resolution has a greater influence as the mass flow drops and the stall boundary is approached. To the author's knowledge, the choice of time step size in most simulations are usually due to computational accuracy or convergence considerations while this paper focuses on the aerodynamic stabilities relevant to flow separation and rotating stall. It was also pointed in [Spalart, 2001] that in the flow close to the body where separated turbulence must be well resolved because higher frequency is likely to be excited. However, no relevant work on how the size of time step influence the stability margin of the compressor was presented in published literature. The conclusions obtained in this study can thus provide useful instructions for the determination of the time step size. Defining the stall margin as:

$$SM = [\frac{PR_s}{PR_{ref}} \times \frac{(\frac{W\sqrt{(T)}}{P})_{ref}}{(\frac{W\sqrt{(T)}}{P})_s)} - 1] \times 100\% \tag{3.2}$$

where PR_s and PR_{ref} are are the total pressure ratio of the NS point and the reference point respectively, and W, T and P are the weight mass flow, the mass-averaged total temperature and the normalized total pressure, respectively. The point of maximum efficiency in uniform inflow at each speed is used as the reference condition and the stall margin loss is defined as the difference

of stall margins between the clean case and the distorted case.

Starting from the same initial (undistorted) solution, time-accurate computations with distortion were conducted with 5 different values of time steps, which correspond to 220, 550, 1,100, 2,200 and 3,300 steps per revolution. The strength of the distortion is fixed for all the computations. Figure 3.24 shows the stall margin loss with abrupt inlet distortion (DC120) at 90% rotational speed. It is seen that the size of the time step has a great influence on the predicted stall boundary of the blade and using a coarse time step will result in an increase in the stall margin. Figure 3.25 shows the mass flow history at the rotor exit for different time resolutions. The cases with 2,200 steps/rev and 3,300 steps/rev become unstable and fall into rotating stall while the cases with coarser time resolution converge to stable solutions. Figure 3.26 shows the instantaneous contours of the axial velocity for 550 time steps/rev and 3,300 time steps/rev at the 10th revolution. While the flow is still stable for 550 time steps/rev, a stall cell (marked with dotted circle) represented by the strong reverse flow area at the tip region of the blade is clearly visible in the case with 3,300 time steps/rev.

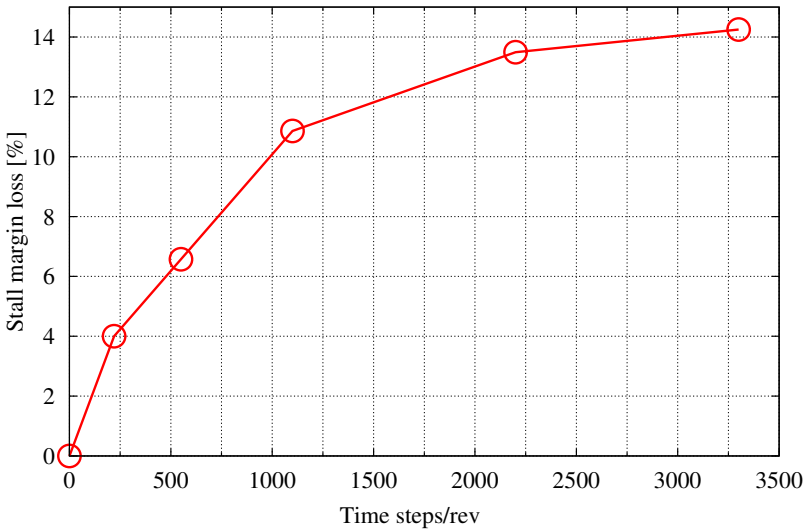


Figure 3.24: Stall margin loss with inlet distortion running with different time steps/rev

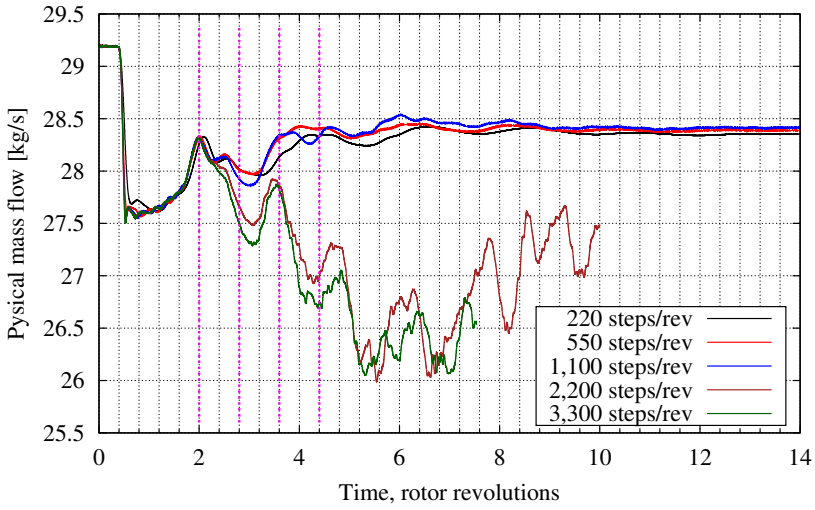


Figure 3.25: Mass flow history at the rotor outlet with different time step size

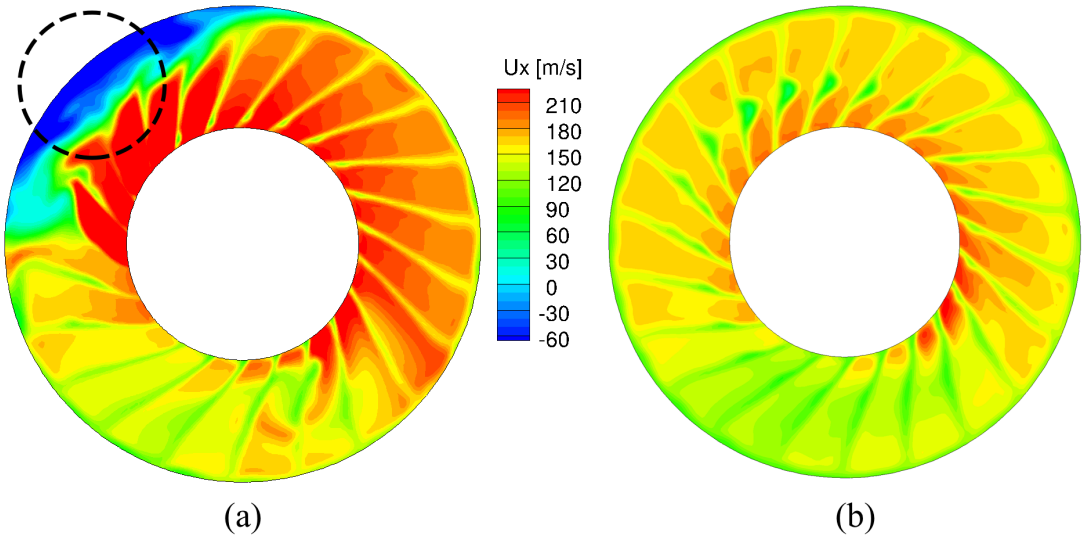


Figure 3.26: Axial velocity of the rotor outlet, (a) 3,300 and (b) 550 time steps/rev

To explain how the size of the time step cause such an obvious difference in the stability of the flow, the circumferential contour of the axial velocity at 98% span of the rotor is plotted for 550 and 3,300 time steps/rev. Four instants of time, which correspond to 2.0, 2.8, 3.6, and 4.4 revolutions in Figure 3.25, are chosen to show the evolution of the flow at the tip as the distortion propagates through the blades. It can be seen from these figures that after 2 revolutions (Figure 3.27, $t = 2rev$) the two solutions are still visually similar. However, considerable deviation appears in terms of flow separation on the blade surface and blockage inside of the passages at $t = 2.8rev$. This behaviour indicates that the development of high frequency unsteady features in the flow field which needs to be modelled with a small time interval. The case with 550 time steps/rev is characterized by flow separation in the distorted region and flow reattachment in the

clean flow region. In contrast, the flow separation in the case with 3,300 steps/rev survives and evolves into a stall cell.

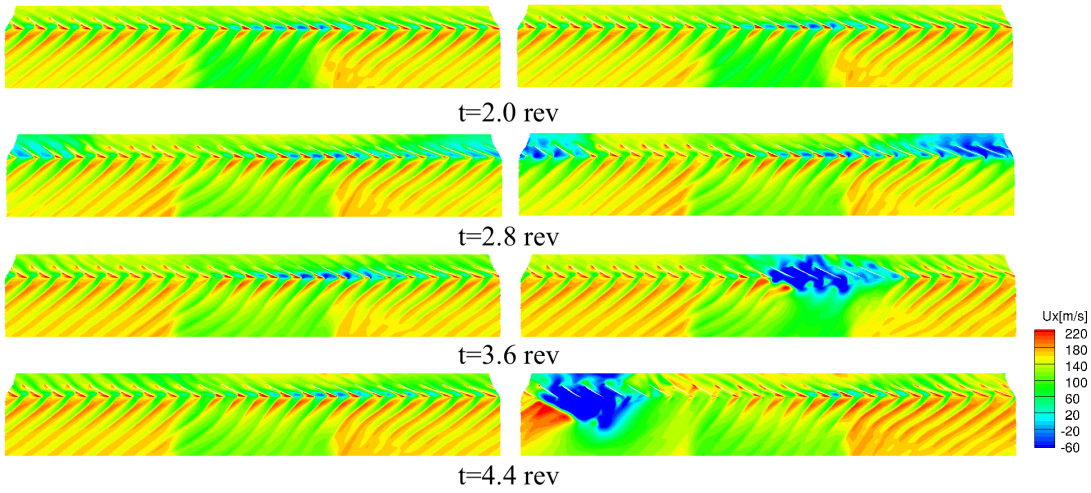


Figure 3.27: Circumferential contour of the axial velocity at 98% rotor span, 550 (left) and 3,300 time steps/rev (right)

It was shown in [Perovic et al., 2015] experimentally that for spike stall, the flow disturbances of frequencies between $0.7f_{bp}$ (blade passing frequency) and $0.9f_{bp}$ (in stationary frame) in the flow field trigger the stalling of the blade. Such frequencies cannot be modelled with larger time-step intervals (550 or 1,100 steps per rev, which will have 55 and 110 time steps per period) in the CFD. For a compressor operating away from the stall line, the flow is relatively stable and no obvious separation happens. Besides, the rotor is capable of attenuating the flow disturbances of high order frequencies, and therefore their accurate numerical modelling is not essential (see Figure 3.23). Consequently, at PE condition there is only a slight difference between the overall performances for different temporal resolutions. The above explanation is supported by the fact that the discrepancy between the simulation results of 400 and 2,200 time steps/rev for the peak efficiency point is minimal (see Figure 3.13 and Figure 3.14).

To further demonstrate the fact that the delay of stall is due to the absence of the flow disturbances of high frequencies in the cases with coarse time steps, a Fourier transform is performed for the static pressure on the casing. A numerical probe is set at 20% rotor chord in front of the rotor leading edge on the casing surface. The position of the probe is fixed in the stationary frame at 0° in Figure 2.1. The static pressure at every time step during the computation is extracted and analysed with Fourier Transform to get the spectrum components of the static pressure during the simulation. In Figure 3.28, (a) is the case with 550 time steps/rev and (b) is the case with 3,300 steps/rev. The time-averaged value is not shown in the plot. It can be seen that up to $1.7revs$ there are no other frequencies except the blade passing frequency and its 2^{nd} harmonic present as the distortion has not reached the blade yet. When the distortion reaches the rotor, broadband high frequencies appear around $0.7f_{bp}$, which are believed to be a pre-cursor to the stall. These disturbances are almost constant (between $2-3revs$) before the stall cell develops at about 3^{rd} revolution. At this point, the amplitude of frequencies around

$0.7f_{bp}$ drop while the amplitude of low frequency components increase. The above observation is quite similar with the experimental results [Perovic et al., 2015]. The spectrum result of the case with 550 time steps/rev does not contain any frequencies except the blade passing frequency and its 2^{nd} harmonic. As can be seen from Figure 3.27 ($t = 2.8rev$ and $t = 3.6rev$), the flow separation generated in the blade passages within the distorted region has almost disappeared before it is carried into the clean flow area. This prevents the stall cell from occurring [Perovic et al., 2015].

It has already been mentioned that AU3D requires about 200 time steps per cycle to accurately resolve a given frequency. Hence to model $0.7 - 0.9f_{bp}$ (which corresponds to wave number of 15∼20) AU3D requires 3,000 4,000 time steps/rev to completely capture these harmonics. This deduction is also supported by Figure 3.24 that shows the stall margin loss gradually becomes flat after 3,300 time steps/rev and hence finer time steps are unnecessary as the frequencies higher than $0.7 - 0.9f_{bp}$ are not relevant to stall inception.

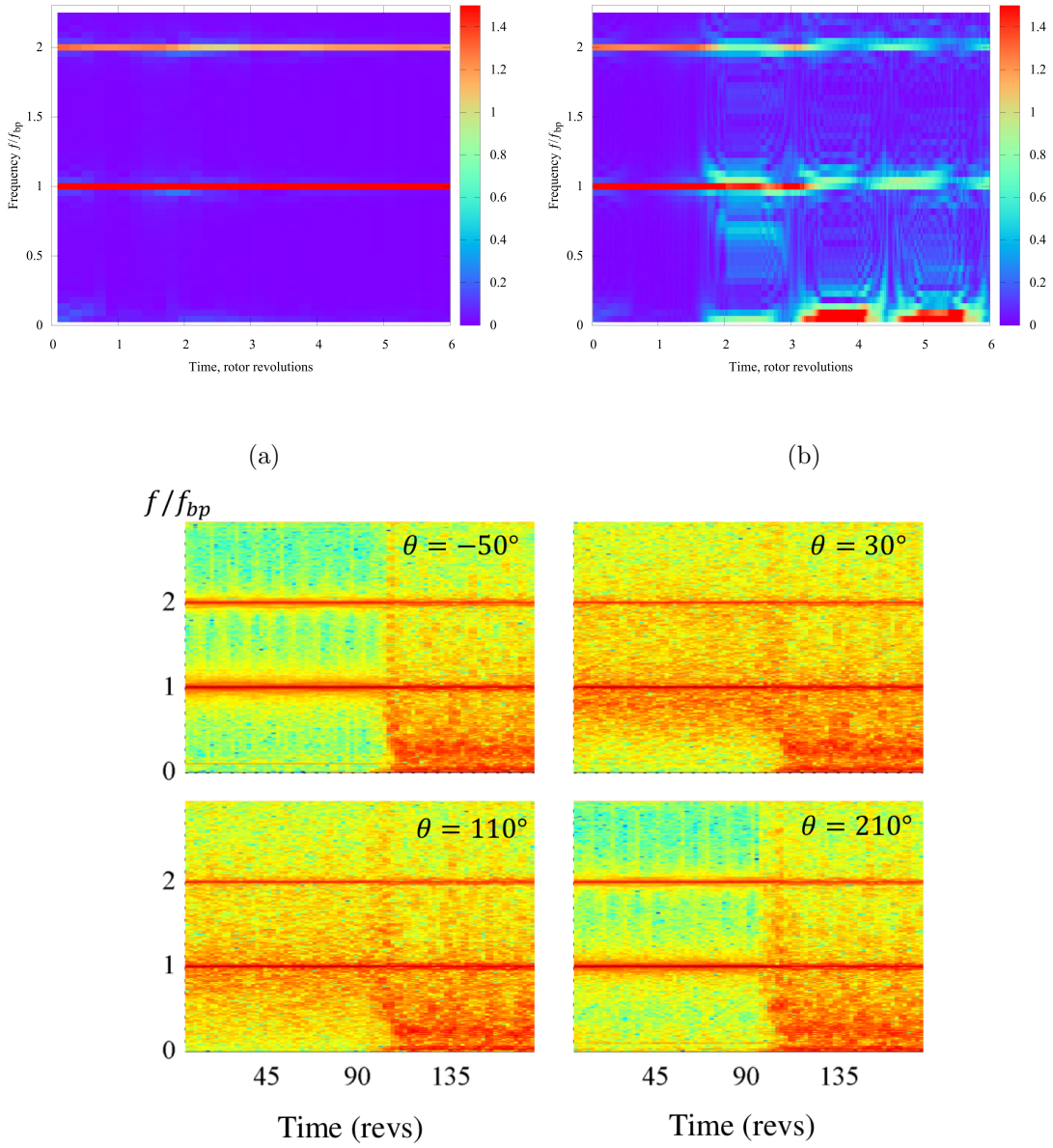


Figure 3.28: Spectrum of the casing static pressure signal for (a) 550 time steps/rev and (b) 3,300steps/rev (c) experimental data [Perovic et al., 2015]

To seek a balance between accuracy and computational cost, the author would suggest that 2,200 steps/rev, i.e., 100 time steps per passage is ideal for the stall margin prediction. This conclusion is based on the fact that the difference between 2,200 and 3,300 time steps/rev is relatively small, which indicates that more refined time step size is not essential.

3.5 Validation of Stall Boundary Prediction

The capability of the code for capturing the performance of the compressor at PE operating condition has already been demonstrated in the above section. Due to the lack of distorted NS

condition as well as the stall boundary data for NASA stage 67, NASA stage 35 was used to validate the stall boundary predicted with the AU3D code. The same set up as above is used for these analysis.

The design total pressure ratio of NASA stage 35 is 1.82 at a mass flow of 20.2 kg/s. The tip speed of the rotor is 455m/s at 100% rotational speed (about 16000 rpm). As a compressor stage, the aspect ratio of the rotor and stator are 1.19 and 1.26, respectively. The rotor row has 36 blades and the stator row has 46 blades. In the experiments, atmospheric air flow into the test stage and was discharged into the collector downstream of the compressor. A mesh screen was placed upstream of the compressor stage to generate consistent total pressure distortion, as shown in Figure 3.29.

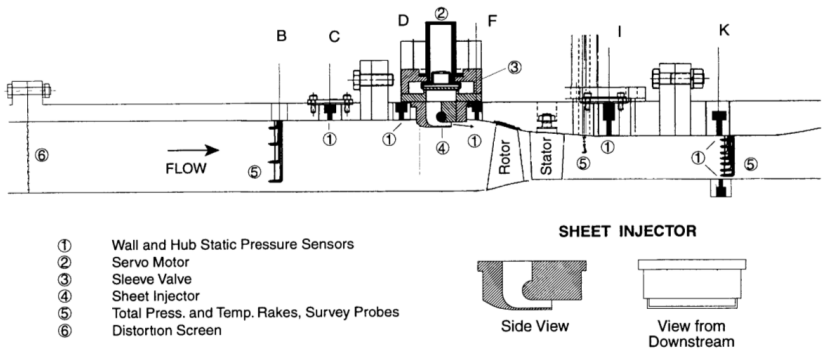


Figure 3.29: NASA stage 35 actuation and instrumentation schematic with inlet distortion

The geometry of the blades (pressure surface and suction surface) are obtained from the [Reid and Moore, 1978]. A FORTRAN code [Crouse et al., 1969] was revised and used to transform the geometry from conical coordinate into the Cartesian coordinate. The LE and TE circle are created with the radius size in [Reid and Moore, 1978]. The computational domain of NASA stage 35 is shown in Figure 3.30, which contains an inlet duct, rotor row, stator row and an exit duct with a nozzle. The rotor has a tip gap of 0.04 cm. The hub clearance of the stator is 0.0762 cm [Chima, 2009]. The rotor mesh has 0.8 million points per passage and 60 radial layers with 10 layers in the tip gap; the stator mesh has 0.3 million points and 50 radial layers with 8 layers in the hub gap. The mesh density is slightly coarser than NASA stage 67 due to the computational cost considerations.

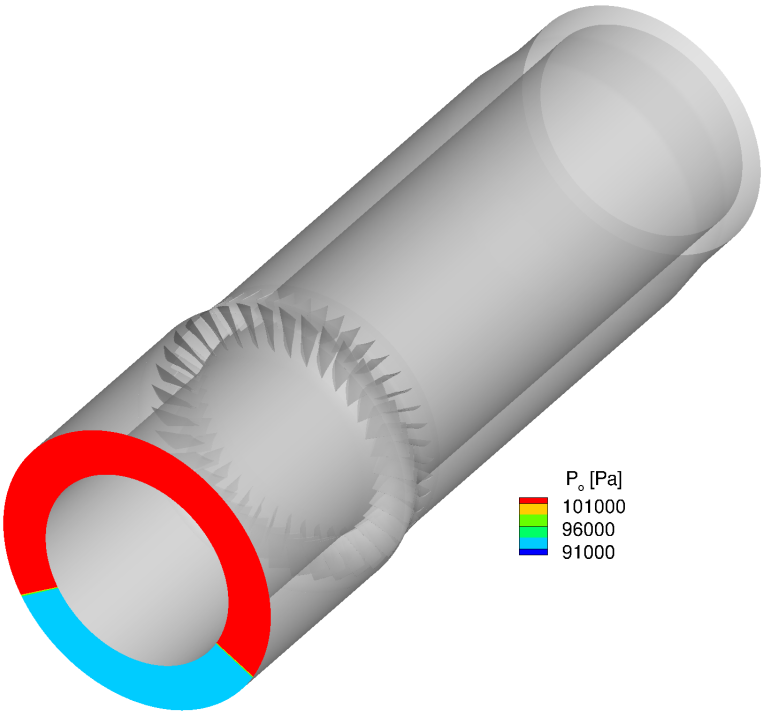
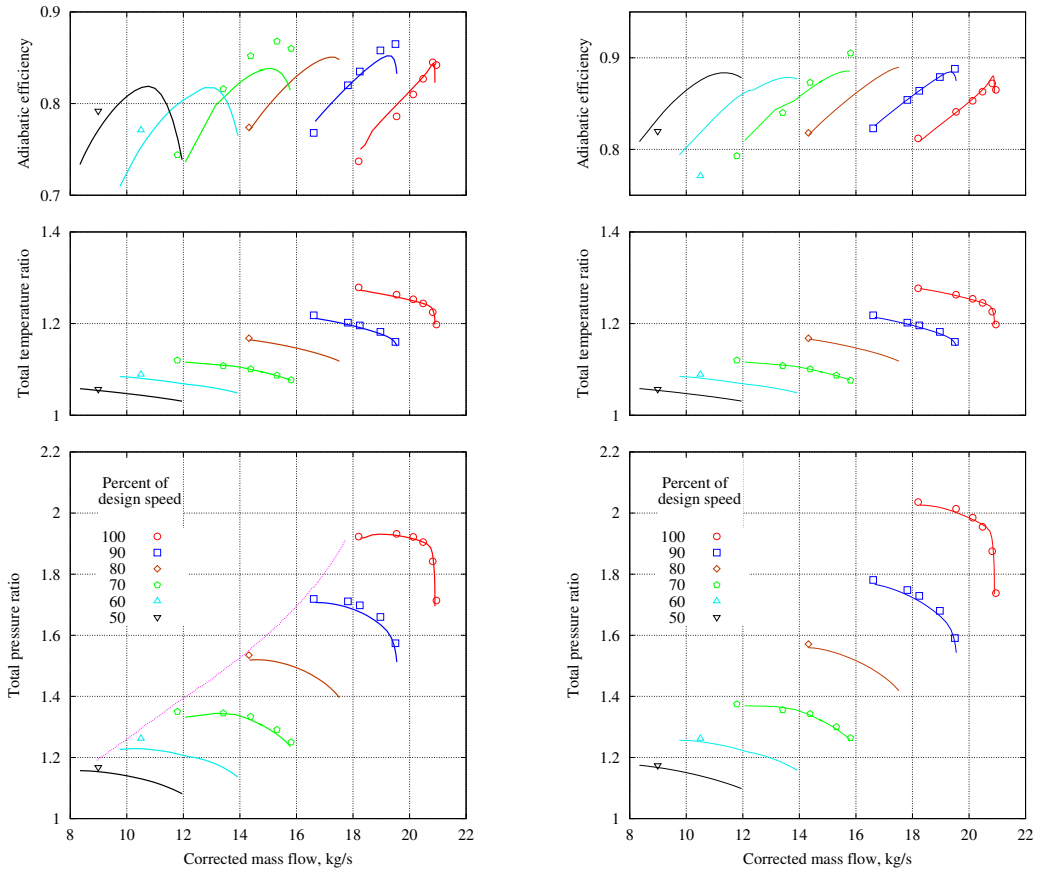


Figure 3.30: Computational domain of stage 35

The distance between the distortion plane and the compressor in the experiments is adopted as the intake length. The length of the intake is 0.8 times of rotor casing diameter for both clean flow and distorted flow simulations. The length of the exit duct is 1.5 rotor casing diameter. At the inlet surface, the measured values of total pressure, total temperature and flow angle were specified. A choked nozzle is attached to the exit duct throttle the compressor from choke to stall.

The numerical strategy used for stage 67 was employed in the steady simulations for stage 35. The steady simulations were performed on a single passage mesh with periodic boundary conditions. The computed overall performance for the rotor alone and whole stage at different rotational speeds are presented in Figure 3.31. It can be seen that the CFD obtains a good match with the experimental data. The total pressure ratio, total temperature ratio, adiabatic efficiency and especially the stall boundary of 100%, 90% and 80% rotational speed are accurately captured. The performance of the simulations at lower rotational speed are less satisfactory when compared with the measurement results. At 70% rotational speed, both the stalling mass flow and stall pressure ratio are under-predicted in CFD. For the 60% and 50% rotational speed, the compressor stalls at a lower mass flow with a reduced total pressure ratio. More validations against measured data can be found in Appendix I.



(a) (b)

Figure 3.31: Compressor map of (a) NASA stage 35 and (b) rotor alone

To predict the stall boundary of stage 35 with inlet distortion, full annulus, time-accurate simulations were performed. Steady simulations showed that the hub leakage flow does not influence the stall boundary of clean inflow significantly, and thus is not modelled in the case with inlet distortion. The distortion pattern is also DC120, which is in accordance with the tests. In the rig test, the compressor is pushed across the stability limit by gradually throttling the mass flow. To maintain consistency with the experiment, a converged solution with inlet distortion is firstly obtained away from stall boundary in CFD and afterwards the nozzle is gradually closed until the compressor falls into stall.

Experimental data was obtained in [Spakovszky et al., 1999]. The stall boundary with inlet distortion was recorded for three speeds (100%, 85% and 70%) but only the strength of the inlet distortion at 85% rotational speed was known. A makeshift method was developed to estimate the distortion strength at the other rotational speeds. In this method, it was assumed that:

1. The strength of the distortion generated with a mesh screen changes linearly with the square of the corrected mass flow at different rotational speed.

2. The distortion strength stays unchanged from near choke to near stall condition on a constant speed line.

These two assumptions were based on the observation in test data. For example, it was shown that in the experiments of NASA stage 11-4 the distortion strength increases almost linearly with the increment of the square of the corrected mass flow [Sanger, 1976]. At higher rotational speed, the total pressure across the mesh screen is larger due to the higher dynamic head. For stage 11-4, the corrected mass flow near stall is 28.1 kg/s for 100% rotational speed and 16.8 kg/s for 70% rotational speed. The strength of the total pressure distortion at 100% rotational speed and 70% rotational speed is 12% and 4% (both at near stall condition), respectively. The square of the mass flow of 100% speed is about 2.8 times of that for 70% speed and the distortion strength of 100% speed is 3 times of that for 70% speed. Based on these relationships between distortion strength and stalled mass flow of different rotational speeds, the distortion strength at near stall point for stage 35 at 100% and 70% speed can be calculated as listed in Table 3.3.

Table 3.3: The strength of the inlet distortion for different rotational speeds

Rotational speed	100%	85%	70%
Distortion strength	14%	10%	7%

At 100% rotational speed, the distortion strength is about 12.8% at PE and 12.0% at NS for stage 11-4. The distortion strength drops at NS condition because the decrease of the mass flow through the mesh screen reduces the dynamic head loss. However, it can be seen that the distortion strength only changes slightly and thus the applicability of a fixed distortion strength can be justified.

In the stall boundary prediction of stage 35, 2,000 time steps/rev was used due to computational cost considerations. Figure 3.32 shows the comparisons of clean and distorted stall boundary of 100%, 85% and 70% speed between CFD and measured data. The blue dashed line is the distorted stall boundary in the experiments. Blue circles are the CFD results with inlet distortion. It can be seen that the predicted stalled mass flow were slightly lower than the experimental data. This is due to the lack of resolution of the high frequency harmonics. The simulated total-to-static pressure ratio is higher than the test results. This phenomenon was also reported in [Herrick et al., 2009]. There was a suspicion that the stator was not set to the reported setting angle in the tests [Adamczyk, 2018]. Another possible reason is the stator endwall geometry. The stator had truncations and recesses at the start and end to reduce stress concentrations. This allowed flow to leak from the pressure to the suction side of a stator blade. In addition, the stator end-gaps were not well sealed which further promote the leakage flow [Shabbir et al., 1997]. Thus the total pressure, which was measured with the probe which immersed in the flow field, may not be influenced while the static pressure measured on the wall surface can be significantly changed. Such stator end wall geometry was not modelled in CFD but it can contribute to the discrepancy between the CFD and the measurements. It is also interesting to note that this difference drops as the rotational speed decreases. This observation further indicates the existence of leakage flow in the stator because the driving force of the leakage is the pressure difference. While the pressure ratio of the compressor drops, the leakage flow will also be reduced.

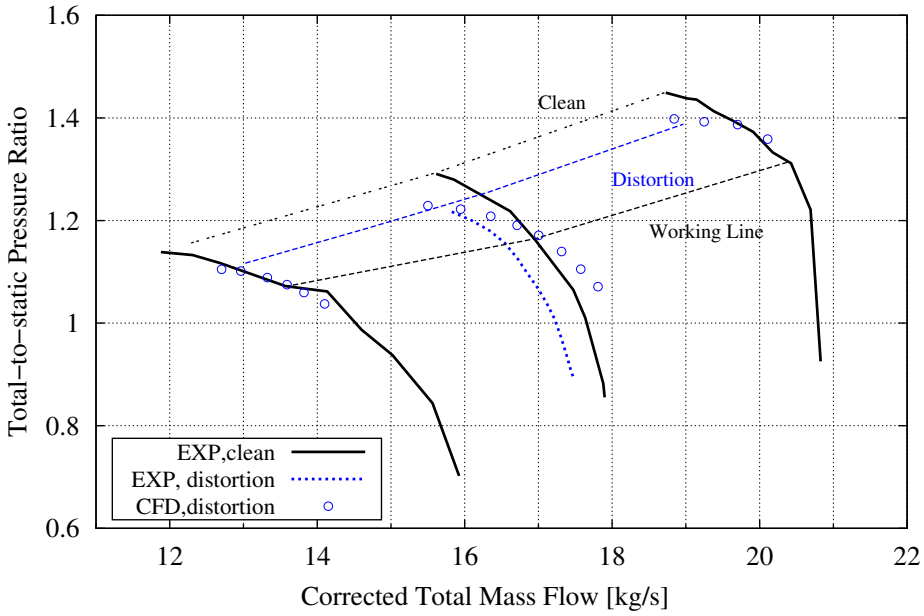


Figure 3.32: Compressor map with DC120 distortion

3.6 Chapter Summery

In this chapter, the numerical strategy used for the simulations with inlet distortion was proposed and validated. Good match was obtained between CFD and experimental data for NASA stage 67. The effect of the inlet distortion on the fan performance was analysed and compared at PE and NS condition. Moreover, the capability of the code for stall boundary prediction with inlet distortion was confirmed using NASA stage 35. The influence of the temporal resolution on the compressor stall margin was also studied. The solution are almost the same with different temporal resolutions when it is away from the stall boundary, the predicted stall margin loss increases as the temporal resolution increases. Coarse time step size cannot resolve the disturbances of high frequency in the flow field and thus the stall inception is postponed. The frequency range of $0.7 - 0.9 f_{bp}$ is important for the stall inception of rotor 67.

The numerical strategy used in the current study was summarised here. In the simulation with inlet distortion, the distortion pattern and amplitude are fixed during the whole process. This setup can be used in the compressor with a straight duct and the inlet surface needs to be away from the fan face. In this situation, the interaction between the distortion and the fan is weak and the distortion pattern can be regarded as stationary. In Chapter 7, simulations will be performed in which the distortion at the fan inlet can receive feedback from the fan and the distortion itself will be adjusted. The exit boundary condition used in this study is a choked nozzle. This boundary condition allows the compressor to generate the local flow field without being over-constrained by the exit static pressure. The modelling of the downstream plenum used in the experiments is unnecessary for stall simulations unless surge occurs. Based on the DFT analysis of the different compressor operating points with inlet distortion, a flexible strategy is

suggested: at PE where high harmonics in the flow field are smaller and less important, relative coarse time steps can be applied. At NS condition, fine time step size is needed to accurately reproduce the solution; for the calculations of stall boundary prediction, rotating stall is mainly caused by flow separation, which is found to be significantly influenced by the size of the time step in a time-accurate computation. Thus, it is proposed that a temporal convergence study must be carried out before carrying on stall simulations.

4 Effect of Abrupt Inlet Distortion on Fan Stability

4.1 Introduction

Studies on inlet distortion usually focus on consistent distortion and obtain the distorted compressor map from choke to stall by gradually closing the downstream throttle. During this process, the strength of the distortion is almost fixed and the operational condition of the compressor changes gradually when throttled. One example of the consistent inlet distortion is the flow separation caused by the S-shape duct in front of a BLI fan. This flow separation imposes complex distortion pattern on the fan and the distortion consistently exits during the whole flight envelope. On another hand, inlet distortion can occur during an abrupt maneuver of the aircraft or when the engine is subjected to an unexpected cross flow or vortex. The weapon firing on the aircraft can bring abrupt total temperature distortion to the engine. Such abrupt distortions may only last for a short time. However, it will be shown in this chapter that they can have larger adverse influence on the compressor than the consistent distortion. In this study, the occurence of the abrupt distortion is simulated as a step drop in the total pressure. Thus the time constant is zero in the simulations here, which is a reasonable approximation. However, in the real situations, the reduction of the total pressure (such as the lip separation caused by the cross wind) still needs finite time to fully develop.

It is considered that designing and manufacturing the fast-response glitch to generate abrupt inlet distortion can be complex in experimental study. It is more economic and efficient to study abrupt inlet distortion numerically. Such kind of study can provide instructions for the future research.

In this chapter, numerical simulation will used to investigate the reaction of the fan blade to the abrupt inflow disturbance and the stall process with abrupt distortion. Two cases of NASA stage 67 with the same DC120 distortion but with different nozzle exit area ratios are computed and analysed at 90% corrected speed. The total pressure loss in the distorted region is 10.5% and it is fixed during the whole computation process. The simulations begin by placing the distortion at the inlet of the uniform inflow solutions. Two nozzle area ratios were considered, which correspond to uniform inflow cases with the corrected mass flow of 29.43 kg/s (NS in Chapter 3) and 29.16 kg/s (rotating stall, RS), as shown with dots in Figure 4.1. After 10 revolutions NS converged to a stable solution (shown with a red square in Figure 4.1). However, for RS, both corrected mass flow and total pressure ratio dropped below the values of those of NS and the rotor went into rotating stall (blue square in Figure 4.1). It can be seen that with such a distortion, the fan can be directly pushed into stall even when it was operating away from stall

boundary in clean flow. Figure 4.2 shows the time history of the physical (uncorrected) mass flow at the rotor outlet for both cases (during the first 10 revolutions), and is used below to discuss the solutions at different instants of time. Figure 4.3 shows the instantaneous contours of the axial velocity at the rotor exit for NS and RS at the 6^{th} revolution. In the case of RS, a stall cell spanning 60%∼100% height is clearly visible. Because of the associated blockage in the tip region, the mass flow of the hub region increases. The results also demonstrate that NS is the last stable point in presence of the abrupt distortion because the RS case with less mass flow will fall into rotating stall.

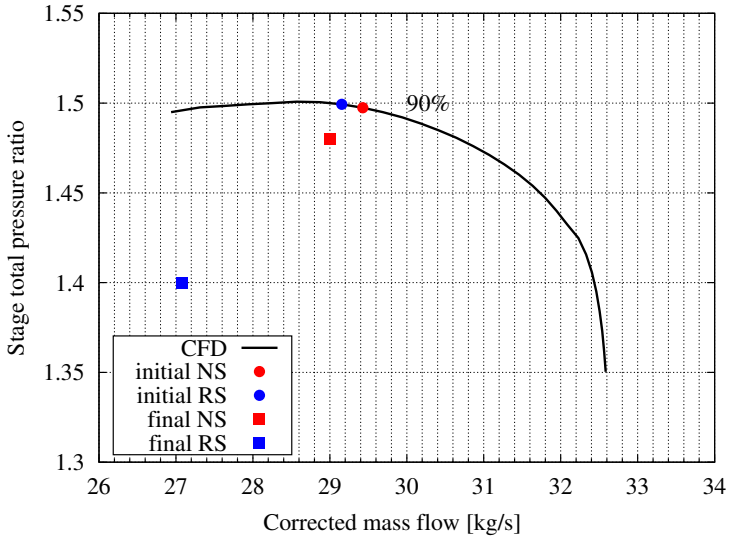


Figure 4.1: Initial clean and final operational points for NS and RS at 90% corrected speed

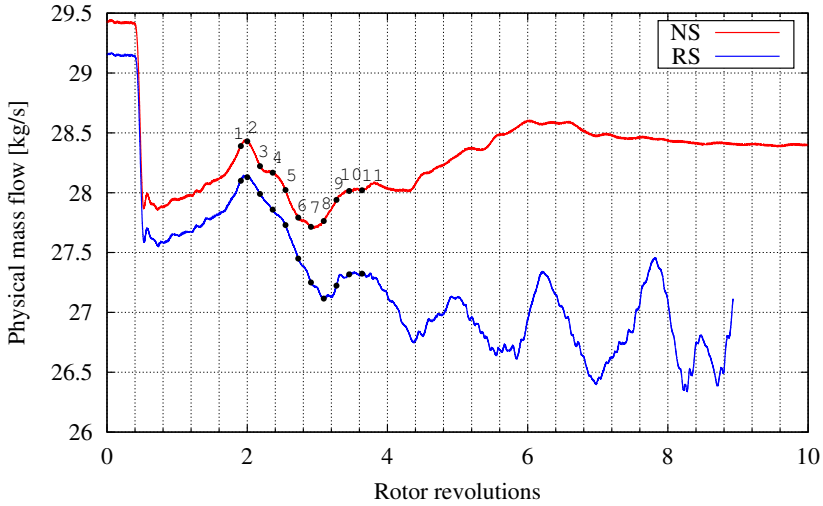


Figure 4.2: Physical mass flow history at the rotor exit for NS and RS

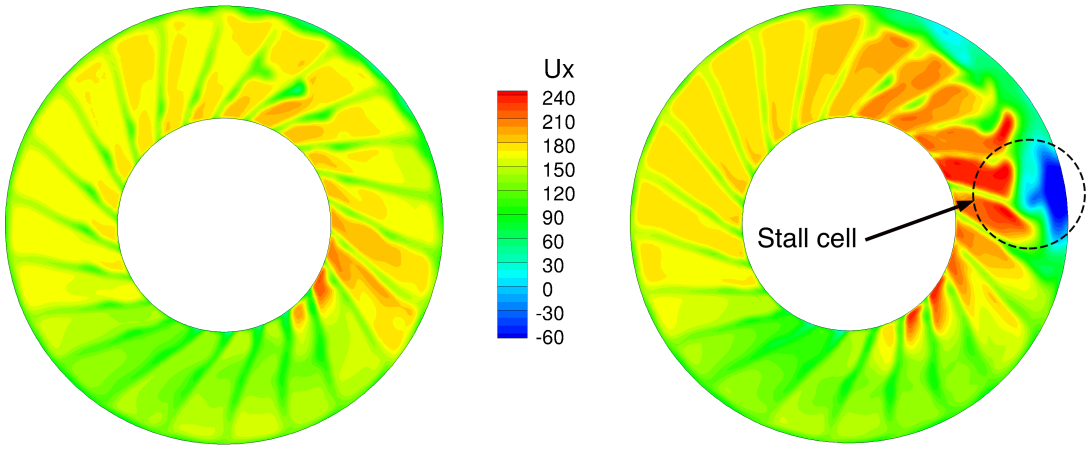


Figure 4.3: Instantaneous contours at the stator inlet for (a) NS and (b) RS at the 6^{th} revolution

4.2 Influence of the Inlet Distortion on Rotor Performance at NS Condition

Before discussing the stall process of RS, a detailed study of the flow field for NS is carried out. Circumferential time-averaged profiles of different flow variables have already been shown in Figure 3.18 to Figure 3.20 in Chapter 3.

The time-averaged circumferential swirl angle and the incidence at mid-span of the rotor inlet are plotted in Figure 4.4. The swirl angle, which is created by the circumferential static pressure gradient, has maxima and minima at the distortion border (located at the circumferential angle 120° and 240°, Figure 3.18) since the static pressure gradient is the largest at these locations. In this plot, a negative value is counter-rotating relative to the rotor. Counter-swirl increases the incidence and hence blade loading, while co-swirl reduces incidence and thus unloads the blade.

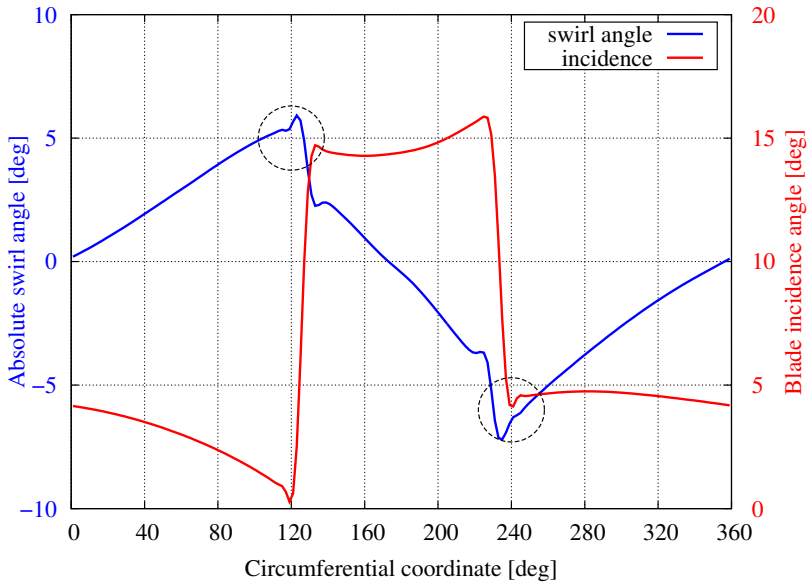


Figure 4.4: Absolute swirl angle and incidence at the rotor inlet, middle span, NS

The performance of the rotor blade as it rotates to different circumferential positions is analysed next. Figure 4.5 shows an instantaneous contour of the axial velocity at 98% span of the rotor for NS condition. The distorted sector can be distinguished by a lower axial velocity upstream of the fan. As the rotor rotates from the clean flow region into the distorted region, a separated region appears as the swirl angle becomes negative (at about 180° in Figure 4.4). The size of separation zone increases as the incidence is increased towards the end of the distorted zone. The separated zone is gradually removed after the rotor enters the clean flow region again and the incidence to the blade decreases.

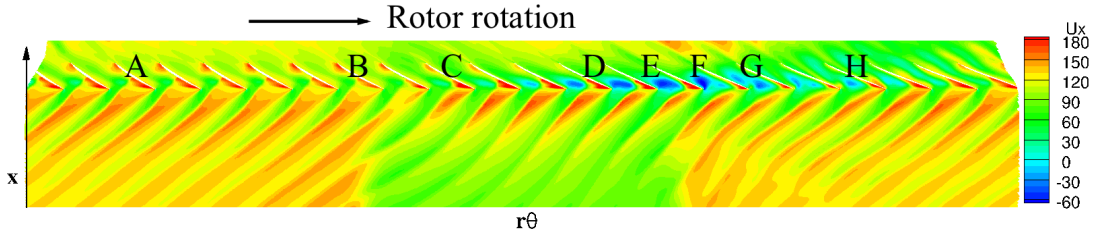


Figure 4.5: Circumferential contour of the axial velocity for NS, 98% rotor span

While Figure 4.5 shows an instantaneous flow condition of the rotor row at 98% span, the orbit method [Fidalgo, 2013] can display the time-averaged performance of each blade. The orbit method uses streamtraces to split the time-averaged flow field of the rotor domain. In this case, streamtraces are released from rotor LE to the rotor TE and the entire rotor domain is sliced into 22 independent parts, and the performance of these separated sectors are calculated. The corrected mass flow and total pressure ratio of the 22 sectors together with the steady (undistorted) characteristic are plotted in Figure 4.6. The 22 sectors (shown with hollow squares) are connected with a line to form an orbit around the operating point of the fan. The initial clean solution for NS is represented by the black dot and the final distorted solution is marked

by the blue square. It is seen from this plot that as the rotor rotates around the circumference, it experiences a considerable change in operational conditions. These changes are caused by flow redistribution and swirl angle due to the inlet distortion. On comparing the PE and NS operating points in Figure 4.6, it is evident that the orbit shape is considerably different. The configuration of the PE orbit (shown as red hollow squares connected with dash lines) has already been demonstrated in Chapter 3. The variation in the positions of the orbit points is mainly due to the flow redistribution and swirl angle upstream of the fan. It should be noted that, the accuracy of the result of the orbit method will be affected when it is performed at the NS condition because the streamtraces can be blocked by the tip leakage vortex and the flow separation. The LE spillage and the backward flow near the TE also increase the difficulty of getting continuous streamtraces. However, considering that the tip region is much smaller than the whole passage, the method can still provide some qualitative information about the operational condition of the rotor.

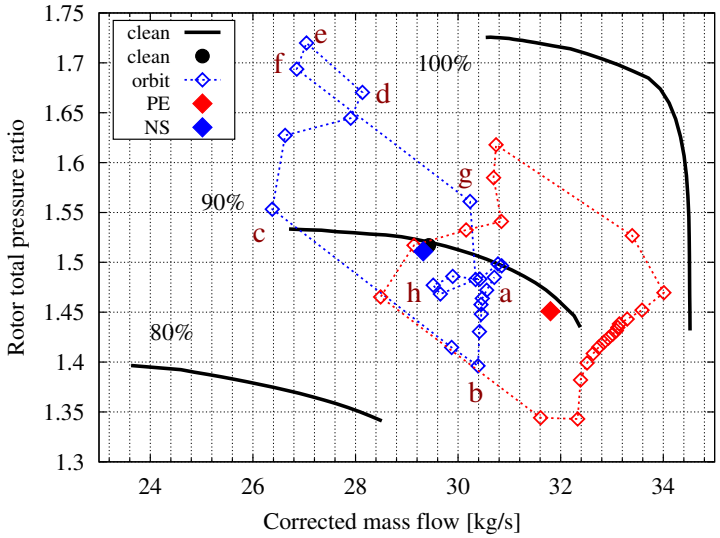


Figure 4.6: Orbit map of the PE and the NS, 22 sectors

A comparison between Figure 4.5 and Figure 4.6 can help to pinpoint the circumferential positions of the orbit sectors. The lower-case letters in Figure 4.6 correspond to the capital letters in Figure 4.5. For example, the squares at a on the orbit map correspond to the passages around position A in Figure 4.5. The squares between a and b correspond to the passages between A and B in Figure 4.5. The shape of the orbit is described and explained as following:

• From a to b, it can be seen that the corrected mass flow does not change significantly but there is a considerable drop in total pressure ratio. It can be seen in Figure 4.7 that the axial velocity and total pressure is nearly constant from A to B and thus the corrected mass flow for these passages are similar. The drop in the pressure ratio is mainly due to the decrease of the incidence that reduces the blade loading.

• From b to c, as the compressor moves into the distorted region, the total pressure ratio increases and corrected mass flow decrease, as shown in Figure 4.6, which corresponds to B to C

in Figure 4.5.

• From c to d, the total pressure ratio continues increasing while the corrected mass flow increases slightly from c to d. The mass flow increase is due to the radial flow migration caused by the spinner.

• From d to e and the total pressure ratio sees a rise while the mass flow keeps decreasing, which means an increment in the blade loading. Flow separation begins to occur on the blade.

• From e to f, both the pressure ratio and mass flow drop. This phenomenon is absent in the orbit shape of the PE condition. Since the drop of corrected mass flow and pressure ratio is a hint at stall inception, it is inferred that stall cell will be initiated at position e, where the blade separation is maximum (E in Figure 4.5).

• From f to g, before the flow separation grows into a stall cell, the operating point is pulled back to a relatively stable state. This is because g enters into the clean flow region with high mass flow and total pressure.

• From g to h, as the rotor enters the clean flow area the mass flow gradually increases. However, the passages around H (Figure 4.5) are still partly blocked at h.

4.3 Behaviour of the Tip Leakage Flow with Inlet Distortion

To further demonstrate the working condition of the blade with inlet distortion at NS point, the tip leakage flow of the blade at different circumferential position is presented and analysed. As the first step, it is important to point out some features upstream of the rotor which play an important part on the tip leakage flow and the consequent stall.

Figure 4.7 shows the vortices formed upstream of the rotor at the edges of the distortion by using the $Lamda - 2$ vortex criterion [Jeong and Hussain, 1995]. This vortex pair is indicated by the spikes (marked with the dashed circles) in Figure 4.4, and as will be shown, has a great influence on the pattern and the size of the tip leakage flow. Moreover, this vortex determines the position where the initial stall cell emerges.

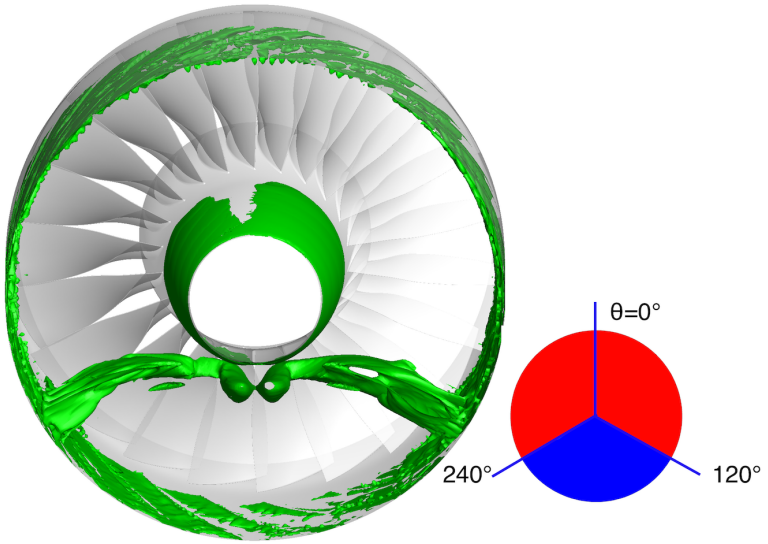


Figure 4.7: The vortex in front of the rotor for NS

An additional revolution was performed after NS had reached a periodic solution. During this revolution, three blades are marked and the instantaneous solutions of these three blade passages are extracted at different circumferential positions as they rotate around the annulus. $Lamda - 2$ vortex criterion is employed to show the pattern and size of the tip leakage flow. To set a benchmark for comparison, the tip leakage vortex of the initial clean flow solution for NS is illustrated in Figure 4.8, which shows the size and location of tip leakage vortex. In Figure 4.9, the thumbnails at the bottom left show the circumferential position of the marked blades and the right column of the figures show the size and pattern of the tip leakage vortex looking downward from the tip. In the thumbnails the marked blades are shown in green, the clean flow area is represented by the red and the distorted region is blue.

In Figure 4.9, the periodic fluctuation of the tip clearance flow during one revolution is displayed. It can be seen that the pattern and the size of the vortices at position I are similar to the clean flow solution shown in Figure 4.8. The tip leakage flow is an indication of the blade loading. The amount of the tip leakage flow is reduced when the 3 blades approach the distortion (position II). Since the inlet total pressure is nearly the same at position I and II, this reduction in loading is mainly caused by the co-swirl at this circumferential position. The strength of the tip leakage vortex continues to decrease towards position III, even though some of the blade passages have already entered the distorted area at this point. The above observation indicates that the rotor reaction to the change of the incoming flow has a hysteresis and thus a time delay exists before the fan operating condition changes. Cousins [Cousins, 2004] showed that the rotor response time for an axial fan blade can be calculated as the time for a flow particle to travel the distance from the leading edge of the aerofoil to the throat of the blade passage (blade time constant), and a rule of thumb suggested that it takes 4 to 5 times of the blade time constant for the stability limit of the compression system to be affected. In the study here, the blade time constant is close to the blade passing time. Meanwhile, the vortex in front of the rotor, as

show in Figure 4.7, reduces the rotor loading at position III. At position IV, this triple-passage is completely within the distorted section. The interface between the tip leakage vortex and the incoming flow gradually becomes parallel to the leading-edge plane, which indicates that these passages are close to stall [Vo et al., 2008]. The size of the tip leakage vortex is at a maximum at position V, where the rotor is just about to leave the distorted area. The tip region of the passages is almost blocked and a small leading edge spillage can also be observed. By the time that the triple-passage reaches position V (and counter-swirl angle reaches its peak), the marked rotor blades have been exposed to distorted flow for a period of time, and hence the cumulative effects of the counter-swirl drive the tip leakage flow to grow. In a similar manner to the triple-passage entering the distorted region at position III, the hysteresis of the blade delays the recovery process even though some of the passages are entirely out of the distorted zone in position V. The vortex in front of the rotor exacerbates the operational condition of the blade. At position VI, the passages entirely rotate into the clean flow area. The LE spillage of the tip leakage flow disappears and the edge of the tip leakage vortex is pushed downstream. The above observation indicates that the blades begin to recover to the initial operating condition, and at position VII (the same circumferential location as position I, but one revolution later in time) the rotor restores to the same operating condition as in position I.

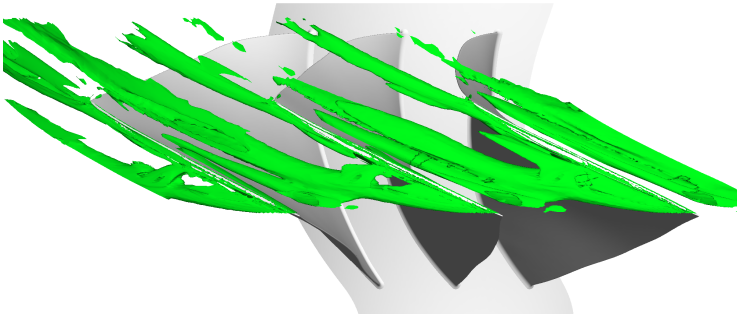
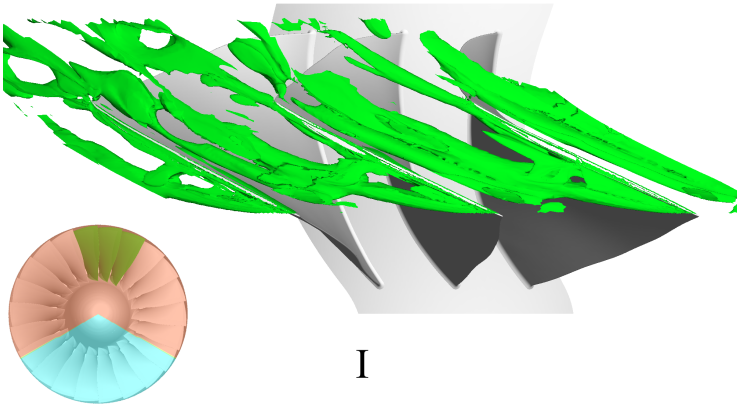
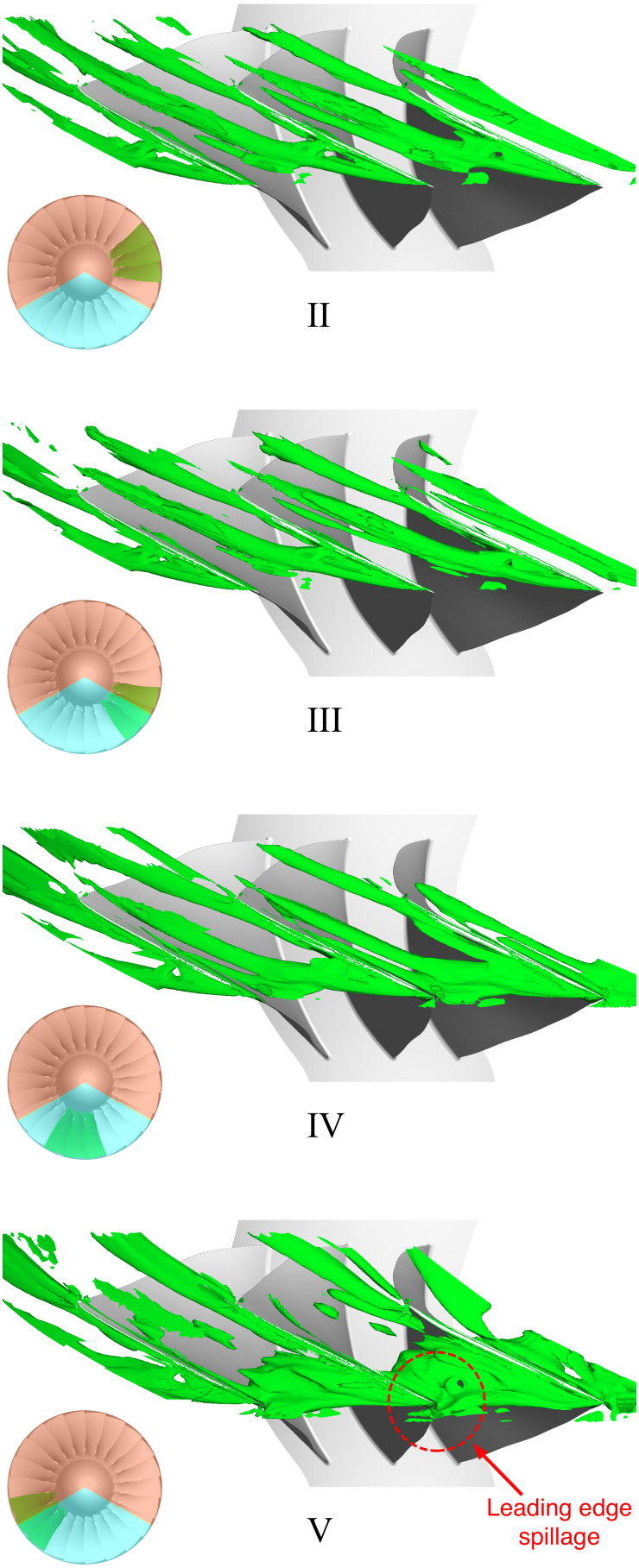


Figure 4.8: Tip leakage flow of the initial clean flow solution for NS




II
III
IV
V
Leading edge
spillage

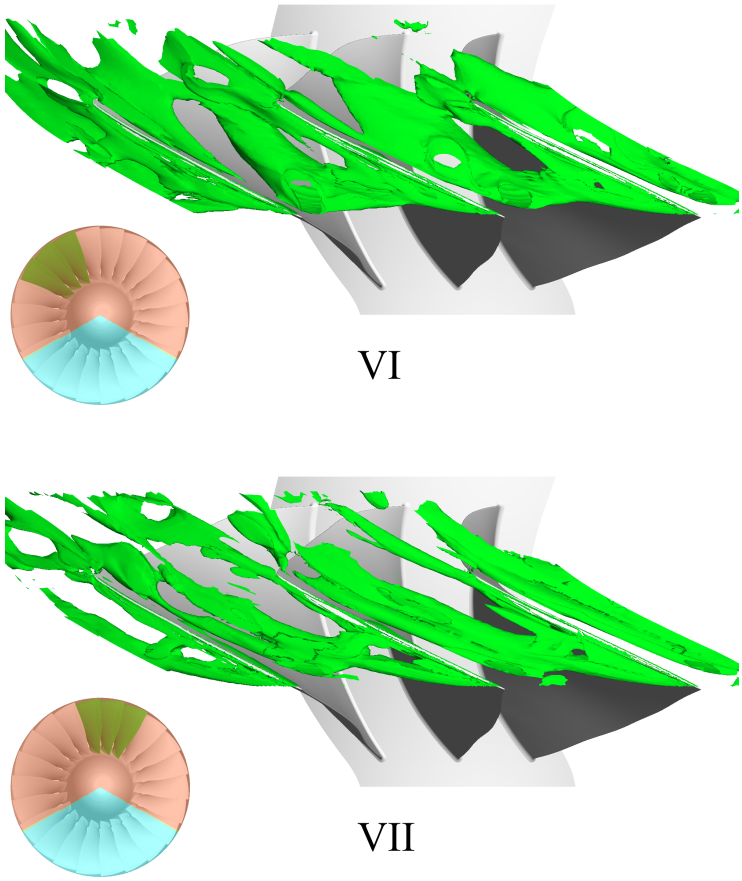


Figure 4.9: Tip leakage flow for NS at different circumferential positions

4.4 Stall Process with Abrupt Inlet Distortion

Next, it will be shown how stall is triggered by the abrupt inlet distortion. It is found in the simulation (Figure 4.3) that, the stall is first initiated in the tip region of the rotor, thus only the rotor domain is analysed and attention is focused on the tip region. Starting from the undistorted solution, Figure 4.10 shows the comparison of the axial velocity at 98% span of the rotor in the stationary frame for NS and RS to display how the flow develops when the distortion is placed upstream of the rotor. In this plot, the blue regions correspond to negative axial velocity and hence flow separation. The positions of the $frame$ 1 to 11 are marked with black dots in Figure 4.2. From $frame$ 1 to $frame$ 3, it can be seen that a separated region appears as the rotor enters the distorted zone and that the separation grows larger in size in this zone. The separation happens in a few neighbouring blade passages simultaneously. A parallelogram box is used to mark 3 blade passages to show the evolution of the flow field. Due to the time delay discussed earlier, the separation region generated in the distorted zone increases initially as the rotor blade enters the high mass flow clean zone, as shown in $frames$ 4 and 5. Up to $frame$ 5 the flow for the two cases looks similar, but obvious differences begin to appear at $frame$ 6. From $frame$ 6 to $frame$ 9, it can be seen that the separated flow for NS is gradually attenuated in the high mass flow region and disappears before the rotors carry it to the distorted region. In contrast, the separation zone created in the distorted region for RS is not attenuated as the rotor passes

through the high mass flow region and is carried into the distorted region. The area of the separation becomes smaller but the reverse flow is stronger and finally evolves to a stall cell which occupies about 4 passages.

The only difference between these two cases is the corrected mass flow of the initial clean flow solution. NS has a slightly larger steady mass flow and thus has a lower datum incidence. The clean flow incidence at 98% height for NS and RS are 6.3° and 6.5°, respectively. It was shown in Figure 4.4 that the flow incidence increases in the distorted region. Therefore, the separation is more inclined to happen and grow in RS. Moreover, the recovery process will be slower in the clean flow area for RS than NS as the incidence is higher. The results suggest that, if the separation can be totally removed in the clean flow region before it reaches the distorted region, the case will be stable (no stall), but if the separation survives the high mass flow region and enters the distorted region again, the separation will grow into a stall cell. A similar conclusion was also obtained in experimental tests [Jahnen et al., 1999]. This observation also indicates that the relation between the rotor response time and the time that the rotor stays in the distorted region is crucial for the blade aerodynamic stability. The generation or elimination of the blade separation is due to the accumulative effect of the incidence angle. Thus, the longer the rotor stays in the distorted region, the larger the separation grows. Cousins [Cousins, 1997] showed that a longer response time for a centrifugal impeller blade gives the blade a greater tolerance to inlet distortions. However, it was observed in the current research that for this axial compressor, while a longer blade response time can reduce the flow separation in the distorted area, it can also increase the recovery time in the clean flow area. Thus, it is difficult to reach a conclusion regarding this axial compressor and more investigation is needed.

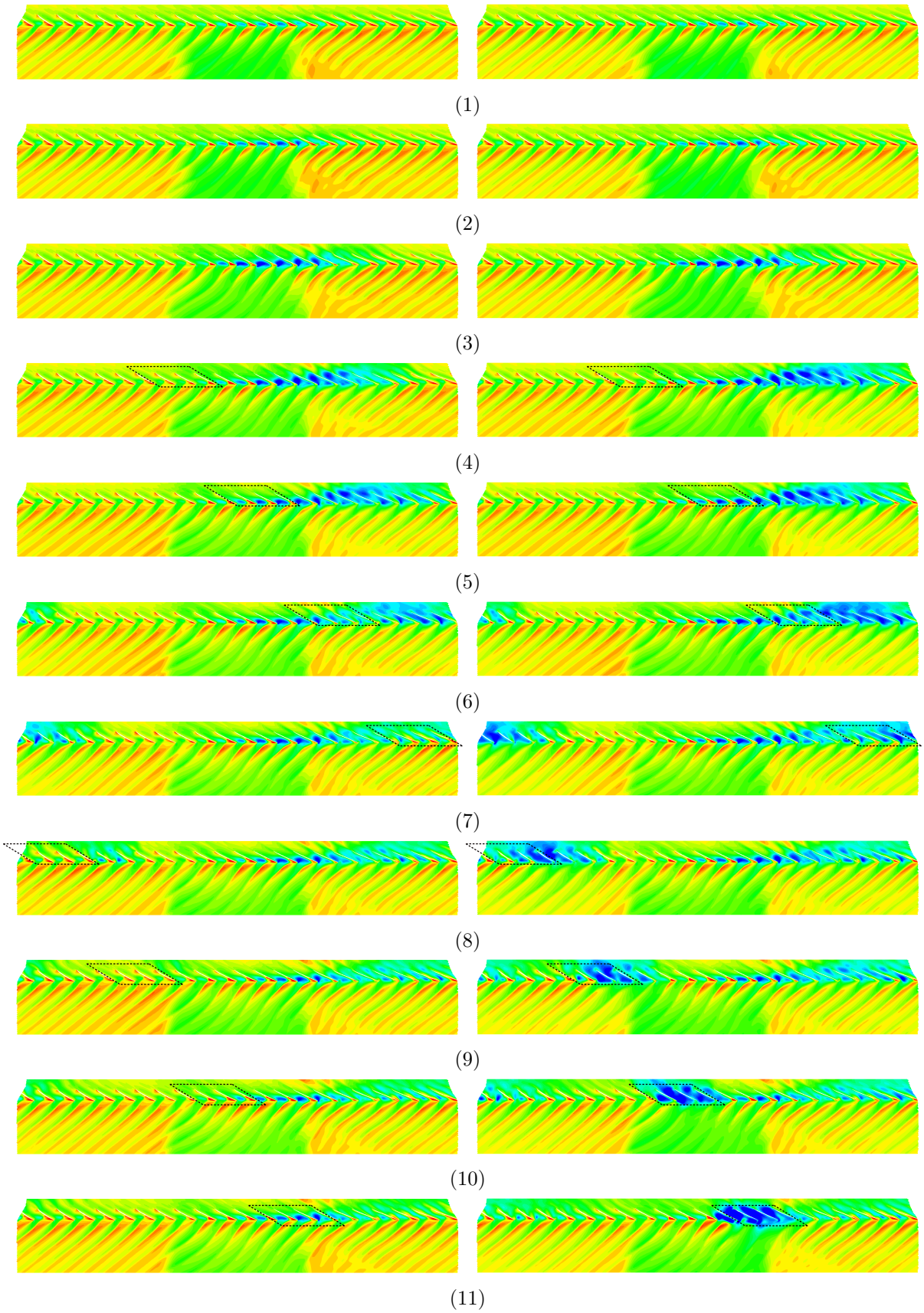


Figure 4.10: The circumferential contour of the axial velocity at 98% span of the rotor for NS (left) and RS (right) at different time (legend is the same with Figure 4.5)

4.5 The Effect of the Abrupt Inlet Distortion Strength

The effect of the abrupt inlet distortion strength on stall margin is demonstrated in this section. Three distortion strength of 10.5%, 5% and 2% are studied. The strength of the inlet distortion is defined by the percentage total pressure loss in the spoiled area. The circumferential angle of the distorted area remains 120° in all the computations. Figure 4.11 shows the stall margin loss of the single rotor case at 90% corrected speed with distortions of different strength. It can be seen from this plot that, for distortion values above 2%, the stall margin loss increases (almost) linearly with the amplitude of the distortion, which is in line with findings of [Reid, 1969].

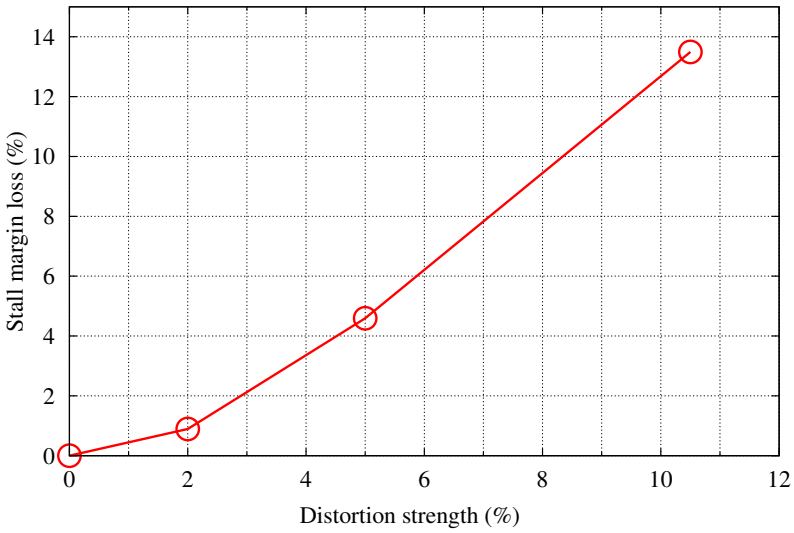


Figure 4.11: The effects of the strength of the inlet distortion on the stall margin loss

For the distortion strength of 2%, the stall boundary in terms of corrected mass flow is slightly lower than clean flow case but the total pressure ratio is higher than the clean flow case as can be seen in Figure 4.12. Similar results can also be found in experimental reports [Sanger, 1976, Sanger, 1979] but no explanation is given for this unusual phenomenon. In general, the inlet distortion is destructive in terms of both mass flow range and total pressure ratio.

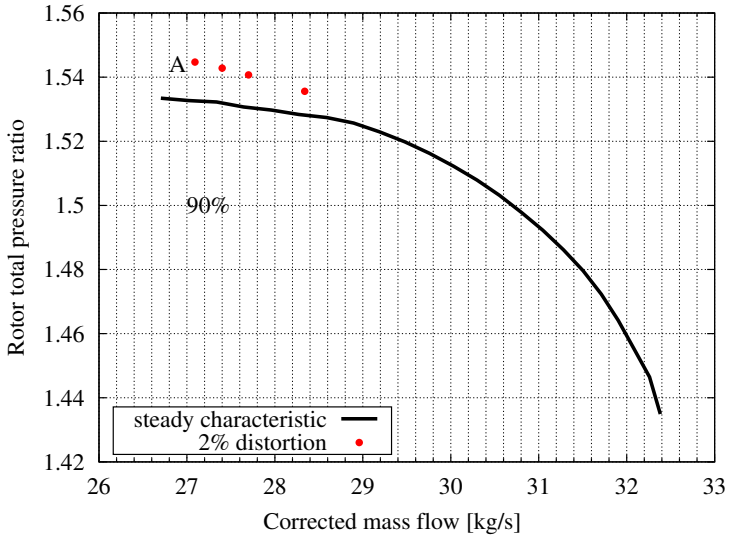


Figure 4.12: The performance of the rotor with 2% inlet distortion

To explain this phenomenon, two full-annulus, time-accurate cases are chosen to demonstrate the influence of the 2% inlet distortion on the performance of the fan when it is near stall. Case I has clean inflow and Case II is conducted with inlet distortion. Both have the same corrected mass flow of 27.7 kg/s, but the total pressure ratios are 1.53 and 1.54, respectively. Figure 4.13 shows the instantaneous contour of the total pressure at the rotor outlet. It can be seen that while a low total pressure "blue spot" exists (at mid-span) in every passage in the clean flow case, the size of these spots differ for different passages in the distorted flow. Figure 4.14a and Figure 4.14b shows the comparison of the radial profile of the circumferentially mass-averaged total pressure and total temperature downstream of the rotor. It can be seen that the total pressure of the clean flow is slightly higher than that in the distorted case at the hub region but is lower from the mid-span to the tip. However, the curves of the total temperature of the two cases show only minor differences, which indicates that the inlet distortion changes the loss but not the blade loading. A detailed analysis of the mid-span, in which the largest difference is observed between the distorted and the clean flow is presented next.

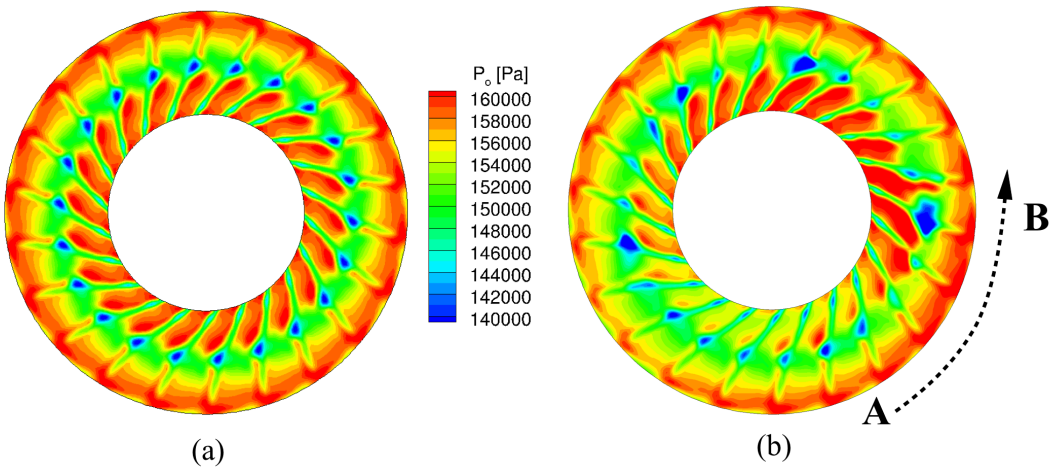


Figure 4.13: Total pressure at the rotor outlet for (a) Case I and the (b) Case II

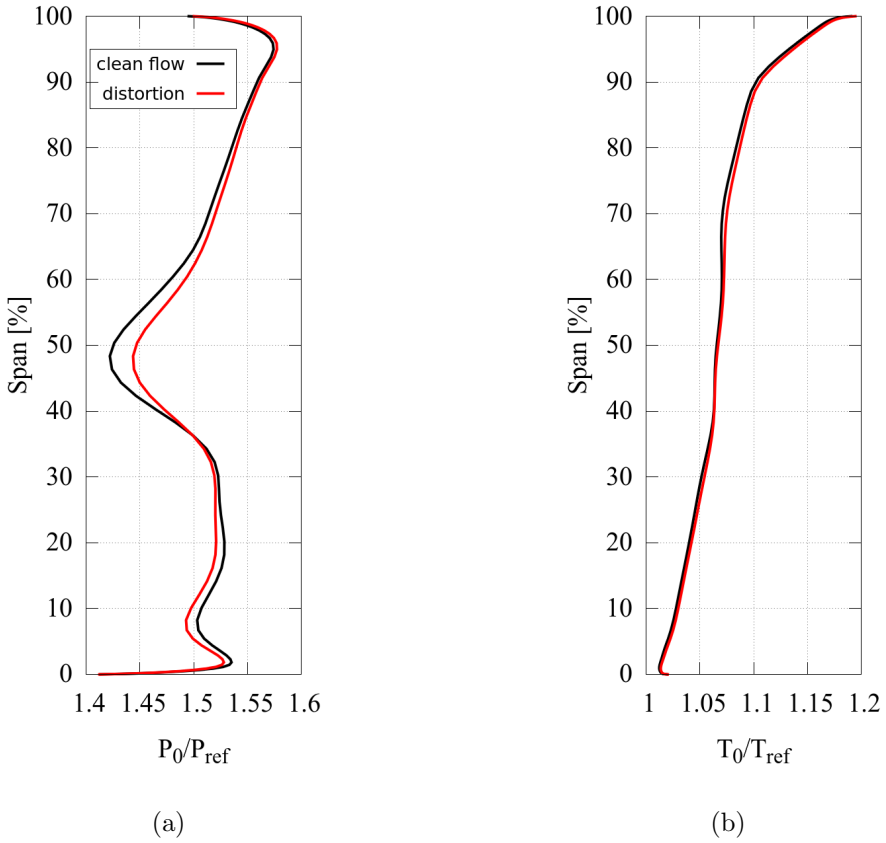
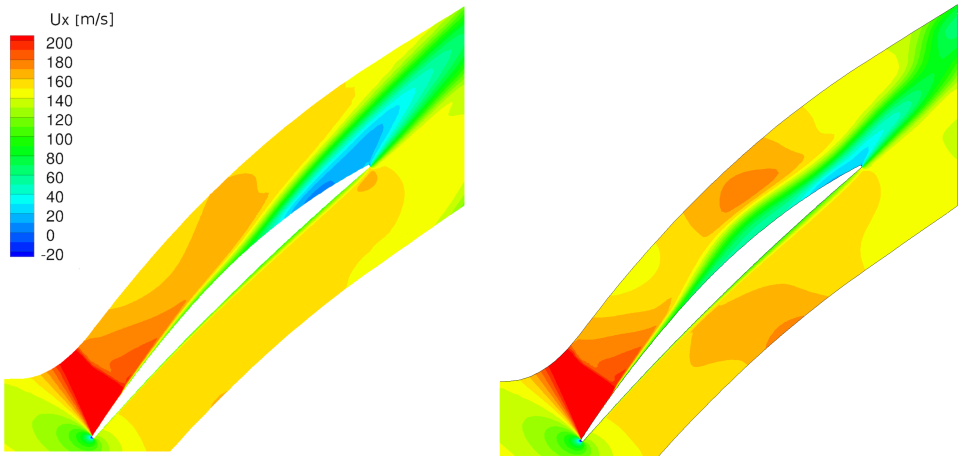


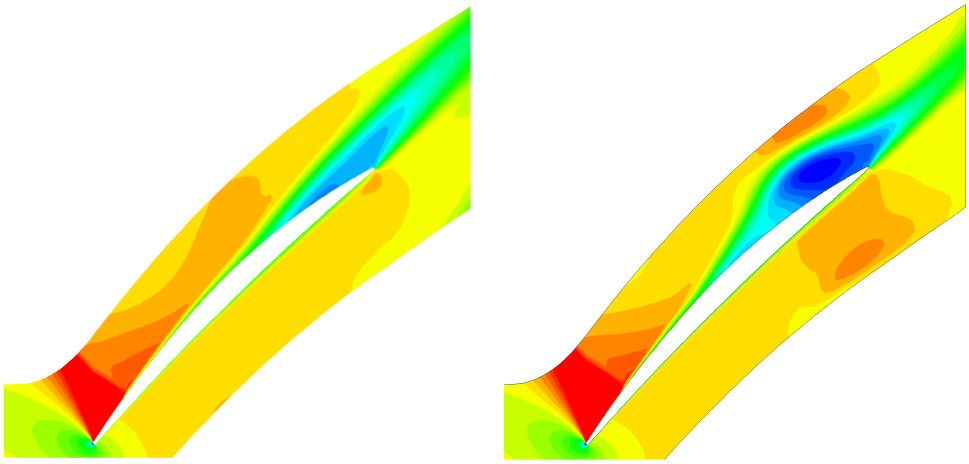
Figure 4.14: (a) Circumferential-averaged radial total pressure (b) Total temperature profile of Case I and Case II

A similar method, as the one used in obtaining the plots in Figure 4.9, is employed to explain the increase in total pressure for the distorted case. A single passage is marked and the mid-span layer in this passage is extracted at different instants of time when this blade rotates from position A to position B in 4.13. Figure 4.15 shows the evolution of the axial velocity contour at 50% span for both cases. These images clearly show a vortex shedding process from the blade

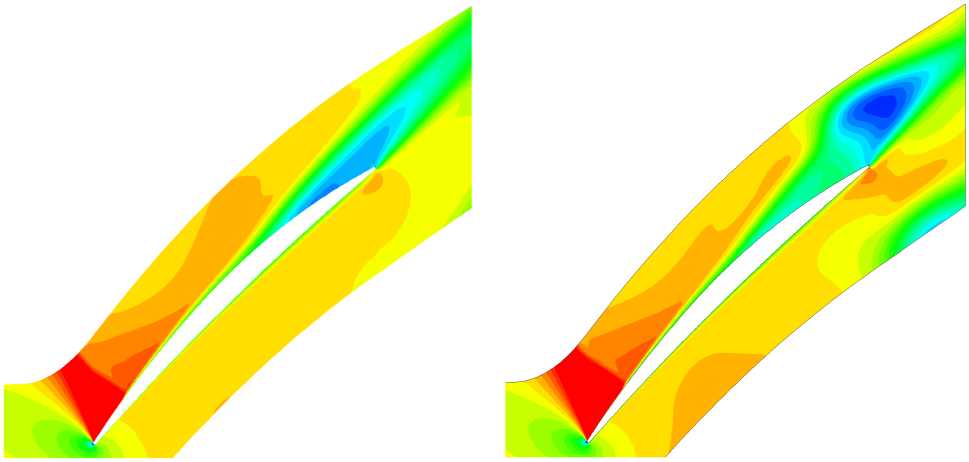
surface in Case II while the thick boundary layer stays stable in Case I. The shedding frequency of the vortex is about $6f_{bp}$. Hah et al. [Hah et al., 1996] have shown that vortex shedding from the blade suction surface can actuate the low-energy fluid and reduce the flow loss. Therefore, it is considered that the distortion-induced vortex shedding in Case II contributes to the removal of the thick boundary layer on the blade suction surface and improves the aerodynamic performance.



(1)



(2)



(3)

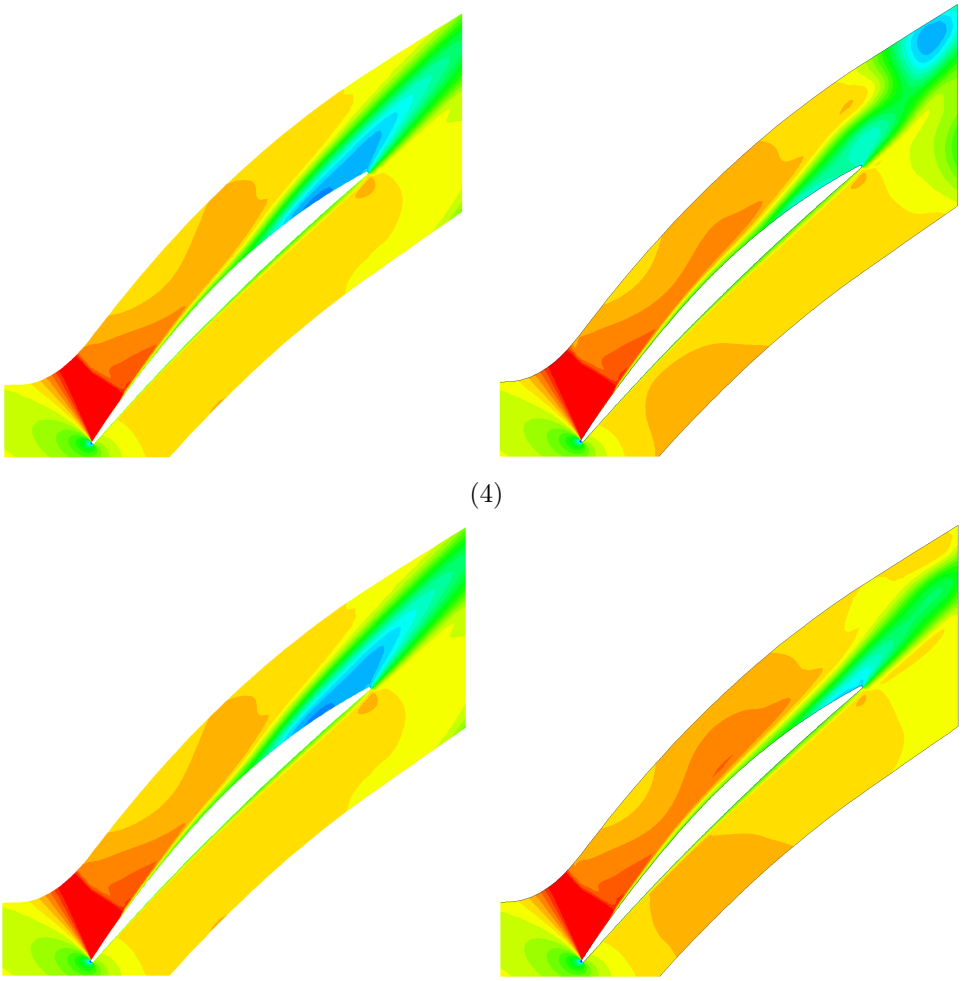


Figure 4.15: Contour of the axial velocity at rotor middle span (a) The thick boundary layer in Case I (b) Vortex shedding in Case II

Previous studies [Khaleghi et al., 2008, Iim et al., 2012] have shown that NASA rotor 67 is tip critical and stall is triggered in the tip region. Therefore, the vortex shedding at mid-span does not facilitate the formation of stall cells. This observation implies that a slight distortion might improve the flow structure inside the passage and help to reduce the losses.

4.6 Influence of the Rotational Speed on Compressor Stall Margin

To investigate how the stall margin changes with the rotational speed of the compressor, simulations were first carried out with the mesh without OGV. Figure 4.16 shows the predicted stall line of this single rotor case with abrupt DC120 distortion. The total pressure loss in the distorted area is fixed at 10.5% for all the speeds. The last stable points of the three rotational speeds

were connected with a fitted parabolic curve. It is found that the stall margin loss increases as the rotational speed drops, as summarised in Table 4.1.

A possible explanation for this finding is that the slope of the characteristic is related to the stability of the compressor when subjected to an inlet distortion. It is considered [Longley and Greitzer, 1992] that the steep characteristic is more robust than the flat characteristic. A compressor with a steep characteristic can achieve considerable pressure rise without a significant change in the mass flow rate. Moreover, steeper characteristics can induce more cross flow upstream of the fan so the axial velocity and swirl angle variations are smaller when the amplitude of the distortion is fixed. As can be seen from Figure 4.16, the shape of the characteristic gradually becomes flatter as the rotational speed decreases, which reduces the ability to repel the impact of disturbances. According to the parallel compressor model [Stenning, 1980], to achieve the same pressure increase of the clean sector, the mass flow of the spoiled sector has to decrease in order to produce a large enough pressure rise and thus the sector is forced to operate closer to stall. For a relatively flat characteristic, the compressor may fail to provide sufficient static pressure rise even when the mass flow is pushed across the stall boundary, which triggers the stall.

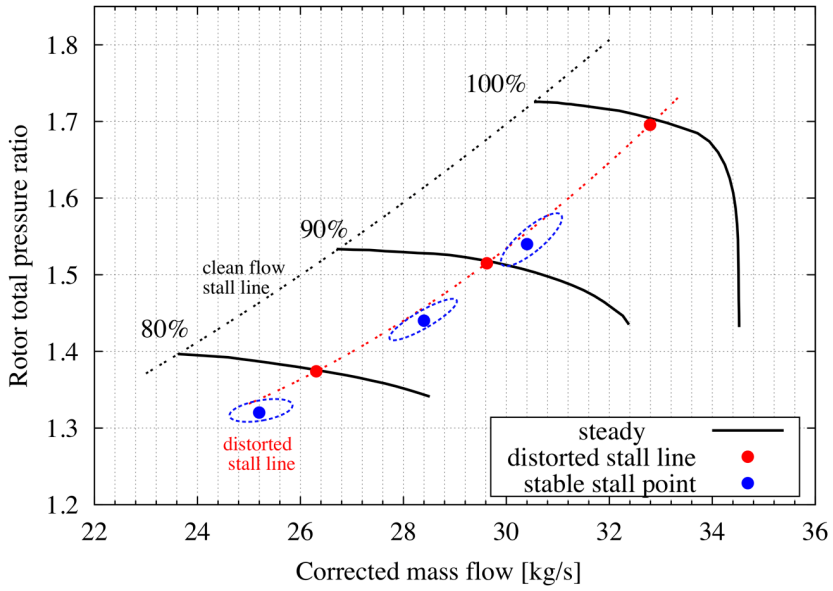


Figure 4.16: Stall lines of the single rotor with inlet distortion at different rotational speeds

Another simple explanation regarding the speed dependency of the stall margin is that, for a fixed amplitude of inlet distortion, the percentage of the dynamic head loss will be larger when the rotational speed drops, and thus the blade experiences a larger incidence addition in the distorted area. The dashed lines and solid lines in Figure 4.17 are the time-averaged incidence values at 98% rotor span (station 1 in Figure 3.2b)) for the last stable operating point in the clean flow and with inlet distortion respectively. It can be seen that, in the clean flow, the compressor can endure larger incidence at lower rotational speed, which is also observed in the experimental data [Jahnen et al., 1999]. The incidence limit at the stall point at 80% speed surpasses that at 100% speed by about 1.3 degrees. However, for the case with distortion, the incidence is nearly the same for all the speeds in the clean flow region of annulus but in the distorted region the

incidence can vary about 4 degrees. As mentioned that rotating stall is triggered when the flow separation generated in the distorted sector fails to be removed when it passes through the clean flow sector. A larger incidence indicates that the separation generated in the distorted region will be more severe and thus the clean flow region needs to have a larger mass flow to remove the separation. That leads to earlier stall at lower rotational speeds.

Also shown in Figure 4.16 are the stable in-stall operating points at each speed. It should be noted that at the stable in-stall point the mass flow and the pressure ratio do not converge to a single value due to the interaction between the distortion and the stall cell, which will be further demonstrated in Chapter 5. The dashed blue ellipse shows the operating point envelope at stalled condition. It can be seen from that the stable in-stall operating points are close to the distorted flow stall line on the fan performance map. Another interesting phenomenon is that the total pressure loss increases as the fan rotational speed increases (as shown in Table 4.1). This is mainly due to fan radial loading distribution changing with rotational speed. In Figure 4.18, the radial variations of total pressure at the rotor exit (normalized by the averaged total pressure) at near stall point of the 3 speeds are plotted. The total pressure distribution clearly shows that the tip loading increases with rotational speed. As a result the pressurisation capability of the stalled rotor will endure larger loss if it is more tip-loaded. The above indicates that the radial loading distribution has a great effect on the loss of total pressure during stall.

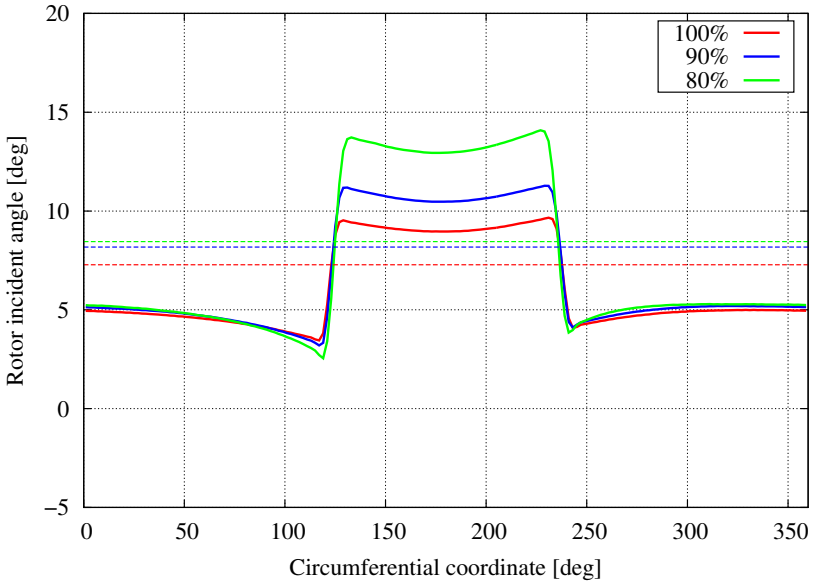


Figure 4.17: Time-averaged incident angle at 98% span of the rotor at the NS condition

Table 4.1: Loss in stall margin and total pressure for different rotational speeds

Rotational speed	$SMloss$	P_o loss
100%	9.72%	10.8%
90%	13.54%	6.06%
80%	14.62%	5.24%

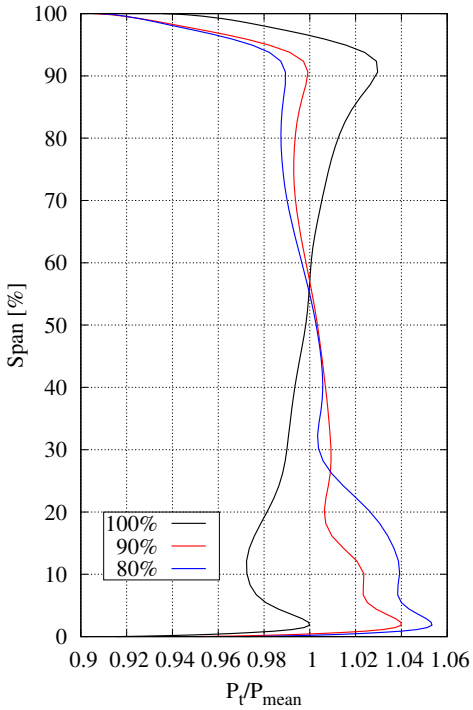


Figure 4.18: Radial distribution of total pressure at rotor exit for the PE condition at different rotational speeds

Figure 4.19 shows the predicted stall margin for both the clean and the distorted inflow with the whole stage case (with stator). Same conclusion can be obtained that the stall margin loss increases as the rotational speed drops.

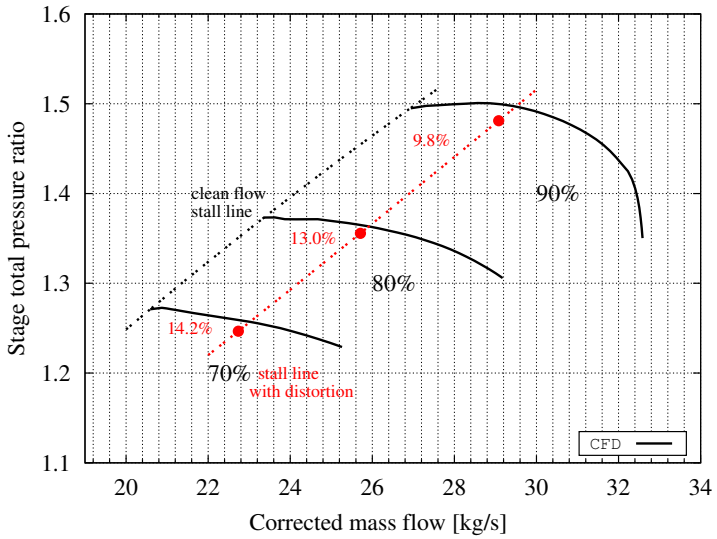


Figure 4.19: Stall margin loss of stage 67 with inlet distortion at different rotational speeds

4.7 Chapter Summery

Based on the simulation strategy developed in Chapter 3, the stall process of NASA stage 67 with abrupt inlet distortion was investigated. The tip leakage vortex shows periodic behaviour as the rotor enters and exits the distorted region at the NS point. Rotating stall occurs when the flow separation generated in the distorted region is not removed in the clean flow area. The separation begins to grow in the low-pressure region and the stall is triggered at the position where the counter-swirl reaches its peak, which is further confirmed with the blade performance at NS condition with the orbit method.

It was observed that for this axial compressor, while a longer blade response time can reduce the flow separation in the distorted area, it can also increase the recovery time in the clean flow area. Thus, it is difficult to reach a conclusion regarding this axial compressor and more investigation is needed.

While the stall margin is reduced linearly with increasing distortion strength, a distortion can improve the total pressure ratio near stall, because the distortion causes vortex shedding on the blade surface and energizes the low momentum fluid in the boundary layer. However, this assumption is not general and depends on the design of the fan blade.

For an inlet distortion with fixed strength, the stall margin loss increases as the rotational speed decreases. However, at the stable in-stall point, the total pressure ratio loss decreases as the rotational speed decreases. The results indicate that the radial distribution of loading has a great effect on the loss of total pressure during stall and a blade with less tip loading will have smaller losses.

5 Stall and Recovery Process with Inlet Distortion

5.1 Introduction

In this chapter, the stall and recovery process (stall hysteresis) of a transonic fan stage with and without inlet distortion is compared. To the author's knowledge, no recovery simulation with inlet distortion has been published in open literature. However, as discussed in Chapter 2, such kind of study is important for evaluating the performance of a fan, as a fan with smaller stall hysteresis will have a larger operational range. To investigate how inlet distortion influences the stall hysteresis of the fan, two different cases with NASA stage 67, Case 1 (uniform inflow) and Case 2 (distorted inflow), are conducted and compared.

The measured test data in the public domain are very limited. One possible reason is that such kind of test requires the compressor to work in stall which can cause damage to the rig. The author appreciates that a validated CFD study can provide instructive results to other researchers. Computations are carried out with a validated CFD code which is stable in such harsh flow environment. In spite of the lack of data, detailed analysis based on past experience and physical reasoning is used to demonstrate the validity on numerical simulations.

5.2 Case Setup

The domain used in this study is the full-annulus stage 67 (as shown in Figure 3.2). In Case 1, one of the rotor blades is mis-staggered by 0.5° to accelerate the stall initialization. It was previously shown that such a setup better mimics the stall inception process of a real compressor [Choi and Vahdati, 2011]. In Case 2, all the rotor blades are identical. Uniform international standard atmospheric total pressure and total temperature are used in Case 1 for clean flow simulation. For the computations with inlet distortion (Case 2), DC120 total pressure distortion is used, which is in accordance with the experimental data. The shaft speed is 90% of the stage design speed. During the stall and recovery process, inlet boundary conditions are fixed. This boundary treatment is justified because experimental results [Anderson and Smith, 2006] have shown that the fan operates with constant mean inlet pressure during rotating stall. In both cases, the time-accurate simulations are divided into two parts; the stall process and the recovery process. Each process is studied separately. During the first part, the fan is pushed into rotating stall by incrementally closing the exit nozzle. The distortion in Case 2 is consistent in front of the fan along the whole characteristic (choke to stall) which mimics the typical procedure in the rig test. This is different with the simulations in the former chapter where the fan falls into rotating

stall due to the sudden appearance of distortion (abrupt distortion). The nozzle is incrementally opened to recover the fan. The distortion stays unchanged during the whole recovery process in Case 2.

5.3 Overview of the Entire Process

Figure 5.1 shows the corrected inlet mass flow for Case 1 and Case 2 plotted against fan revolution during the stall and recovery processes. It is seen from this plot that after the initial drop in mass flow, which is due to reduced nozzle area (up to 2^{nd} rev), the two cases exhibit different behaviours. In Case 1, the fan initially undergoes large-amplitude oscillations in mass flow, with a peak-to-peak variation reaching 25% of the mean mass flow. The time-scale of these oscillations is several revolutions. After about 20 revolutions, the large amplitude oscillation settles down and higher-frequency fluctuations with an amplitude of less than 2% of the mean mass flow appear. At this point, the mean mass flow does not change. The recovery process is initiated at the 24^{th} revolution by increasing the nozzle area ratio by 0.007 every 5 revolutions (the difference in nozzle area ratio between choke and stall is 0.2 for Case 1). During the recovery process, the mean mass flow rises linearly and the amplitude of the high-frequency fluctuations decreases. Finally, the stall cells disappear. At this point, the exit nozzle is not opened any further and the mass flow stabilizes.

In Case 2, the initial mass flow oscillations are much smaller than in Case 1 and the mass flow reaches a periodic state at the 20^{th} revolution, at which point the recovery process is initiated. The mass fluctuations during recovery are larger than in Case 1 and survive during the whole recovery process, although their amplitudes are reduced as the mass flow is increased. This behaviour will be discussed in detail later. From the starting point (0 rev) in Figure 5.1, it can be seen that the fan stalls at a larger corrected mass flow with inlet distortion. However, it recovers faster and to a similar mass flow as the clean inflow case.

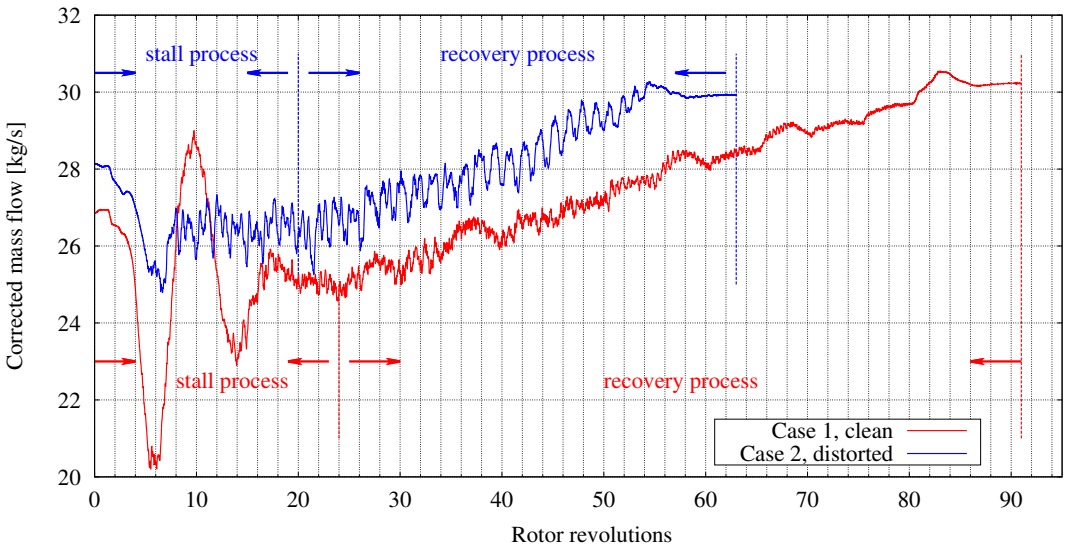
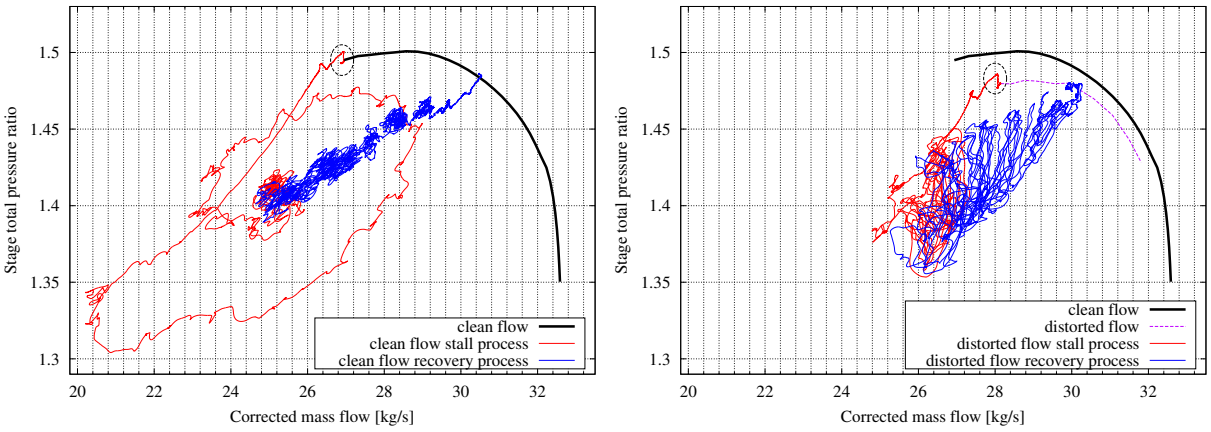


Figure 5.1: Mass flow history of the stall and recovery process for Case 1 and Case 2

The corrected mass flow at the rotor inlet and total pressure ratio of the stage during the entire stall and recovery process and the steady (stable) fan characteristic are shown in Figure 5.2. For Case 2, the steady (stable) characteristic with inlet distortion is also shown. The dashed black circle shows the stall point for each case. It is clear that the stall point is shifted to a larger mass flow and total pressure ratio is reduced with inlet distortion. In both cases, the initial stall transient, i.e. the small fluctuations around a steady operating point, as well as the mass flow increase during the recovery process are visible. However, the stall hysteresis, measured as the mass flow difference between the near stall point and the recovery point, is noticeably smaller in the case with inlet distortion.



(a) (b)

Figure 5.2: Computed hysteresis curves in (a) Case 1 and (b) Case 2

5.4 Comparisons of the Stall Process

In this section, the stall process of Case 1 and Case 2 are compared in detail. Figure 5.3 shows the contour of axial velocity at the stator inlet for Case 1 during the stall process. At $t = 0\ rev$, the nozzle is closed slightly from the last unstalled operating point. By the 2^{nd} revolution, the mass flow across the rotor has already dropped (see Figure 5.1) but the fan is still stable. It is noted that, although one of the rotor blades is slightly re-staggered, the stall cells are generated in multiple positions around the annulus and merge to form six small stall cells by revolution 5. Between the 5^{th} and the 8^{th} revolution, the stall cells merge, and two large stall cells are formed. In the next 2 revolutions, these two stall cells shrink and by the 10^{th} revolution the small one disappears. Between the 14^{th} to 18^{th} revolution, the stall cell shrinks and finally stabilizes at $t = 20\ rev$.

The stall process of the case with abrupt inlet distortion has already been explained in Chapter 4. Closer to stall, when the flow separation generated in the distorted region is not removed in the clean flow area, rotating stall occurs. The stall process with consistent inlet distortion (Case 2) is shown in Figure 5.4. At the near stall point at $t = 0\ rev$, the separation generated in the distorted region is completely removed in the clean flow region. Two revolutions later, the separation in the distorted area has grown and been carried into the clean flow area. Due to the reduced mass flow at this operational point, the clean flow sector is less capable of removing the

separation. As a result, the separation travels around the full circumference and grows when it enters the low-pressure region again. A large stall cell appears when the separated blades enter the clean flow area again ($t = 5\ rev$). The whole process takes about 2-3 rotor revolutions and only one large stall cell is generated. This is in contrast to the clean flow case where six stall cells are visible. This difference is likely to be due to the strong inlet distortion. The inlet distortion is dominant when compared to the disturbances within the rotor, thus the position where the stall cell is formed is fixed and is determined by the distortion configuration. As a result, the stall process of Case 2 is quite different from that of Case 1.

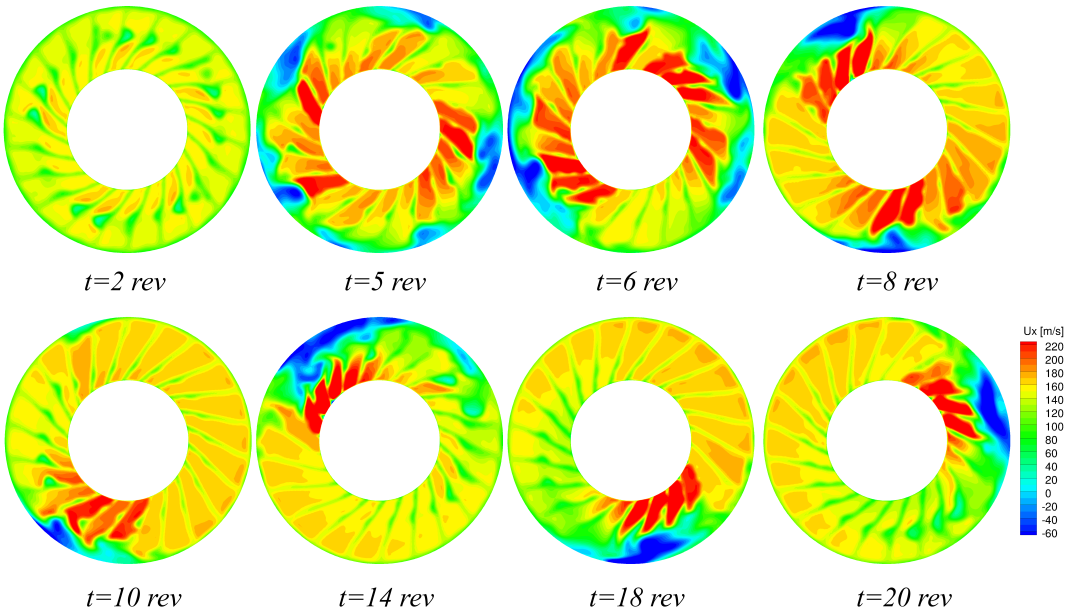


Figure 5.3: Axial velocity contours of stator inlet at different time during stall process, Case 1

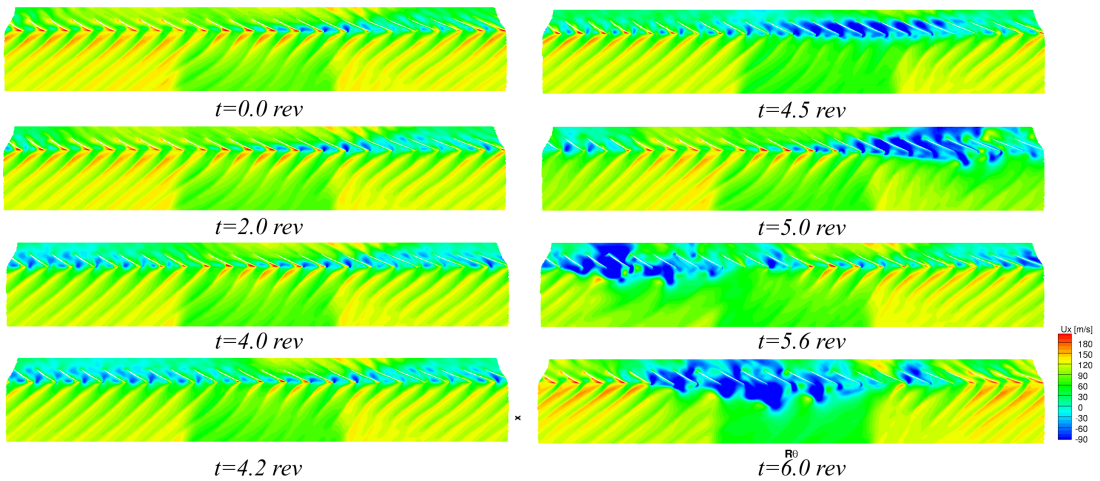


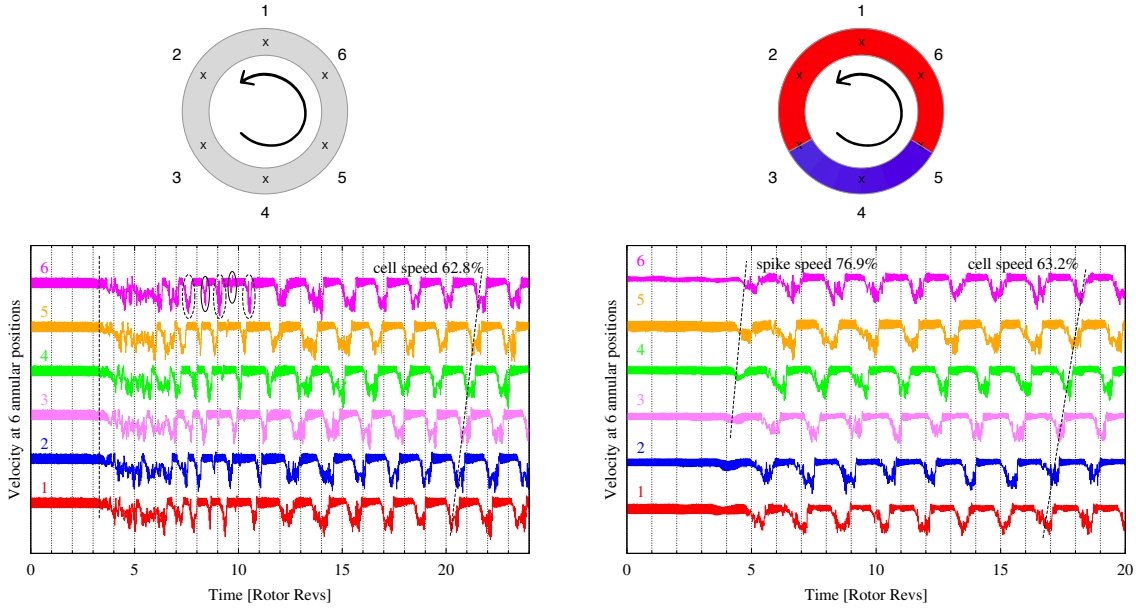
Figure 5.4: Axial velocity at 98% rotor span (stationary frame) during stall process of Case 2

In order to investigate the process further and estimate the rotational speed of the stall cell, time traces of axial velocity are shown in Figure 5.5. Six probes, positioned 20% chord upstream

of the leading edge, are uniformly distributed around the casing (see Figure 5.5) for both cases. In Case 1, a few spikes appear simultaneously at different circumferential positions between the 3^{th} and 4^{th} revolution, as indicated by the near vertical line in Figure 5.5a. The dashed circles and solid circles mark the appearance of two different stall cells which swipe over probe 6 alternatively. Between revolutions 8 and 10, the larger stall cell, characterized by a larger and wider velocity deficit, shrinks while the small stall cell disappears entirely. After 12 revolutions, both amplitude and size of the stall cell grow until a stable state is reached at approximately the 15^{th} revolution. The absolute rotational speed of the stable stall cell is about 63% of the rotor shaft speed. The speed of the stall cell is estimated from the slope of the dashed line which connects the troughs of the velocity traces.

In the corresponding plot for Case 2, the axial velocity first sees a mild deficit at the 4^{th} revolution at probe 3. This is delayed with respect to the stall inception seen in Figure 5.4 as the upstream probe is not very sensitive to flow separation inside the passage. The fully developed stall cell is clearly visible in the axial velocity time traces after 5 revolutions. This time scale for the appearance of the stall cell is a characteristic of spike-type stall inception. The rotational speed of the stable stall cell is approximately 63% of the shaft speed, which is the same to that in the clean flow. It is inferred that the size of the stall cell in both cases are also comparable because the rotational speed of a stall cell shows a close relationship with its size as proposed by [He, 1997] and confirmed by [Day et al., 1999]. To verify this assumption, a method to calculate the size of the stall cell is proposed in this paper. In the first step, an iso-surface of zero axial velocity U_x (Figure 5.6a) is generated in an instantaneous solution for the full-annulus stage domain. This iso-surface can be regarded as the boundary of the stall cell and the volume enclosed by the iso-surface is taken as the volume of the stall cell. For the case with distortion, the shape and size of the stall cell changes as it rotates around the annulus. Therefore, the volume of the stall cell is approximated by averaging it around the annulus. The volume of the stall cell is normalised with the rotor passage volume, which is marked with the black box in Figure 5.6b. The normalised volume of the stall cell in Case 1 and Case 2 is 13.8% and 11%, respectively, which confirms that the cells have similar sizes in clean and distorted flow.

The above results have shown that in both cases, with and without inlet distortion, the stable stalled operating condition only contains one stall cell. This behaviour is consistent with [He, 1997], which showed that multiple short-scale stall cells are more difficult to sustain in a two-blade-row configuration than in a single-blade-row configuration. Moreover, the computations show a part-span rotating stall for both cases which only exist in the tip region of the blade (Figure 5.6).



(a) (b)

Figure 5.5: Time traces of axial velocity of 6 upstream probes, (a) Case 1 and (b) Case 2

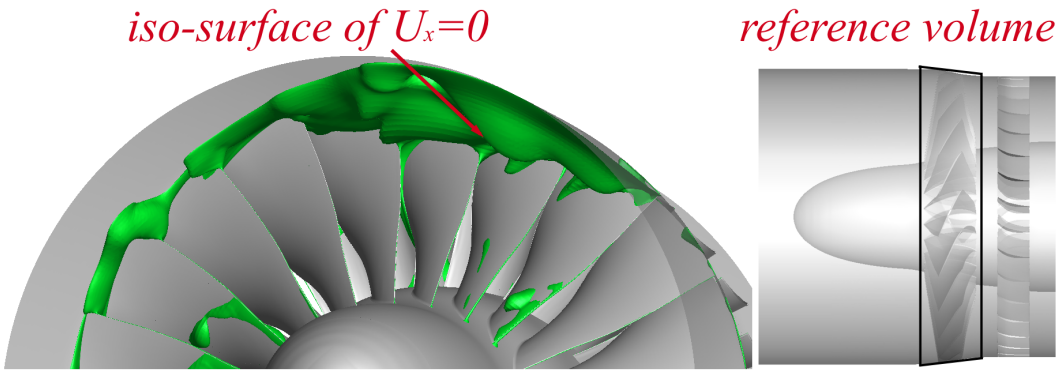


Figure 5.6: (a) Stall cell size defied with the volume enveloped by the iso-surface of zero axial velocity (b) Reference volume marked with black box

Two phenomena will be discussed in detail next: (1) the large mass flow oscillations in the initial transient which exist in Case 1 but are absent in Case 2; (2) the mass flow fluctuations after the initial transient in Case 2.

It can be seen from Figure 5.1 and Figure 5.2 that the pressure ratio and mass flow in Case 1 exhibit oscillations with decaying amplitude after the initial drop. It is found that the strong interaction between the rotating stall and downstream volume is responsible for this phenomenon. In Figure 5.7, the mass flow history at the rotor inlet and the exit of the nozzle are plotted (left-hand scale) together with the static pressure at the stator exit (right-hand scale) for both cases during the stall process. In a compression system, the exit duct behaves like a high-pressure air

reservoir. The mass flow at the nozzle exit is reduced when the nozzle is closed. However, at this instant, the inflow of the fan does not change, and the fan is still pumping air into the exit duct. As a result, the static pressure in the exit duct rises and this in turn increases the static pressure at the fan exit. This process is indicated by the overshoot of total pressure marked by the dashed circle in Figure 5.5. The increased static pressure raises the fan blade loading and reduces the mass flow, as shown in Figure 5.7 at $t = 2\ rev$. In Case 1, the pressurisation capability of the fan blade is reduced when stall occurs and the passages are blocked by multiple stall cells. Therefore, the mass flow and static pressure of the flow entering the exit duct are both reduced from revolution 2 to 6 (see Figure 5.7a). The nozzle exit mass flow responds with a time lag and reduces between revolution 3 and 7. At the same time, the blockage area in the rotor row is reduced as the number of stall cells drops from 6 to 2. As the exit duct is gradually emptying the static pressure in the duct decreases, the backpressure and consequently the fan loading is decreased. Subsequently the fan begins to restore its pressurisation capability and both the mass flow and the static pressure increase from the 6^{th} to the 10^{th} revolution. Within these 4 revolutions, one of the stall cells disappears and the other one shrinks which increases the mass flow. The exit duct is re-charged once the fan is able to pump more high pressure into the exit duct and consequently the static pressure in the exit duct rises again. This forces the fan to work with a higher backpressure and the stall cell grows bigger again from the 10^{th} to the 14^{th} revolution. The above process continues until a balance between the fan and the exit duct is achieved. The size of the stall cell also evolves with the oscillation of mass flow. In summary, the large mass flow and pressure ratio oscillation in the initial transient is caused by the interaction between the stalled fan and the exit duct: the appearance of multiple stall cells leads to a large pressure ratio drop perturbing the compression system, and the large oscillations happen while the perturbation is gradually damped out.

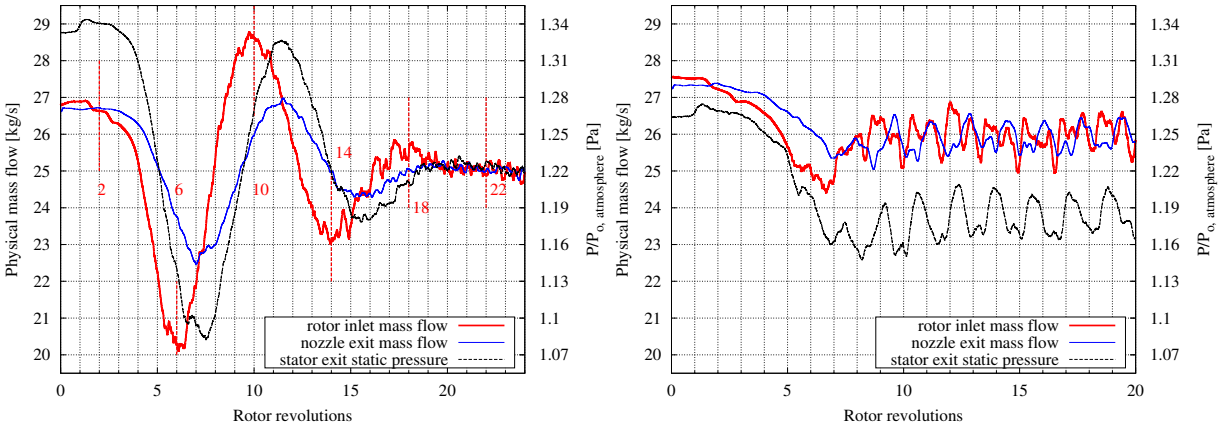


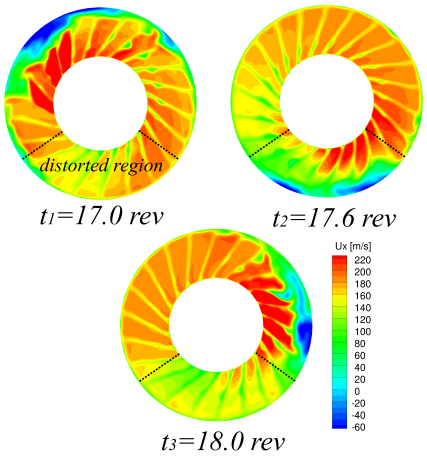
Figure 5.7: Mass flow and static pressure oscillations during stall process in (a) Case 1 and (b) Case 2

In Case 2, the initial mass flow and pressure ratio perturbation caused by the rotating stall is smaller than in Case 1 (see Figure 5.1). This can be explained by comparing the operating point and evolution of stall cells of the two cases: In Case 1, the stall is triggered when the

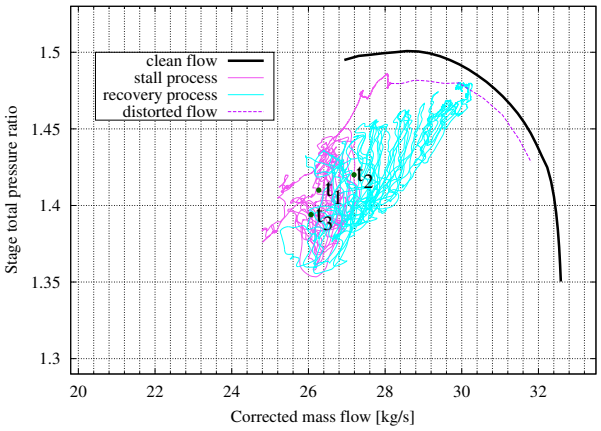
mass flow through the whole annulus is reduced past a critical point and becomes unstable. Once the stall cells appear, they block most of the annulus which causes a large mass flow and pressure ratio drop. However, in Case 2, stall cells appear in the distorted region while the mass flow through most of the annulus is still in the stable region. According to parallel compressor theory [Mazzawy, 1977], the mass flow in the clean flow sector of Case 2 is larger than that in Case 1, and therefore the averaged incidence for the clean flow sector in Case 2 is lower than that at near stall of Case 1. At 98% rotor span these incidence values are 8.4° and 8.8° for Case 2 and Case 1 respectively (the incidence in clean flow changes from 4.3° to 8.8° from choke to stall in Case 1). As a result, the development of a stall cell generated in the distorted region is immediately suppressed when it enters the clean flow region. In addition, the large-amplitude inlet distortion appears to dominate the pressure oscillation in the exit volume, such that Case 2 converges to a periodic state quicker than Case 1.

The mass and pressure ratio oscillations during the stall inception process, analysed above, are a known feature of a compression systems transient response. It has been shown in [Greitzer, 1976] that the rotational speed of the compressor and the volume of the exit plenum are two important parameters influencing this transient. The results above show that the stall cell evolution also has a significant effect on the system transient response.

The second phenomenon seen in the time histories, i.e. the fluctuations in mass flow and pressure ratio occurring after the initial transient with inlet distortion (Figure 5.1), are described next. These fluctuations occur because the stall cell changes in shape around the annulus as well as it blocks the clean and distorted regions alternatively. This phenomenon is shown with the snapshots of axial velocity at different instants of time at stator inlet in Figure 5.8a. The black dots correspond to the operating conditions of the snapshots in Figure 5.8b. The size of the stall cell at t_1, t_2 and t_3 is 10.0%, 10.3% and 10.1%, respectively. Consequently the size of the stall cell does not change much though its shape alters. It is noted that the corrected mass flow and pressure ratio of the compressor is larger when the stall cell is submerged in the distorted area, and smaller when the stall cell moves into the clean flow region. This is due to the total distorted flow sector (i.e. distorted and stall region together) being smaller at these instants of time. The compressor will have lower performance once the clean flow area is blocked by the stall cell.



(a)



(b)

Figure 5.8: Influence of the inlet distortion on stall cell pattern

5.5 Comparisons of the Recovery Process

The recovery process is generally similar for both cases but the amplitude of fluctuations in mass flow and pressure ratio differs. The size of the single stall cell decreases while its rotational speed increases. This is clearly shown in the time trace of axial velocity captured by the numerical probes in Figure 5.9 and Figure 5.10. It can be seen that the width of the low-speed trough is decreasing as the mass flow increases. Examples of these low-speed troughs are marked by three dashed circles on the trace of probe 1 in Figure 5.9. The instantaneous profile of the stall cell at these instants of time is shown in in Figure 5.11. Moreover, less rotor revolutions is needed for Case 2 to recover.

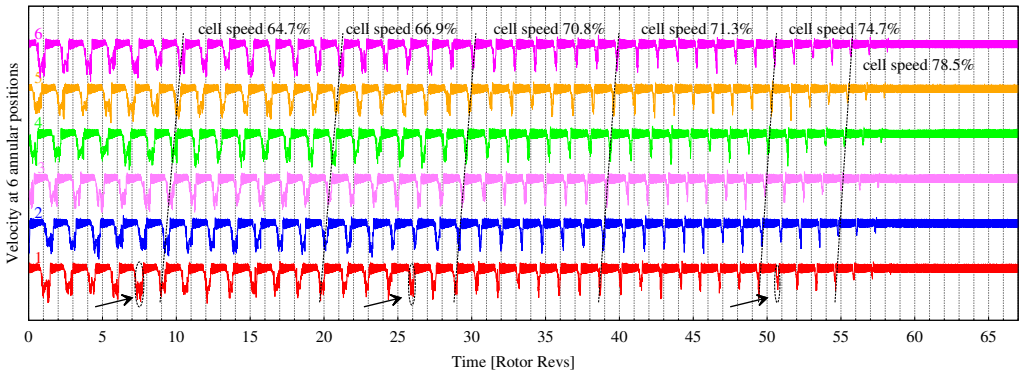


Figure 5.9: Time traces of axial velocity from 6 upstream probes during recovery process, Case 1

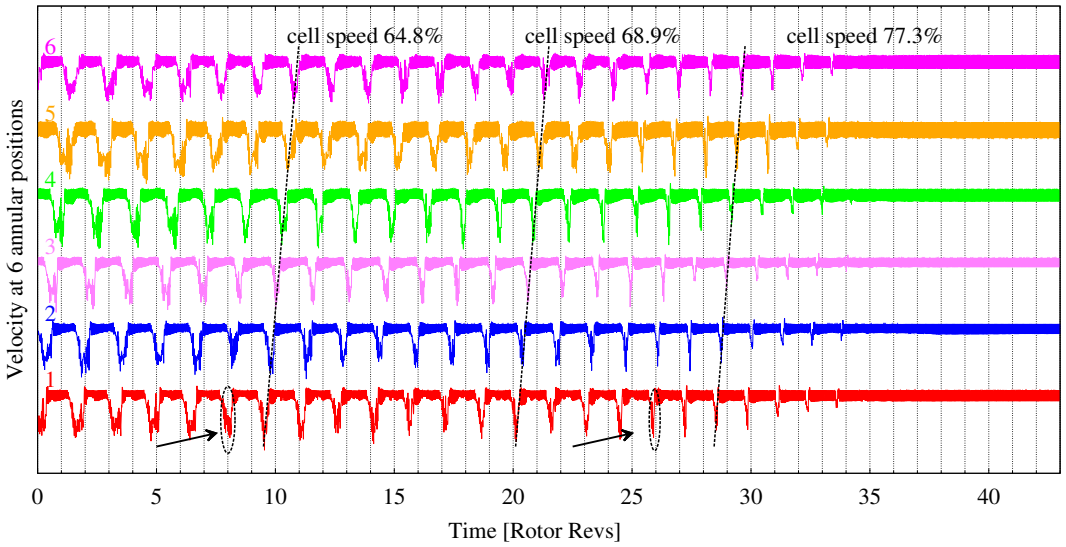


Figure 5.10: Time traces of axial velocity from 6 upstream probes during recovery process, Case 2

The axial velocity contours at 98% rotor span for both cases are plotted in Figure 5.12. The plots are in the stationary frame of reference. In Case 1, the size and the strength of the stall cell decreases with time before it is totally removed. In Case 2, the stall cell retains when it enters the distorted region and is only removed in the clean flow region.

Although Case 1 and Case 2 stall at different mass flow conditions, both cases recover to a similar mass flow under the current throttling approach (incremental opening of the nozzle every five revolutions). Moreover, the nozzle area ratios are the same for both cases at recovery point.

It is considered that the removal of the stall cell requires the incidence to drop below a critical value in the clean flow area. According to parallel compressor theory, the averaged flow condition in the clean flow region in Case 2 is very similar to that of Case 1 when the area ratios of both cases are the same. At the point of recovery, the circumferentially averaged incidence in the clean flow region of Case 2 is 6.2°, while it is 6.0° in the undistorted case. This finding proves that the clean flow sector in Case 2 plays a key role in removing the flow separation.

To test this conclusion further, the opening rate of the nozzle was halved in the simulations (10 revolutions per opening). It was found that this setup does not influence the recovery point which further confirms the suitability of the numerical strategy.

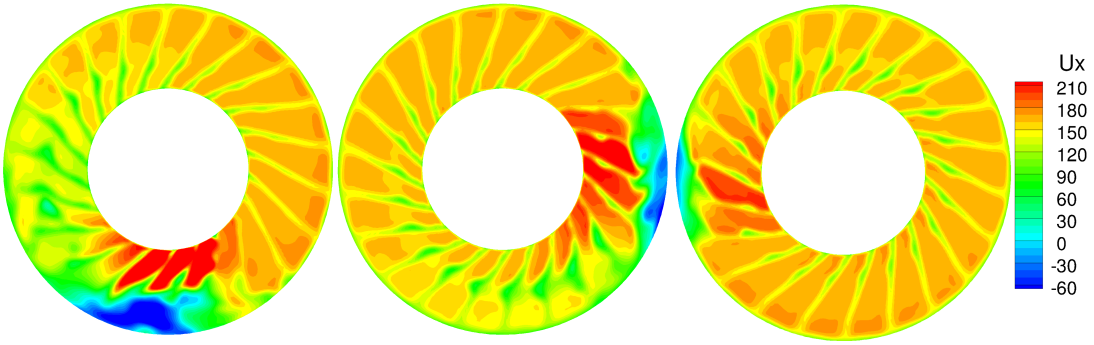


Figure 5.11: Axial velocity of stator inlet at different instants of time

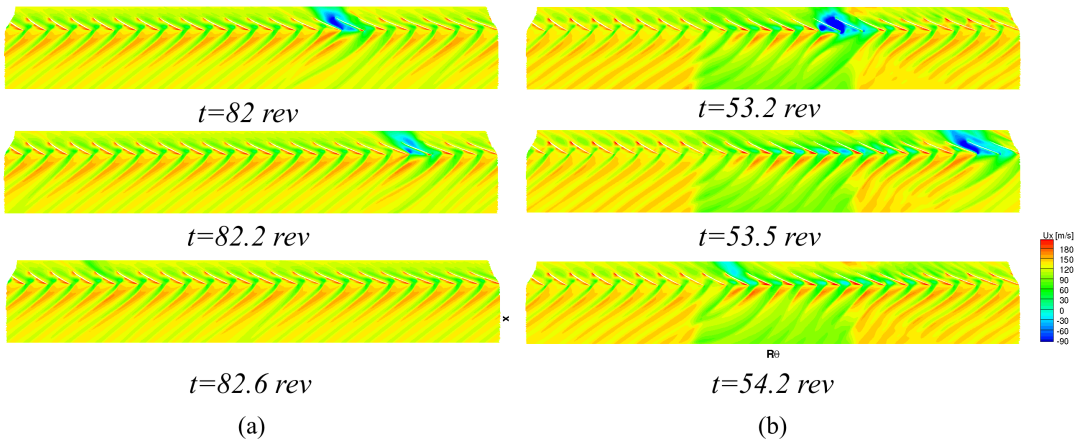


Figure 5.12: Axial velocity contours at 98% rotor span during recovery process: (a) Case 1 and (b) Case 2

5.6 Comparisons of the Stall Hysteresis between Two Types of Inlet Distortion

The detailed stall process for stage 67 with transient inlet distortion as well as consistent inlet distortion have already been shown in section and section 5.4. In this section, a rough comparison of the overall stall and recovery process between the cases with abrupt inlet distortion and consistent inlet distortion is presented. It needs to be mentioned that after the fan stalls with abrupt inlet distortion, the distortion retains in the following recovery process. The computed mass flow and total pressure ratio of stage 67 with two types of distortion are plotted in Figure 5.13. It can be seen that the abrupt inlet distortion is more harmful to the stall margin of the compressor. An operational condition which can resist consistent inlet distortion will fall into stall when the abrupt distortion of the same strength occurs. Because the case with consistent distortion stalls at lower corrected mass flow, the stable in-stall operational point has lower corrected mass flow and pressure ratio than the case with abrupt distortion. However, both cases recover to the same operational condition. As a result, the case with abrupt inlet distortion has less stall hysteresis.

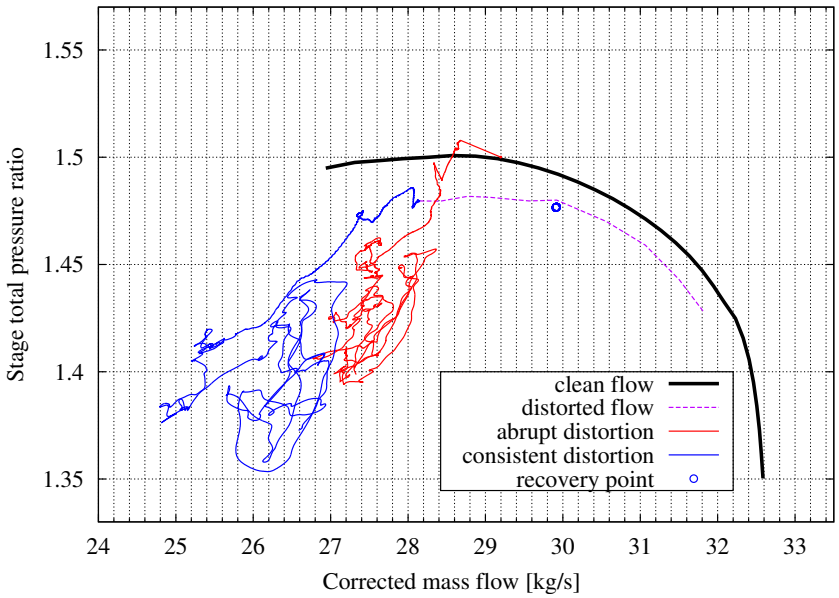


Figure 5.13: Computed hysteresis for the cases with abrupt distortion and consistent distortion

5.7 Chapter Summery

Full annulus URANS simulations were carried out to simulate the whole stall and recovery process with and without consistent inlet distortion to investigate its effects on the stall hysteresis of NASA stage 67. The fan blade stalls at higher mass flow with inlet distortion but recovers to a similar mass flow as the clean flow case, i.e. the case with inlet distortion has less hysteresis. Moreover, the time required for the recovery process with inlet distortion is shorter than the clean flow case.

The presence of inlet distortion changes the stall process of the fan. Under clean inflow conditions, six stall cells appear in the tip region simultaneously as the mass flow is reduced. Thereafter, an interaction between the exit duct volume and stalled fan induces large mass flow oscillations and the stall cells merge. Only one stall cell exists when the fan reaches a stable state. For the case with inlet distortion, the stall cell is formed when the flow separation generated in the distorted sector fails to be removed in the clean flow sector and re-enters the distorted sector. Only one stall cell is generated during the stall process but the structure of the stall cell changes due to interactions with the distortion.

Although the stall process is different in presence of a distortion, the stable rotating stall shows the same characteristic in terms of number, size and rotational speed of cells. During the recovery process, the size of the stall cell becomes smaller, and its rotational speed increases, as the mass flow increases. Both cases recover at the same nozzle area ratio, which indicates that the clean flow part of the annulus plays a very important role in recovery process.

By comparing the stall hysteresis of the abrupt inlet distortion and consistent inlet distortion, it is has been shown that the abrupt distortion is more detrimental to the stall boundary of the fan while the recovery point remains the same. This suggests that the stall boundary obtained from the experimental tests with consistent distortion can be over-optimistic when transient distortion

occurs. Further study of the influence of the abrupt inlet distortion on fan stall margin is still needed.

It is noted that the distortion configuration used in this research is simple and not necessarily representative of a distortion in a real engine. However, the results suggest that the recovery process is driven by the clean flow region, and this still expected to stand as long as the inflow can be roughly divided into a clean flow region and distorted region. The simulation of the BLI distortion in Chapter 7 will show the effect of the real distortion pattern on the performance of the fan.

6 Influence of the Exit Duct on Fan Stall Margin

6.1 Introduction

The influence of downstream structure on compressor stall has long been noticed and investigated [Greitzer et al., 1978]. It has been shown (analytically and experimentally) that downstream geometries such as the exit duct, nozzle and diffuser to have significant impact on compressor stability. Moreover, it has also been shown that the mode of compressor instability, rotating stall or surge, is determined by the volume size downstream of the machine [Greitzer, 1976]. In a typical test rig [Brandstetter et al., 2019], an exit duct is used between the compressor and the throttle, as shown in Figure 6.1.

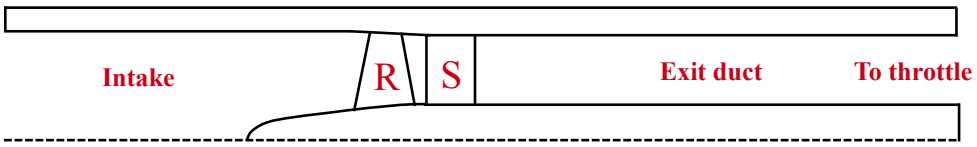


Figure 6.1: Typical compressor test rig

In this chapter, the effect of exit duct length on the fan stall margin is studied. When the fan operates far from the stall boundary, the length of the exit duct has minimal influence on the performance. However, during this study it was found that it can have a significant effect on the unsteady behaviour of the rotor near the stall boundary, and thereby influences the stall margin. Two cases were studied. In the first case, an abrupt distortion is placed upstream of the fan and the interaction between the distortion and the exit duct is analysed. It is then shown that a case with clean inflow shows a similar behaviour.

6.2 Influence of the Length of the Exit Duct on Fan Stall Margin with Inlet Distortion

Calculations were carried out for NASA stage 67 with abrupt inlet distortion (DC120) on two different computational domains, as shown in Figure 6.2. The fan stage is attached to the same nozzle with two inviscid exit ducts of different length. Therefore, from a steady point of view the two flows are identical. The length of the short exit duct and long exit duct are 0.75D (rotor diameter) and 2.25D, respectively. The grid density is the same for both ducts. The nozzle is choked with a sonic zone in the throat. Starting from uniform inflow solutions, computations

are initiated by introducing an abrupt DC120 inlet distortion. The starting solution for both calculations is identical and corresponds to a stable operating condition with a corrected mass flow of 29.4 kg/s.

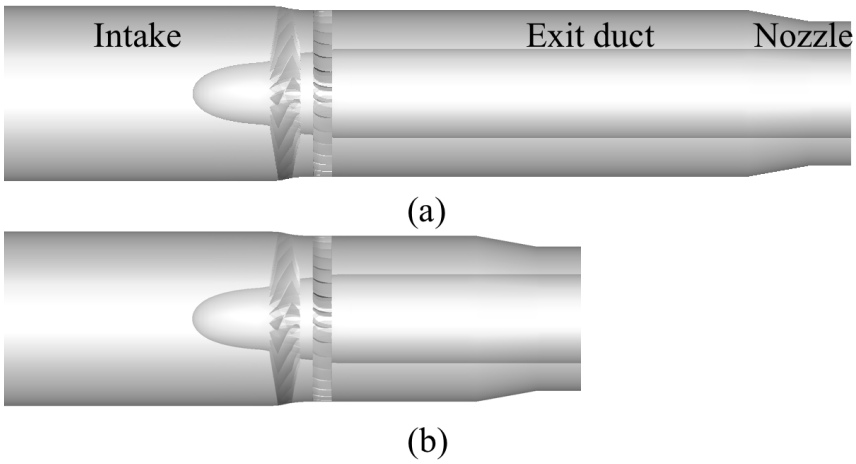


Figure 6.2: Computational domain of NASA Stage 67 with (a) long and (b) short exit duct

The initial (clean flow) and fully developed operating condition for these two setups are illustrated on the compressor map shown in Figure 6.3. The dashed lines in this plot show the trace of transient flow as distortion is placed upstream of the fan. Despite the same numerical setup, nozzle area ratio and starting solution, the case with short exit duct remains stable whereas the case with long exit duct results in significant reduction in mass flow and total pressure ratio and moves to a stalled operating point. The difference in the fully developed solutions can be visualized by the contour of axial velocity at fan exit, which is plotted in Figure 6.4. It can be seen from the figure that a stall cell appears in the case with long exit duct.

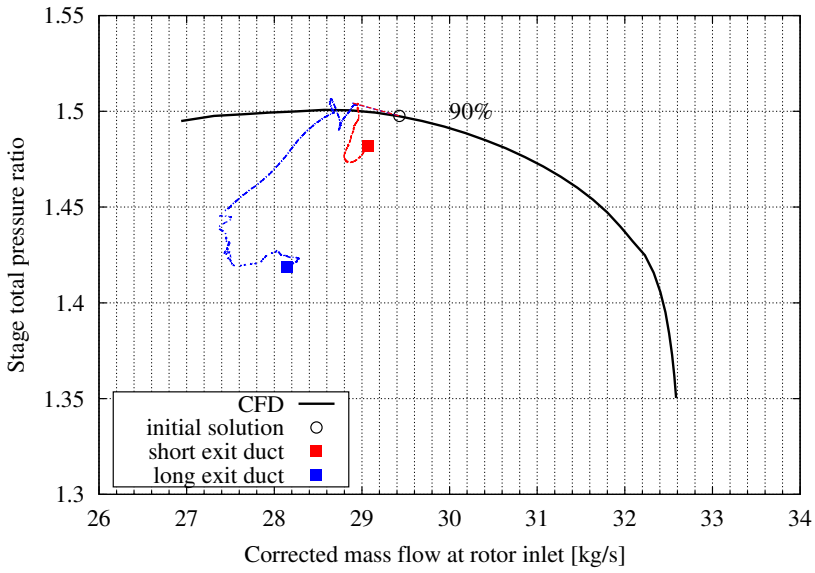


Figure 6.3: Compressor map for 90% corrected speed

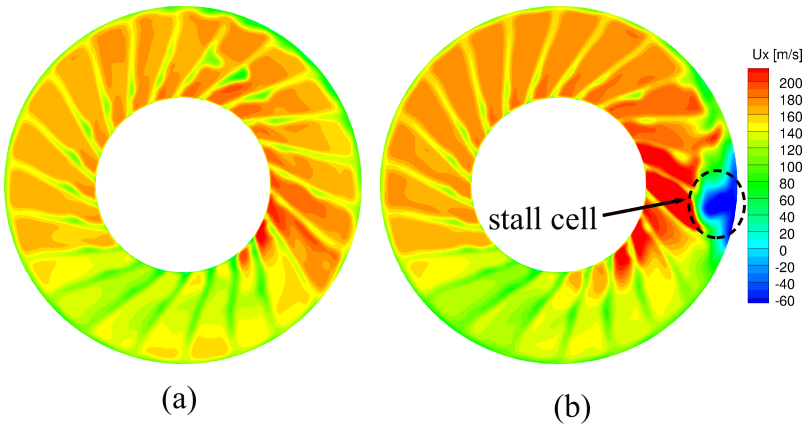


Figure 6.4: Axial velocity contour at fan exit for the case with (a) short exit duct and (b) long exit duct

In order to further study the physical mechanism responsible for the observed phenomenon, transient flow solution in the duct downstream of the fan stage is examined. The analysis approach is illustrated schematically in Figure 6.5. In step 1, instantaneous flow solutions at mid-span surface of the duct are extracted with a sampling frequency of 110 frames per rotor revolution. The static pressure perturbation, defined as the difference in static pressure between steady initial solution and the extracted solutions, is calculated. In step 2, a circumferential discrete Fourier transforms (DFT) is carried out on the mid-span surface at each time frame to obtain circumferential modal content of the static pressure perturbation in the exit duct. The obtained Fourier coefficient amplitude at *rev* 2 are plotted as contour in Figure 6.6 as a function of circumferential mode order and axial position. In this plot the amplitudes of Fourier coefficient are normalized by the clean inlet total pressure. It can be seen from Figure 6.6 that the dominant flow perturbation is the 0^{th} harmonic, i.e. the planar wave. Similar observations were made at other time instances. The finding is in agreement with the experimental study in [Brandstetter et al., 2019], which shows that the circumferential asymmetry has much smaller effect than the planar wave downstream of the compressor. Therefore, analyses in this paper focus on the planar wave; effects of higher harmonics are assumed to be negligible.

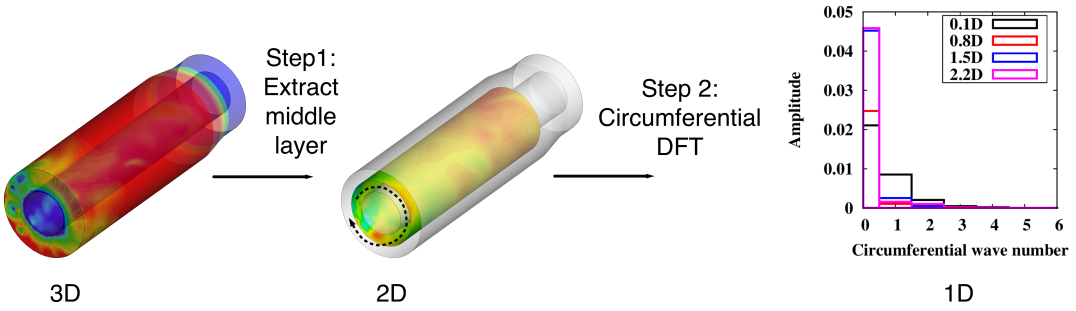


Figure 6.5: Analysis approach in the exit duct (contour is only for illustration)

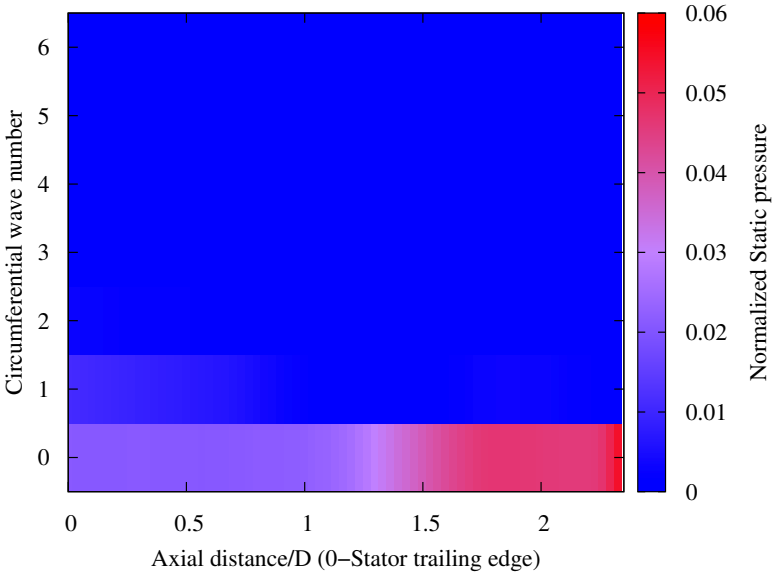


Figure 6.6: Circumferential modal contents of static pressure perturbations at *t=2 rev*

In the next step, the collected snapshots of axial profile for the planar wave are combined and plotted with respect to space and time. The final form of the results is presented as a contour plot shown in Figure 6.7, which shows how static pressure changes with time at various axial locations. In these plots, the static pressure is normalized using total pressure of clean inflow and the axial location is normalised by the rotor diameter (D) where zero denotes the stator trailing edge. Furthermore, for the purpose of discussion, the time history of mass flow at the stator exit is plotted in Figure 6.8. The effect of exit duct length on fan stability is discussed in the following paragraphs by examining the results in Figures 6.7 and Figure 6.8.

It is seen from Figure 6.7 that an expansion pressure wave P1 initially appears at the stator trailing edge at approximately revolution 0.6 ($t = T_0$), at which time the mass flow for both cases sees a significant decrease as shown in Figure 6.8 (the cause of this phenomenon will be explained in detail in the next section). The origin of the expansion wave P1 can be traced back to the abrupt change of inlet conditions at the inlet boundary. Upon examining the time difference between the appearance of flow distortion at the inlet (*rev* 0) and the detection of wave P1 at stator trailing edge (rev $0.6, t = T_0$), it is concluded that P1 is the transmitted component of the distortion-generated disturbances propagating with a speed of $U + c$, where U is the speed of main flow and c is the local sonic speed.

After the expansion pressure wave P1 passes the rotor (at time T_0) the mass flow gradually increases as the fan begins to recover. At this time no stall cell is detected in the fan. When the pressure wave P1 arrives at the nozzle, it is reflected as another expansion pressure wave R1. The reflected wave propagates upstream with a speed $U - c$, and reaches the stator trailing edge at approximately *rev* 1.2 ($t = T_1$) for the short duct case and at *rev* 2.5 for the long duct case. The decrease in back pressure, induced by the arrival of the reflected expansion wave R1, results in a further increase in mass flow for the short duct case. This phenomenon can be clearly seen after $T1$ in Figure 6.7, where solutions of these two models diverge. Between time $T1$ and $T2$,

the mass flow for the case with short exit duct rises faster than the case with long exit duct, which is a result of the arrival of expansion wave R1.

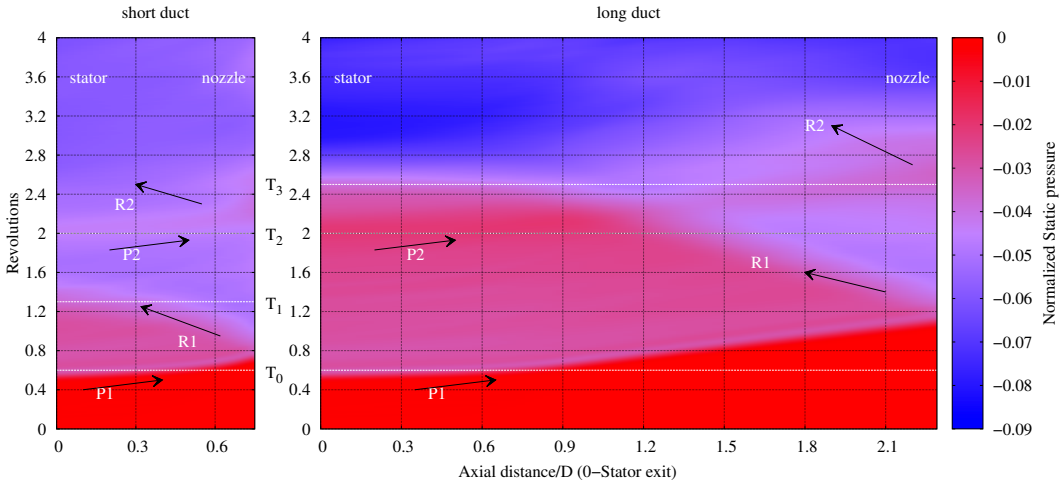


Figure 6.7: Time history of static pressure axial profile at middle span in the short and long exit duct

At approximately revolution 2 ($t = T_2$), another pressure wave P2 is observed at the stator trailing edge in both cases. The physical nature of P2 will be investigated later. It is however of compression type, i.e. increased static pressure, as opposed to P1 and R1. By the time $t = T_2$, the case with short exit duct has recovered to a mass flow significantly higher than the case with long exit duct. The increase in compressor back pressure, driven by the arrival of wave P2, leads to a reduction in mass flow in both cases (shown in Figure 6.8). For the case with short exit duct, the mass flow drops to 28.0 kg/s (point B in Figure 6.8), which is higher than 27.8 kg/s (point A in Figure 6.8), consequently the compressor can withstand P2 and restore to a stable operating point without stall. However, for the case with long exit duct, the arrival of P2 causes a larger drop in mass flow (to point C (27.5 kg/s)) which results in the compressor stalling. The low static pressure after *rev* 2.8 in Figure 6.8 for the case with long exit duct is due to the formation of a stall cell as shown in Figure 6.4.

The observed key effect of the exit duct length is as follows: for the case with short exit duct, the upstream propagating expansion wave R1 reflected from the nozzle (beneficial) arrives at the compressor earlier than the appearance of the downstream propagating compression wave P2 (detrimental), which prevents the rotor from going into stall; on the other hand, for the case with long nozzle, the compression wave P2 emerges at the compressor exit earlier than the reflected wave R1, which leads to rotating stall.

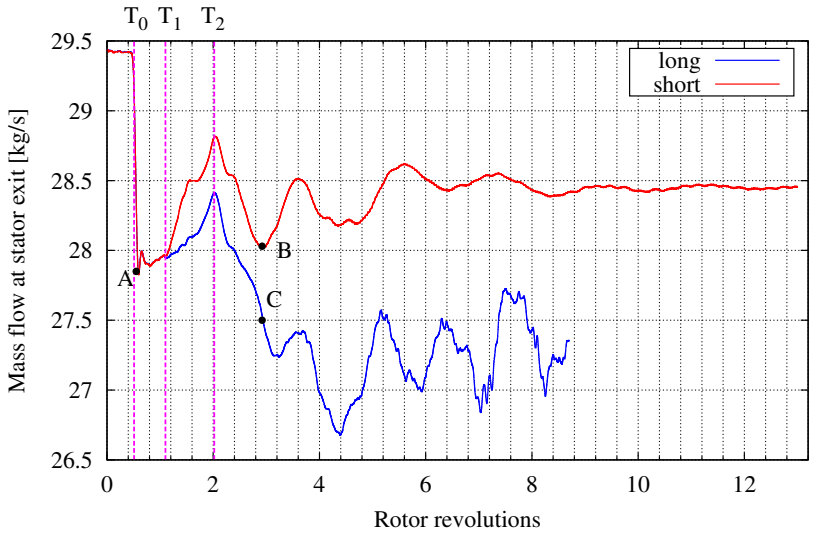


Figure 6.8: Time history of the mass flow at the stator exit

Figure 6.9 shows the effect of exit duct on the stall margin loss of the fan at 90% speed. It can be seen that as the exit duct becomes longer, the stall margin loss of the blade increases. The stall margin loss will finally converge to a stable value. The stall margin of different exit ducts can vary 3% and this corresponds to a corrected mass flow variance of 0.6 kg/s. This is about 11% of the overall mass flow range with clean inflow at the same rotational speed (26.9∼32.1 kg/s). It should be noted that a choked nozzle is used at the exit boundary for all the computations.

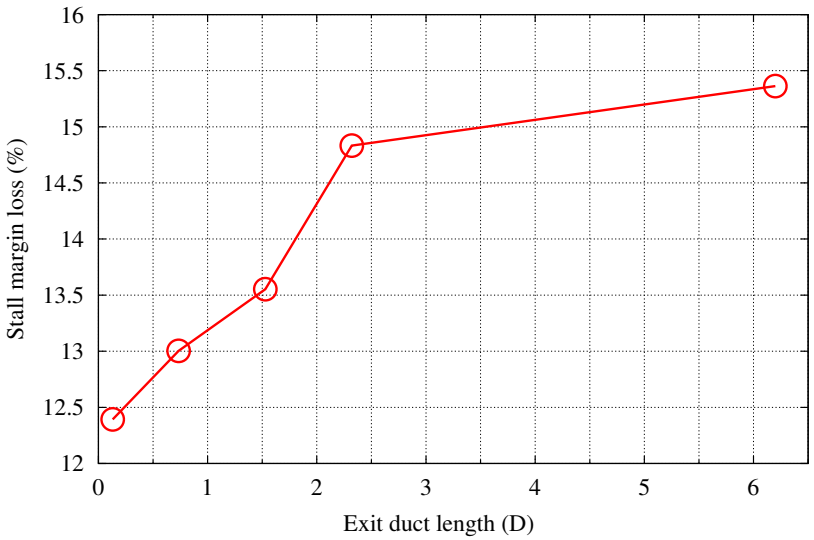


Figure 6.9: Stall margin loss for different exit duct length

6.3 Wave Propagation within the Exit Duct

Having known how wave propagation behaviour in the exit duct influences the compressor stability, this section attempts to address the following questions:

1. How does inlet distortion generate waves which travel downstream into and past the compressor?
2. How does the distortion-generated waves influence the flow field?
3. For models with choked nozzle, is reflection attributed to the sonic zone in the choked nozzle or the nozzle contraction geometry?

Traditionally, investigation of such geometrical effect on compressor stability is carried out using simplified steady or quasi-steady models such as parallel compressor theory [Greitzer et al., 1978] or lumped model [Greitzer, 1976]. These models are based on the steady state flow in the compressor and are used to study the downstream volume effects. Consequently, they cannot predict the transient response of a compressor with the dynamic feedback from downstream structures. Dynamic response from the downstream structure can have a significant impact on the initialization and development of stall, however its physical nature is poorly understood. To answer the above questions, analyses are carried out using simplified CFD models to study the property of waves generated by inlet distortion, their reflections at the nozzle and the consequent interaction with the compressor flow field. Furthermore, it will be shown that the timing of reflected expansion wave can be predicted accurately by analytical models.

6.3.1 Computational Model for Isolated Exit Duct

The computational model (Figure 6.10) used in this work is a circumferential sector of the annular duct, which consists of three main geometric components: a straight duct with constant cross-sectional area and a nozzle contraction followed by another straight duct. At the inlet surface, total pressure, total temperature and flow angle are imposed as boundary conditions. Total pressure and total temperature are circumferentially and radially uniform. The flow at inlet is purely axial. Hub and tip are set as inviscid walls. Constant static pressure boundary conditions are imposed at the exit surface. Depending on the magnitude of imposed exit pressure, the nozzle can be choked or unchoked. The benefit of a choked exit nozzle has been discussed in Chapter 3. It was shown that the final flow solution is independent of the exit boundary profile [Vahdati et al., 2005]. Moreover, numerical reflection from the domain exit boundary can be avoided due to supersonic flow in the throat. The spatial grid size in the duct is the same as that used in the simulation with NASA stage 67. For time-accurate computations, the time stepping is kept the same as the compressor simulation, which is 2,200 time steps per revolution.

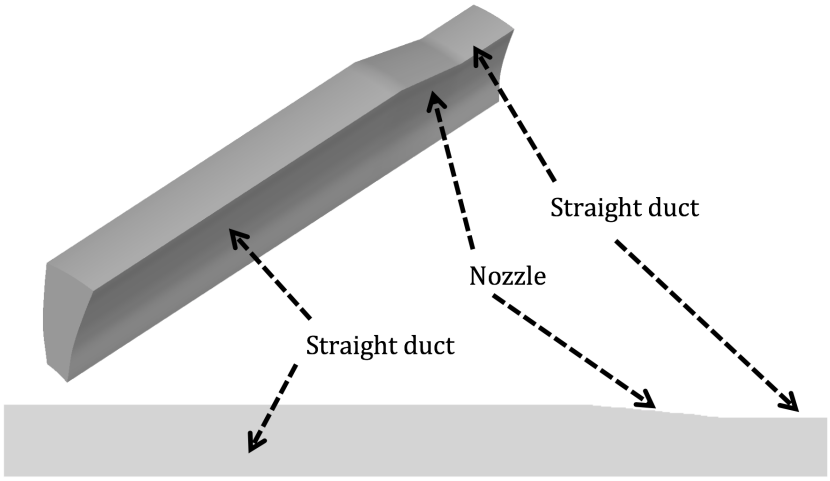


Figure 6.10: 3-D and meridian view of the computational domain

In the first step, steady solution is obtained using the aforementioned boundary conditions. In the next step, by using the converged steady solution as an initial condition, time-accurate computations are performed by reducing the total pressure at the inlet by 2% (ΔP_o) while keeping total temperature and flow angle constant. The total pressure reduction is circumferentially and radially uniform, which mimics the sector affected by the sudden occurrence of flow distortion.

For a choked nozzle, both the geometry variation and the presence of the sonic zone may impact wave reflection. Therefore, their effects are studied individually with two different cases, shown in Table 6.1. The inlet conditions for both cases are exactly the same. The nozzle is choked in Case 1 by lowering the exit static pressure.

Table 6.1: Setups for two different exit duct cases

	Nozzle throat	Nozzle area ratio	Inlet condition
Case 1	Choked	0.98	-2% P_o distortion
Case 2	Unchoked	0.76	

For Case 1 the nozzle has an area ratio 0.98, which minimises the effects of geometrical change on wave reflection. Figure 6.11a shows the meridian outline of the computational domain. Figure 6.11b shows the contour of mean flow Mach number on the periodic boundary prior to the introduction of inlet distortion. The nozzle is choked and a sonic zone ($Ma = 1$) can be seen at the throat ($x = 2.8$).

At the start of unsteady computations, total pressure distortion specified in Table 6.1 is introduced at the inlet boundary. Analysis was carried out to study the generation, propagation and reflection of flow disturbances induced by the distortion.

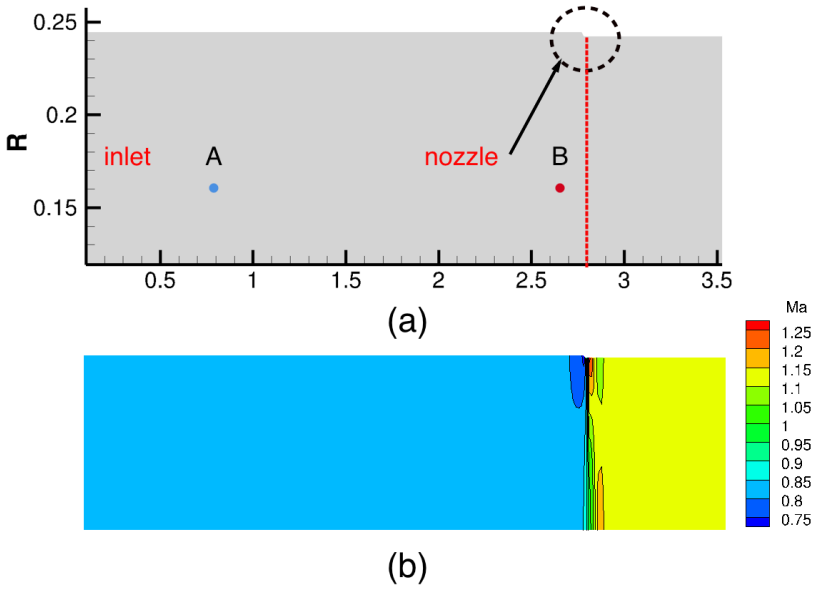


Figure 6.11: (a) Meridian view of the exit duct and nozzle; (b) Clean flow Mach number contour on the periodic boundary (Case 1)

6.3.2 Propagation of Distortion-induced Waves

The propagation of waves induced by the inlet distortion can be analysed using quasi one-dimensional analytical methods for channel flows [Hirsch, 1990]. Based on Euler flow equations, it can be shown that perturbations in the flow field travel as waves with different speeds characterised by Riemann invariants. For 1-D flow, there exist three Riemann invariants, namely

$$\delta w_1 = c^2 \cdot \delta\rho - \delta p \tag{6.1}$$

$$\delta w_2 = \rho c \cdot \delta u + \delta p \tag{6.2}$$

$$\delta w_3 = \rho c \cdot \delta u - \delta p \tag{6.3}$$

where ρ is the gas density, p is static pressure, u is axial velocity and c is local sonic speed. $\delta\rho$, δp and δu are the perturbations in static pressure, density and axial velocity respectively. δw_1, δw_2 and δw_3 denote the three Riemann invariants for 1-D flow. The Riemann invariants δw_1, δw_2 and δw_3 correspond to convected entropy wave, downstream propagating acoustic wave and upstream propagating acoustic wave, which propagate with speeds U, $U + c$ and $U - c$ respectively. For subsonic mean flow ($U < c$), the entropy wave δw_1 and the acoustic wave δw_2 travel downstream, and the acoustic wave δw_3 propagates upstream. For supersonic flow ($U > c$), all three waves travel downstream[1] several features. For the case studied here, the abrupt distortion at the inlet induces flow disturbances which travel downstream into the computation domain as entropy wave δw_1 and acoustic wave δw_2.

[1]Hence no numerical boundary reflection for a choked nozzle

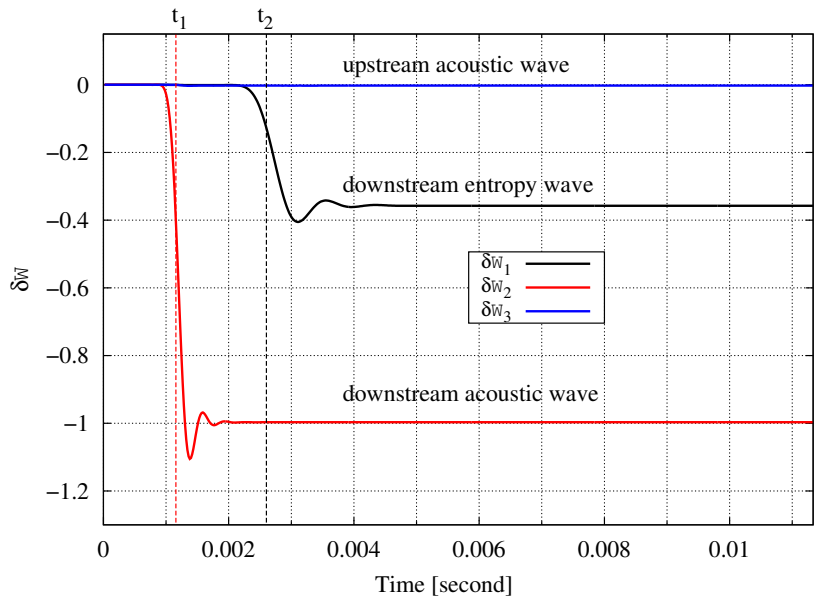


Figure 6.12: Time history of Riemann invariants at station A

Figure 6.12 shows the time history of the three Riemann invariants calculated from unsteady CFD solution at station A (marked in Figure 6.11a) for Case 1. The values of these invariants are normalised by the total pressure drop ΔP_o at the inlet. This normalisation will be applied to all the following plots of this type. The downstream propagating acoustic wave δw_2 arrives at station A at time $t = t_1$, which is followed by the slower travelling entropy wave δw_1 arriving at time $t = t_2$. The amplitude of δw_1 is less than δw_2. The value of δw_3 remains zero for the time range shown in this figure since none of the reflected waves has reached station A. The time of arrival for the two downstream propagating waves δw_1 and δw_2 calculated using the above analytical theories for wave propagation speed are also marked in Figure 6.12 at $t = t_1$ and $t = t_2$ as vertical dashed lines. A good agreement can be seen between the theoretical calculations and the CFD results, indicating that the calculations based on the analytical method can be used to model wave propagation for such problems.

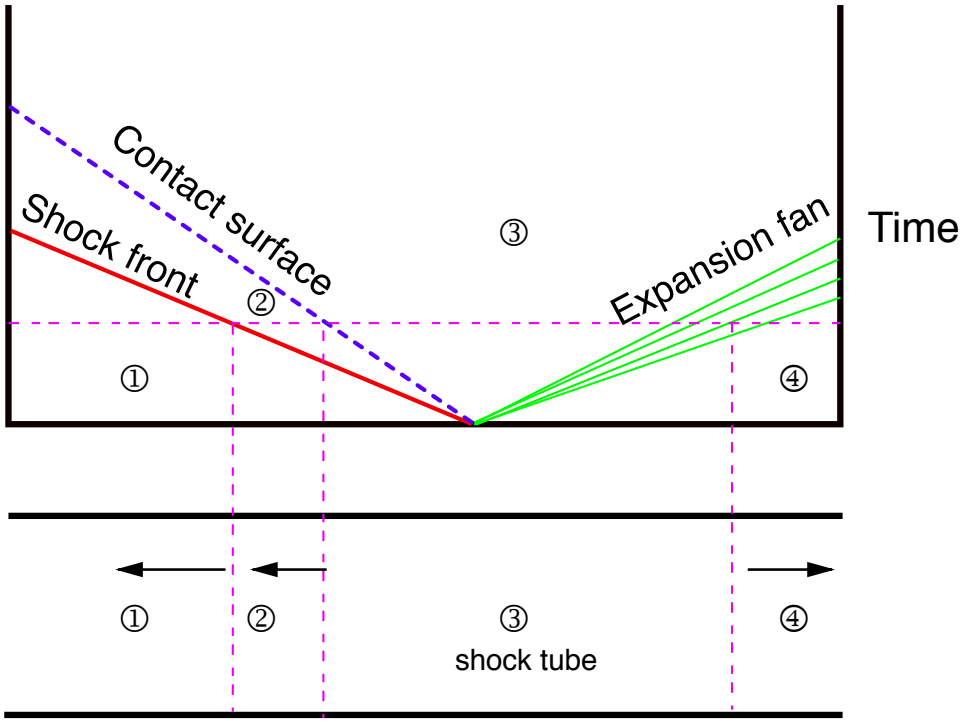


Figure 6.13: Standard shock tube model

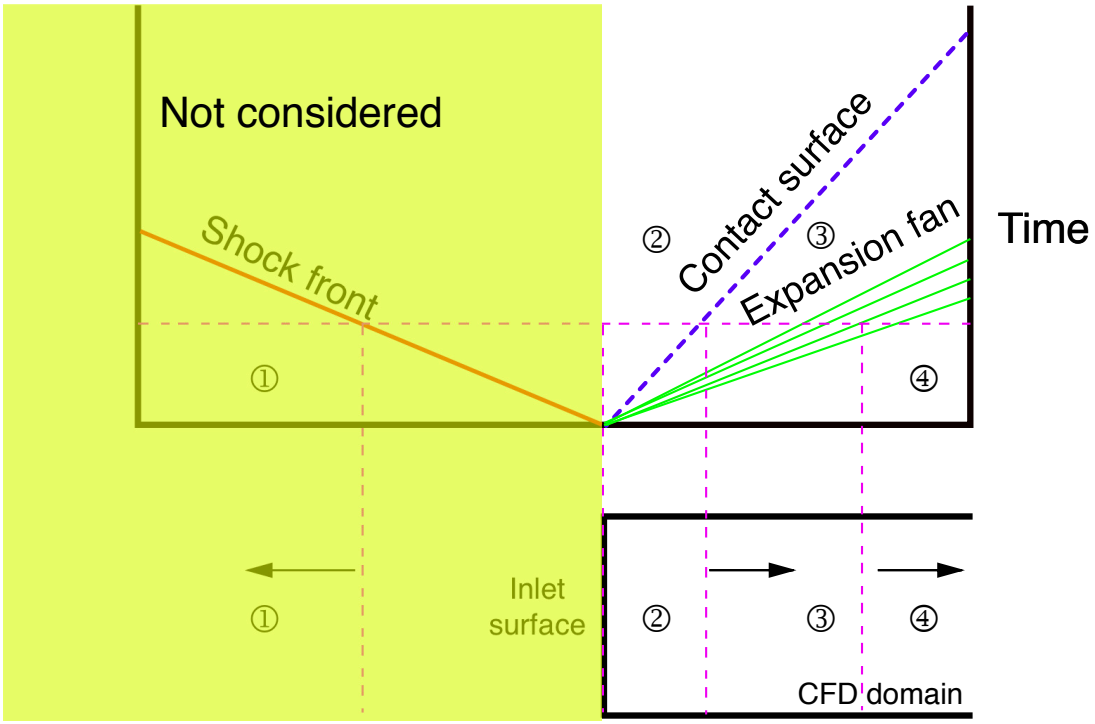


Figure 6.14: Half shock tube model

The flow discontinuity at the wave front can be analysed using a shock tube model. Figure 6.13 illustrates schematically a classical shock tube model. The shock tube contains high-pressure gas and low-pressure gas separated by a diaphragm. When the diaphragm is removed, the high-

pressure gas flows into the low-pressure region manifesting as a shock wave. On the other hand, the rarefaction of the high-pressure gas generates an expansion wave which propagates into the high-pressure volume. The expansion is a continuous process and takes place inside a well-defined region called expansion fan consisting of a series of expansion waves.

For the case studied here, no shock front exists in the computational domain as its direction of propagation is upstream out of the inlet. It should also be noted that for a standard shock tube problem, the gas separated by the diaphragm is stationary, whereas for the case studied here, the mean flow has a uniform axial velocity component. Therefore, the generation and propagation of waves induced by inlet distortion can be analysed using a "half shock wave tube" model with mean flow, which is illustrated schematically in Figure 6.14. As shown in Figure 6.14, the left part of the shock tube model (highlighted with yellow) is not considered since it is outside the computation domain. The contact surface lies inside the computation domain due to the convection of mean flow.

The relations between different zones in Figure 6.14 are defined in Equation 6.4 to Equation 6.10.

The flow parameters in Zone 4 are known and correspond to the steady solution without distortion. Total pressure and total temperature in Zone 2 are given by the distorted inlet boundary conditions:

$$P_{o_2} = P_2 \cdot (1 + \frac{\gamma - 1}{2} Ma_2^2)^{\frac{\gamma}{\gamma - 1}} \tag{6.4}$$

$$T_{o_2} = \frac{P_2}{\rho_2 R_g} \cdot (1 + \frac{\gamma - 1}{2} Ma_2^2) \tag{6.5}$$

$$V_2 = Ma_2 \cdot c_2 \cdot = Ma_2 \cdot \sqrt{\frac{\gamma P_2}{\rho_2}} \tag{6.6}$$

Across the contact surface pressure and velocities are continuous, i.e.

$$U_2 = U_3 \tag{6.7}$$

$$P_2 = P_3 \tag{6.8}$$

In order to simplify the calculation, the expansion fan which separates Zone 4 and Zone 3 is approximated using one single expansion wave. The following equations have to be satisfied for the expansion wave:

$$\frac{P_3}{P_4} = (1 - \frac{\gamma - 1}{2} \cdot \frac{U_4 - U_3}{c_4})^{\frac{2\gamma}{\gamma - 1}} \tag{6.9}$$

$$\frac{\rho_3}{\rho_4} = (1 - \frac{\gamma - 1}{2} \cdot \frac{U_4 - U_3}{c_4})^{\frac{2}{\gamma - 1}} \tag{6.10}$$

The expansion wave propagates with local sonic speed relative to the mean flow, i.e. $U + c$. The contact surface is convected downstream with the local air speed U. This is different to the typical shock tube model where the contact surface moves in the opposite direction to the expansion fan.

Equation 6.4 to Equation 6.10 are solved analytically and compared with results obtained from CFD. Figure 6.15 shows the time history of pressure, density and axial velocity perturbations (percentage values) at station A (marked in Figure 6.11a). The perturbations in this plot (and all the following plots of this type) are normalised by their respective steady solutions. Results obtained from unsteady CFD computations are shown using solid curves and calculations based on the shock tube model are plotted as dashed curves. A good agreement can be seen between the analytical calculations and CFD solutions. Minor discrepancies are attributed to the assumption of single expansion wave as opposed to an expansion fan.

It is essential to know how these distortion-generated waves change the flow field when they pass by. It can be seen from Figure 6.15 that as the acoustic wave δw_2 passes point A (at $t = t_1$), all the flow variables (density, velocity and static pressure) decrease. This rapid decrease in density and velocity explains the initial drop of mass flow observed at $t = T_1$ in Figure 6.8. It is also seen in Figure 6.15 that the passing of the wave δw_1 (at $t = t_2$) only induces density perturbation, hence the name entropy wave [Giles, 1990]. Regarding the propagation speed and effects on the flow field, the acoustic wave δw_2 resembles the expansion fan in the half shock tube model while the entropy wave δw_1 is similar to the contact surface.

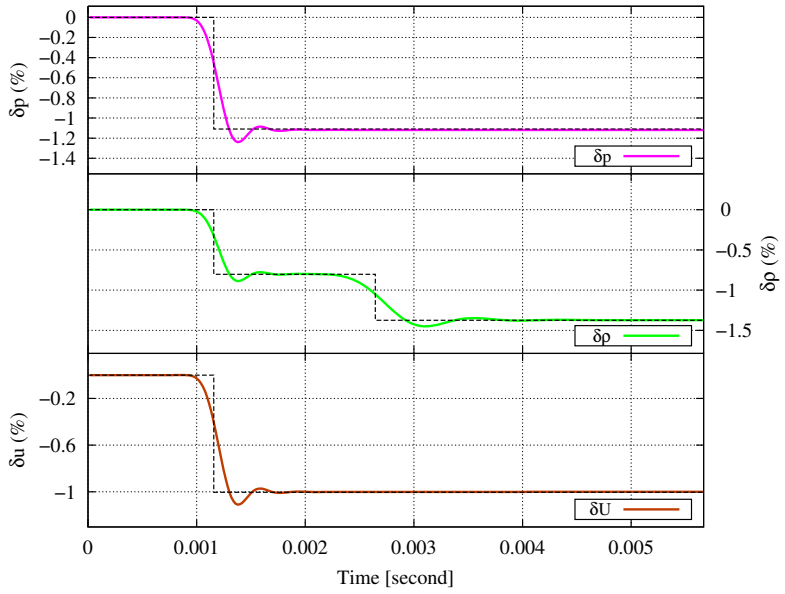


Figure 6.15: Time history of static pressure, density and axial velocity perturbations at station A

The nature of P2 in Figure 6.7 can be identified based on the findings from Figure 6.15. As already mentioned, P2 emerges at $t = T_2$. At this time, the distortion-generated convected wave (entropy and vortical wave) arrive at the stator trailing edge from the inlet with a speed of U. However, P2 propagates downstream with a speed of $U + c$, which is the feature of an acoustic wave. In addition, P2 changes the static pressure when it passes by but an entropy wave only changes density. Thus P2 is an acoustic wave which is generated when the distortion-generated convected wave (entropy or vertical) impinges on the rotor. Similar phenomenon was also mentioned in [Greitzer et al., 2007] that the vorticity disturbance can generate acoustic

disturbance when it interacts with a cascade airfoil.

6.3.3 Reflection by the Sonic Front in Choked Nozzle

Upon reaching the sonic front in the nozzle throat, part of the incident wave is transmitted and travels toward the domain exit and part of it is reflected [Greitzer et al., 2007]. This phenomenon is illustrated schematically in Figure 6.16.

Figure 6.17 shows the simulated time history of three Riemann invariants at station B (marked in Figure 6.11a) which is just upstream of the sonic front. It can be seen in Figure 6.17 that the downstream propagating pressure wave δw_2 arrives at the sonic front and is reflected with approximately 75% of its amplitude as an upstream propagating acoustic wave δw_3 at $t = t_3$. The reflection of entropy wave δw_1 occurs at $t = t_4$, giving rise to another upstream acoustic wave shown by the step change in the amplitude of δw_3. It is evident from this plot that a significant amount of reflection is induced when the downstream propagating waves impinge on the sonic front, and the amplitudes of the reflections are of the similar level as the incident pressure waves.

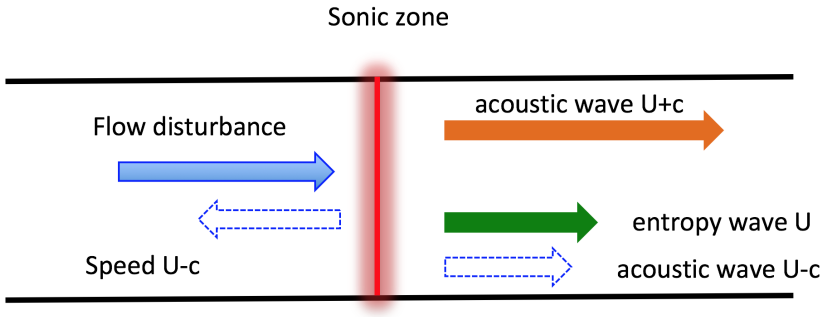


Figure 6.16: Wave transmission and reflection at the sonic front

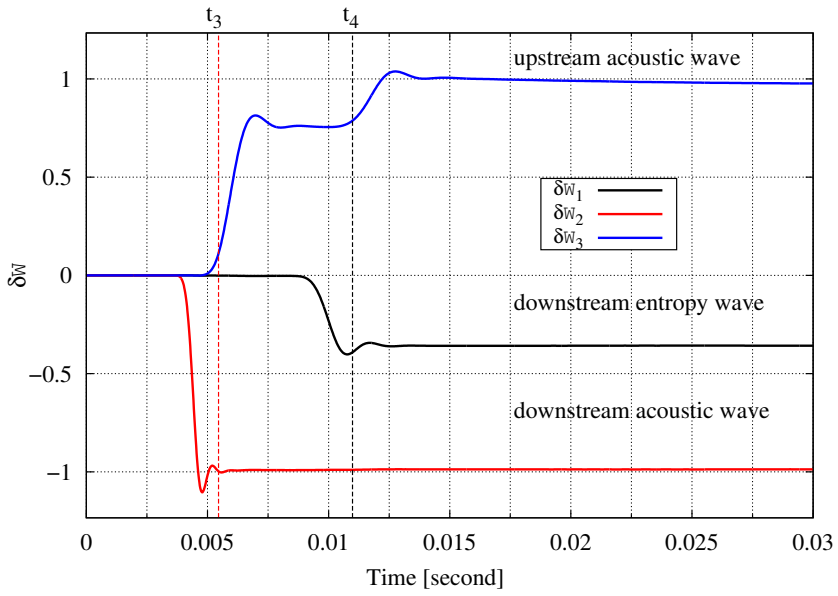


Figure 6.17: Time history of Riemann variables at station B

Figure 6.18 shows the time history of different physical flow variables at station B. It is observed that the reflections of distortion-generated acoustic wave δw_2 (at $t = t_3$) and entropy wave (at $t = t_4$) have similar impact on the flow field: both are expansion waves which reduce static pressure and density but increase axial velocity. The trends for the simple test case can be used to explain the observations for the case with short exit duct in Figures 6.7 and Figure 6.8. In Figure 6.7, it can be seen that the static pressure at stator trailing edge is reduced when R1 arrives. The arrival of R1 wave reduces the instantaneous loading of the compressor and postpones stall initiation. The mass flow increase at T_1 in Figure 6.8 is mainly due to the reduction of the loading. The direct contribution of R1 to the mass flow is neglectable.

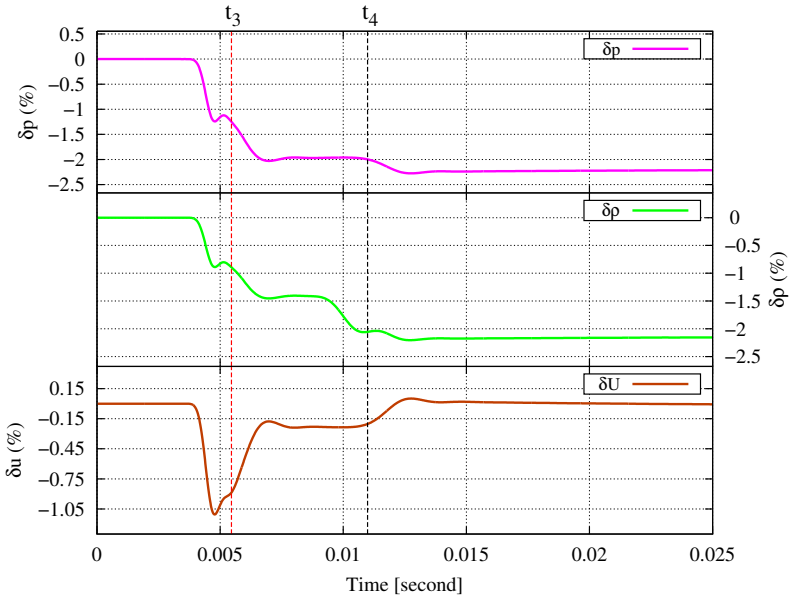


Figure 6.18: Time history of static pressure, density and axial velocity perturbations at station B

6.3.4 Reflection due to Geometry Change

The exit nozzle in aero-engines and experimental rigs usually operates unchoked. However, reflection can also occur due to the change in duct geometry, such as the area contraction at the exit nozzle. This type of reflection is studied in this section using Case 2 listed in Table 6.1 with an unchoked nozzle. Figure 6.19 shows the meridian view of the computational domain which has an area ratio of 0.76. The exit boundary is placed sufficiently far to avoid any numerical reflections for the time scales studied here.

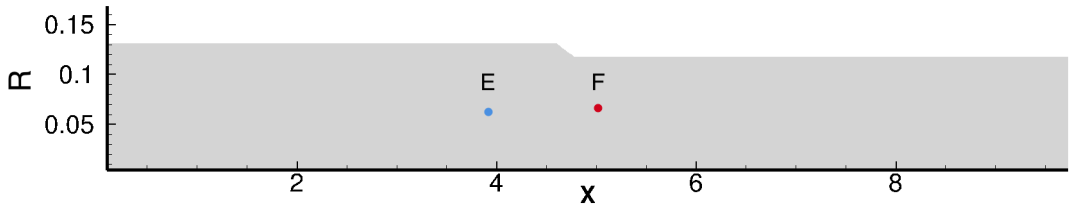


Figure 6.19: Meridian view of the exit duct and nozzle

Figure 6.20 shows the time histories of the Riemann invariants amplitude at stations E (solid line) and F (dash line). The location of these two stations is illustrated in Figure 6.19, where station E is just upstream of the nozzle while station F is just downstream of the nozzle. It should be noted that for the range of time shown in Figure 6.20, numerical reflections from the exit domain boundary has yet to reach stations E and F. This[2] is clearly indicated with the absence of any perturbations in δw_3 at station F. The following observations can be made from Figure 6.20:

• At time $t = t_1$, the distortion-generated pressure wave (which has propagation speed of $U + c$) arrives at station E.

• The wave is reflected at the nozzle and produces an upstream propagating acoustic wave passing station E at $t = t_2$. The reflection occurs due to geometrical change of the duct and has an amplitude of approximately 50% of the incident wave.

• At time $t = t_3$, the entropy wave generated by the inlet distortion arrives at station E.

• At time $t = t_4$, reflection of the entropy wave is detected at station E.

It is evident from these observations that duct geometry change at the nozzle results in reflection of similar order of magnitude with that caused by the sonic front.

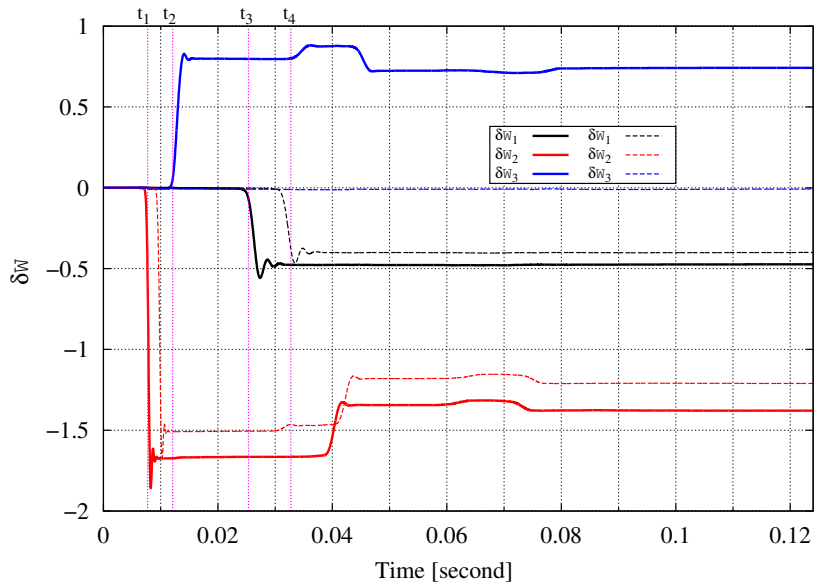


Figure 6.20: Time history of Riemann variables at station E (solid curves) and station F (dashed curves)

Figure 6.21 shows the time history of static pressure, density and axial velocity perturbations at station E. Similar to trends observed for Case 1 with the choked nozzle, expansion waves are reflected from the unchoked nozzle (at $t = t_2$) which contributes to the reduction in compressor back pressure.

[2]The numerical reflections are artificial and depend on the boundary treatment in each CFD code and therefore not considered here

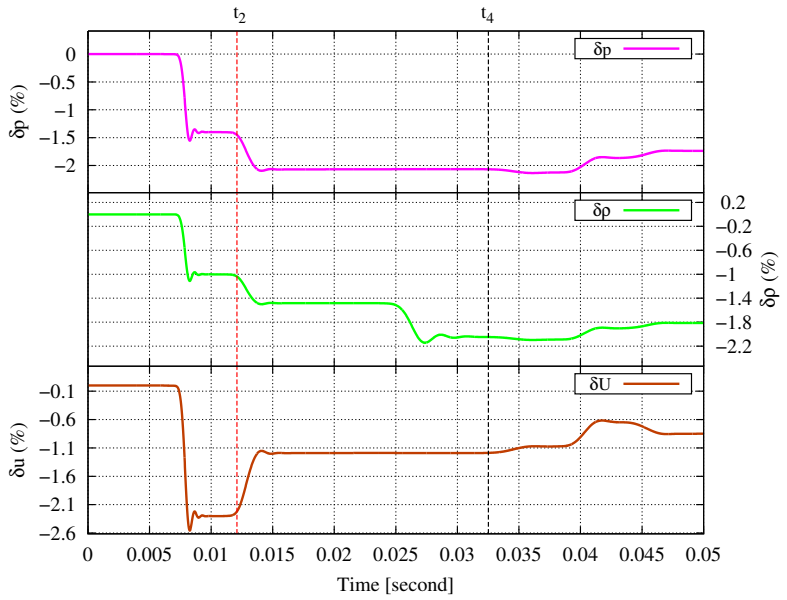


Figure 6.21: Time history of static pressure, density and axial velocity perturbations at station E

The exit duct and nozzle studied so far have simplified geometries as opposed to their real-life counterparts. In an aero-engine, the duct wall surface is usually smooth and the cross-sectional area of the duct varies slowly. Reflection from such geometries is subsequently investigated. Figure 6.22 shows the schematic for a computational model with a slow contracting nozzle. The nozzle throat area is kept the same as Case 2, so that the same mean flow is achieved upstream of the nozzle.

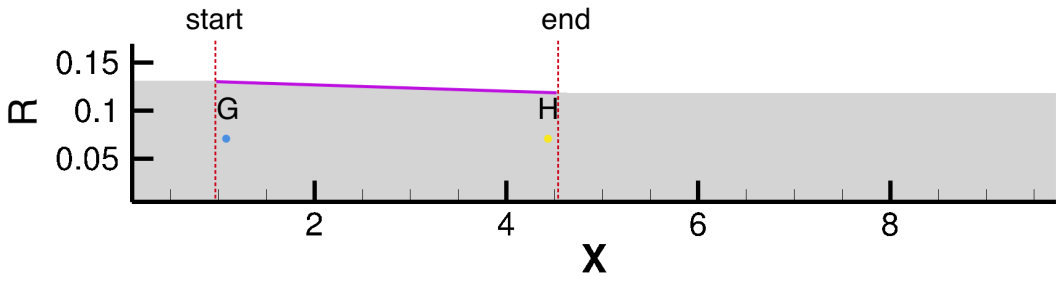


Figure 6.22: Meridian view of the slowly varying exit duct

Figure 6.23 shows the time history of the Riemann invariants at stations G (solid line) and H (dash line). It is seen that significant reflections are generated even though a smoothly varying duct geometry is used. Instead of a burst like reflections as observed in Figure 6.20, reflections in a slowly varying duct take place in a longer period of time as a result of longer axial length scale of the nozzle. Moreover, it is noticed that the final total amplitude of reflection (by $t = 0.06s$) is approximately 50% of the incidence, which is very similar to that observed in Case 2 (shown in Figure 6.20). The observations have two major implications: (1) the final state of the flow field upstream of the exit nozzle is determined by the nozzle area ratio and not by the cross section geometry; (2) variation in cross section geometry of the nozzle results in different dynamic

response in terms of acoustic reflection, which can vary from a short period burst to a long period continuous feedback. Nevertheless, dynamic response from the exit duct is evident regardless of the nozzle geometry.

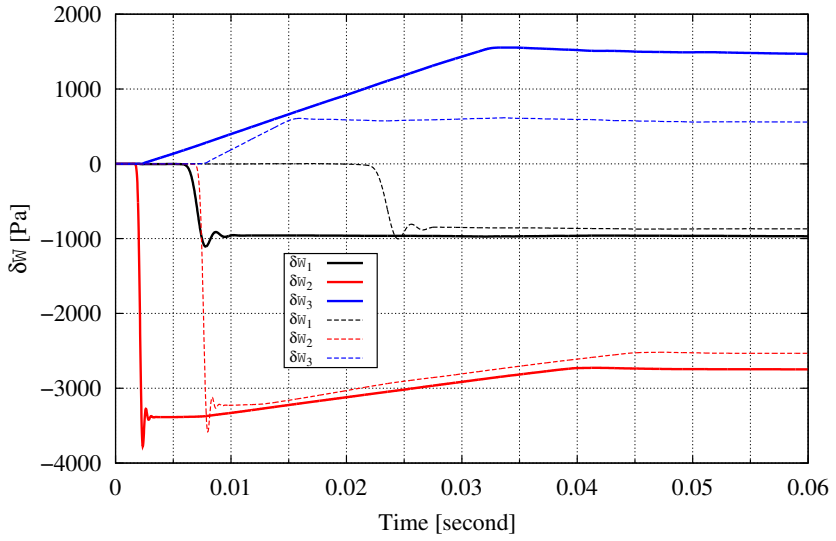


Figure 6.23: Time history of Riemann variables at station G (solid curves) and station H (dashed curves)

A typical choked nozzle has both shock wave and geometric change, this is common especially in military engines. One question that of interest is the ratio between the contributions of shock wave and geometric change in the reflected wave. This will be case dependent because the reflection of the shock wave is determined by strength from the shock wave and the extent of the change of the geometry affects the strength of the reflected wave. The reflected wave has an amplitude of approximately 75% and 50% of the incident wave in Case 1 and Case 2, respectively.

6.3.5 Compression System Geometry and Aerodynamic Stability

Further examination of Figure 6.7 indicates that the aerodynamic stability is dependent on the order of the following two events: the arrival of reflected wave R1 and the generation of compression wave P2. In this section, two different circumstances will be considered: (1) when the reflected wave R1 arrives at compressor trailing edge earlier than P2, the decrease in back pressure helps prevent the formation of stall cells in the rotor; (2) rotating stall has already fully developed when the reflected wave R1 arrives at the compressor exit much later than P2. In this case the exit duct needs to be long enough to delay the arrival of R1. The timing associated with these two events is determined by the flow conditions as well as the geometry (axial length) of the compression system. Estimation of this timing would allow one to evaluate the final state of the compressor, i.e. stable or rotating stall, due to dynamic response from the exit duct. To achieve this goal, a simplified model is built to derive the relations between the main flow parameters and axial length of the compression system. The model is illustrated schematically in Figure 6.24. The whole flow domain is decomposed into two parts. The first part starts from the inlet

surface and extend to the rotor trailing edge. The second part includes the stator and the exit duct. It is assumed that stall occurs in the rotor domain and thus the timing when reflected waves arrives at the rotor is more important. L_1 and L_2 are the axial length of the first part and second part respectively. U_x and c are the averaged axial velocity and local sound speed for the steady flow solution. For the first circumference, the following equation must be satisfied to ensure the simultaneous arrival of the P2 and the R1 at the rotor trailing edge:

$$\frac{L_1}{U_{x1}} = \frac{L_1}{c_1 + U_{x1}} + \frac{L_2}{c_2 + U_{x2}} + \frac{L_2}{c_2 - U_{x2}} \tag{6.11}$$

which simplifies to

$$L_2 = L_1 \cdot \frac{c_2^2 - U_{x2}^2}{U_{x1}(c_1 + U_{x1})} \cdot \frac{c_1}{2c_2} \tag{6.12}$$

The flow parameters are substituted and a critical length ratio between L_1 and L_2 can be obtained. For the initial solution of NASA stage 67 (black dot in Figure 6.3), the critical length ratio of L_2 to L_1 is:

$$L_2 = 0.76L_1 \tag{6.13}$$

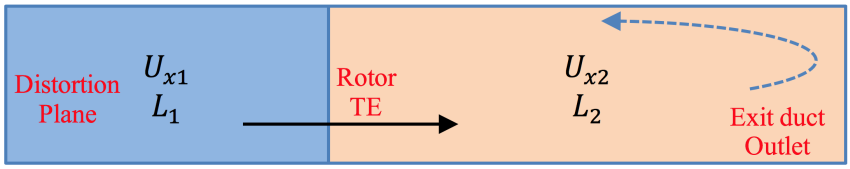


Figure 6.24: Schematic illustration of the simple model

When the length of exit duct (L_2) is shorter than the critical value ($0.76L_1$), the reflected wave R1 arrives at the rotor before compression wave P2 is generated, which prevents the stalling of compressor.

This is justified by the unstalled case with short exit duct whose length ratio of L_2 to L_1 is 0.6, and the stalled case with long exit duct whose length ratio of L_2 to L_1 is 1.6. It is worth noting that Equations 6.12 introduced here is an approximate classification of whether the duct(s) connected to the compressor is beneficial or detrimental to its aerodynamic stability, due to sudden appearance of inlet distortion.

The 2^{nd} condition required for the compressor to become unstable is that the exit duct is long enough, such that the stall cell has fully formed by the time the reflected wave returns to the rotor. The time for the stall cell to develop can be estimated as the time it takes for the distortion (the vortical and entropic waves) to reach the rotor, plus the time it takes the initial separated flow region, which was formed in the distorted region, to complete one revolution. This is because the separated flow develops into a fully developed stall cell when it enters the distorted region again (as shown earlier). Assuming that the speed of a mature stall cell is 50% of the rotor speed, 2 rotor revolutions is sufficient to guarantee fully developed stall before the reflections from the exit nozzle arrives at the rotor. For the stage 67 computations performed

here, it takes 2 revolutions for a mature stall cell to form as indicated in Figure 6.7 and Figure 6.8. The above finding is in agreement with a similar experimental study of [Perovic et al., 2015]. Under such conditions, the acoustic reflection from the nozzle will have no influence on the rotor stall inception process. Thus the influence of acoustic reflection can be ruled out if the length of the exit duct is larger than the critical value given by

$$\frac{L_1}{U_{x1}} + 2 \cdot t_{rev} = \frac{L_1}{c_1 + U_{x1}} + \frac{L_2}{c_2 + U_{x2}} + \frac{L_2}{c_2 - U_{x2}} \tag{6.14}$$

$$L_2 = \frac{c_2^2 - U_{x2}^2}{2c_2} \cdot [\frac{L_1 \cdot c_1}{U_{x1}(c_1 + U_{x1})} + 2 \cdot t_{rev}] \tag{6.15}$$

In equation 6.15, t_{rev} denotes the time for one rotor revolution. For the case studied the critical length of the exit duct is:

$$L_2 = 1.88 L_1 \tag{6.16}$$

This length corresponds to 3.77D.

6.3.6 Influence of the Exit Duct Length on Stall Margin with Clean Inflow

Another question which needs to be answered is whether the length of the exit duct still influences the stall margin for a clean inflow. In this section, two Stage 67 unsteady computations with clean inlet but with different exit duct lengths (1.5D and 4.5D) were carried out. The computations start from the same steady state solution. Figure 6.25 shows the mass flow history of the two cases when the downstream nozzle is slightly closed from the steady state model. Both cases have the same initial mass flow as the length of the exit duct does not affect the operating condition of the fan when it is stable. Again, the case with shorter exit duct (1.5D) converges to a stable solution while the case with longer exit duct (4.5D) falls into rotating stall.

In this case, an acoustic wave travelling upstream is produced when the nozzle is closed. Most of the underlying mechanisms are similar to the one described above but a brief description of the wave propagation process within the exit duct is nevertheless discussed here. The same method as used for Figure 6.7 is used to generate the circumferentially averaged static pressure history at the mid-span of the exit duct and it is plotted as Figure 6.26. The whole process can be described as follows:

• When the nozzle is closed, a pressure wave (P1) is generated which propagates upstream in both cases. It increases the static pressure as it passes through the exit duct. The mass flow is reduced when this wave hits the stator vane at $t = T_0$ in the case with short exit duct and $t = T_2$ in the case with long exit duct, as shown in Figure 6.25.

• Immediately after, two reflected waves (R1 and R2) which travel faster than P1 appear in the exit duct and propagate downstream towards the nozzle. R1 is produced due to the interactions between P1 and the stator and R2 results from the interaction between P1 and the rotor. It can be seen in 6.26 that both R1 and R2 reduce the pressure as they pass by. Moreover, R1 increases the mass flow for a short instance (at $t = T_1$ for the case with short exit duct and $t = T_4$ for the

case with long exit duct) as shown in Figure 6.25. R2, on the other hand, decreases the mass flow at $t = T_3$ for the case with short exit duct and $t = T_6$ for the case with long exit duct.

• When the wave R1 arrives at the nozzle, another reflected wave is generated which is very weak and hard to distinguish on this plot. However, the reflected wave R3, which is due to the interaction of wave R2 and the nozzle is stronger and moves upstream towards the fan.

• In accordance with the observation in Figure 6.26, for the shorter exit duct R3 arrives at the fan at $t = T_5$ which reduces its back pressure, hence the fan can stabilise. While for the longer exit duct the reflection arrives at a later time of $t = T_7$ and is not able to stabilise the fan, and it falls into rotating stall. At time $t = T_7$ the flow separation on the blades starts to grow in the case with long exit duct. The dark blue region after the 8^{th} rev ($t = T_8$) indicates the low static pressure caused by rotating stall. It can be seen that 2 revolutions are needed for the case with longer exit duct to stall after R2 appears.

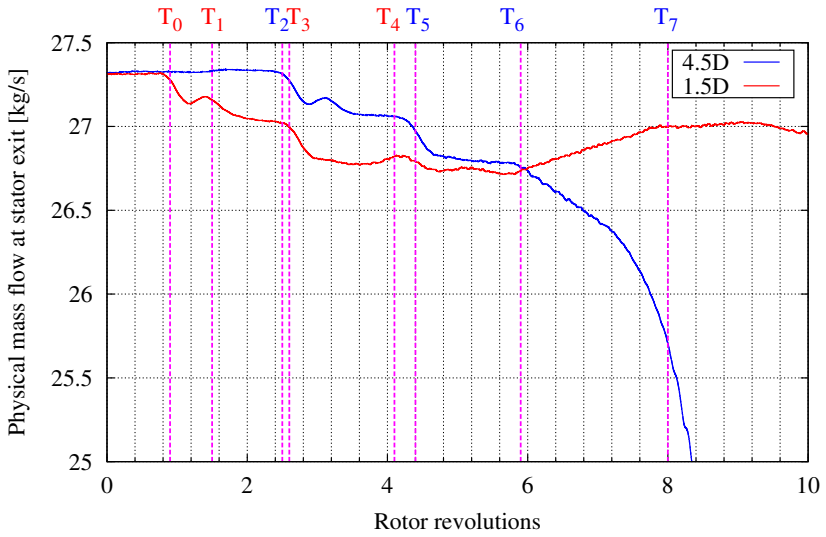


Figure 6.25: Time history of the mass flow at the stator exit

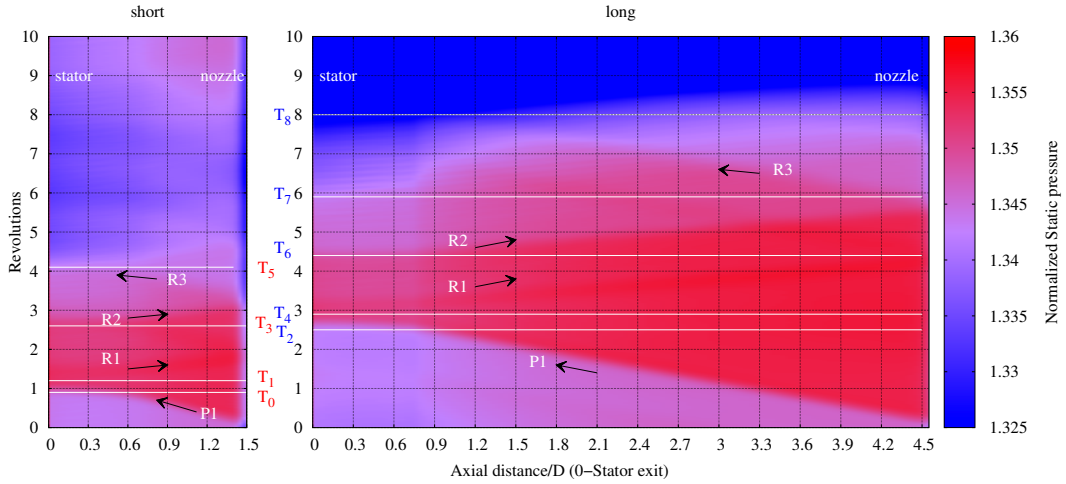


Figure 6.26: Time history of static pressure axial profile at middle span in the short (left) and long (right) exit duct

Estimating the critical length of the exit duct in clean flow is more difficult than in the case with inlet distortion because it is difficult to accurately predict the time needed for stall inception. However, the propagation time of the waves in the exit duct can still be accurately calculated. With a long exit duct, the stall inception takes place at $t = T_7$ in Figure 6.26. It is assumed that the compressor is stable if the reflection wave R3 can reach the rotor before T_7. If the exit duct is long and R3 arrives at the rotor later than T_8 (when the rotating stall has matured), the compressor will irreversibly stall. For the condition under which the compressor is stable:

$$T_7 - T_6 = \frac{L_2}{a_2 + U_{x2}} + \frac{L_2}{a_2 - U_{x2}} \tag{6.17}$$

And the compressor will stall when the length of the exit duct satisfies the following equation:

$$T_8 - T_6 = \frac{L_2}{a_2 + U_{x2}} + \frac{L_2}{a_2 - U_{x2}} \tag{6.18}$$

6.4 Chapter Summery

To assess the aerodynamic stability of fan blades due to distortions, rig tests are usually carried out to establish the stall margin. In such test campaigns, an exit duct (which is followed by a nozzle) is placed downstream of the fan blade and the operational condition of the fan is controlled by this nozzle. In this chapter the interaction mechanism of abrupt inlet distortion, exit duct reflection and compressor stability is investigated. To the best of the author's knowledge, this is the first time that the length of the exit duct is shown to be influential on the rotor stall margin. In the simulation of NASA stage 67, the stall margin can vary 3 % when the exit ducts of different lengths were used. The observed process is as following: abrupt distortion causes two different pressure waves propagating downstream to the nozzle. These waves interact with the nozzle and produces expansion waves and move back to the fan. The stability/instability of the fan is linked to the arrival of expansion wave. Early arrival of this expansion wave contributes to a decrease in

the compressor back pressure, thus preventing the initiation of stall. The dominant component of the waves travelling in the exit duct is the planar wave. Effects of higher circumferential harmonics are negligible. Thus, such wave reflection phenomenon is general and irrelevant to the distortion pattern.

To investigate the underlying physics of the interaction, analyses were carried out using both analytical methods and simplified CFD models, which can accurately predict the propagation of waves and thus the timing at which they arrive at the compressor. It was proved that both the sonic front and the geometry variation in the nozzle contribute to the reflection of waves. Reflection also occurs with smooth varying ducts and the accumulative amplitude of reflection depends on the area ratio only. However, the effects of such continuous reflection on stall margin of the compressor was not studied.

Based on above analysis and the stall simulation results, a quantitative critical length ratio of the compression system is introduced. This length relation determines whether a duct setup would have beneficial or detrimental effects on compressor aerodynamic stability. It can be evaluated using 1-D analytical methods without time-accurate simulation.

In the last section of this chapter, it was shown that the length of the exit duct influences the fan stall margin for the clean inflow. These results indicate that the dynamic wave propagation in the downstream components of the compressor can generally influence its stall margin, which can provide useful instructions in the test rig and engine design.

7 Performance of the Boundary Layer Ingesting Fan

In the previous chapters, the effects of DC120 distortion on the fan performance were investigated. However, the configuration of DC120 is relatively simple when compared with real inlet distortion, such as generated by the S intake ahead of the fan in a BLI propulsion engine. In this chapter, an S intake is installed in front of NASA stage 67 to explore the performance of the fan and the interactions between the fan and the intake. In the test cases with DC120 the distortion configuration and strength were fixed and did change with fan operation. In this chapter the operational condition of the fan can modulate the flow within the S intake which means the distortion upstream of the fan can be changed. In addition, the conclusions obtained with DC120 are also inspected to see if they are consistent with complex distortion patterns.

7.1 Computational Domain with S Intake

Figure 7.1 shows the computational domain of the simulations with S intake. The design of the S intake is based on the prototype of Inlet A in [Berrier et al., 2005]. The main geometry parameters of the intake are shown in Figure 7.2. The cross section of the inlet surface is semi-circular and the exit surface is a circle. NASA stage 67 is attached to the S intake. The original spinner was shortened to reduce the distance between the fan and the exit of the S intake, as shown in Figure 7.3. Station 1 in the figure represents the exit surface of the S intake and station 2 is the rotor inlet surface in the computational domain. The length of the exit duct is 1.5 times of the rotor diameter (D), which the same as the cases used in chapter 4.

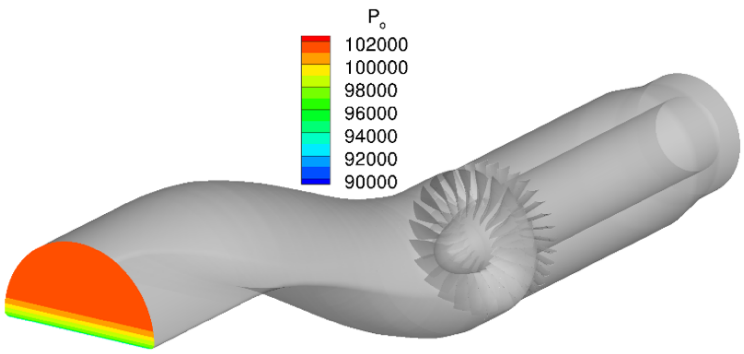


Figure 7.1: Computational domain of the NASA stage 67 with S intake

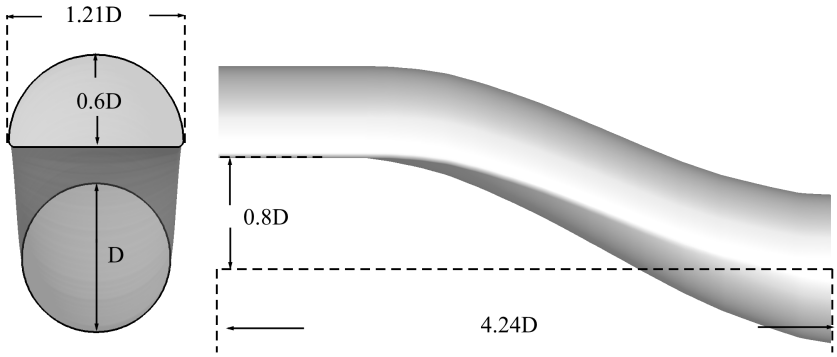


Figure 7.2: Main geometry parameters of the S duct (normalized by the rotor diameter D)

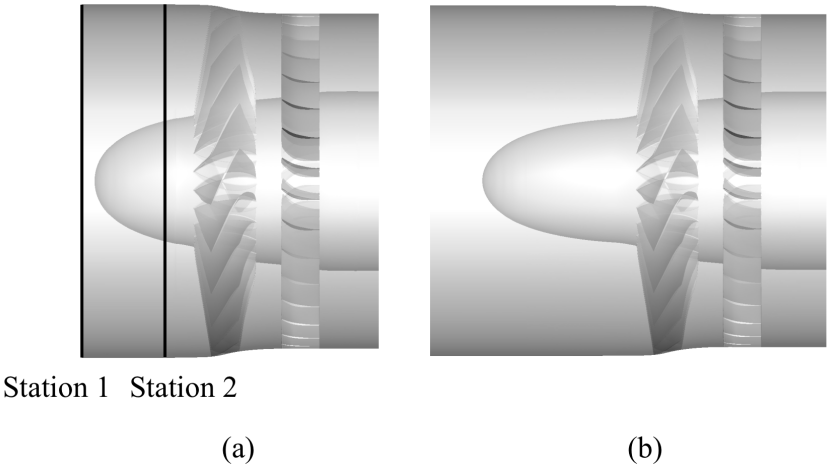
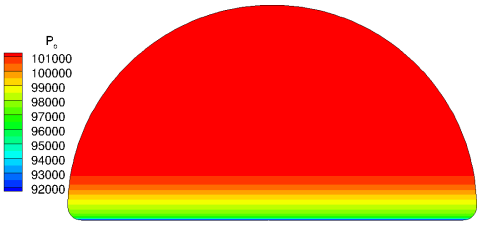
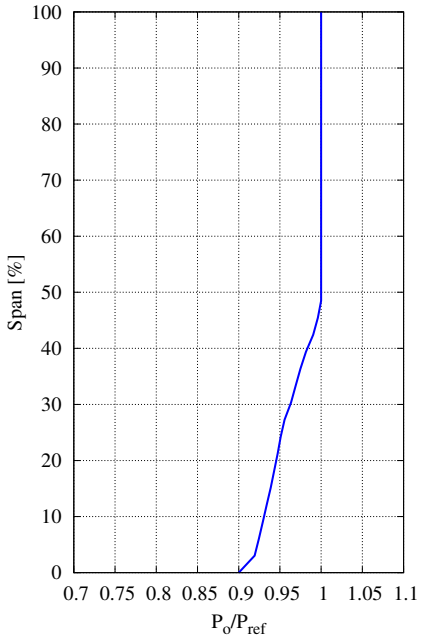


Figure 7.3: Comparisons of the nose geometry: (a) original and (b) shorted

The total pressure contour at the inlet surface of the S intake is plotted in Figure 7.4a (which is a function of inflow Mach number) is obtained from [Berrier et al., 2005]. The largest total pressure loss is 10% of the main stream value near the hub which extends 40% height upwards from the hub, as shown in Figure 7.4b. Such pattern is used to mimic the thick boundary layer accumulated on the fuselage of the airplane. During the whole computation, the boundary layer pattern at the inlet is fixed. Due to the duct turning as well as the cross-section area change along the centre line, secondary flow will develop as the flow passes through the S intake. As a result, the fan downstream of the intake will see a combination of the total pressure deficit caused by the ingestion of the boundary layer as well as the swirl flow induced by the duct geometry change. The nozzle downstream of the fan stage is choked. The temporal resolution used is 2,200 time steps/rev in the time-accurate computations.



(a)



(b)

Figure 7.4: (a) Contour of the total pressure (b) Radial distribution of the total pressure at the inlet surface of the S intake

The computational domain for the steady solution is composed of the S intake, a single-passage rotor, a single-passage stator and an exit duct with a nozzle. Mixing planes are used between different components and periodic boundaries are applied for the single-passage domains. For the full-annulus computations, sliding planes are adopted. By gradually throttling the nozzle, the steady characteristic of the stage is obtained and plotted in Figure 7.5. The results of time-accurate simulations with full-annulus domain is plotted as blue circles. It can be seen that the steady computations can accurately capture the near stall performance as well as the stability boundary. Also shown in this figure is the undistorted characteristic of NASA stage 67 with straight intake (Chapter 3). While the corrected choked mass flow for both cases are similar, it can be seen that the stage suffers a large loss in the operational mass flow range with the S intake. The isentropic efficiency of the stage with the S intake sees a considerable drop of 2.6%. It is also observed that the total pressure ratio is nearly the same for both cases at the same corrected mass flow.

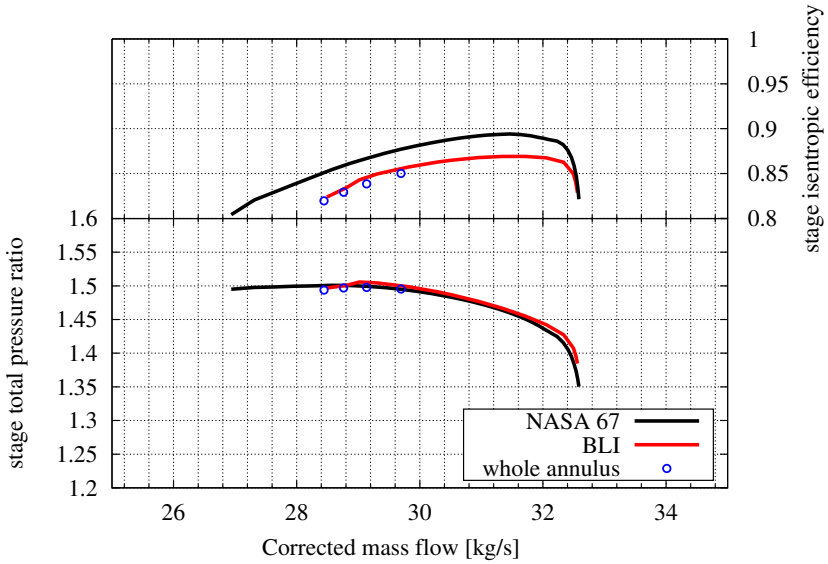


Figure 7.5: Compressor map of NASA stage 67 with straight intake and S intake

7.2 Analysis of the Distortion Pattern

The distortion pattern upstream of a BLI fan is very complex and thus a detailed analysis can assist interpreting its influence on the fan. The test case of stage 67 with S intake at NS condition (corrected mass flow of 28.8 kg/s) is taken as an example. The focus are the total pressure distortion and swirl distribution. Figure 7.6a shows the total pressure contour at the rotor inlet (station 2 in Figure 7.3). Similar flow patterns can be found in [Berrier et al., 2005, Giuliani et al., 2014]. In this case, the total pressure contour can be divided into 3 parts radially: Zone 1, Zone 2 and Zone 3. Figure 7.6b plots the contour of the circumferential flow angle at the rotor inlet. Negative value denotes that the direction of the swirl angle is opposite to the fans rotation and the fan sees higher incidence. The distribution of the radial flow angle at the rotor inlet is plotted as Figure 7.6c in which the positive direction is from hub to tip. Figure 7.6d shows the pattern of the vortices upstream of the fan using $Lamda - 2$ vortex criterion. Detailed analysis is as following:

• In Zone 1(the annulus between the hub and 60% span), the total pressure distribution is almost uniform and there is a small total pressure loss at the lower annulus. This is also confirmed by the circumferential total pressure profile (solid lines are for NS condition and dashed lines are for PE condition) of 10% span and 50% span from the hub in Figure 7.7. The magnitude of the circumferential angle and radial flow angle are large, as shown in Figure 7.6b and Figure 7.6c. In Figure 7.8 it can be seen that the profile of the circumferential angle at 10% span and 50% span resembles a sinusoidal wave with a peak value of 10 degrees. The circumferential flow is mainly caused by the pressure gradient between Zone 1 and the lower-pressure region in Zone 2. The secondary flow inside the S intake also contributes to the formation of the circumferential and radial flow. In Zone 1, the radial flow migrates from hub to tip. It results from the downward turning of the S intake (the flow thus moves downwards along the curvature of the duct) as well

as the diversion effect of the spinner (the flow moves along the spinner surface centrifugally).

• In Zone 2 (the annulus between 60% span and 85% span), both the circumferential angle and radial angle decrease compared to those in Zone 1. The circumferential distribution of the total pressure comprises of a higher total pressure region at the upper annulus and a lower total pressure at the lower annulus. This lower total pressure region evolves from the boundary layer at the inlet of the S intake. According to the circumferential total pressure distribution at 75% span in Figure 7.7, the distorted region occupies a circumferential sector of around 120 degree with a 4% total pressure loss, which resembles a DC120 pattern. Moreover, the total pressure loss increases at higher span.

• In Zone 3 (the annulus between 85% span and the casing), the total pressure distribution is very similar to that in Zone 2. The upper annulus has higher total pressure and the lower annulus has a total pressure deficit of 120 degree, as shown by the circumferential total pressure curve at 98% span in Figure 7.7. The total pressure loss is about 8% in the sectors between 0∼120 degree and 240∼360 degree and is about 11% in the sector between 120∼240 degree. The radial flow angle is relatively small but it exits in the whole upper annulus, as shown in Figure 7.6c. The pattern of the circumferential angle is complex in this zone, as shown in Figure 7.6b and Figure 7.7. Such a swirl angle distribution is induced by the radial flow in Zone 1. The radial flow moves downwards and it is dispersed to both sides when hitting the bottom of the duct. This generates two regions with opposite rotating vortices at about 120 degree and 230 degree near the casing. This is also clearly shown by the $Lamda - 2$ method illustrated in Figure 7.6d.

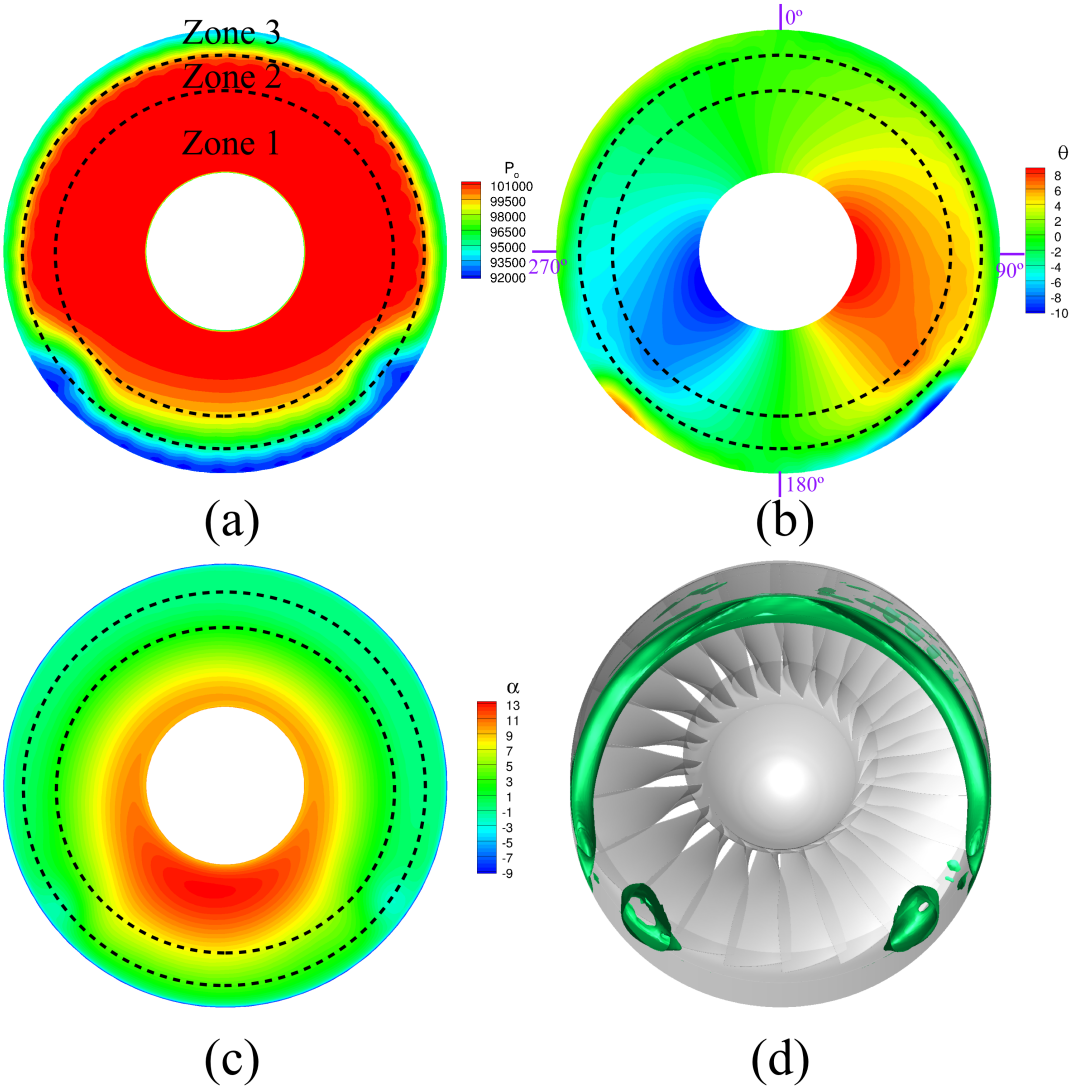


Figure 7.6: Flow pattern at NS condition at the exit of the S intake: (a) total pressure contour, (b) swirl angle, (c) radial angle (d) vortex pattern upstream of the rotor

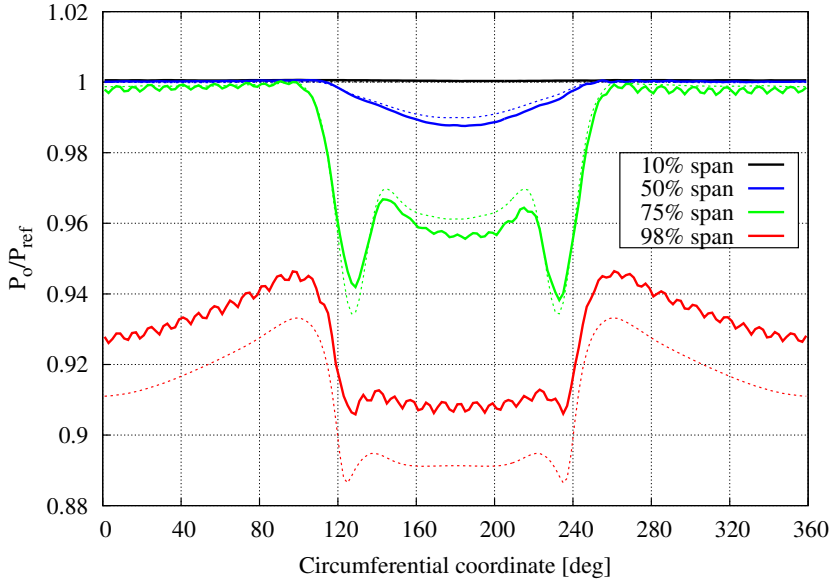


Figure 7.7: Circumferential Total pressure profile at different radial positions (NS - solid line and PE - dashed line), rotor inlet (circumferential coordinate is marked in 7.6b)

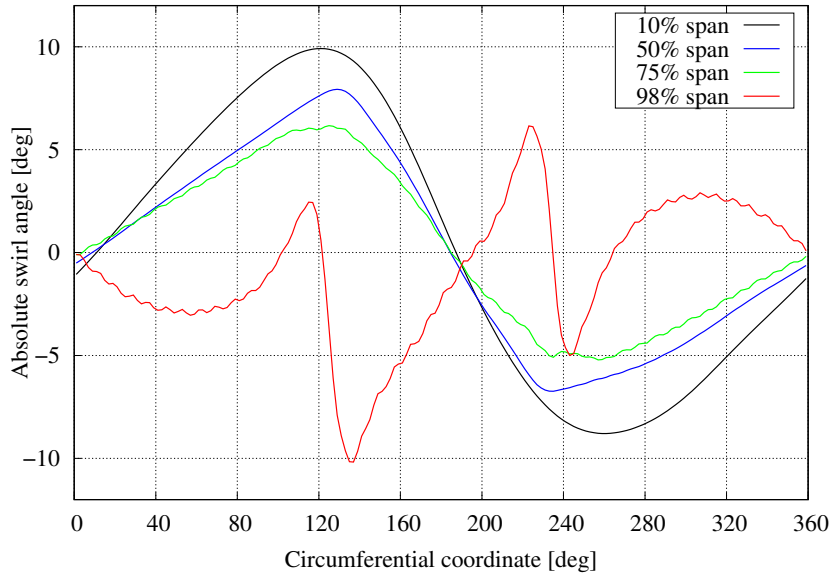


Figure 7.8: Circumferential swirl angle profiles at different radial positions at NS condition, rotor inlet

7.3 Coupling between the S Intake and the Fan

In this section, how the BLI distortion influences the operation of the fan is analysed. As indicated in Figure 7.5, the stage with S intake have the same total pressure ratio but lower efficiency than that with the straight intake at the same corrected mass flow. To explain this observation two cases are selected to compare the operational conditions of the stage. Both cases have the same corrected mass flow of 28.8 kg/s and a total pressure ratio of 1.50. The total pressure ratio

and efficiency of both cases are listed in Table 7.1. Figure 7.9 demonstrates the circumferential-averaged radial profile of the total pressure ratio (calculated as the ratio of total pressure at the rotor TE to the LE of the same span) in the full annulus time-accurate computation. It can be seen that the distortion created by the S intake obviously changes the loading distribution of the blade and its overall effects vary radially. Consequently, the radial distribution of the total pressure can also be divided into three zones of the same range in Figure 7.6a:

• In Zone 1, the loading distribution differs along the span between the two cases but the averaged total pressure ratio is almost the same.

• In Zone 2, the total pressure ratio of the rotor with S intake has higher value and the discrepancy increases at higher span.

• In Zone 3, the case with S intake has larger total pressure increment. As the fan with S intake has obviously higher loading, the fan stalls at larger corrected mass flow.

The inflow is purely axial in the case with straight intake while large swirl angle variations exit ahead of the rotor with the S intake. As can be seen in Figure 7.6a, the circumferential swirl angle around the annulus in Zone 1 and Zone 2 is almost symmetric with respect to the x-axis, which implies that the averaged swirl angle is nearly zero. Therefore, the magnitude of circumferential averaged total pressure ratio is similar to the case with straight intake.

Table 7.1: Total pressure ratio and isentropic efficiency of the cases with straight intake and S intake

	Rotor P_o ratio	Stage P_o ratio	Rotor efficiency	Stage efficiency
Straight intake	1.52	1.5	89.3%	86.1%
S intake	1.54	1.5	88.7%	83.4%

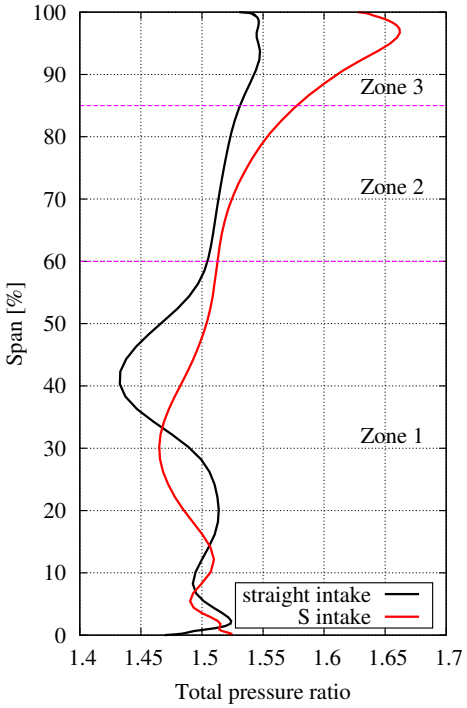
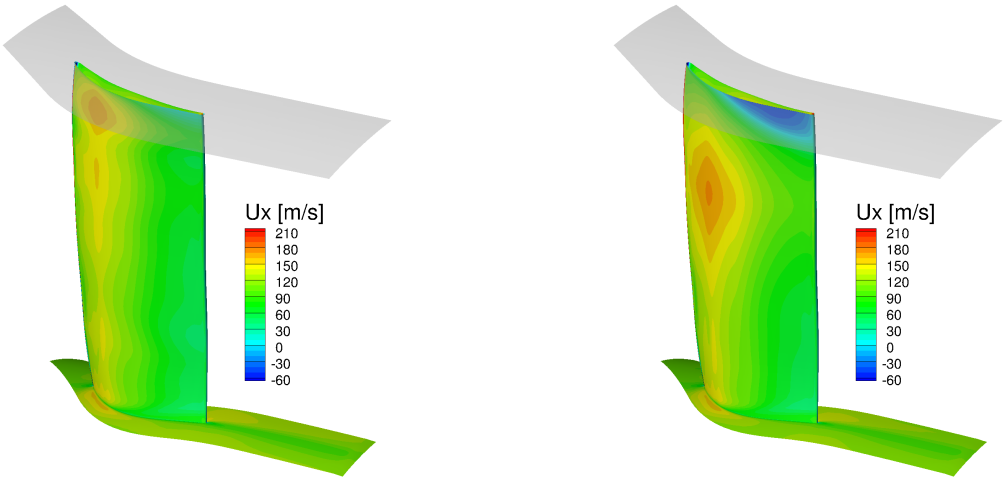


Figure 7.9: Circumferential averaged radial profile of the rotor total pressure ratio

Based on the results in Table 7.1, it can be concluded that the main flow loss of the stage with S intake occurs in the stator. Figure 7.10 shows the axial velocity contour on the suction surface of the stator in the steady computations for both cases. As can be seen, flow separation occurs in the tip region of the stator with S intake due to the large incidence angle at the rotor exit, as plotted in Figure 7.11 where the circumferential flow angle ahead of the stator tip is higher in the case with S intake. While the rotor can still obtain considerable pressure rise with inlet distortion, the stator should be re-designed to reduce the flow loss. A plausible method to tackle the circumferential distortion is the asymmetric stator design in [Gunn and Hall, 2017].



(a) (b)

Figure 7.10: Comparisons of the axial velocity of on the stator with (a) straight intake and (b) S intake

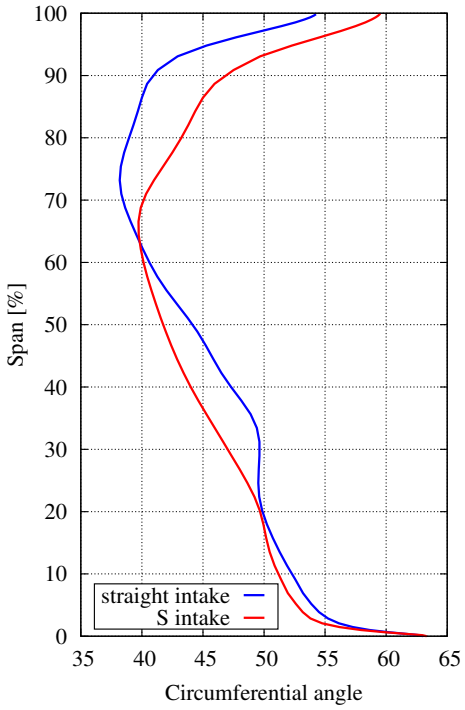
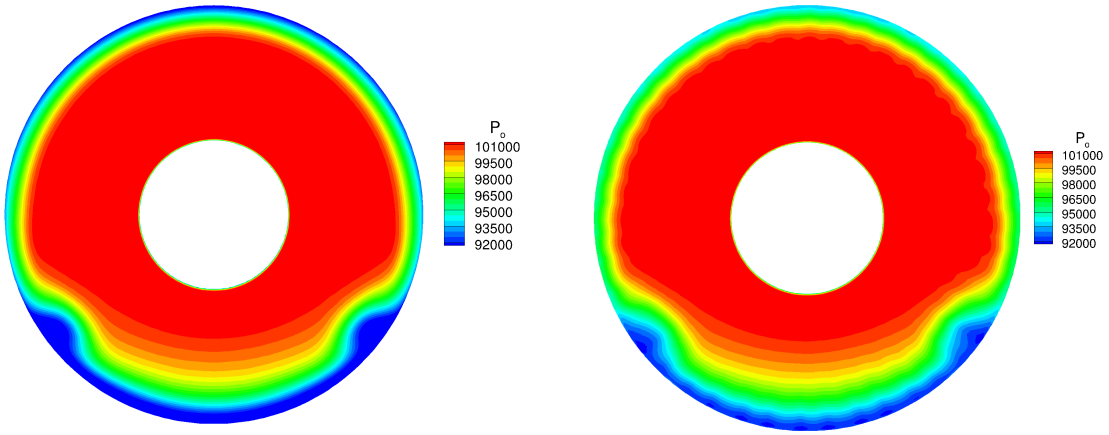


Figure 7.11: Radial profile of the inflow circumferential angle at stator inlet

Above analysis demonstrates how the flow in the S intake influences the operational condition of the fan. In the following part, how the operating condition of the fan affects the flow field in the S intake is briefly discussed. The PE condition (corrected mass flow=31.3 kg/s) and NS condition (corrected mass flow=28.8 kg/s) are chosen and the total pressure contour at the inlet of the rotor in two cases are plotted in Figure 7.12. It can be seen that the total pressure loss

is slightly higher at PE condition near the casing in Zone 3. The total pressure contour in Zone 1 and Zone 2 is not affected by operating condition of the rotor. This finding is also confirmed in Figure 7.7. It was experimentally shown in [Berrier et al., 2005] that the thickness of the boundary layer increases with inlet Mach number, which leads to larger distortion magnitude near the casing. The corrected mass flow of the fan has little influence on the total pressure at 10% span and 50% span. At 75% span, the distorted region of PE has a slightly lower total pressure while the circumferentially averaged value is almost the same. At 98% span, the total pressure loss is 2% higher at PE condition. This demonstrates that as the compressor is pushed nearer to the stall boundary, the flow loss inside the S intake decreases and the distortion strength upstream of the rotor is decreasing.



(a) (b)

Figure 7.12: Total pressure contour at the rotor inlet of (a) PE and (b) NS

The influence of the fan on the S intake can be stronger when the fan falls into rotating stall. Figure 7.13 shows the stall cell can cause blockage to the flow inside the S intake when the stall cell is at different circumferential positions. Difference in the axial velocity distribution can be observed by comparing the regions with dashed circles.

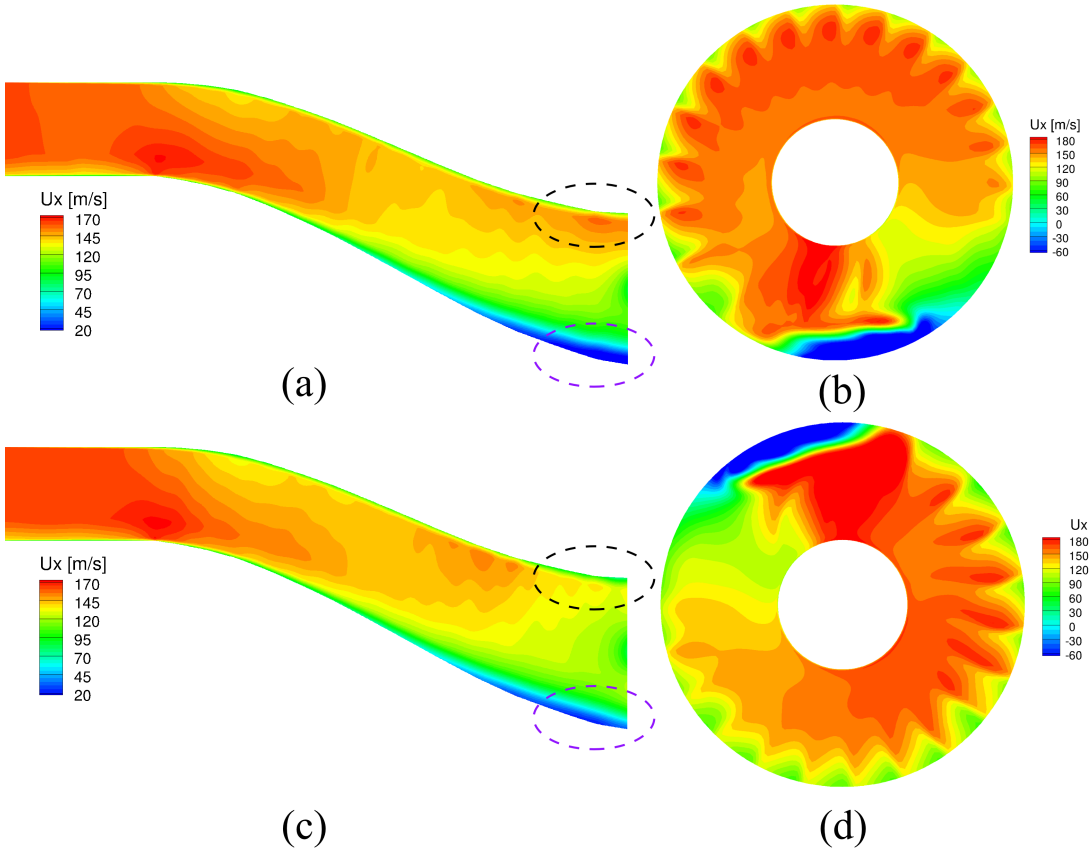


Figure 7.13: Meridian contour of the axial velocity in the S intake with stall cell at lower annulus:(a) and (b), stall cell at upper annulus: (c) and (d)

7.4 Stall Process of the BLI Fan

Before the stall process is investigated, the performance of the fan at NS condition was inspected. Figure 7.14 shows the contour of the axial velocity at 98% rotor span. In general, flow separation occurs on the blade when it enters the low-pressure region and the separation is removed when it enters the high-pressure region. This finding is exactly the same with that in Chapter 4. The only difference is that when the blade moves out of the distorted region, the blade separation is literally strengthened though the total pressure in this position is higher (as shown by the passages with dashed circle). However, in Figure 4.5 the separation is instantaneously reduced at the same circumferential position. This is due to the positive swirl upstream of the rotor in this region which is between 260∼360° in Figure 7.8, which leads to a larger incidence in the blade tip and hence postpones the recovery of the blade.

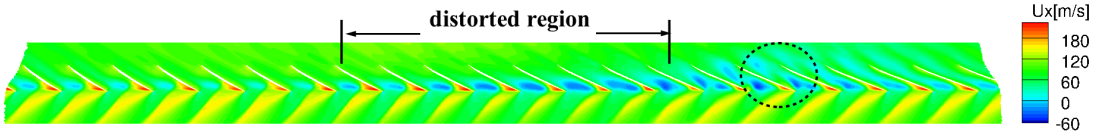


Figure 7.14: Axial velocity contour at 98% span

Orbit method was also used to show the operational condition of the blade around the annulus, as shown in Figure 7.15. Different with Figure 4.6, the orbits here is less scattered on the compressor map due to two reasons: (1) the circumferential total pressure difference within Zone 1 and Zone 2 are very small and the corrected mass flow difference around the annulus is reduced; (2) though the swirl angle upstream of the rotor in Zone 1 and Zone 2 is slightly higher than that in Figure 4.6, it is smaller in Zone 3 (not shown here) where the pressure ratio is higher, so there is no obvious corrected speed change in the orbits when compared with Figure 4.6.

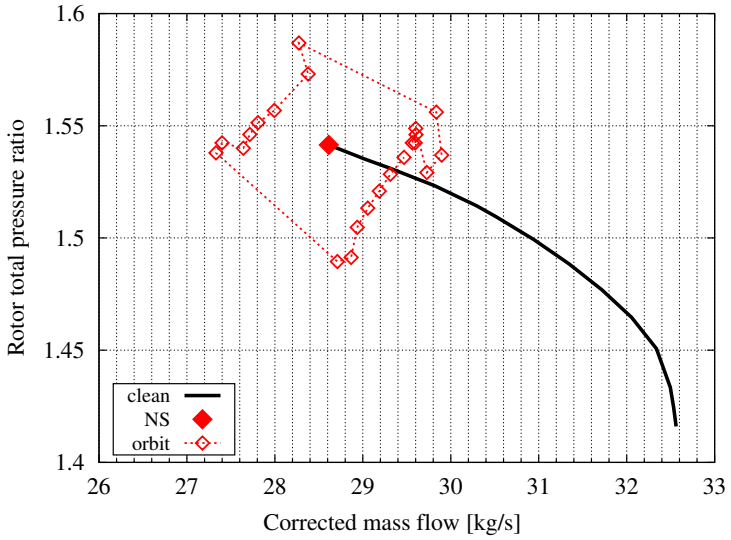


Figure 7.15: Orbits of the BLI fan at NS condition

The fan is pushed into rotating stall as the downstream of the nozzle is gradually closed. Figure 7.16 shows the mass flow history at the rotor exit. The mass flow fluctuation results from the interaction between the stall cell and the S intake.

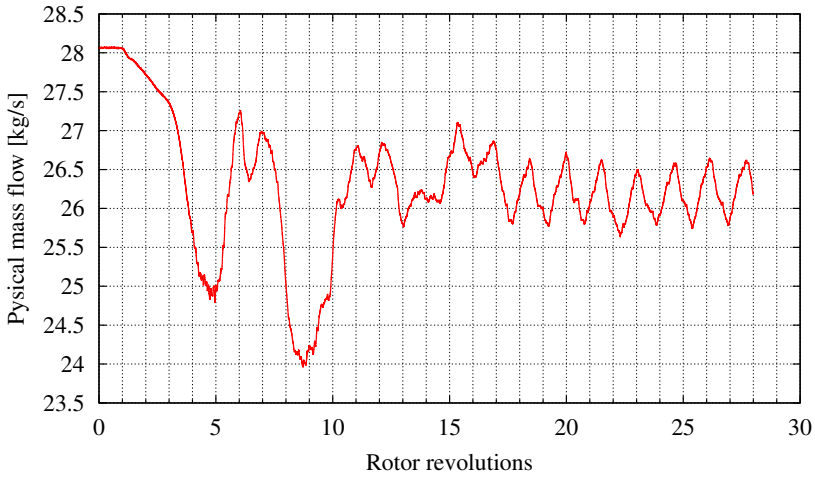


Figure 7.16: Physical mass flow at the rotor inlet

Figure 7.17 demonstrates the stall process of the fan with the contour plot of the axial velocity at 98% rotor span. The plot is in the stationary frame and the rotor rotates from left to right. The downstream nozzle is slightly closed at $t = 0$ rev. It can be seen that at the 2.5^{th} rev, the flow separation on the blade in the distorted region grows larger due to the reduced mass flow. When the separation fails to be removed by the clean flow region and it enters the distorted region again at $t = 3.0$ rev, the separation develops rapidly and rotating stall occurs at $t = 3.5$ rev. Initially, the stall cell occupies nearly all the tip region around the annulus ($t = 4.0$ rev), but it shrinks circumferentially and expands axially as shown at $t = 5.0$ rev. At $t = 17.0$ rev in Figure 7.17, the solution converges and only one stall cell exits in the flow field. Though the distortion pattern caused by the ingestion of the boundary layer is more complex than a DC120 distortion, the whole stall process is very similar with the Case 2 in Chapter 5, which further confirmed the conclusions obtained in the former chapters can be applied to real distortion patterns.

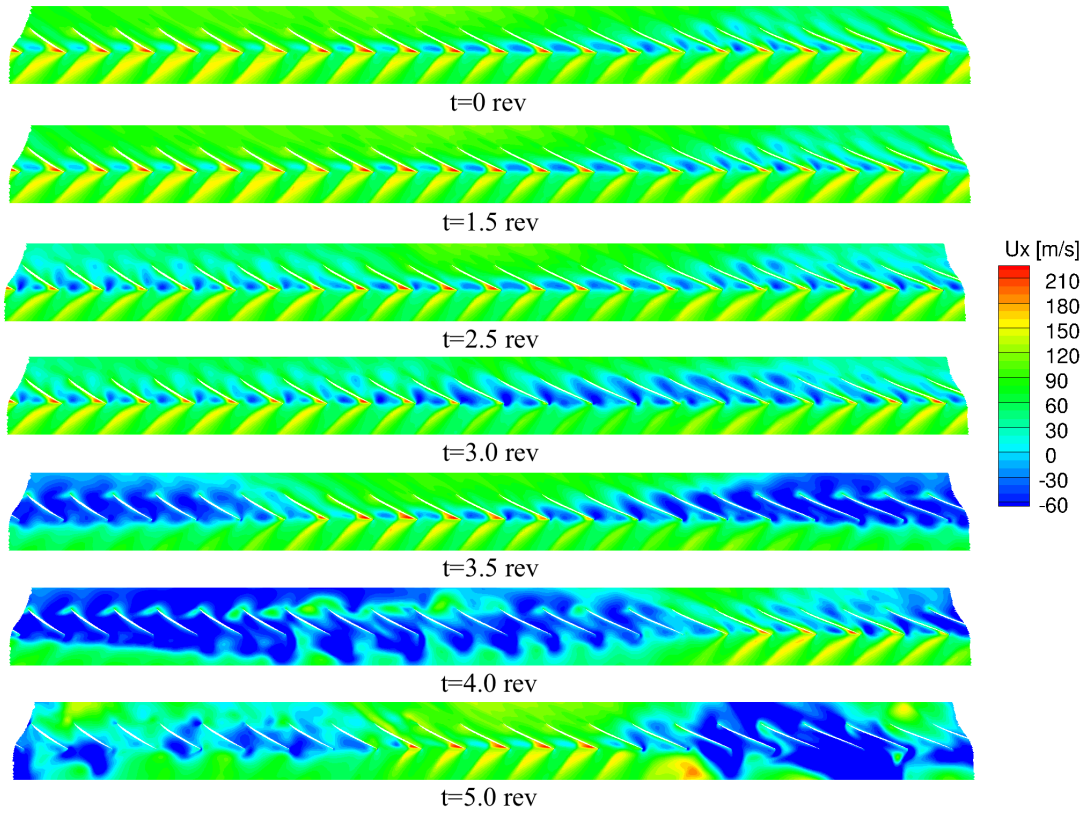
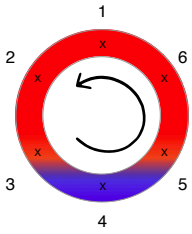
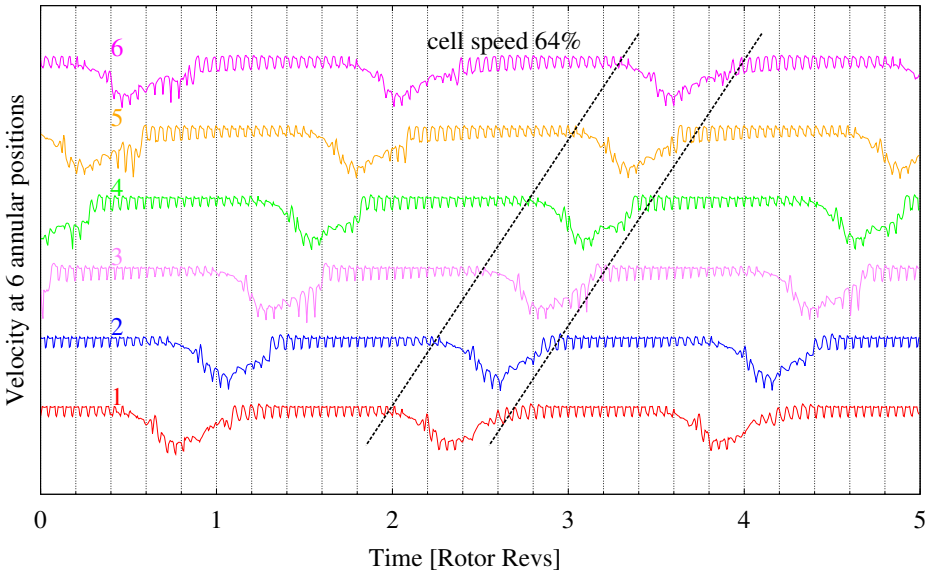


Figure 7.17: Contour of the axial velocity at 98% span of the rotor

Figure 7.18 shows the history of the axial velocity at 6 numerical probes on the casing 20% chord upstream of the rotor between $t = 23\ rev$ and $t = 28\ rev$ in Figure 7.16. It can be seen that the rotational speed of the stall cell is about 64% of the shaft speed. The average size of the stall cell is 14.3% of the reference volume, which is obtained by calculating the size of the volume enclosed with the iso-surface of zero axial velocity.



(a)



(b)

Figure 7.18: History of the axial velocity of 6 numerical probes

It is worthy to mention that a test case without S intake was also tried to simulate the stall process. In this case, the S intake was removed and total pressure pattern at the exit of the S intake was directly imposed upstream of the rotor as inlet boundary. The distance between the rotor LE and the inlet boundary is 2.0 times of the rotor axial chord length. During the calculation, unphysical solution occurred when the fan was pushed to NS condition. This confirms that during the stall process, the fan will inevitably change the flow condition at the exit of the S intake especially when the distance between the rotor and the S duct is short. Such a coupling between the S intake and the fan prohibits the use of an inlet boundary condition with fixed total pressure pattern.

7.5 Chapter Summary

In this chapter, the performance of the fan with S intake was investigated. Computations show that the ingestion of the boundary layer will reduce the operational mass flow range and decrease the efficiency. The analysis of the distortion pattern at the exit of the S intake shows that the distortion can be radially divided into three zones. Different zones are dominated by different distortions. The zone which extends from the hub to 65% span is governed by swirl distortion while there is almost no total pressure distortion. At higher span, the swirl distortion is weakened

and the strength of the total pressure distortion becomes larger. The configuration of the total pressure distortion at higher span is very similar to a DC120 distortion and the magnitude of the total pressure distortion decreases as the fan approaches stall. The loading of the blade at the tip is higher and the fan stalls much earlier than that with the straight intake. In the case studied here, the efficiency loss of the stage mainly results from the flow separation in the stator vane.

The stall process with S intake is very similar with the case with DC120 distortion. This proves that the conclusions obtained in the former chapters are general when the inflow pattern can be circumferentially divided into a distortion region and a clean flow region. The conclusions obtained with DC120 are general and are instructive in complex distortion patterns.

8 Conclusions and future work

8.1 Conclusions

The developments of low-speed fans with shorter intakes and the BLI propulsion necessitate further investigation of inlet distortion. To this end, time-accurate, high-fidelity RANS simulations were carried out with a transonic fan to validate the numerical strategy and investigate how inlet distortion influences the aerodynamic stability of the fan. In this chapter, the most important findings of this research are summarised with respect to the objectives outlined in Chapter 1. It should be noted that, although the computations have been performed for NASA rotor 67, some of the conclusions are completely general and valid for modern fan/compressor designs.

1. Establish a suitable computational strategy to accurately reproduce the performance of the fan with inlet distortion; Compare CFD against available experimental data

An appropriate numerical strategy was proposed and validated with extensive experimental data. It was shown that the code AU3D can accurately capture the performance of the fan under different operational conditions. The study highlighted the importance of temporal resolution on fan stall boundary prediction. A coarse time step cannot resolve disturbances with high frequency in the flow field and thus the stall inception is postponed. For NASA stage 67, the frequency range of 0.7-0.9 f_{bp} is important for the stall inception. At the operating condition of higher mass flow, the compressor can attenuate the higher frequencies and thus only the first few harmonics of the flow variables need to be resolved. It is thus suggested that a relative coarse time step can be applied when the compressor is operating far from stall boundary, but a fine time step must be used for the stall computations.

2. Determine how inlet distortion affects the working condition of the fan especially at the near stall point, identify the stall and recovery process of the fan with abrupt inlet distortion; investigate the performance of a BLI fan with an S intake

It was shown that the highest loading occurs when the blade is just leaving the distorted region where the rotor incidence reaches its peak. The fan will stall when the flow separation generated in the distorted region is not removed in the clean flow region. The whole stall process takes about two revolutions via spike stall route. In addition, the abrupt distortion can cause a larger stall margin deficit than the consistent distortion (which is typically tested in the experiments). This indicates that the stall boundary obtained from tests with consistent inlet distortion can underestimate the adverse effects of abrupt distortion.

To investigate how inlet distortion influence the stall hysteresis, three different cases were conducted and compared: the case with (a) uniform inflow, (b) consistent distortion and (c) abrupt distortion of the same pattern. The cases with inlet distortions have less stall hysteresis when compared with the case with uniform inflow. In addition, only one stall cell is present during the whole stall process in the distorted cases, but the structure of the stall cell changes due to the interactions with distortion. For the stall process of the case with uniform inflow, stall cells appear in different circumferential positions simultaneously but merge into one stall cell eventually. The stable rotating stall shows the same characteristic in terms of number, size and rotational speed in both uniform and distorted flow cases. During the recovery process, the size of the stall cell becomes smaller and its rotational speed increases as the mass flow increases. All three cases recover at a similar corrected mass flow, which indicates that the clean flow part of the annulus plays a very important role in the recovery process. The stall process with consistent inlet distortion is very similar to the case with abrupt distortion. However, the case with abrupt distortion has less hysteresis due to the early stall at larger mass flow but a similar recovery point.

Computational results revealed that the fan suffers significant loss in the operational mass flow range and efficiency with S intake when compared with the straight intake. The analysis of the distortion pattern at the exit of the S intake shows that the distortion can be radially divided into different zones. The loading of the blade at the tip is higher and the fan stalls at larger corrected mass flow condition than with a straight intake. The stall process of the fan with S intake is very similar to the case with DC120 distortion. This proves that the conclusions obtained in chapter 5 are general when the inflow pattern can roughly be circumferentially divided into a distortion region and a clean flow region.

3. Conduct a parametric study to explore how different parameters influence the stall margin of a fan with inlet distortion and the underlying mechanism

A parametric study was conducted to figure out how abrupt distortion strength and compressor rotational speed influence the stall margin. It was found that the stall margin is almost reduced linearly with the increase of distortion strength. However, a distortion with small magnitude can increase the total pressure ratio near stall. The underlying mechanism is that the vortex shedding at mid-span energises the low-momentum flow on the blade surface. For an abrupt distortion with fixed strength, the stall margin loss increases as the rotational speed decreases. When the fan falls into rotating stall, the total pressure ratio loss drops as the rotational speed decreases because NASA rotor 67 is more tip-loaded at higher rotational speeds. Consequently, as the stall cell exists in the tip region, it cripples the pressurisation capability of the fan to a larger extent.

The most important finding in this part is the interaction between abrupt inlet distortion, exit duct reflection and fan stability. To the author's knowledge, this is the first time that the length of the exit duct is found to affect the stall margin of the fan. Based on the observations from the simulations, the occurrence of abrupt distortion generates an acoustic wave and an entropy wave which propagate downstream of the fan. The acoustic wave interacts with the downstream

nozzle and produces an expansion wave which propagates upstream to the fan. Early arrival of this expansion wave decreases the back pressure of the fan, thus preventing the initiation of stall. DFT decomposition of the disturbance in the flow field showed that the dominant component of the waves travelling in the exit duct are the planar waves, and higher circumferential harmonics have negligible effect. Therefore, such wave reflection phenomenon is general and irrelevant to the distortion pattern.

An analytical model called "half shock tube" was proposed to explain how abrupt distortion generates the waves. Simplified CFD computations were also carried out to study the effects of the distortion-induced waves and reflected waves on the flow field. The reflected waves from the nozzle result from the sonic front at the nozzle throat as well as the geometry variation. Reflection can also be produced in smoothly varying ducts due to the change in cross-section area and the accumulative amplitude of reflection is only determined by the nozzle area ratio. Based on the observations from the stall simulations, a critical length ratio of the compression system was derived. This length relation can be used to judge whether a duct setup would be beneficial or detrimental to the compressor aerodynamic stability. Further computations also showed the same conclusion with uniform inflow. These results indicate that the downstream components of the compressor can influence its stall margin due to the wave propagation.

8.2 Recommendations for Future work

The recommendations for further research include 3 topics:

1. Investigation of how the stall margin changes with the circumferential angle of the inlet distortion

Experimental study [Reid, 1969] has shown that a critical angle exists beyond which the stalled compressor static pressure will no longer change. However, there is no detailed explanation of the underlying mechanism in open publications. Based on the findings about the stall process with inlet distortion in this research, the following two objectives are expected: (1) Identify the mechanism of critical angle and accurately predict its value for a given blade design at specific flow parameters (such as rotational speed and distortion strength); thereafter a quantitative formula for the calculation of the critical angle can be derived. This is important as a larger critical angle means that the compressor can be more robust to inlet distortion. Therefore, the investigations of the critical angle will provide useful instructions for blade design; (2) a simple correlation between the circumferential range and the compressor stall margin is needed. A low-fidelity model can be built for the prediction of the stall margin with inlet distortions of different circumferential angles. To achieve the above goals, large amount of high-fidelity, full-anulus computations have to be conducted.

2. Investigation of the effects of inlet distortion on the performance and stability of the modern

low-speed fan

Civil engines are moving towards low-speed fans with larger diameter and shorter intakes. The fans operate on the flat part of the constant speed characteristic and are more prone to aerodynamic instabilities than conventional high-speed fans. Therefore, it is essential to study the stability of a low-speed fan with inlet distortion.

Figure 8.1 shows the computational domain of a low-speed fan. For a typical low-speed fan, the blade is not tip-loaded but the highest loading appears at the middle span. Preliminary study [Lee et al., 2019] shows that the stall behaviour of a low speed fan in uniform inflow is different from that of a high-speed fan. When the fan approaches the stall boundary, radial flow migrates from the middle span towards the tip. The tip is thus blocked and rotating stall is initialised. Considering that the inlet distortion can significantly change the radial loading distribution of the blade, the stall behaviour of a low-speed fan will be very different and how inlet distortion influences the stall process will be of interest.

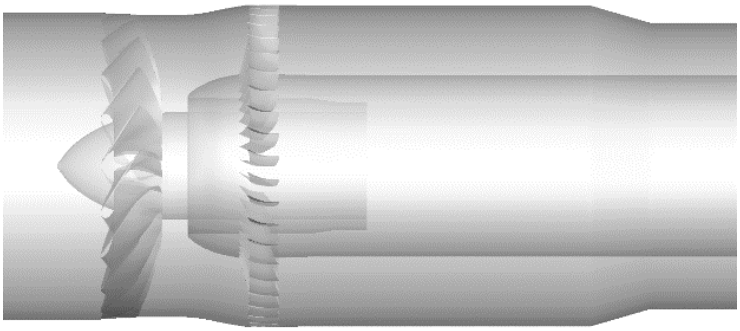


Figure 8.1: Computational domain of a low-speed fan stage

3. Performing simulations of the fan with both inlet distortion and tip injection (for stall control); providing useful instructions on injection system design with a parametric study

It has been shown in [Spakovszky et al., 1999] that tip injection can extend the operational mass flow range of a compressor when subjected to circumferential inlet distortion. In [Spakovszky et al., 1999], 12 injectors were uniformly and symmetrically arranged around the annulus. Considering injection consumes large amount of high-pressure air which decreases the overall efficiency of the compression system, it is essential to minimise the injection air but pertain the control effects. One possible idea is, by exploring the most effective circumferential positions for stall control, the injectors can be merely applied at one or a few specified positions to reduce the injection air.

Based on the study in current research, it is known that the blade separation occurs in the distorted region and stall is initialised when the blade is leaving the distorted region. The injection in the distorted area can suppress the separation and thus rotating stall. Moreover, the investigation of the recovery process of the fan from rotating stall revealed that the clean flow region plays an important role in the removal of the stall cell. The injection in the clean

flow region can improve the recovery capability of the blade (if the blade successfully carries the separation into the distorted region again, rotating stall will occur). The injection in both regions has the potential to suppress the occurrence of rotating stall but their effect needs to be investigated. Based on above analysis, it is beneficial to evaluate the best circumferential positions for tip injection. Further explorations can be carried out to find the most suitable parameters (like the injection angle, total pressure of the injection air, the size and shape of the injector) of the injection system.

9 Appendix I

More validation results with NASA Stage 35 is shown in this part. Figure 9.1 shows the comparison of the radial profiles of the flow angle, total temperature, normalized total pressure and Mach number downstream of the stator between CFD and EXP in clean flow. The operational point is the PE condition (corrected mass flow = 21.0 kg/s) of 100% rotational speed. Good agreement is obtained in the overall distribution of these parameters apart from the flow angle. The simulated flow angle has a deviation of 3 degrees from the experimental data. Similar simulated results can also be found in [Herrick et al., 2009]. The Mach number is over predicted in the tip region. This discrepancy may be caused by the unknown stator geometry near the casing, which cannot be reproduced in the CFD mesh. The differences of the radial profiles between CFD and EXP are more significant at the lower 15% span range near the hub. For this compressor blade, CFD study has been conducted to investigate how the hub leakage flow influences the radial profile. It was demonstrated that the total pressure deficit in the hub region is caused by the flow leakage emitting forward of the rotor, between the rotor disc and the stationary centrebody [Shabbir et al., 1997].

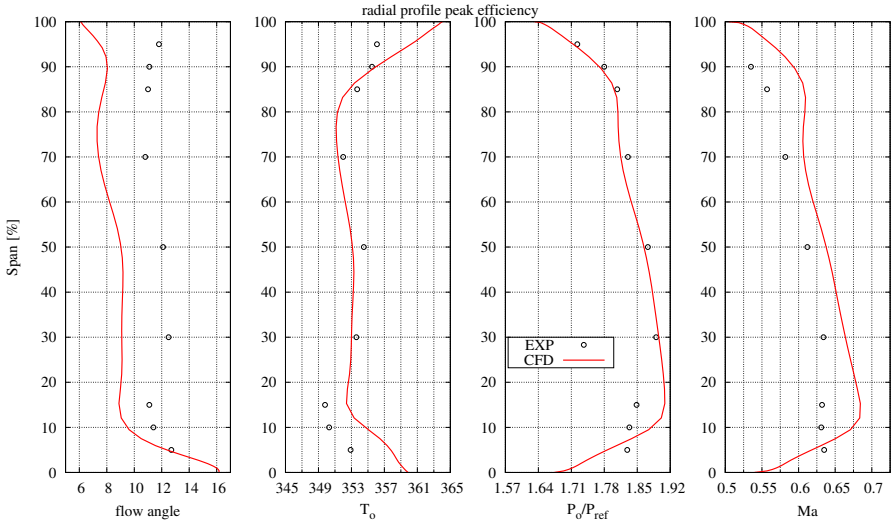


Figure 9.1: Radial profiles downstream of the stator, 100% rotational speed, corrected mass flow=21.0 kg/s

To validate the above statement, the radial profiles with and without hub leakage flow are compared against the measured results at a lower mass flow of 19.64 kg/s of 100% rotational speed, as shown in Figure 9.2. The bleeding slot is set in front of the rotor (Figure 9.3). A mass flow boundary condition is applied for the bleeding slot, which is the same as [Shabbir et al., 1997]. Due to the unknown exact leakage flow in this experiment, a 0.1% leakage is tested

based on the numerical study in [Shabbir et al., 1997]. The flow angle is still less than the tested results. The total pressure distribution is under-predicted, which is consistent with the overall performance where the CFD results have a lower total pressure (Figure 3.31). The total temperature and Mach number show a better match between CFD and experimental data in the simulation with hub leakage flow.

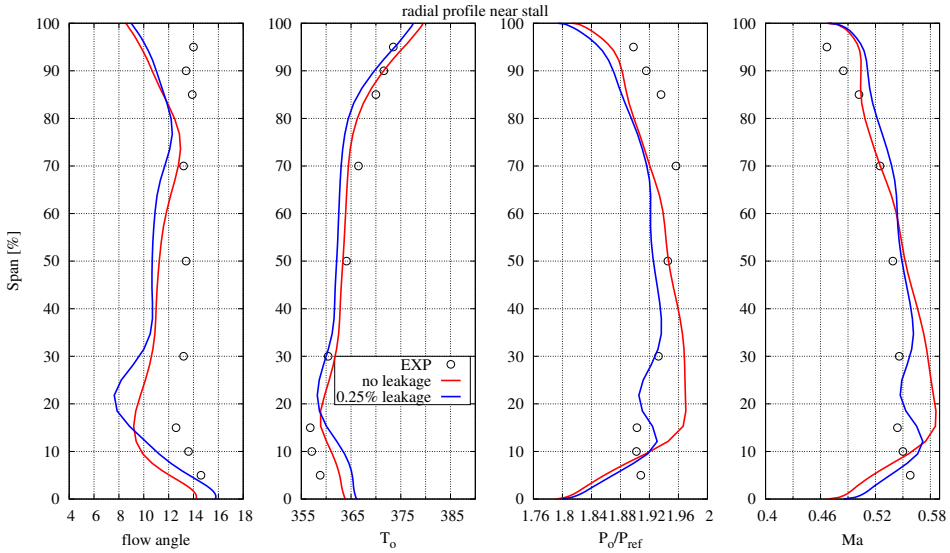


Figure 9.2: Radial profile downstream of the stator, 100% rotational speed, corrected mass flow=19.6 kg/s

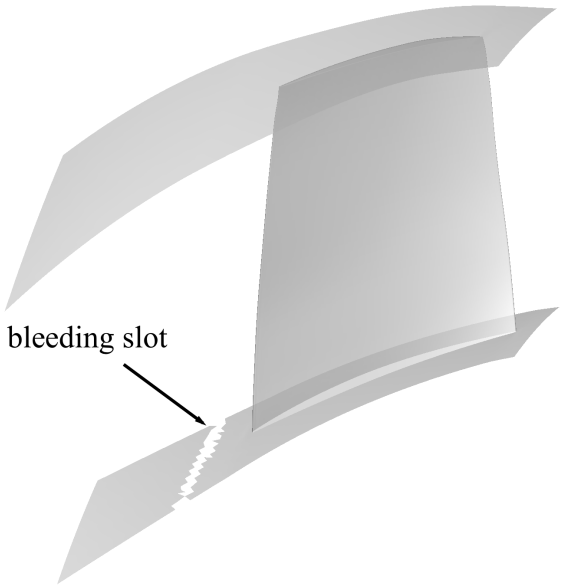


Figure 9.3: Bleeding slot in front of the rotor

Figure 9.4 shows the radial profiles downstream of the stator at the operating condition with a corrected mass flow of 14.46 kg/s at 70% rotational speed. Hub leakage flow is not modelled in this case. As can be seen, the difference between CFD and measured data in flow angle is much

smaller at this lower rotational speed. The CFD and EXP match well for total pressure and total temperature while the Mach number is overestimated.

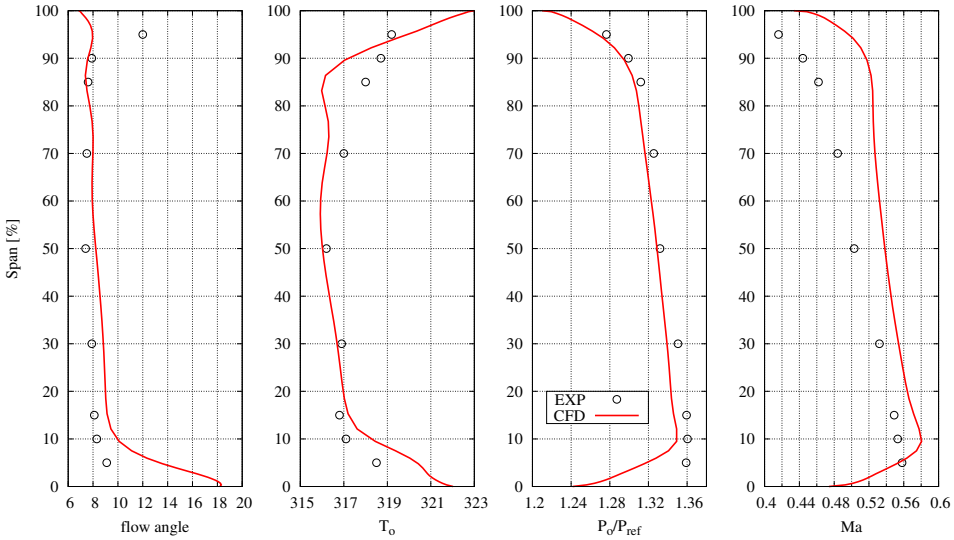


Figure 9.4: Radial profiles downstream of the stator, 70% rotational speed (corrected mass flow=14.46 kg/s)

Bibliography

[Adamczyk, 2018] Adamczyk, J. (2018). *Private talk with John Adamczyk.*

[Allan et al., 2006] Allan, B., Owens, L., and Lin, J. (2006). Optimal design of passive flow control for a boundary-layer-ingesting offset inlet using design-of-experiments. In *44th AIAA Aerospace Sciences Meeting and Exhibit*, page 1049.

[Anders et al., 2004] Anders, S., III, W. S., and Washburn, A. (2004). Active flow control activities at nasa langley. In *2nd AIAA Flow Control Conference*, page 2623.

[Anderson and Smith, 2006] Anderson, S. J. and Smith, N. (2006). *Analysis of unsteady casing pressure measurements during surge and rotating stall*, pages 293–312. Unsteady Aerodynamics, Aeroacoustics and Aeroelasticity of Turbomachines. Springer.

[Arend et al., 2017] Arend, D. J., Wolter, J. D., Hirt, S. M., Provenza, A., Gazzaniga, J. A., Cousins, W. T., Hardin, L. W., and Sharma, O. (2017). Experimental evaluation of an embedded boundary layer ingesting propulsor for highly efficient subsonic cruise aircraft. In *53rd AIAA/SAE/ASEE Joint Propulsion Conference*, page 5041.

[Arima et al., 1997] Arima, T., Sonoda, T., Shirotori, M., Tamura, A., and Kikuchi, K. (1997). A numerical investigation of transonic axial compressor rotor flow using a low reynolds number k- turbulence model. In *ASME 1997 International Gas Turbine and Aeroengine Congress and Exhibition*, page V001T03A017. American Society of Mechanical Engineers.

[Arnone, 1994] Arnone, A. (1994). Viscous analysis of three-dimensional rotor flow using a multigrid method. *Journal of turbomachinery*, 116(3):435–445.

[Arshad et al., 2018] Arshad, A., Li, Q., Li, S., and Pan, T. (2018). Effects of inlet radial distortion on the type of stall precursor in low-speed axial compressor. *Proceedings of the Institution of Mechanical Engineers, Part G: Journal of Aerospace Engineering*, 232(1):55–67.

[Bailey and Voit, 1970] Bailey, E. E. and Voit, C. H. (1970). Some observations of effects of porous casings on operating range of a single axial-flow compressor rotor. *NASA TM X-2120.*

[Bakhle et al., 2018a] Bakhle, M. A., Reddy, T. S., Coroneos, R., Min, J. B., Provenza, A. J., Duffy, K. P., Stefko, G. L., and Heinlein, G. (2018a). Aeromechanics analysis of a distortion-tolerant fan with boundary layer ingestion. In *2018 AIAA Aerospace Sciences Meeting*, page 1891.

[Bakhle et al., 2018b] Bakhle, M. A., Reddy, T. S., Coroneos, R., Min, J. B., Provenza, A. J., Duffy, K. P., Stefko, G. L., and Heinlein, G. (2018b). Aeromechanics analysis of a distortion-tolerant fan with boundary layer ingestion. In *2018 AIAA Aerospace Sciences Meeting*, page 1891.

[Barakos et al., 2001] Barakos, G., Vahdati, M., Sayma, A., Breard, C., and Imregun, M. (2001). A fully distributed unstructured navier-stokes solver for large-scale aeroelasticity computations. *The Aeronautical Journal*, 105(1050):419–426.

[Barrera-Medrano et al., 2017] Barrera-Medrano, M. E., Newton, P., Martinez-Botas, R., Rajoo, S., Tomita, I., and Ibaraki, S. (2017). Effect of exit pressure pulsation on the performance and stability limit of a turbocharger centrifugal compressor. *Journal of Engineering for Gas Turbines and Power*, 139(5):052601.

[Berrier and Allan, 2004] Berrier, B. and Allan, B. (2004). Experimental and computational evaluation of flush-mounted, s-duct inlets. In *42nd AIAA Aerospace Sciences Meeting and Exhibit*, page 764.

[Berrier et al., 2005] Berrier, B. L., Carter, M. B., and Allan, B. G. (2005). High reynolds number investigation of a flush-mounted, s-duct inlet with large amounts of boundary layer ingestion. *NASA TP-2005-213766*.

[Biesiadny et al., 1986] Biesiadny, T. J., Braithwaite, W. M., Soeder, R. H., and Abdelwahab, M. (1986). Summary of investigations of engine response to distorted inlet conditions. *NASA TM-87317*.

[Brandau, 1968] Brandau, J. H. (1968). Performance of waterjet propulsion systems-a review of the state-of-the-art. *Journal of Hydronautics*, 2(2):61–73.

[Brandstetter et al., 2019] Brandstetter, C., Paoletti, B., and Ottavy, X. (2019). Compressible modal instability onset in an aerodynamically mistuned transonic fan. *Journal of Turbomachinery*, 141(3):031004.

[Burstadt et al., 1971] Burstadt, P. L., Calogeras, J. E., and Mehalic, C. M. (1971). Experimental investigation of the effect of screen induced total pressure distortion on turbojet stall margin. *NASA TM X-2239*.

[Camp and Day, 1998] Camp, T. R. and Day, I. J. (1998). A study of spike and modal stall phenomena in a low speed axial compressor. *Journal of Turbomachinery*, pages 393–401.

[Campbell et al., 2005] Campbell, R., Carter, M., Pendergraft, O., Friedman, D., and Serrano, L. (2005). Design and testing of a blended wing body with boundary layer ingestion nacelles at high reynolds numbers. In *43rd AIAA Aerospace Sciences Meeting and Exhibit*, page 459.

[Cao et al., 2017] Cao, T., Vadlamani, N. R., Tucker, P. G., Smith, A. R., Slaby, M., and Sheaf, C. T. (2017). Fanintake interaction under high incidence. *Journal of Engineering for Gas Turbines and Power*, 139(4):041204.

[Carter et al., 2006] Carter, M. B., Campbell, R. L., Pendergraft, O. C., Friedman, D. M., and Serrano, L. (2006). Designing and testing a blended wing body with boundary-layer ingestion nacelles. *Journal of Aircraft*, 43(5):1479–1489.

[Chen et al., 1987] Chen, G., GREITZER, E., and EPSTEIN, A. (1987). Enhancing compressor distortion tolerance by asymmetric stator control. In *23rd Joint Propulsion Conference*, page 2093.

[Chima, 2009] Chima, R. (2009). Swift code assessment for two similar transonic compressors. In *47th AIAA Aerospace Sciences Meeting Including the New Horizons Forum and Aerospace Exposition*, page 1058.

[Chima, 2006] Chima, R. V. (2006). A three-dimensional unsteady cfd model of compressor stability. In *ASME Turbo Expo 2006: Power for Land, Sea, and Air*, pages 1157–1168. American Society of Mechanical Engineers.

[Choi and Vahdati, 2011] Choi, M. and Vahdati, M. (2011). Recovery process from rotating stall in a fan. *Journal of Propulsion and Power*, 27(6):1161–1168.

[Copenhaver and Okiishi, 1993] Copenhaver, W. W. and Okiishi, T. H. (1993). Rotating stall performance and recoverability of a high-speed 10-stage axial flow compressor. *Journal of Propulsion and Power*, 9(2):281–292.

[Cornelius et al., 2014] Cornelius, C., Biesinger, T., Zori, L., Campregher, R., Galpin, P., and Braune, A. (2014). Efficient time resolved multistage cfd analysis applied to axial compressors. In *ASME Turbo expo 2014: Turbine technical conference and exposition*, page V02DT44A035. American Society of Mechanical Engineers.

[Cousins, 1997] Cousins, W. T. (1997). The dynamics of stall and surge behavior in axial-centrifugal compressors. *Ph.D. thesis, Virginia Polytechnic Institute and State University.*

[Cousins, 2004] Cousins, W. T. (2004). History, philosophy, physics, and future directions of aircraft propulsion system/inlet integration. In *ASME Turbo Expo 2004: Power for Land, Sea, and Air*, pages 305–320. American Society of Mechanical Engineers.

[Cousins and Davis, 2011] Cousins, W. T. and Davis, M. W. (2011). Evaluating complex inlet distortion with a parallel compressor model: Part 1concepts, theory, extensions, and limitations. In *ASME 2011 Turbo Expo: Turbine Technical Conference and Exposition*, pages 1–12. American Society of Mechanical Engineers.

[Cousins et al., 2017] Cousins, W. T., Voytovych, D., Tillman, G., and Gray, E. (2017). Design of a distortion-tolerant fan for a boundary-layer ingesting embedded engine application. In *53rd AIAA/SAE/ASEE Joint Propulsion Conference*, page 5042.

[Crouse et al., 1969] Crouse, J. E., Janetzke, D. C., and Schwirian, R. E. (1969). A computer program for composing compressor blading from simulated circular-arc elements on conical surfaces. *NASA TN D-5437.*

[Cumpsty, 1989] Cumpsty, N. A. (1989). *Compressor aerodynamics*. Longman Scientific & Technical.

[Cumpsty, 2010] Cumpsty, N. A. (2010). Preparing for the future: reducing gas turbine environmental impactigti scholar lecture. *Journal of turbomachinery*, 132(4):041017.

[Davis, 1991] Davis, M. W. (1991). Parametric investigation into the combined effects of pressure and temperature distortion on compression system stability. In *27th Joint Propulsion Conference*, page 1895.

[Davis and Cousins, 2011] Davis, M. W. and Cousins, W. T. (2011). Evaluating complex inlet distortion with a parallel compressor model: Part 2applications to complex patterns. In *ASME 2011 Turbo Expo: Turbine Technical Conference and Exposition*, pages 13–23. American Society of Mechanical Engineers.

[Day, 1991] Day, I. J. (1991). Stall inception in axial flow compressors. In *ASME 1991 International Gas Turbine and Aeroengine Congress and Exposition*, page V001T01A034. American Society of Mechanical Engineers.

[Day, 1993] Day, I. J. (1993). Stall inception in axial flow compressors. *Journal of Turbomachinery*, 115(1):1–9. SO: Journal of Turbomachinery January 1, 1993 115(1):1.

[Day, 2016] Day, I. J. (2016). Stall, surge, and 75 years of research. *Journal of Turbomachinery*, 138(1):011001.

[Day et al., 1999] Day, I. J., Breuer, T., Escuret, J., Cherrett, M., and Wilson, A. (1999). Stall inception and the prospects for active control in four high-speed compressors. *Journal of turbomachinery*, 121(1):18–27.

[Day and Cumpsty, 1978] Day, I. J. and Cumpsty, N. A. (1978). The measurement and interpretation of flow within rotating stall cells in axial compressors. *Journal of Mechanical Engineering Science*, 20(2):101–114.

[Denton, 1990] Denton, J. D. (1990). The calculation of three dimensional viscous flow through multistage turbomachines. In *ASME 1990 International Gas Turbine and Aeroengine Congress and Exposition*, pages V001T01A009–V001T01A009. American Society of Mechanical Engineers.

[Denton, 2017] Denton, J. D. (2017). Multall: An open source, cfd based, turbomachinery design system. In *ASME Turbo Expo 2017: Turbomachinery Technical Conference and Exposition*, page V02BT41A027. American Society of Mechanical Engineers.

[Dodds and Vahdati, 2015] Dodds, J. and Vahdati, M. (2015). Rotating stall observations in a high speed compressorpart ii: Numerical study. *Journal of Turbomachinery*, 137(5):051003.

[Evanbar and Thurston, 1966] Evanbar, M. and Thurston, S. (1966). Efficiency of a propulsor on a body of revolution-inducting boundary-layer fluid. *Journal of Aircraft*, 3(3):270–277.

[Felder et al., 2011] Felder, J., Kim, H., Brown, G., and Kummer, J. (2011). An examination of the effect of boundary layer ingestion on turboelectric distributed propulsion systems. In *49th AIAA aerospace sciences meeting including the new horizons forum and aerospace exposition*, page 300.

[Fidalgo, 2013] Fidalgo, V. J. (2013). Fan-distortion interaction in novel aircraft installations. *Ph.D. Dissertation, Univ. of Cambridge.*

[Fidalgo et al., 2012] Fidalgo, V. J., Hall, C. A., and Colin, Y. (2012). A study of fan-distortion interaction within the nasa rotor 67 transonic stage. *Journal of Turbomachinery*, 134(5):051011.

[Flitcroft et al., 1987] Flitcroft, J. E., Dunham, J., and Abbott, W. A. (1987). Agard cp-400, engine response to distorted inflow conditions, munich, september 89, pp. 13-113-11. *Transmission of inlet distortion through a fan.*

[Florea et al., 2015] Florea, R. V., Matalanis, C., Hardin, L. W., Stucky, M., and Shabbir, A. (2015). Parametric analysis and design for embedded engine inlets. *Journal of Propulsion and Power*, 31(3):843–850.

[Freeman et al., 1997] Freeman, C., Wilson, A. G., Day, I. J., and Swinbanks, M. A. (1997). Experiments in active control of stall on an aeroengine gas turbine. In *ASME 1997 International Gas Turbine and Aeroengine Congress and Exhibition*, page V004T15A021. American Society of Mechanical Engineers.

[Genssler et al., 1987] Genssler, H. P., Meyer, W., and Fottner, L. (1987). Development of intake swirl generators for turbo jet engine testing. *AGARD Propulsion and Ener- getics 68th (A) Specialists Meeting, Munich, Germany, Sept. 1012, Paper No. AGARD-CP-400.*

[Giles, 1990] Giles, M. B. (1990). Nonreflecting boundary conditions for euler equation calculations. *AIAA journal*, 28(12):2050–2058.

[Giuliani, 2016] Giuliani, J. E. (2016). Jet engine fan response to inlet distortions generated by ingesting boundary layer flow. *Doctoral dissertation, The Ohio State University.*

[Giuliani and Chen, 2016] Giuliani, J. E. and Chen, J.-P. (2016). Fan response to boundary-layer ingesting inlet distortions. *AIAA Journal*, 54(10):3232–3243.

[Giuliani et al., 2014] Giuliani, J. E., Chen, J. P., Beach, T. A., and Bakhle, M. A. (2014). Numerical simulation of boundary layer ingesting (bli) inlet/fan interaction. In *50th AIAA/ASME/SAE/ASEE Joint Propulsion Conference*, page 3731.

[Gong, 1999] Gong, Y. (1999). A computational model for rotating stall and inlet distortions in multistage compressors. *Ph.D. Thesis, Massachusetts Institute of Technology.*

[Greitzer, 1973] Greitzer, E. M. (1973). Upstream attenuation and quasi-steady rotor lift fluctuations in asymmetric flows in axial compressors. In *ASME 1973 International Gas Turbine Conference and Products Show*, page V001T01A030. American Society of Mechanical Engineers.

[Greitzer, 1976] Greitzer, E. M. (1976). Surge and rotating stall in axial flow compressorspart i: Theoretical compression system model. *Journal of Engineering for Power*, 98(2):190–198.

[Greitzer et al., 2010] Greitzer, E. M., Bonnefoy, P. A., DelaRosaBlanco, E., Dorbian, C. S., Drela, M., Hall, D. K., Hansman, R. J., Hileman, J. I., Liebeck, R. H., and Levegren, J. (2010). N 3 aircraft concept designs and trade studies. volume 1. *NASA/CR-2010-216794/VOL1.*

[Greitzer and Griswol, 1976] Greitzer, E. M. and Griswol, H. R. (1976). Compressor-diffuser interaction with circumferential flow distortion. *Journal of Mechanical Engineering Science*, 18(1):25–38.

[Greitzer et al., 1978] Greitzer, E. M., Mazzawy, R. S., and Fulkerson, D. A. (1978). Flow field coupling between compression system components in asymmetric flow. *Journal of Engineering for Power*, 100(1):66–72.

[Greitzer and Moore, 1986] Greitzer, E. M. and Moore, F. K. (1986). A theory of post-stall transients in axial compression systems: part iiapplication. *Journal of Engineering for Gas Turbines and Power*, 108(2):231–239.

[Greitzer et al., 2007] Greitzer, E. M., Tan, C. S., and Graf, M. B. (2007). *Internal flow: concepts and applications*, volume 3. Cambridge University Press.

[Guimares et al., 2017] Guimares, T., Lowe, K. T., and OBrien, W. F. (2017). Streamvane turbofan inlet swirl distortion generator: Mean flow and turbulence structure. *Journal of Propulsion and Power*, 34(2):340–353.

[Gunn and Hall, 2017] Gunn, E. and Hall, C. (2017). Non-axisymmetric stator design for boundary layer ingesting fans. In *ASME Turbo Expo 2017: Turbomachinery Technical Conference and Exposition*, pages V001T01A003–V001T01A003. American Society of Mechanical Engineers.

[Gunn and Hall, 2014] Gunn, E. J. and Hall, C. A. (2014). Aerodynamics of boundary layer ingesting fans. In *ASME Turbo Expo 2014: Turbine Technical Conference and Exposition*, page V01AT01A024. American Society of Mechanical Engineers.

[Gunn et al., 2013] Gunn, E. J., Tooze, S. E., Hall, C. A., and Colin, Y. (2013). An experimental study of loss sources in a fan operating with continuous inlet stagnation pressure distortion. *Journal of Turbomachinery*, 135(5):051002.

[Hah et al., 1996] Hah, C., Rabe, D. C., Sullivan, T. J., and Wadia, A. R. (1996). Effects of inlet distortion on the flow field in a transonic compressor rotor. In *ASME 1996 International Gas Turbine and Aeroengine Congress and Exhibition*, page V001T01A135. American Society of Mechanical Engineers.

[Hall et al., 2017] Hall, D. K., Huang, A. C., Uranga, A., Greitzer, E. M., Drela, M., and Sato, S. (2017). Boundary layer ingestion propulsion benefit for transport aircraft. *Journal of Propulsion and Power*, 33(5):1118–1129.

[Hardin et al., 2012] Hardin, L., Tillman, G., Sharma, O., Berton, J., and Arend, D. (2012). Aircraft system study of boundary layer ingesting propulsion. In *48th AIAA/ASME/SAE/ASEE Joint Propulsion Conference & Exhibit*, page 3993.

[Hathaway, 2002] Hathaway, M. D. (2002). Self-recirculating casing treatment concept for enhanced compressor performance. In *ASME Turbo Expo 2002: Power for Land, Sea, and Air*, pages 411–420. American Society of Mechanical Engineers.

[Haug and Niehuis, 2018] Haug, J. and Niehuis, R. (2018). Full annulus simulations of a transonic axial compressor stage with distorted inflow at transonic and subsonic blade tip speed. *International Journal of Turbomachinery, Propulsion and Power*, 3(1):7.

[Hawthorne and Horlock, 1962] Hawthorne, W. R. and Horlock, J. H. (1962). Actuator disc theory of the incompressible flow in axial compressors. *Proceedings of the institution of Mechanical Engineers*, 176(1):789–814.

[Hawthorne et al., 1978] Hawthorne, W. R., Mitchell, N. A., McCune, J. E., and Tan, C. S. (1978). Nonaxisymmetric flow through annular actuator disks: Inlet distortion problem. *Journal of Engineering for Power*, 100(4):604–617.

[He, 1990] He, L. (1990). An euler solution for unsteady flows around oscillating blades. *Journal of Turbomachinery*, 112(4):714–722.

[He, 1997] He, L. (1997). Computational study of rotating-stall inception in axial compressors. *Journal of Propulsion and Power*, 13(1):31–38.

[He, 2010] He, L. (2010). Fourier methods for turbomachinery applications. *Progress in Aerospace Sciences*, 46(8):329–341.

[Herrick, 2011] Herrick, G. (2011). Effects of inlet distortion on aeromechanical stability of a forward-swept high-speed fan. In *46th AIAA/ASME/SAE/ASEE Joint Propulsion Conference & Exhibit*, page 6711.

[Herrick et al., 2009] Herrick, G., Hathaway, M., and Chen, J.-P. (2009). Unsteady full annulus simulations of a transonic axial compressor stage. In *47th AIAA Aerospace Sciences Meeting including The New Horizons Forum and Aerospace Exposition*, page 1059.

[Hirsch, 1990] Hirsch, C. (1990). Numerical computation of internal and external flows. vol. 2-computational methods for inviscid and viscous flows(book). *Chichester, England and New York, John Wiley & Sons, 1990, 708.*

[Hodder, 1981] Hodder, B. K. (1981). An investigation of engine influence on inlet performance.[conducted in the ames 40-by 80-foot wind tunnel]. *NASACR 166136.*

[Horlock, 1958] Horlock, J. H. (1958). *Some Actuator-Disc Theories for the Flow of Air Through an Axial Turbo-Machine.* HM Stationery Office.

[Hughes, 2011] Hughes, C. (2011). The promise and challenges of ultra high bypass ratio engine technology and integration. *HQ-STI-11-012*.

[Hynes and Greitzer, 1987] Hynes, T. P. and Greitzer, E. M. (1987). A method for assessing effects of circumferential flow distortion on compressor stability. *Journal of Turbomachinery*, 109(3):371–379.

[Iim et al., 2012] Iim, H., Chen, X.-Y., and Zha, G. (2012). Detached-eddy simulation of rotating stall inception for a full-annulus transonic rotor. *Journal of Propulsion and Power*, 28(4):782–798.

[Jahnen et al., 1999] Jahnen, W., Peters, T., and Fottner, L. (1999). Stall inception in a 5-stage hp-compressor with increased load due to inlet distortion. In *ASME 1999 International Gas Turbine and Aeroengine Congress and Exhibition*, page V001T03A067. American Society of Mechanical Engineers.

[Jansen et al., 2016] Jansen, R., Bowman, C., and Jankovsky, A. (2016). Sizing power components of an electrically driven tail cone thruster and a range extender. In *16th AIAA Aviation Technology, Integration, and Operations Conference*, page 3766.

[Jennions and Turner, 1993] Jennions, I. K. and Turner, M. G. (1993). Three-dimensional navier-stokes computations of transonic fan flow using an explicit flow solver and an implicit solver. *Journal of Turbomachinery*, 115(2):261–272.

[Jeong and Hussain, 1995] Jeong, J. and Hussain, F. (1995). On the identification of a vortex. *Journal of fluid mechanics*, 285:69–94.

[Jiang et al., 2009] Jiang, H., Lu, Y., Yuan, W., and Li, Q. (2009). Experimental investigation of the influence of inlet distortion on the stall inception in a low speed axial compressor. In *ASME turbo expo 2009: power for land, sea, and air*, pages 1533–1542. American Society of Mechanical Engineers.

[Joo and Hynes, 1997] Joo, W. G. and Hynes, T. P. (1997). The simulation of turbomachinery blade rows in asymmetric flow using actuator disks. *Journal of turbomachinery*, 119(4):723–732.

[Jothiprasad et al., 2012] Jothiprasad, G., Murray, R. C., Essenhigh, K., Bennett, G. A., Saddoughi, S., Wadia, A., and Breeze-Stringfellow, A. (2012). Control of tip-clearance flow in a low speed axial compressor rotor with plasma actuation. *Journal of Turbomachinery*, 134(2):021019.

[Jr and Braithwaite, 1974] Jr, E. J. G. and Braithwaite, W. M. (1974). Summary of recent investigations of inlet flow distortion effect on engine stability. *NASA-TM-X-71505*.

[Kawai et al., 2006] Kawai, R. T., Friedman, D. M., and Serrano, L. (2006). Blended wing body (bwb) boundary layer ingestion (bli) inlet configuration and system studies. *NASA/CR-2006-214534*.

[Khaleghi et al., 2008] Khaleghi, H., Boroomand, M., Tousi, A., and Teixeira, J. (2008). Stall inception in a transonic axial fan. *Proceedings of the Institution of Mechanical Engineers, Part A: Journal of Power and Energy*, 222(2):199–208.

[Koch, 1970] Koch, C. C. (1970). Experimental evaluation of outer case blowing or bleeding of single stage axial flow compressor, part 6 final report. *NASA CR-54592*.

[Lee et al., 2019] Lee, K.-B., Wilson, M., and Vahdati, M. (2019). Effects of inlet disturbances on fan stability. *Journal of Engineering for Gas Turbines and Power*, 141(5):051014.

[Leinhos et al., 2000] Leinhos, D., R., N. S., and Fottner, L. (2000). The influence of transient inlet distortions on the instability inception of a low-pressure compressor in a turbofan engine. *Journal of Turbomachinery*, 123(1):1–8. SO: Journal of Turbomachinery February 1, 2000 123(1):1.

[Liebeck et al., 1998] Liebeck, R., Page, M., and Rawdon, B. (1998). Blended-wing-body subsonic commercial transport. In *36th AIAA Aerospace Sciences Meeting and Exhibit*, page 438.

[Liebeck, 2004] Liebeck, R. H. (2004). Design of the blended wing body subsonic transport. *Journal of Aircraft*, 41(1):10–25.

[Lieser et al., 2010] Lieser, J. A., Albrecht, P., and Biela, C. (2010). Planning of a compressor rig test with advanced inflow distortion simulation. In *Second Symposium" Simulation of Wing and Nacelle Stall*.

[Lin et al., 2005] Lin, F., Li, M., and Chen, J. (2005). Long-to-short length scale transition: A stall inception phenomenon in an axial compressor with inlet distortion. In *ASME Turbo Expo 2005: Power for Land, Sea, and Air*, pages 247–260. American Society of Mechanical Engineers.

[Longley, 1990] Longley, J. P. (1990). Measured and predicted effects of inlet distortion on axial compressors. In *ASME 1990 International Gas Turbine and Aeroengine Congress and Exposition*, page V001T01A067. American Society of Mechanical Engineers.

[Longley and Greitzer, 1992] Longley, J. P. and Greitzer, E. M. (1992). Inlet distortion effects in aircraft propulsion system integration. *AGARD Lecture Series, 1*.

[Longley et al., 1996] Longley, J. P., Shin, H.-W., Plumley, R. E., Silkowski, P. D., Day, I. J., Greitzer, E. M., Tan, C. S., and Wisler, D. C. (1996). Effects of rotating inlet distortion on multistage compressor stability. *Journal of Turbomachinery*, 118(2):181–188.

[Marble, 1948] Marble, F. E. (1948). The flow of a perfect fluid through an axial turbomachine with prescribed blade loading. *Journal of the Aeronautical Sciences*, 15(8):473–485.

[Mazzawy, 1977] Mazzawy, R. S. (1977). Multiple segment parallel compressor model for circumferential flow distortion. *Journal of Engineering for Power*, 99(2):288–296.

[McDougall et al., 1990] McDougall, N. M., Cumpsty, N. A., and Hynes, T. P. (1990). Stall inception in axial compressors. *Journal of Turbomachinery*, 112(1):116–123.

[Mehalic, 1988] Mehalic, C. (1988). Effect of spatial inlet temperature and pressure distortion on turbofan engine stability. In *24th Joint Propulsion Conference*, page 3016.

[Mehdi, 2014] Mehdi, A. (2014). Effect of swirl distortion on gas turbine operability. *Ph.D. Thesis, Cranfield University*.

[Micklow and Jeffers, 1981] Micklow, J. and Jeffers, J. (1981). Semi-actuator disk theory for compressor choke flutter. *NASA-CR-3426*.

[Motycka, 1985] Motycka, D. L. (1985). Reynolds number and fan/inlet coupling effects on subsonic transportinlet distortion. *Journal of Propulsion and Power*, 1(3):229–234.

[Nie et al., 2006] Nie, C., Zhang, J., Tong, Z., and Zhang, H. (2006). The response of a low speed compressor on rotating inlet distortion. *Journal of Thermal Science*, 15(4):314–318.

[Ochs et al., 2016] Ochs, S. S., Tillman, G., Joo, J., and Voytovych, D. M. (2016). Computational fluid dynamics-based analysis of boundary layer ingesting propulsion. *Journal of Propulsion and Power*, 33(2):522–530.

[Owens et al., 2008] Owens, L. R., Allan, B. G., and Gorton, S. A. (2008). Boundary-layer-ingesting inlet flow control. *Journal of Aircraft*, 45(4):1431–1440.

[Page et al., 2018] Page, J. H., Hield, P., and Tucker, P. G. (2018). Effect of inlet distortion features on transonic fan rotor stall. *Journal of Turbomachinery*, 140(7):071008.

[Pazur and Fottner, 1990] Pazur, W. and Fottner, L. (1990). The influence of inlet swirl distortions on the performance of a jet propulsion two-stage axial compressor. In *ASME 1990 International Gas Turbine and Aeroengine Congress and Exposition*, page V005T16A005. American Society of Mechanical Engineers.

[Pearson and McKenzie, 1959] Pearson, H. and McKenzie, A. B. (1959). Wakes in axial compressors. *The Aeronautical Journal*, 63(583):415–416.

[Perkins, 1979] Perkins, J. N. (1979). An actuator disk analysis of an isolated rotor with distorted inflow. *ADA069884, Technical rept. Jan 76-Dec 78*.

[Perovic et al., 2015] Perovic, D., Hall, C. A., and Gunn, E. J. (2015). Stall inception in a boundary layer ingesting fan. In *ASME Turbo Expo 2015: Turbine Technical Conference and Exposition*, page V02AT37A031. American Society of Mechanical Engineers.

[Peterson et al., 2017] Peterson, M. W., Gorrell, S. E., and List, M. G. (2017). Fourier descriptors for improved analysis of distortion transfer and generation. In *ASME Turbo Expo 2017: Turbomachinery Technical Conference and Exposition*, page V001T01A029. American Society of Mechanical Engineers.

[Plourde et al., 1968] Plourde, G., ROBERTS, F., and SMAKULA, F. (1968). Insights into axial compressor response to distortion. In *4th Propulsion Joint Specialist Conference*, page 565.

[Prince et al., 1975] Prince, D. C., Wisler, D. C., and Hilvers, D. E. (1975). A study of casing treatment stall margin improvement phenomena. In *ASME 1975 International Gas Turbine Conference and Products Show*, page V01AT01A059. American Society of Mechanical Engineers.

[Rabe et al., 1995] Rabe, D., Bolcs, A., and Russler, P. (1995). Influence of inlet distortion on transonic compressor blade loading. In *31st Joint Propulsion Conference and Exhibit*, page 2461.

[Reid, 1969] Reid, C. (1969). The response of axial flow compressors to intake flow distortion. In *ASME 1969 gas turbine conference and products show*, page V001T01A029. American Society of Mechanical Engineers.

[Reid and Moore, 1978] Reid, L. and Moore, R. D. (1978). Performance of single-stage axial-flow transonic compressor with rotor and stator aspect ratios of 1.19 and 1.26, respectively, and with design pressure ratio of 1.82. *NASA-TP-1338*.

[Sabo and Drela, 2015] Sabo, K. M. and Drela, M. (2015). Benefits of boundary layer ingestion propulsion. In *53rd AIAA Aerospace Sciences Meeting*, page 1667.

[Saddoughi et al., 2015] Saddoughi, S., Bennett, G., Boespflug, M., Puterbaugh, S. L., and Wadia, A. R. (2015). Experimental investigation of tip clearance flow in a transonic compressor with and without plasma actuators. *Journal of Turbomachinery*, 137(4):041008.

[SAE Standard, 2013] SAE Standard, 2013, A. (2013). Inlet total-pressure-distortion considerations for gas-turbine engines. ID: AIR1419B.

[SAE Standard, 2017] SAE Standard, 2017, A. (2017). A methodology for assessing inlet swirl distortion. ID: AIR5686.

[Salunkhe and Pradeep, 2010] Salunkhe, P. B. and Pradeep, A. M. (2010). Stall inception and its control in an axial flow fan under dynamic inflow distortion. *Proceedings of the Institution of Mechanical Engineers, Part A: Journal of Power and Energy*, 224(3):383–398.

[Sanger, 1976] Sanger, N. L. (1976). Performance of a 1.57 pressure-ratio transonic fan stage with a screen-induced 90 deg circumferential inlet flow distortion. *NASA-TN-D-8163*.

[Sanger, 1979] Sanger, N. L. (1979). Effect of rotor meridional velocity ratio on response to inlet radial and circumferential distortion. *NASA-TP-1278*.

[Sayma et al., 2000] Sayma, A. I., Vahdati, M., Sbardella, L., and Imregun, M. (2000). Modeling of three-dimensional viscous compressible turbomachinery flows using unstructured hybrid grids. *AIAA Journal*, 38(6):945–954.

[Schalkwyk et al., 1997] Schalkwyk, C. M. V., Paduano, J. D., Greitzer, E. M., and Epstein, A. H. (1997). Active stabilization of axial compressors with circumferential inlet distortion. In *ASME 1997 International Gas Turbine and Aeroengine Congress and Exhibition*, page V004T15A020. American Society of Mechanical Engineers.

[Sghaier et al., 2013] Sghaier, T. B., Mehdi, A., Pachidis, V., and MacManus, D. (2013). A parametric numerical study of the effects of inlet swirl distortion on a transonic compressor stage. In *ASME Turbo Expo 2013: Turbine Technical Conference and Exposition*, page V06AT35A007. American Society of Mechanical Engineers.

[Shabbir et al., 1997] Shabbir, A., Celestina, M., Adamczyk, J., and Strazisar, A. (1997). The effect of hub leakage flow on two high speed axial flow compressor rotors. In *ASME 1997 International Gas Turbine and Aeroengine Congress and Exhibition*, pages V001T03A053–V001T03A053. American Society of Mechanical Engineers.

[Sharma et al., 2013] Sharma, G., Zori, L., Connell, S., and Godin, P. (2013). Efficient computation of large pitch ratio transonic flow in a fan with inlet distortion. In *ASME Turbo Expo 2013: Turbine Technical Conference and Exposition*, page V06CT42A025. American Society of Mechanical Engineers.

[Shaw et al., 2014] Shaw, M. J., Hield, P., and Tucker, P. G. (2014). The effect of inlet guide vanes on inlet flow distortion transfer and transonic fan stability. *Journal of Turbomachinery*, 136(2):021015.

[Sheoran and Bouldin, 2008] Sheoran, Y. and Bouldin, B. (2008). A versatile design of a controlled swirl distortion generator for testing gas turbine engines. In *ASME Turbo Expo 2008: Power for Land, Sea, and Air*, pages 81–92. American Society of Mechanical Engineers.

[Sheoran et al., 2010] Sheoran, Y., Bouldin, B., and Krishnan, P. M. (2010). Compressor performance and operability in swirl distortion. In *ASME Turbo Expo 2010: Power for Land, Sea, and Air*, pages 2453–2464. American Society of Mechanical Engineers.

[Small and Lewis, 1985] Small, C. and Lewis, J. (1985). High speed compressor rig as a stall recovery research tool. In *21st Joint Propulsion Conference*, page 1428.

[Smith, 1947] Smith, A. (1947). The jet airplane utilizing boundary layer air for propulsion. *Journal of the Aeronautical Sciences*, 14(2):97–109.

[Smith and Cumpsty, 1984] Smith, G. and Cumpsty, N. A. (1984). Flow phenomena in compressor casing treatment. *Journal of Engineering for Gas Turbines and Power*, 106(3):532–541.

[Soeder and Bobula, 1982] Soeder, R. H. and Bobula, G. A. (1982). Effect of steady-state pressure distortion on inlet flow to a high-bypass-ratio turbofan engine. *NASA-TM-82964*.

[Soeder et al., 1985] Soeder, R. H., Mehalic, C. M., and Stancik, K. (1985). Effect of steady-state temperature distortion on inlet flow to a high-bypass-ratio turbofan engine. *NASA-TM-86896*.

[Spakovszky et al., 1999] Spakovszky, Z. S., Weigl, H. J., Paduano, J. D., Schalkwyk, C. M. V., Suder, K. L., and Bright, M. M. (1999). Rotating stall control in a high-speed stage with inlet distortion: Part iradial distortion. *Journal of Turbomachinery*, 121(3):510–516.

[Spalart, 2001] Spalart, P. (2001). Young-person's guide simulation grids to detached-eddy. *Seattle, Washington, NASA/CR-2001-211032*.

[Stenning, 1980] Stenning, A. (1980). Inlet distortion effects in axial compressors. *Journal of Fluids Engineering*, 102(1):7–13.

[Strazisar et al., 1989] Strazisar, A. J., Wood, J. R., Hathaway, M. D., and Suder, K. L. (1989). Laser anemometer measurements in a transonic axial-flow fan rotor. *NASA-TP-2879*.

[Suder et al., 2013] Suder, K., Delaat, J., Hughes, C., Arend, D., and Celestina, M. (2013). Nasa environmentally responsible aviation project's propulsion technology phase i overview and highlights of accomplishments. In *51st AIAA Aerospace Sciences Meeting including the New Horizons Forum and Aerospace Exposition*, page 414.

[Sun et al., 2018] Sun, D., Li, J., Dong, X., Gu, B., and Sun, X. (2018). Effects of rotating inlet distortion on two-stage compressor stability with stall precursor-suppressed casing treatment. In *ASME Turbo Expo 2018: Turbomachinery Technical Conference and Exposition*, page V02AT45A025. American Society of Mechanical Engineers.

[Takata and Tsukuda, 1977] Takata, H. and Tsukuda, Y. (1977). Stall margin improvement by casing treatmentits mechanism and effectiveness. *Journal of Engineering for Power*, 99(1):121–133.

[Tan et al., 2010] Tan, C. S., Day, I., Morris, S., and Wadia, A. (2010). Spike-type compressor stall inception, detection, and control. *Annual Review of Fluid Mechanics*, 42:275–300.

[Uranga et al., 2014] Uranga, A., Drela, M., Greitzer, E., Titchener, N., Lieu, M., Siu, N., Huang, A., Gatlin, G. M., and Hannon, J. (2014). Preliminary experimental assessment of the boundary layer ingestion benefit for the d8 aircraft. In *52nd Aerospace Sciences Meeting*, page 0906.

[Uranga et al., 2017] Uranga, A., Drela, M., Greitzer, E. M., Hall, D. K., Titchener, N. A., Lieu, M. K., Siu, N. M., Casses, C., Huang, A. C., and Gatlin, G. M. (2017). Boundary layer ingestion benefit of the d8 transport aircraft. *AIAA Journal*, pages 3693–3708.

[Uranga et al., 2018] Uranga, A., Drela, M., Hall, D. K., and Greitzer, E. M. (2018). Analysis of the aerodynamic benefit from boundary layer ingestion for transport aircraft. *AIAA Journal*, 56(11):4271–4281.

[Vahdati et al., 2005] Vahdati, M., Sayma, A. I., Freeman, C., and Imregun, M. (2005). On the use of atmospheric boundary conditions for axial-flow compressor stall simulations. *Journal of turbomachinery*, 127(2):349–351.

[VanZante et al., 2009] VanZante, D. E., Podboy, G. G., Miller, C. J., and Thorp, S. A. (2009). Testing and performance verification of a high bypass ratio turbofan rotor in an internal flow component test facility. *NASA/TM-2009-215661*.

[Visbal and Shang, 1989] Visbal, M. R. and Shang, J. S. (1989). Investigation of the flow structure around a rapidly pitching airfoil. *AIAA Journal*, 27(8):1044–1051.

[Viswanath and Govardhan, 1996] Viswanath, K. and Govardhan, M. (1996). Effect of circumferential inlet flow distortion and swirl on the flow field of an axial flow fan stage. In *ASME 1996 International Gas Turbine and Aeroengine Congress and Exhibition*, page V001T01A081. American Society of Mechanical Engineers.

[Vo et al., 2008] Vo, H. D., Tan, C. S., and Greitzer, E. M. (2008). Criteria for spike initiated rotating stall. *Journal of turbomachinery*, 130(1):011023.

[Wadia, 2011] Wadia, A. R. (2011). Experimental investigation of a forward swept rotor in a multistage fan with inlet distortion. *International Journal of Aerospace Engineering*, 2011.

[Wadia et al., 2004] Wadia, A. R., Hah, C., and Rabe, D. (2004). The impact of forward sweep on tip clearance flows in transonic compressors. In *24th International Congress of the Aeronautical Sciences, Yokohama, Japan, Paper No. ICAS20046.2*, volume 1.

[Wadia et al., 2002] Wadia, A. R., Szucs, P. N., Crall, D. W., and Rabe, D. C. (2002). Forward swept rotor studies in multistage fans with inlet distortion. In *ASME Turbo Expo 2002: Power for Land, Sea, and Air*, pages 11–21. American Society of Mechanical Engineers.

[Welstead and Felder, 2016] Welstead, J. and Felder, J. L. (2016). Conceptual design of a single-aisle turboelectric commercial transport with fuselage boundary layer ingestion. In *54th AIAA Aerospace Sciences Meeting*, page 1027.

[Weston et al., 2015] Weston, D. B., Gorrell, S. E., Marshall, M. L., and Wallis, C. V. (2015). Analysis of turbofan performance under total pressure distortion at various operating points. In *ASME Turbo Expo 2015: Turbine Technical Conference and Exposition*, page V02AT37A028. American Society of Mechanical Engineers.

[Wick et al., 2015] Wick, A. T., Hooker, J. R., and Zeune, C. H. (2015). Integrated aerodynamic benefits of distributed propulsion. In *53rd AIAA Aerospace Sciences Meeting*, page 1500.

[Wislicenus, 1960] Wislicenus, G. F. (1960). Hydrodynamics and propulsion of submerged bodies. *ARS Journal*, 30(12):1140–1148.

[Xu, 2002] Xu, L. (2002). Assessing viscous body forces for unsteady calculations. In *ASME Turbo Expo 2002: Power for Land, Sea, and Air*, pages 323–331. American Society of Mechanical Engineers.

[Yang and G., 2012] Yang, B. and G., C. G. (2012). The effects of radially distorted incident flow on performance of axial-flow fans with forward-skewed blades. *Journal of Turbomachinery*, 135(1):12. SO: Journal of Turbomachinery October 31, 2012 135(1):011039.

[Yao et al., 2007] Yao, J., Gorrell, S., and Wadia, A. (2007). A time-accurate cfd analysis of inlet distortion induced swirl in multistage fans. In *43rd AIAA/ASME/SAE/ASEE Joint Propulsion Conference & Exhibit*, page 5059.

[Yao et al., 2010a] Yao, J., Gorrell, S. E., and Wadia, A. R. (2010a). High-fidelity numerical analysis of per-rev-type inlet distortion transfer in multistage fanspart i: Simulations with selected blade rows. *Journal of Turbomachinery*, 132(4):041014.

[Yao et al., 2010b] Yao, J., Gorrell, S. E., and Wadia, A. R. (2010b). High-fidelity numerical analysis of per-rev-type inlet distortion transfer in multistage fanspart ii: Entire component simulation and investigation. *Journal of Turbomachinery*, 132(4):041015.

[Yeh, 1959] Yeh, H. (1959). An actuator disc analysis of inlet distortion and rotating stall in axial flow turbomachines. *Journal of the Aerospace Sciences*, 26(11):739–753.

[Zhao et al., 2018] Zhao, F., Dodds, J., and Vahdati, M. (2018). Poststall behavior of a multistage high speed compressor at off-design conditions. *Journal of Turbomachinery*, 140(12):121002.